A Design Procedure
for Low and High Head Inducers

Vom Fachbereich Maschinenbau und Verfahrenstechnik
der Technischen Universität Kaiserslautern
zur Verleihung des akademischen Grades

Doktor-Ingenieur (Dr.-Ing.)
genehmigte
Dissertation

von

Herrn

Dipl.-Ing. Matthias Mohr
aus Saarbrücken

Vorwort

Diese Arbeit entstand im Rahmen meiner Beschäftigung als wissenschaftlicher Mitarbeiter am Lehrstuhl für Strömungsmechanik und Strömungsmaschinen (SAM) der TU Kaiserslautern.

Mein besonderer Dank gilt meinem Doktorvater Herrn Prof. Dr.-Ing. Martin Böhle. Er gab mir nicht nur alle Freiheiten bei der Gestaltung dieser Arbeit, sondern ermöglichte mir auch die Übernahme interessanter Tätigkeiten in der Lehre sowie die Zusammenarbeit mit verschiedenen Projektpartnern aus Forschung und Industrie. Herrn Prof. Dr.-Ing. Andreas Brümmer danke ich für die Übernahme des Koreferats und für sein entgegengebrachtes Interesse an meiner Arbeit. Herrn Prof. Dr.-Ing. Jörg Seewig danke ich für die Übernahme des Vorsitzes der Prüfungskommission.

Meinen Kolleginnen und Kollegen am SAM danke ich für anregende Diskussionen und die stets freundschaftliche Atmosphäre. Besonderer Dank gilt meinem Kollegen Björn Gwiasda, der immer ein offenes Ohr für mich hatte und mir mit Rat und Tat zur Seite stand. Meinen Bürokolleginnen und -kollegen Annika Fleder, Gunther Müller und Andreas Baum danke ich für das nette Miteinander und dafür, dass sie mich von morgens bis abends ertragen haben.

Ferner richtet sich mein Dank an meine ehemaligen Studenten, die im Rahmen ihrer Abschlussarbeiten und Tätigkeiten als Hilfswissenschaftler maßgeblich zum Gelingen dieser Arbeit beigetragen haben.

Meiner Familie und meinen Freunden danke ich von ganzem Herzen für ihre bedingungslose und liebevolle Unterstützung während meines gesamten Werdegangs.

Contents

Nomenclature

Symbols

A	Area	(m^2)
b	Blade blockage	$(-)$
C	Absolute velocity $\times$ local radius	$(\mathrm{m}^2\mathrm{s}^{-1})$
c	Absolute flow velocity	$(\mathrm{m\,s}^{-1})$
c'	Chord in conformal cascade	$(-)$
d	Diameter	(m)
f_c	Correction factor	$(-)$
g	Gravitational acceleration	(ms^{-2})
H	Head	(m)
I	Turbulence intensity	$(-)$
i	Incidence angle	$(°)$
k	Hub blockage factor	$(-)$
k	Turbulent kinetic energy	$(\mathrm{m}^2\mathrm{s}^{-2})$
l	Length	(m)
M	Torque	(Nm)
m	Meridional coordinate	(m)
m'	Radius normalized meridional coordinate	$(-)$
N	Basis function	$(-)$
N_{SS}	Suction specific speed (US definition)	(min^{-1})
NPSH	Net positive suction head (NPSH value)	(m)
n	Rotational speed	(min^{-1})
n_{SS}	Suction specific speed (European definition)	(min^{-1})
P	Power	(W)
p	Pressure	(Pa)
Q	Volume flow	$(\mathrm{m}^3\mathrm{s}^{-1})$
r	Radius	(m)
s	Spacing	$(-)$
s'	Spacing in conformal cascade	$(-)$
U	Knot vector	$(-)$
u	Circumferential velocity	$(\mathrm{m\,s}^{-1})$
u	Curve parameter	$(-)$
u_i	Velocity component (index notation)	$(\mathrm{m\,s}^{-1})$
u_j	Knot value (at index j)	$(-)$

W	Relative velocity $\times$ local radius	$(\mathrm{m^2 s^{-1}})$
w	Relative flow velocity	$(\mathrm{m\,s^{-1}})$
x	x-coordinate	(m)
y	Specific work	$(\mathrm{m^2 s^{-2}})$
y	y-coordinate	(m)
z	z-coordinate	(m)
Z	Number of blades	$(-)$
α	Absolute flow angle	$(°)$
α_a	Angle of attack	$(°)$
β	Relative flow angle	$(°)$
β_b	Blade angle	$(°)$
Γ	Circulation	$(\mathrm{m^2 s^{-1}})$
γ	Vorticity density	$(\mathrm{m^2 s^{-1}})$
γ	Slip factor	$(°)$
δ	Deviation angle	$(°)$
ϵ	Tolerance value	$(-)$
ε	Inclination angle	$(°)$
η	Efficiency	$(-)$
η_h	Hydraulic efficiency	$(-)$
θ	Circumferential coordinate or wrap angle	(rad)
λ	Performance coefficient	$(-)$
λ	Helical lead	$(\mathrm{m\,rad^{-1}})$
μ	Dynamic viscosity	$(\mathrm{Pa\,s})$
μ_t	Turbulent viscosity	$(\mathrm{Pa\,s})$
ν	Hub to shroud diameter ratio	$(-)$
ξ	Loss coefficient	$(-)$
ρ	Density	$(\mathrm{kg\,m^{-3}})$
σ	Cavitation coefficient	$(-)$
σ'	Solidity in conformal cascade	$(-)$
τ	Shear stress	$(\mathrm{N\,m^{-2}})$
φ	Flow coefficient	$(-)$
Ψ	Stokes' stream function	$(\mathrm{m^3 s^{-1}})$
ψ	Head coefficient	$(-)$
Ω_{SS}	Suction specific speed	$(-)$
ω	Angular velocity	$(\mathrm{rad\,s^{-1}})$
ω	Turbulent frequency	$(\mathrm{s^{-1}})$
ω	Relaxation factor	$(-)$

C	Parametric curve
c	Absolute velocity
n	Normal vector
P	Control point
Q	Interpolation point
u	Circumferential velocity
W	Relative velocity in conformal cascade
w	Relative velocity

Indices

ax	Axial
b	Blade
c	Corrected
d	Design point
eff	Effective
h	Hub or hydraulic
le	Leading edge
m	Meridional or mean
max	Maximum
min	Minimum
opt	Optimum
ps	Pressure side
r	Radial
s	Shroud
ss	Suction side
te	Trailing edge
th	Theoretical
θ	Circumferential
tot	Total
$*$	Normalized or relative
ref	Reference value
rms	Root mean square value or value at root mean square radius
z	Axial (in z-direction)

Acronyms / Abbreviations

BEP	Best Efficiency Point
CAD	Computer Aided Design
CAE	Computer Aided Engineering
CFD	Computational Fluid Dynamics
EXP	Experiment
GCI	Grid Convergence Index
NPSH_a	Net Positive Suction Head available
NPSH_r	Net Positive Suction Head required
SHP	Simple Head Prediction
SMA	Simple Meridional Analysis
SOR	Successive Over-Relaxation

Abstract

The present thesis describes the development and the evaluation of a design procedure of inducer with arbitrary meridional and blade shape. This special type of pump impeller, which is usually mounted upstream of a main pump impeller, is employed in many applications demanding the realization of low NPSH values. An inducer basically increases suction performance by producing mostly a small pressure rise while allowing for a greater degree of cavitation, that is the formation of vapor bubbles, at its inlet than a conventional pump impeller. This is achieved by specially designed blade channels promoting the collapse of the produced vapor bubbles.

The main focus of the present thesis is the description of the design method, which enables the generation of the three-dimensional blade geometry. The method is based on a parametric representation of the geometry considering the particular requirements for inducers and the publicly available design practice. Within this approach the sequence of design steps is adapted from the classical design process of mixed flow and radial impellers. As a consequence leading and trailing edge blade angles are determined based on simplifications and certain empirical assumptions for multiple blade sections and are used to design the blade camber curves. Along the camber curves the blade profile is generated following a thickness distribution that has to be prescribed. A special feature of the newly developed method is that arbitrary shaped, asymmetric thickness distributions can be realized.

Due to the detailed description of the design and calculation steps a fully comprehensible procedure is outlined, which covers the development of inducer bladings from an initial set of duty parameters to the final three-dimensional blade geometry. The components involved in the design procedure are tested by designing two exemplary inducers and they are assessed by comparison with numerical simulations. Functioning of these inducers in the real application is finally demonstrated with water tests.

The main result of this dissertation is a design software for inducers allowing for the design of three-dimensional, asymmetrically profiled bladings. The developed software is free of commercial third-party libraries. As a consequence a program is available that can be modified and extended as desired. As potential future development goals inducers with splitter and tandem blades as well as an integrated design of inducer and impeller are proposed.

Kurzfassung

Die vorliegende Dissertation beschreibt die Entwicklung und Erprobung einer Auslegungsprozedur für Inducer mit beliebiger Meridian- und Schaufelgeometrie. Dieser spezielle Typ eines Pumpenlaufrades, der in der Regel stromauf des eigentlichen Laufrads angeordnet ist und deshalb auch als Vorsatzläufer bezeichnet wird, kommt in vielen Anwendungen zum Einsatz, in denen niedrige NPSH-Werte realisiert werden müssen. Ein Inducer erhöht die Saugfähigkeit der Pumpeneinheit, indem er einen meist geringen Vordruck generiert und dabei bedingt durch seine Formgebung ein wesentlich höheres Ausmaß an Kavitation, d.h. das Entstehen von Dampfblasen, an seinem Eintritt toleriert als ein konventionelles Pumpenlaufrad. Dieser Effekt wird durch speziell gestaltete Schaufelkanäle erzeugt, die den Zerfall von entstehenden Dampfblasen begünstigen. Kern der vorliegenden Arbeit ist daher die Beschreibung einer parametrischen Auslegungsprozedur, die eine Generierung der dreidimensionalen Schaufelgeometrie ermöglicht. Das Verfahren beruht auf einer parametrischen Abbildung der Geometrie unter Berücksichtigung der besonderen Anforderungen an Inducer und der bestehenden, öffentlich zugängigen Auslegungspraxis. Die Abfolge der Auslegungsschritte und den entsprechenden Berechnungen ist dabei der klassischen Auslegung von Diagonal- und Radialrädern nachempfunden. Das bedeutet insbesondere, dass die Ein- und Austrittswinkel auf verschiedenen Schaufelschnitten basierend auf vereinfachten und zum Teil empirischen Annahmen bestimmt und zur Gestaltung der Schaufelskelettlinien verwendet werden. Entlang dieser Skelettlinien wird das Schaufelprofil gemäß einer zu definierenden Dickenverteilung erzeugt. Eine Besonderheit der neu entwickelten Methode besteht dabei darin, dass beliebig geformte, asymmetrische Dickenverteilungen realisiert werden können. Durch die detaillierte Darstellung der einzelnen Auslegungs- und Berechnungsschritte wird ein vollständig nachvollziehbares Vorgehen dargelegt, welches die Entstehung der Inducerbeschauflung, ausgehend von vorgegebenen Betriebsdaten bis hin zur dreidimensionalen Schaufelgeometrie abdeckt. Die einzelnen Komponenten der Auslegungsprozedur werden anhand der Auslegung zweier Beispielinducer erprobt und durch den Vergleich mit Strömungssimulationen bewertet. Die Funktionsfähigkeit dieser Inducer in der realen Anwendung wird schließlich im Wasserversuch demonstriert.

Ergebnis dieser Dissertation ist eine Auslegungssoftware für Inducer, die das Erzeugen einer dreidimensionalen, assymetrisch profilierten Beschaufelung ermöglicht. Das Programm ist frei von kommerziellen Bibliotheken von Fremdanbietern, sodass es in Zukunft beliebig modifiziert und erweitert werden kann. Als mögliche Weiterentwicklungsziele werden insbesondere Inducer mit Splitter- und Tandembeschaufelungen sowie die integrierte Auslegung von Inducer und Laufrad angesehen.

1 Introduction

1.1 Problem Statement

Transporting and pressurizing some sort of fluid is an integral part of various applications ranging from processes in the chemical industry or in power plants and water distribution systems to cooling and fuel supply systems. When fluids can be considered as incompressible and a continuous fluid flow is required this process is very likely performed by centrifugal pumps.

The rotating motion of the impeller blades of centrifugal pumps inevitably causes a local pressure drop at the inlet portion of the blade channels. High rotational speeds, low inlet pressures or fluids that are stored and fed to the pump at a state close to the saturation pressure increase the risk of cavitation in this region. Cavitation, that is the transition of the fluid from the liquid to the vapor phase and the subsequent collapse of the vapor regions, is feared due to its potentially disastrous effect on pump performance and the damage it can cause to the pump impeller and other pump components.

Out of the application-specific need to operate pumps even under circumstances where cavitation can't be avoided the so-called inducer has been developed. The inducer basically is an auxiliary impeller, which is able to produce a comparatively small pressure rise even under heavily cavitating conditions at its inlet. Mounted upstream of the regular pump the inducer is used to generate the pressure required for cavitation free inlet flow to the subsequent impeller. This effectively reduces the risk of cavitation breakdown of the whole pump and allows for operation way beyond the suction capabilities of standard pumps.

Successful usage of inducers are reported from all sort of pump applications but the one that is most popular and may have contributed most to the development of this type of impeller is the liquid rocket engine. The concurrent desire to reduce the engine weight and increase its performance lead to the development of turbopumps, which operate at very high rotational speeds to generate the fuel pressure required for injection. Combining this with low inlet pressures required to minimize fuel tank weight, these pumps have to provide the highest suction performance known in the field.

The use of inducers in this sort of high performance machine but also in a broad range of other applications produced well known design guide lines. These are mainly based on empirical knowledge, which was obtained over years of design and test experience. With the increasing availability of computing resources steadily improving numerical methods emerge enabling researchers to investigate the features of new designs in more detail. Modern 3D-CFD methods also help to understand the complex internal flow patterns

specific to inducers. Of course this resulted in improvement of design techniques. But, in spite of these improvements, there still is no definite publicly available standard for inducer design and some parameters are still chosen based on expert knowledge treasured by the industry and not available to independent researchers.

Even if performance data and some basic dimensions of tested inducers are regularly provided, geometric details and the reasoning behind them is only rarely published. This is especially true for geometric features like angle and thickness distributions, which are among the most important parameters used by the designers to tweak the performance. Furthermore commercial turbomachinery design software often hides the internal geometrical processes from the user and only offers a limited selection of parameters to determine the final blade shape. While this certainly helps in reducing time and effort needed to obtain reasonable designs, understanding of the influence of certain parameters might be complicated.

For these reasons this thesis aims to provide a fully comprehensible design procedure enabling the future designer to investigate the influence of important geometric features in a parametrical, systematic and very detailed way. Thus, it can be seen as a first step to a better understanding of inducer design and performance.

1.2 Scope of this Work

This thesis wants to provide a description of a parametric inducer design procedure, which is implemented in computer code. It enables the design engineer to create inducer blades by specification of a parameter set. The choice of parameters is particularly focused on the characteristic features of inducers but can be easily adapted for general turbomachinery design. Whenever possible the parameters are adopted from publicly available and accepted design practice. A most flexible procedure is realized by using B-spline curves for the meridional section design as well as for the blade shape design. Special emphasis is placed on the possibility to create asymmetric and sharpened blade profiles, which are typical for inducers with high suction performance. An interface to modern CAD and CFD tools is provided to enable a smooth transition to manufacturing and numerical simulation.

This approach shall open the door to future studies of the influence of single or multiple parameters on the performance characteristics of inducer-pumps. Throughout the inducer design procedure analytical equations are preferred over empirical relations wherever possible in order to facilitate systematic parameter variations.

Besides the geometrical design features a simplified two-dimensional meridional flow computation is integrated in the design process to provide the blade design with a

simple but physical foundation by using the streamlines extracted from the flow solution. Furthermore a basic non-cavitating head prediction method that operates in the two-dimensional cascade planes is provided. These simple methods can be used by the designer to obtain a direct feedback on the influence of the parameter changes on the head produced by the inducer. Both methods, the meridional flow analysis and the head prediction procedure, are verified and validated and their features as well as their limitations are discussed. However, the geometrical design procedure does not rely in any way on these analysis methods such that more advanced methods can be added to the procedure in future projects easily.

The application of the design procedure is demonstrated and assessed by experimental validation of a real inducer-pump setup. An existing test bench is modified to allow for investigation of the influence of the inducer on the pump. In this test setup not only on the head and efficiency characteristics but also the suction performance is investigated. By utilizing a special casing design the inducer head is estimated during operation of the whole pump unit. This will on the one hand show the potential of the prototypes developed in this thesis and the other hand it will deliver indications pointing to possible extensions and further developments of the design program.

Eventually, an equally important goal of this thesis is to offer a complete and comprehensible description of the steps needed to obtain a three-dimensional blade geometry. It can therefore serve as a guide to students and researchers concerned with the design of inducers or any other related device. The code developed is non-commercial and only uses publicly available packages, so that it can be edited and extended as needed.

1.3 Outline

Chapter 2 deals with the theoretical fundamentals of this thesis. After a summary of the historical background of inducer development, a classification of this special type of impeller and an overview of the necessary design steps is provided. The fundamentals of turbomachinery design are summarized and the mathematical notation used in this thesis is explained. Since the design methods rely heavily on the usage of B-splines a brief discussion of geometrical design is provided. Furthermore, a detailed description of the meridional analysis and the head prediction method developed in the course of this thesis is given. At the end of this chapter the relevant equations involved in performing the CFD simulations presented in this thesis are summarized. In Chapter 3 the developed procedure is presented and the implementation of the design steps is explained in detail. The description essentially follows the sequence of design steps. Verification and validation of the components of the design system is presented in Chapter 4. After

introducing the test cases the methods for the meridional flow analysis and the head estimation are verified and validated by comparison with different types of numerical simulations. The prototypes manufactured on the basis of the test case geometries are eventually tested in a real pump unit in order to demonstrate that inducers generated with the design procedure work as expected. Some concluding remarks and an outlook to future research is given in Chapter 5.

2 Theoretical Fundamentals and Methods

2.1 The Inducer

2.1.1 Purpose and Applications

The inducer is a special type of axial pump impeller, which is especially designed to improve suction performance of a centrifugal pump. In the pioneering work of Ross and Banerian [63] these devices are also denoted by "cavitating inducers" in order to point out that these impellers are intended to operate with "considerable cavitation". The need to operate pumps in a state that is normally avoided due to the increased risks of damage and performance breakdown primarily originated from rocket engine development. The simple reason for this is that pumps with improved suction performance can be operated at higher rotational speeds, which in turn allows for a reduction of pump weight. As it turned out, higher rotational speeds could also prove advantageous in other commercial applications where reduction in weight could lead to cheaper pump units and high-speed drives could be employed [63]. Furthermore, applications requiring increased suction performance are those, that are utilized to transport fluids at temperatures close to their saturation pressure as it is the case for boiler feed pumps of e.g. thermal power stations or in processes handling hydrocarbons or cryogenic fluids. Other commercial applications making use of inducers are fuel feed systems and water jet propulsion [46].

2.1.2 Historical Background and State of the Art of Inducer Design

Inducers have been developed in the last century due to the increasing demand for pumps that have high suction capabilities. This was a direct result of increasing pump speed and the use of fluids that need to be handled close to their saturation pressure. As already mentioned, the most popular application where both of these requirements have to be met are liquid rocket engines. In this type of engine pumps that are driven by turbines, so-called turbopumps, are used to pressurize cryogenic fuels. Obviously high rotational speeds and low tank pressures are helpful in this kind of application in order to increase the power-to-weight ratio, which is one of the key development goals in turbopump and the whole rocket engine development [53]. Driven by research interest of the aerospace industry but also by other industries a vast amount of publications focusing on inducers appeared in the past and still new results are published on a regular basis. Because of this only a brief overview of the work done in the past is presented and only those findings are explicitly referenced that are most relevant for the present work.
The research in this field can be roughly categorized into the following groups:

1. Influence of design details on non-cavitating and cavitating performance

2. Analysis of flow phenomena and related effects

3. Prediction of non-cavitating and cavitating performance

4. Establishing of design rules

Since most publications cover aspects of more than one of the above groups a strict assignment of a single reference to one of the categories is hardly possible. As a matter of fact, in most of the publications belonging (more or less) to the first group some existing inducer designs are investigated and the influence of distinct geometrical features on the performance is analyzed. For this purpose different theoretical, numerical and experimental methods are used and the results are interpreted. Consequently, aspects of the second, third and even the fourth group may be included as well.

Research topics belonging to the second group can be categorized further into investigations of non-cavitating and cavitating flow phenomena. While the non-cavitating phenomena include effects like inlet recirculation (backflow), tip clearance flow and secondary flow effects, the former deals with phenomena like rotating cavitation, cavitation instabilities, thermal effects on cavitation and the influence of cavitation on rotordynamics. Since these topics are of minor interest in the context of the current work, they are not mentioned explicitly in the remainder of this section but discussion of these phenomena can be found in the well-known review papers also discussed below (see e.g. Acosta [2], Janigro and Ferrini [37], Lakshminarayana [46]).

Methods described in research results of the third category can also be divided into non-cavitating and cavitating performance prediction methods. The methods can range from simple empirical relations to complex three-dimensional computational methods [46]. As already mentioned above only some of the most relevant methods are addressed and discussed briefly below.

Clearly, the references belonging to the fourth group are the most valuable in the context of the present work. They summarize past design experience and formulate the state of the art of inducer design. Appearing in form of review papers or monographs, the knowledge summarized in these works is used as the basis for the geometry parametrization applied in the design procedure developed in the course of this thesis.

Theoretical aspects about inducers were (publicly) discussed for the first time in the already cited work of Ross and Banerian [63] but not much details about the actual design are provided. Experimental investigations and some theoretical considerations were presented by Carpenter [19], who investigated three-bladed helical inducers with different solidity ranging from 2.5 to 3.25. It was noted by the author of this work that

the upper limit of practical solidity might be well below the values under investigation. Acosta [1] investigated two-, three-, and four bladed inducers in the same range of solidity and analyzed the influence of tip clearance on cavitating and non-cavitating performance. It was found that similar to non-cavitating performance an increase in tip clearance reduces suction performance. In addition to this a visual study of different cavitation phenomena was conducted.

Parallel to the aforementioned investigations theoretical and numerical methods describing the flow through inducers and estimating their performance evolved. The work of Stripling and Acosta [66] and Stripling [65] for example, focused on the leading edge design and presents a theoretical method to estimate the cavity shape and extend. A method to predict the non-cavitating and cavitating (suction) performance was proposed by Cooper [23]. The authors developed an approximate, three-dimensional approach to compute the single and two-phase flow through inducers.

Many technical reports dealing with the design not only of the inducers of turbopumps but of the whole rocket engine were produced by researchers at NASA at that time and are publicly available today directly from NASA archive servers. Regarding the design of the inducers the monograph by Jakobsen [36] is the most valuable one, because it contains the state-of-the-art design guidelines of that time and considers all the relevant details of the inducer design that are still applied today.

Besides giving a good overview of the topic and the reasoning of why inducers are useful devices, the work of Janigro and Ferrini [37] also provides some valuable thoughts about the design practice of inducers. Furthermore, the off-design behavior of the inducer is discussed in the case of non-cavitating and cavitating flow and the influence of solidity, tip-clearance, leading edge thickness and sweepback on cavitating performance at design flow rate are investigated. Of special interest to the designer are the tendencies mentioned about the beneficial impact of the leading edge backward sweep on cavitation instabilities, which occur mostly at off-design operation. Valuable are also the attempts to explain rotating cavitation and unstable cavitation, which are phenomena covered by the second group of publications.

The three-dimensional flow field of non-cavitating rocket pump inducers was studied extensively by Lakshminarayana [45] and Lakshminarayana and Gorton [48]. Perhaps the most well-known survey of the major findings in this field at that time, considering mainly non-cavitating performance of inducers, is given by Lakshminarayana [46]. The work mainly focuses on internal flow structures and the most relevant theoretical methods, which have been developed so far and have been used for the analysis of the complicated flow in inducers.

Extensive information with a focus on preliminary design considerations not only for

inducers but also for the different types of turbomachinery used in turbopump development is given by Wisclicenus [71]. Although inducer design only is addressed in one of the chapters useful hints especially for choosing the basic dimensions of the inducer-impeller combination are provided.

A method to estimate the NPSH of inducers, was published by Furst and Desclaux [30]. It is based on the assumption of two-dimensional sheet cavitation and is not easy to apply due to a complicated empirical relation [38].

One of the most concise description of the inducer, its applications and its flow phenomena is given in the more recent review paper by Acosta [2]. Besides summarizing the most important features and design parameters of inducers, some more practical implications of inducer applications are discussed. Especially the influence of the inducer on system dynamics is described.

Bakir et al. [12] proposed a design procedure including performance estimation for axial inducers, relying to some extent on the design guidelines of [36]. However, not all design steps are documented and the details of performance estimation are not included in full detail in the paper.

In the latest review paper published by Japikse [38] a historical overview of established design practice is given and a survey of the corresponding literature is provided. However, the author states that generalization of the results extracted from these sources might be difficult. According to the author CFD simulations are mandatory in the inducer design process and should be applied to obtain improved designs.

In fact, with the increasing availability of computing power the number of studies using three-dimensional, viscous CFD simulations also increased. Examples can be found in references [14, 22, 24, 41] and many others.

Interestingly the comparatively old-fashioned topic of performance prediction by simple analytical and semi-empirical methods that produce results a lot faster than any CFD code available today was rediscovered recently. Although it was already concluded by Lakshminarayana [46] that inviscid methods for performance prediction don't really help in understanding the real flow phenomena and fundamentally depend upon the empirical models, they still can prove useful in preliminary design iterations. In what follows two examples of such methods are described. In the first approach published by Bramanti et al. [16] and by d'Agostino et al. [25] the single-phase flow through an inducer is modeled as incompressible, inviscid and irrotational. The basic idea of the method is the superposition of an axisymmetric meridional flow with a two-dimensional slip velocity correction. This correction is applied on axial cross sections where the axial velocity is assumed to be constant along the radial coordinate. Because fully guided flow is assumed in the method, a model equation is used to account for flow deviation at

the inducer trailing edge. Losses that are caused by incidence and friction are included by using a combined loss function. This loss function depends on different coefficients that are functions of inlet flow and inducer geometry. Unfortunately, these functions are not published together with the validation data, which attests very good agreement between the predicted and the test results.

In the second approach, Li [51] proposed a method consisting of a singularity method in combination with a loss model and demonstrated its application to axial-flow inducers. Under the assumption of steady, axisymmetric, inviscid and incompressible flow and uniform inlet velocity the coaxial streamlines are computed by basic application of the continuity equation. Using published experimental data of 17 different inducers a correction factor to the model given in Kita et al. [42] was derived. All the inducers investigated are designed with a cylindrical meridional section and only two of the investigated inducers have blades with variable lead. Furthermore some assumptions have to be made in the cases where thickness and tip clearance values have not been reported. Despite its simplicity the results produced by the method show very good agreement with experimental data. However, the original approach discussed in Li [51] is limited to axial-flow inducers and the way the meridional flow is estimated cannot directly be transferred to inducers with different hub and / or shroud shapes. This is why in the present work an attempt is presented to extend the method to arbitrary shaped inducers.

To conclude this section it shall be remarked that advices and guidelines regarding the design of inducers can also be found in the textbooks by Brennen [17], Japikse et al. [39] and Gülich [31]. In principal, they reflect the knowledge extracted from the sources mentioned above (and others) but also include design experience of the authors. However, this brief review of literature contributing to the topic of the inducers is by no means complete. Almost certainly substantially broader knowledge is available in pump and rocket propulsion companies that are developing inducers for commercial reasons.

2.1.3 Classification

Inducers are commonly divided into the group of *low-head* and *high-head* inducers. According to Jakobsen [36] inducers with head coefficients of $\psi \leq 0.15$ belong to the first group and inducers with a head coefficient of $\psi > 0.15$ to the latter. Note that head coefficient in this case was defined as $\psi = gH/u^2$, where H is total head and u the circumferential velocity at the inducer's inlet diameter. Wisclicenus [71] instead uses the hub to shroud diameter ratio defined as d_{2h}/d_{2s} at the outlet location to classify inducers claiming that this parameter is directly related to the head rise capability.

(a) Low-head, cylindrical hub and shroud   (b) Low-head, tapered hub and shroud

(c) High-head, tapered hub, cylindrical shroud   (d) High-head, tapered hub and shroud
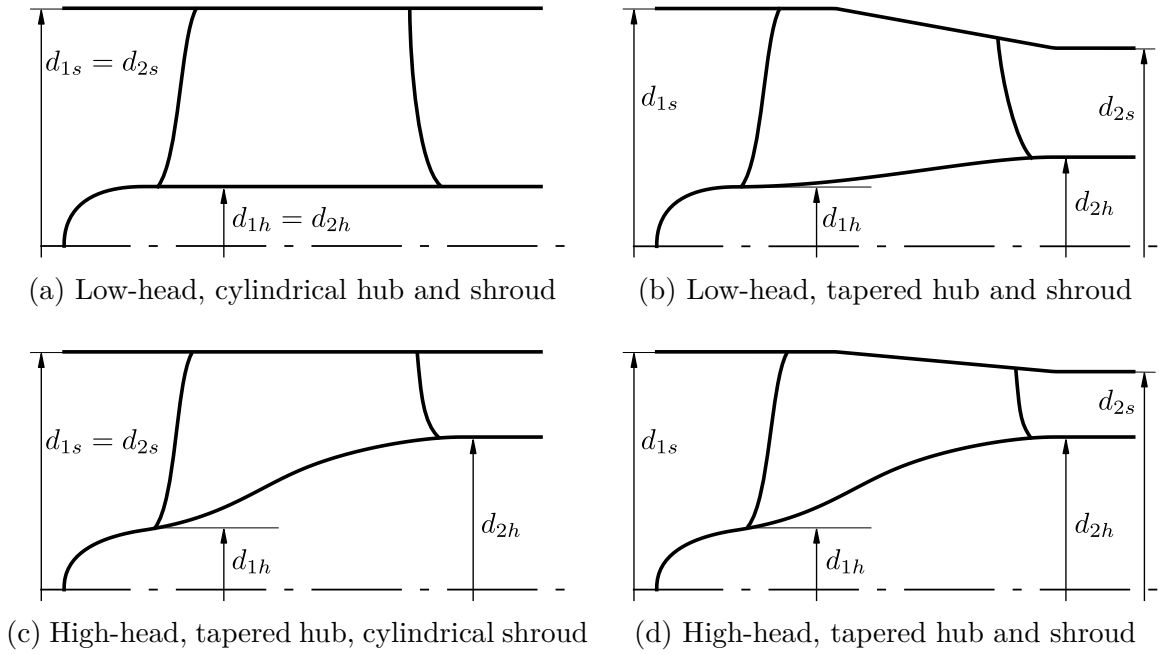
Figure 2.1: Geometrical classification of inducers

Inducers with hub diameter ratios of less than 0.5 are considered low-head inducers and inducers with higher hub diameter ratios high-head inducers. Additionally, inducers can be classified with respect to their meridional shape [36]. Figure 2.1a shows a classical low-head inducer with cylindrical hub and shroud. In this example the hub to shroud diameter ratio defined as discussed above amounts to $d_{2h}/d_{2s} = 0.25$. Alternatively the hub and shroud sections can be designed in a tapered way as depicted in Figure 2.1b. Despite the increase of hub diameter ratio, which in this case amounts to 0.45, the maximum possible head rise at the hub is not affected drastically such that the inducer can still be assigned to the group of low-head inducers. Tapering of the shroud section on the other hand can be used to match the inducer to the downstream impeller inlet. Of course this measure also affects the head which can be provided by the inducer and additionally tends to complicate the inducer flow by guiding the flow in the inward direction [37, 71]. If the hub diameter ratio at the discharge location is further increased the transition to the high-head inducer takes place. Figures 2.1c and 2.1d depict high-head inducers with cylindrical and tapered shroud. The discharge hub diameter ratios of these examples amount to 0.64 and 0.7 respectively. It should be noted however that a higher discharge hub diameter ratio not automatically leads to an increased head of the inducer because the final blade design has crucial influence on the head generation on each blade section. The discharge hub diameter ratio can rather be seen as a parameter to match the inducer to the geometrical dimensions and the head rise requirements of

the downstream impeller.

Independent of the meridional shape inducers can be categorized into shrouded and unshrouded types. Although shrouded and even hubless inducers are documented [36] their application is less common and the unshrouded version is most prevalent.

Inducers can be further differentiated according to the type of blading which is employed. Early designs mainly used helical blades with constant blade angle and thickness. These types are also called flat plate helical inducers, which are reminiscent of screws. Improvement of suction capability could be obtained by manually sharpening the blade leading edges or by machining swept back blades. More recent or advanced designs employ helical blades of variable lead or even three-dimensionally and inversely designed blades [9, 10, 70]. High-head inducers can also be considered to be composed of different blade types [36] and can make use of splitter or tandem blades [2, 46].

2.1.4 Characteristics

The non-cavitating performance characteristics of inducers correspond very well to the characteristics generally observed for axial machines. The head increases almost linearly with decreasing flow coefficient, while a quite distinct peak of maximum efficiency is obtained. Opposed to radial machines the power consumption rises steadily when advancing into part load, that is towards lower flow coefficients. One special feature, which will be discussed in detail in Section 3.5.5, is that inducers are normally designed for flow coefficients above the nominal value of the whole pump. Consequently most of the time inducers operate with positive incidence angles.

Considering operation under cavitating condition, which is the real purpose of inducers, as explained above, some very distinct characteristics have been discovered very early in the development of these devices. In Figure 2.2, which is adapted from Janigro and Ferrini [37], the different modes of operation are depicted for a typical swept back inducer. The dashed line shows suction performance curves for an industrial inducer application. A safety margin is applied in order to ensure that damage, head breakdown and unstable operation are avoided. Nevertheless, this exemplary diagram makes clear that tip vortex cavitation and vane tip cavitation already occur at normal operation and moderate values of NPSH. This is even true for design conditions because typically inducers are designed to operate with significant values of incidence, as already mentioned above. In Figure 2.2 this region is found left from the zero incidence line. A very important conclusion drawn by Janigro and Ferrini [37] is that the backward sweep of the leading edge effectively reduces the region of unstable cavitation and moves it away from typical operation limits.
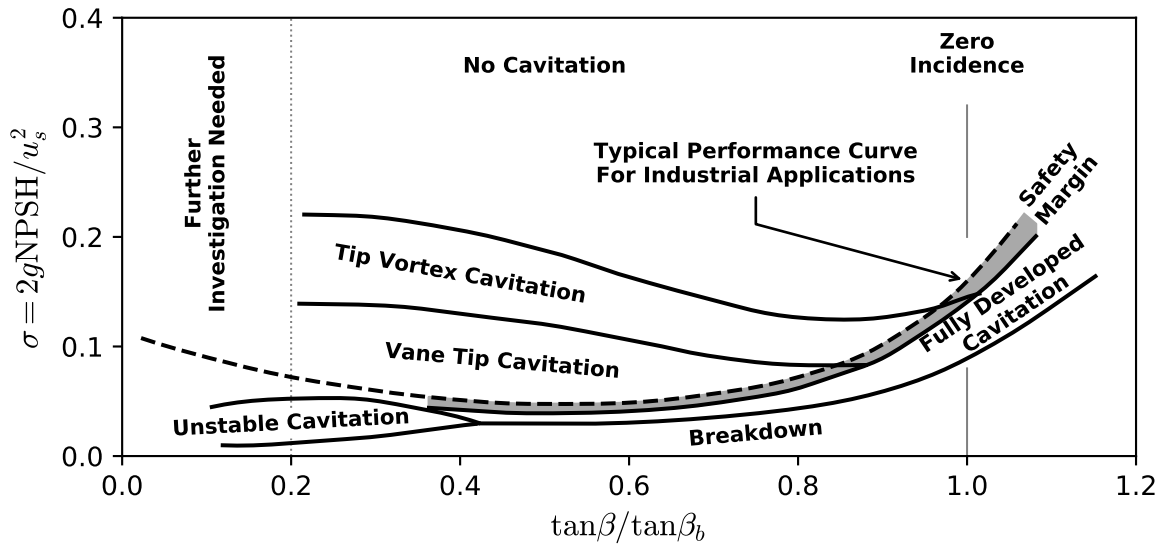
Figure 2.2: Typical modes of cavitation of an industrial, swept back inducer (adapted from Janigro and Ferrini [37])

The internal flow structure of inducers have been declared as one of the most complex in the field of turbomachinery by Lakshminarayana [47]. Despite the broad availability of CFD and the advancements in measurement equipment and techniques it is still not fully understood, which geometrical parameters have influence on the specific flow patterns and cavitation instabilities observed in inducers.

2.2 Turbomachinery Basics

2.2.1 Description of Turbomachinery Geometry

Traditionally, the impeller design starts with the definition of the meridional section as illustrated exemplarily in Figure 2.3a. The meridional section consists of curves representing the contours of hub and shroud as well as projections of the leading and trailing edge. When designing the hub and shroud curves the basic dimensions of the impeller have to be considered in order to ensure the compliance with design requirements. These basic dimensions, which for example determine the inlet and outlet diameters and the axial length of an impeller, are either chosen based on experience or calculated based on theoretical reasoning. Once the dimensioning is accomplished, the designer has great freedom in drawing the hub and shroud curves. However, a smooth transition from the inlet to the outlet location is usually desired. To provide the designer with a simple but flexible way to specify these lines parametric B-splines are used to describe these curves. This is explained in detail in Chapter 2.3.
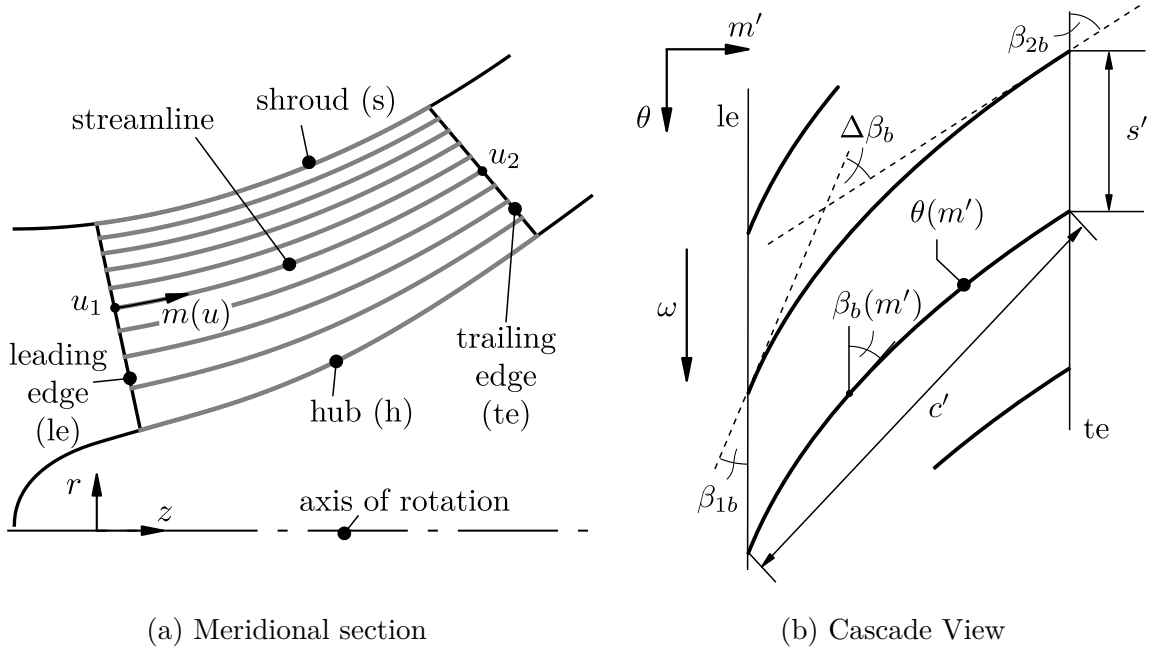
(a) Meridional section   (b) Cascade View

Figure 2.3: Description of geometry and coordinate conventions

After the hub and shroud curves are defined the leading edge (le) and trailing edge (te) of the blade can be designed (Figure 2.3a). These curves are also defined by means of B-splines to give the designer full control of the curve shape. In the next step streamlines are constructed between the hub and shroud curves ranging from leading to trailing edge of the impeller, as indicated in Figure 2.3a. These streamlines, including the segments of the hub and shroud curves, are used to generate surfaces of rotation, also called streamsurfaces, on which the sections of the blade geometry are defined. The number of streamlines is a design parameter and has impact on the spanwise blade shape. These streamlines can in principle be drawn arbitrarily but a choice based on some physical reasoning can be expected to approximate the path of the fluid flow more appropriately. As a consequence, it can be assumed that these streamlines are well suited to be used as foundation of the blade shape design.

The initial step of the blade design consists of developing the cascade plane for each of the streamlines (Figure 2.3b). Ideally, a method is used that allows an angle conserving mapping of this two-dimensional cascade (or blade-to-blade) plane to the three-dimensional and arbitrarily shaped surfaces of revolution. Supposing that this condition is fulfilled, the cascade plane can be used to construct the two-dimensional camber curves or theta curves $\theta(m')$ representing the distribution of the real and undistorted local blade angle $\beta_b(m')$. By transferring these curves back to the streamsurface, the three-dimensional camber curves are obtained as indicated in Figure 2.4a. Contrary to the traditional definition used in axial machine design (see e.g. Dixon and Hall [27]), in this work the

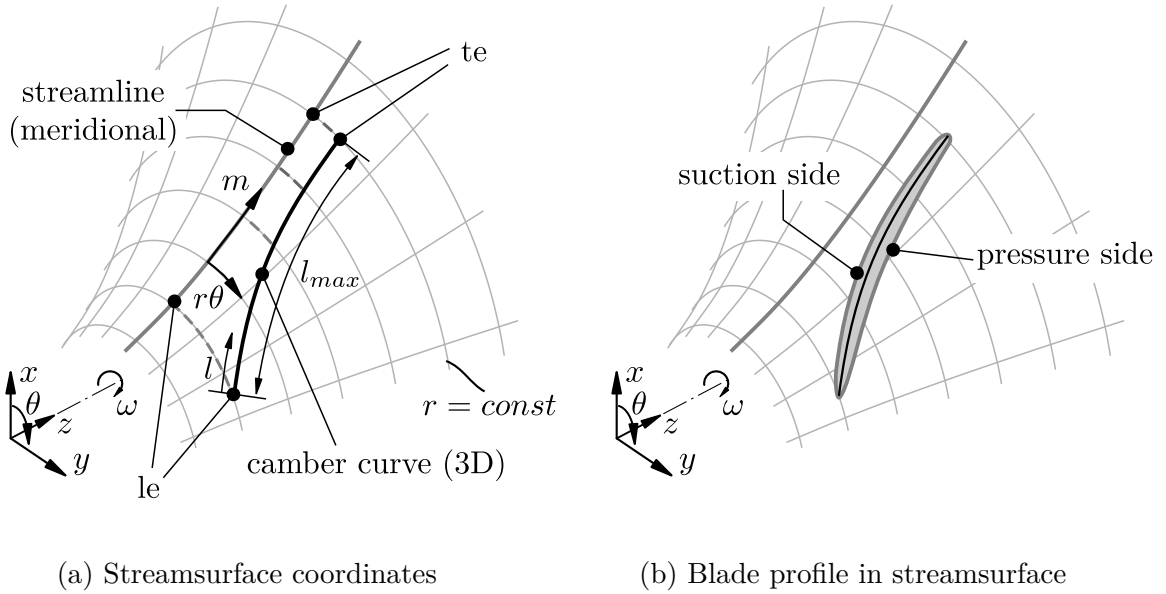(a) Streamsurface coordinates   (b) Blade profile in streamsurface

Figure 2.4: Streamsurface and blade profile geometry

camber curve is not considered to be identical to the mean camber line lying equidistantly between the suction and pressure side of the blade profile in the streamsurface (see Figure 2.4b). The reason for this choice is that the design of asymmetrical profiles, which are a typical feature of inducer blades, is substantially facilitated. Figure 2.5 exemplarily shows a distribution of thickness value t over length coordinate l. It gets clear that by the aforementioned interpretation of the camber curve it only requires the definition of two different thickness distributions, one for the suction ($t_{ss}(l)$) and one for the pressure side ($t_{ps}(l)$) of the blade section under consideration. The thickness values
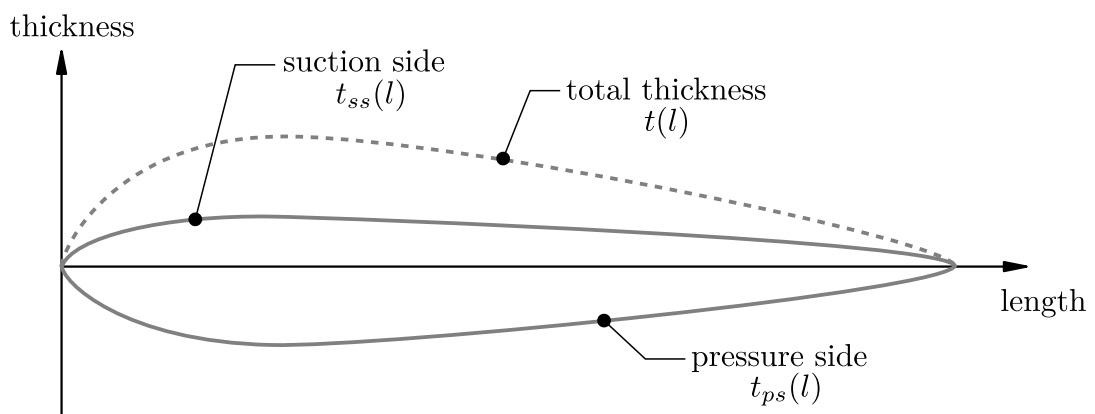

Figure 2.5: Thickness distribution

of the pressure side are deliberately chosen to be negative, mainly in order to facilitate illustration in the remainder of this thesis. Since any other definition of signs would also be conceivable, the total thickness $t(l)$ is calculated by adding the absolute values of both thickness distributions:

$$t(l) = |t_{ss}(l)| + |t_{ps}(l)| \tag{2.1}$$

To generate an asymmetric blade profile, the thickness values prescribed by the thickness distributions just have to be applied to the opposite sides of the camber curve. Thus, the suction and pressure side curves of the blade profile (or the blade section) lying on the streamsurface are produced (Figure 2.4b). Some attention has to be paid to the way this step is performed as there are different conceptions of how the thickness distribution is used to obtain the blade profile [54]. This mainly concerns the choice of the direction in which the thickness distribution is added to the camber curve and the definition of the length coordinate. Since inducer blades are usually very thin relative to their length and since the final profile shape can, from experience, be considered crucial for suction performance [38], an adequate method has to be selected for this step. The technique applied in the present work will be discussed in detail in Section 3.5.9.

An example for a three-dimensional blade profile constructed on the streamsurface generated by the corresponding streamline is depicted in Figure 2.6a. By *lofting* the blade sections on all the streamlines used for the design the blade surface is finally obtained
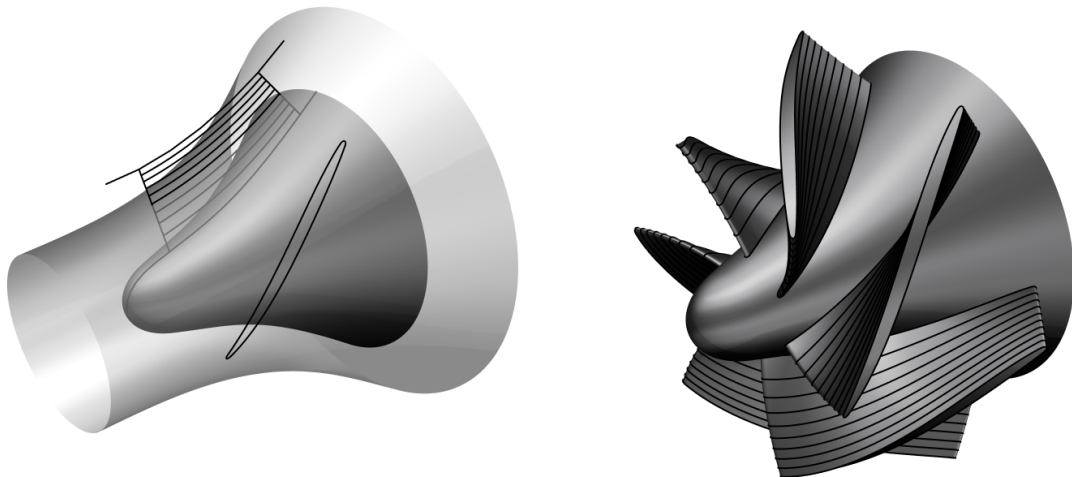
(a) Blade section constructed on streamsurface

(b) Final blade geometry

Figure 2.6: Three dimensional design of exemplary mixed flow impeller

[54]. This step can be understood as a kind of stacking or sweeping of the three-dimensional blade sections that are lying on the streamsurfaces as depicted in Figure 2.6b.

2.2.2 Coordinate System and Velocity Notation

Throughout this thesis an cartesian x, y, z - coordinate system is used as the absolute reference coordinate system. The x, y, z - coordinate system by default is oriented right-handed with the z-axis definining the axis of rotation of the machine. At any axial position z the radial coordinate r is computed by:

$$r = \sqrt{x^2 + y^2} \tag{2.2}$$

As already explained in the preceding section, the meridional view is obtained by circumferential projection of the edges of the blades and the hub and shroud contours into the x, z - plane. In this thesis the meridional section is drawn in z, r coordinates, as shown in Figure 2.3a for a generic mixed-flow impeller. In-between the hub and shroud curves any desired number of streamlines may be used to define arbitrarily shaped surfaces of revolution, so called streamsurfaces, which are used for the blade design. Figure 2.4a shows an exemplary streamsurface of a generic mixed-flow impeller. Along each of the streamlines the meridional coordinate m is defined as

$$m(u) = m(z(u), r(u)) = \int_{u_1}^{u} \sqrt{(\mathrm{d}z/\mathrm{d}u)^2 + (\mathrm{d}r/\mathrm{d}u)^2}\, \mathrm{d}u, \tag{2.3}$$

where u is the curve parameter along the curve describing the streamline. It is convenient to choose the curve parameter to range from 0 to 1, such that for $u_1 = 0$ the leading edge and for $u_2 = 1$ the trailing edge location is obtained. A more in-depth discussion of parametric curves is given in Section 2.3.

The circumferential coordinate $r\theta$ increases in the direction of positive angular coordinate θ as defined by the right hand rule. Accordingly, rotation direction is considered to be right, if it is in direction of positive circumferential or θ coordinate. In this case, the value of angular velocity ω is assumed to be positive as well. With the angular velocity ω the circumferential velocity u at any radial position r is computed as:

$$u = \omega\, r = 2\pi n\, r \tag{2.4}$$

Although the same symbol is used for the circumferential velocity and the curve parameter introduced above, it should be clear from the context and the physical units which

(a) General velocity triangle
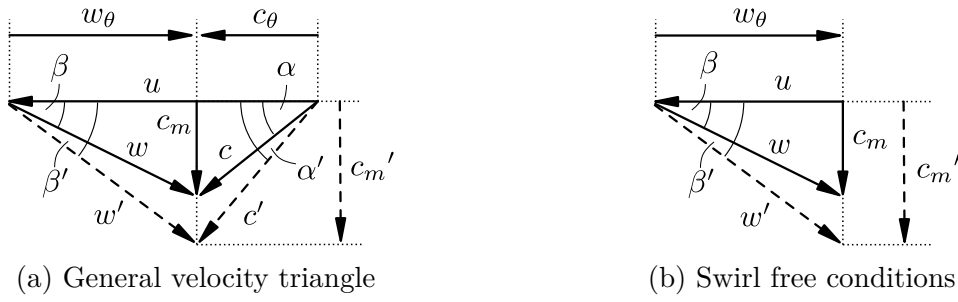
(b) Swirl free conditions

Figure 2.7: Velocity triangles

quantity it refers to.

The magnitude of absolute flow velocity is calculated from its components along the coordinate directions as follows:

$$c = \sqrt{c_z^2 + c_r^2 + c_\theta^2} \tag{2.5}$$

Neglecting the circumferential component yields the meridional velocity:

$$c_m = \sqrt{c_z^2 + c_r^2} \tag{2.6}$$

Viewed from the absolute frame of reference, which is stationary in the absolute coordinate system, the flow-field that would be observed inside of the turbomachine would be inherently unsteady. A fundamental approach in turbomachinery analysis therefore is the concept of relative flow velocity [27]. The relative flow velocity is considered steady and is observable in a frame of reference that is stationary relative to the rotating component.

On the streamsurfaces the circumferentially averaged flow conditions are described by velocity triangles as depicted in Figure 2.7. Formally, the absolute velocity vector $\boldsymbol{c}$ is obtained by vector addition of circumferential velocity $\boldsymbol{u}$ and relative velocity $\boldsymbol{w}$, i.e. $\boldsymbol{c} = \boldsymbol{u} + \boldsymbol{w}$. Strict application of vector addition implies opposite signs of the circumferential components of absolute and relative velocities, as can be seen from Figure 2.7a. If the circumferential components were both considered positive in the direction of u, this would lead to a negative velocity component w_θ and also to a negative flow angle β. To avoid negative angles for the general velocity triangle of Figure 2.7a, which is common for pump applications, a different sign convention is employed when performing componentwise calculations. The circumferential component of absolute flow velocity c_θ is considered positive in the direction of u, whereas the circumferential velocity of relative flow velocity w_θ is defined positive against the direction of u. This leads to the

following relations between the components of absolute and relative flow velocity:

$$w_m = c_m \tag{2.7}$$

$$w_\theta = u - c_\theta \tag{2.8}$$

Of course the sign of the circumferential component would have to be corrected accordingly if the actual vector orientation of the relative flow velocity was required.

By convention the flow angle is measured against circumferential velocity (Figure 2.7a). According to the convention introduced above relative flow and absolute flow angles are obtained as follows:

$$\beta = \arctan \frac{w_m}{w_\theta} = \arctan \frac{c_m}{u - c_\theta} \tag{2.9}$$

$$\alpha = \arctan \frac{c_m}{c_\theta} \tag{2.10}$$

The velocity triangle depicted in Figure 2.7b, where the absolute flow has no circumferential component ($c_\theta = 0$), represents the so-called swirl free condition, which is often assumed in case of axial inflow ducts. To describe the swirl condition at the inlet the swirl number can be used:

$$\delta_r = 1 - \frac{c_\theta}{u} \tag{2.11}$$

For $\delta_r = 1$ the swirl free inlet condition is obtained, for $\delta_r < 1$ the swirl is considered positive and for $\delta_r > 1$ negative.

When designing the blade angles the effect of blade blockage can be incorporated in the velocity triangle concept as already indicated in Figures 2.7a and 2.7b by dashed arrow lines. Typically, it is assumed that only the meridional component is influenced by the blade blockage while the circumferential component is not influenced. Thus, blade blockage is introduced by means of the blockage factor b, which is used to correct the meridional component as follows:

$$c'_m = b \, c_m \tag{2.12}$$

The blockage factor is computed by relating the pitch of the impeller ($2\pi r/Z$) to the pitch reduced by the tangential projection of the blade thickness ($t/\sin\beta_b$):

$$b = \frac{2\pi r/Z}{2\pi r/Z - t/\sin\beta_b} = \left(1 - \frac{t \, Z}{2\,\pi\,r\,\sin\beta_b}\right)^{-1} \tag{2.13}$$

As a consequence, the corrected flow angles are obtained by:

$$\beta' = \arctan \frac{w'_m}{w_\theta} = \arctan \frac{b\,c_m}{u - c_\theta} \tag{2.14}$$

$$\alpha' = \arctan \frac{c'_m}{c_\theta} = \arctan \frac{b\,c_m}{c_\theta} \tag{2.15}$$

Because the blade blockage factor b itself is dependent upon the blade angle, which is in general not known a priori, an iterative procedure is necessary to perform the blade blockage correction. Alternatively, some reasonable estimate can be used to avoid the iterative computation process. In the design procedure developed during the work on this thesis the iterative blade blockage factor correction is included in the blade angle computation.

For the most simple configuration of an axial machine with cylindrical hub and shroud contours, the initial design of the blade profiles could be performed on a chosen number of coaxial sections (at constant radii) between hub and shroud based on the assumption that the streamlines are also of constant radius. Development of the sections into conformal cascade views with an infinite number of blades can then be obtained by using z as the axial and $r\theta$ as the circumferential coordinate.

For mixed-flow and radial machines this approach cannot be adopted directly because naturally the radius along the streamlines is varying. However, it can be shown that a conformal transformation exists that can be used to obtain an equivalent representation of the mixed flow cascade [49]. To accomplish the coordinate transformation, the radius-normalized meridional coordinate m' is introduced as follows:

$$m'(u) = \int_{u_1}^{u} \frac{\mathrm{d}m}{r(u)} \tag{2.16}$$

By using the angular coordinate θ as the second coordinate the theta curve (or camber curve) can be designed in the $m' - \theta$ system. While the transformation conserves the blade angle, the length and thickness is not represented without distortion in the transformed view. Consequently, the desired blade profile cannot be designed in this cascade view alone. To circumvent this problem, Miller [54] presents a different approach of blade profile construction. The method actually chosen and implemented in the design procedure described in this thesis is explained in Section 3.5.9.

Figure 2.3b depicts an exemplary version of a transformed cascade. The blade theta curve $\theta(m')$ is depicted as a solid black line. Although the theta curve, strictly speaking, is only equal to the camber curve in case of a symmetrical thickness distribution, they are treated as being identical in this thesis. In analogy to the blade angle distribution the

theta curve can also be considered as the wrap angle distribution. The general relation between blade angle, wrap angle and the radius-normalized meridional coordinate in the angle conserving cascade plane can generally be stated as:

$$\tan \beta_b = \frac{\mathrm{d}m'}{\mathrm{d}\theta} \tag{2.17}$$

Analogously to the definitions for axial machines the pitch or spacing s' of the conformal cascade in the $m' - \theta$ plane is given by

$$s' = \frac{2\pi}{Z} \tag{2.18}$$

and the chord c' is the straight connection of leading and trailing edge:

$$c' = \sqrt{(m_2' - m_1')^2 + (\theta_2 - \theta_1)^2} \tag{2.19}$$

Consequently, solidity (or chord to pitch ratio) of the conformal cascade can be expressed as:

$$\sigma' = \frac{c'}{s'} \tag{2.20}$$

The camber angle, denoted by $\Delta\beta_b$ in Figure 2.3b, is defined as the difference between the blade angle at the trailing edge and the leading edge:

$$\Delta\beta_b = \beta_{2b} - \beta_{1b} \tag{2.21}$$

This angle is one of the parameters that have huge influence on the energy transmission of the blades discussed in the following section.

2.2.3 Basic Equations

The energy transmission realized by any type of centrifugal pump is described by Euler's pump equation, which is a direct consequence of the conservation of angular momentum. It relates the specific work transferred to the fluid to the average absolute flow velocities at the impeller entry and exit locations:

$$y_{th} = g\,H_{th} = \omega\,(r_2\,c_{\theta 2} - r_1\,c_{\theta 1}) \tag{2.22}$$

Considering the sign convention for w_θ (Equation 2.8) and using the velocity triangle

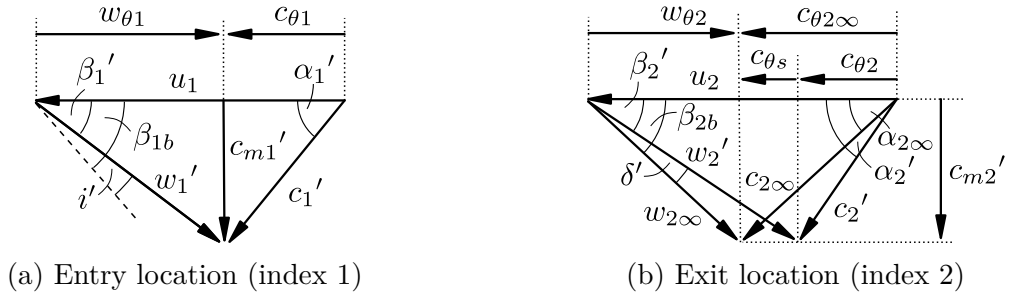(a) Entry location (index 1) (b) Exit location (index 2)

Figure 2.8: Velocity triangles at blade entry and exit locations

notation as depicted in Figures 2.8a and 2.8b Equation 2.22 can be rewritten in terms of the relative flow as follows:

$$y_{th} = \omega^2 \left(r_2^2 - r_1^2\right) - \omega \left(r_2\, w_{\theta 2} - r_1\, w_{\theta 1}\right) \tag{2.23}$$

From Equation 2.23 it can be derived that the energy transmission is essentially composed of two parts. The first portion $\omega^2 \left(r_2^2 - r_1^2\right)$ is entirely due to the change in radius while the second portion $\omega \left(r_1\, w_{\theta 1} - r_2\, w_{\theta 2}\right)$ describes the part due to the fluid deflection. The specific work effectively transferred to the fluid is expressed in terms of the total pressure rise from entry to exit:

$$y = \frac{p_{tot,2} - p_{tot,1}}{\rho} \tag{2.24}$$

Instead of specific work usually the head of the pump is considered. It is defined as:

$$H = \frac{y}{g} = \frac{p_{tot,2} - p_{tot,1}}{\rho\, g} = \frac{p_2 - p_1}{\rho\, g} + \frac{c_2^2 - c_1^2}{2\, g} + z_2^2 - z_1^2 \tag{2.25}$$

Since Equation 2.22 is valid for viscous flow, it includes the losses occurring in the impeller due to friction. The relation between the theoretical head and the effectively available head is expressed by the hydraulic efficiency:

$$\eta_h = \frac{y}{y_{th}} = \frac{H}{H_{th}} \tag{2.26}$$

Using a reasonable estimate for the hydraulic efficiency of the impeller, provided for example by mathematical correlations based on earlier designs, it should be possible to compute the exit flow conditions needed to produce the desired amount of head. The designer now is confronted with the task to develop a blade shape that produces the required flow conditions.

An important design parameter, not specific to inducers, is the incidence angle, which

is defined as the difference between blade and flow angle:

$$i = \beta_{1b} - \beta_1 \tag{2.27}$$

If blade blockage is to be considered at the inlet as illustrated in Figure 2.8a, the definition is modified as follows:

$$i' = \beta_{1b} - \beta_1' \tag{2.28}$$

The choice of design incidence angle not only affects the position of the point of best efficiency but is also critical for the stagnation point location on the blade profiles [31]. Positive values of incidence produce a stagnation point on the pressure side and negative values on the suction side of the blade. Experience has shown that best suction performance of inducers is obtained for positive values of incidence angles [36], which cause cavitation to start on the suction side surface of the blade [31].

An additional difficulty arises because the flow, even in the inviscid case, can't be perfectly guided by a finite number of blades. This can be explained illustratively either by the relative eddy concept [27] or by the reasoning of Gülich [31], who attributes the deviation between flow and blade angle to the differences in velocity on blade pressure and suction sides and the contribution of Coriolis acceleration.

Traditionally in axial machine design this deviation from the perfectly guided flow is described by means of the deviation angle, which is defined by

$$\delta = \beta_{2b} - \beta_2 \tag{2.29}$$

or, in case of consideration of blade blockage as depicted in Figure 2.8b, by

$$\delta' = \beta_{2b} - \beta_2'. \tag{2.30}$$

Empirical relations to estimate the deviation angle for certain types of profiles have been derived for compressor blades [20, 52] and applied in a modified version to inducers [36]. However, as stated by Jakobsen [36], the estimation process remains a trial-and-error approach. Another formula which relates the deviation angle to the blade geometry (blade angles and spacing-to-length ratio s/l) can be found in Gülich [31]:

$$\delta = \left(2 + \frac{\beta_{2b} - \beta_{1b}}{3}\right) \left(\frac{s}{l}\right)^{1/3} \tag{2.31}$$

Unfortunately no details about the origin of this formula is given.

As a consequence of the deviation phenomenon a specific amount of *slip*, denoted with $c_{\theta s}$, will exist between the circumferential components of the absolute velocity $c_{\theta 2\infty}$, which would result from a flow that is leaving the rotor under the blade angle β_{2b}, and the actually realized value $c_{\theta 2}$. For radial and mixed-flow machines this effect is considered by means of the so-called *slip-factor* or *Abströmbeiwert* as defined by e.g. Japikse et al. [39] or Gülich [31]:

$$\gamma = 1 - \frac{c_{\theta 2\infty} - c_{\theta 2}}{u_2} \tag{2.32}$$

The slip leads to a change in velocity triangles as depicted in Figure 2.8b. There is also a different definition of slip-factor used by e.g. Lewis [49] and Dixon and Hall [27]. This version is denoted by $\tilde{\gamma}$ and is related to the previous definition by

$$\tilde{\gamma} = \frac{c_{\theta 2}}{c_{\theta 2\infty}} = 1 - \frac{(1 - \gamma)u_2}{c_{\theta 2\infty}} \tag{2.33}$$

From Figure 2.8b the relation between slip factor γ and the deviation angle δ' can be readily derived:

$$\gamma = \frac{c_{m2}'}{u_2} \left(\frac{1}{\tan(\beta_{2b} - \delta')} - \frac{1}{\tan \beta_{2b}} \right) \tag{2.34}$$

While different in its mathematical formulation, the concept of slip is equivalent to the idea of *Minderleistung* and the corresponding *Minderleistungsfaktor* explained in detail by [58]. Similar to the slip factor approach empirical input is needed to perform the computations that are required to obtain the value of the *Minderleistungsfaktor*. However, in the design procedure presented in this thesis the *slip-factor* is used.

Different correlations are available to estimate the slip factor. Overviews of slip factors used in practice can be found for example in Dixon and Hall [27] or Japikse et al. [39]. Up to now, no correlation is known to the author that has been proven to be applicable to inducers, although there exists an approach to unify the theories for axial and radial machines published by Qiu et al. [61] and Qiu et al. [62]. The present design procedure therefore employs a user specified slip factor as will be described in Section 3.5.6. Of course, any desired slip factor (or deviation angle) correlation could be implemented in a future program version.

In axial machine design usually blade profiles are applied, which can be selected from existing catalogs or computed by analytical relations. Experimental data of cascade tests or theoretical calculations of these airfoils (or hydrofoils) can then be used to estimate deviation angle and e.g. pressure distributions. Since in the design procedure which

is developed in this thesis, the inducer is designed similar to a mixed flow machine where angle and thickness distributions are prescribed along curved streamlines in a user controlled way, the slip-factor approach is used to determine the exit blade angle. However, because the physical meaning is the same and the equivalent deviation angle can be computed easily, the extension of the design procedure to work with predefined profiles is straightforward.

2.2.4 Characteristic Curves and Coefficients

The performance of a pump is described by the quantities head H, power P, efficiency η and the net positive suction head NPSH. These quantities vary with the volume flow rate Q and the rotational speed n. Characteristic curves are commonly obtained by plotting the above quantities against flow rate Q while maintaining constant rotational speed. As already stated in Equation 2.25 the head is a measure of the total pressure rise provided by the pump. The hydraulic power P_h of the pump can be computed for every operating point as follows:

$$P_h = \rho g Q H \tag{2.35}$$

If the torque M needed to drive the pump is known, the power P, in this case also called shaft power, can be calculated by

$$P = M\omega = M 2\pi n \tag{2.36}$$

By relating the hydraulic Power P_h to the shaft power P the efficiency η is obtained:

$$\eta = \frac{P_h}{P} \tag{2.37}$$

Suction capability of a pump is rated by means of its NPSH, which is defined as

$$\text{NPSH} = \frac{p_{tot,1} - p_v}{\rho g} = \frac{p_1 - p_v}{\rho g} + \frac{c_1^2}{2g} \tag{2.38}$$

NPSH (or NPSH_r) is a measure for the total pressure at the pump inlet required for the pump to operate under a certain amount of head loss due to cavitation. The percentage of acceptable head loss is commonly defined as 3% in which case the NPSH is denoted by NPSH_3 [26]. Since inducers are designed to operate under heavy cavitation and contribute only little (around 10% [37]) to the pumps overall head, higher percentages are applied. Reported values for rocket engine turbopump inducers are e.g. 10% [36]

or even values of up to 50 % [38]. The NPSH of the pump can only be estimated during the design process and has to be verified by NPSH or suction tests. During these tests the head of the pump is recorded while lowering the inlet pressure. This is equal to reducing the available NPSH (commonly denoted by $\mathrm{NPSH_a}$) of the system. Usually the head data is plotted against the values of $\mathrm{NPSH_a}$ to visualize the head drop.

Expressing the duty of turbomachines by means of dimensionless parameters allows a comparison between different types and sizes of machines. Although these dimensionless quantities are commonly used in the whole field, the mathematical definition and used notation can differ slightly in the open literature as well as in the different industries. This is why the parameters employed in the remainder of this thesis are explained shortly in this section. The flow coefficient, which is used in the current work to give a dimensionless measure of volume flow, is defined as the ratio between meridional flow velocity and the circumferential blade velocity:

$$\varphi = \frac{c_m}{u} \tag{2.39}$$

It can be defined with respect to different locations on different streamlines such that its exact definition depends on the actual purpose. Its specific definition will be provided whenever this coefficient is used (e.g. in the presentation and discussion of numerical or test results). The same is true for the head coefficient which can generally be defined as follows:

$$\psi = \frac{2gH}{u^2} \tag{2.40}$$

For radial impellers the head coefficient usually is defined with respect to the impeller exit diameter d_2 such that the circumferential velocity $u_2 = \pi d_2 n$ referring to this diameter is employed in the formula of the head coefficient. Combining efficiency with the flow and the head coefficients as defined above, the performance coefficient λ can be obtained [27]:

$$\lambda = \frac{\varphi \psi}{\eta} \tag{2.41}$$

A dimensionless measure of NPSH is given by the cavitation coefficient according to Gülich [31] (alternatively called cavitation parameter by Jakobsen [36]) which is given as:

$$\sigma = \frac{2g\mathrm{NPSH}}{u^2} \tag{2.42}$$

The coefficients introduced above can be used to obtain dimensionless versions of the characteristic curves as well as the head drop curves obtained from suction performance tests. Only these dimensionless quantities are used in the discussion of the results of this thesis.

2.3 Geometrical Design

2.3.1 Parametric Curves

The parametric representation of curves has some important advantages over explicit and implicit equations when they are used for computer-aided geometric design. By using parametric equations, arbitrary shaped and bounded curves can be described and modified in an intuitive way, which facilitated the development of numerically stable algorithms in the past [59]. Thus, the representation of curves by parametric equations is preferred in most situations over the use of explicit and implicit equations [55].

The coordinates along parametric curves are explicit functions of an independent parameter u [59]. Consequently, the general parametric representation of a curve C in the three-dimensional space can be written as:

$$C(u) = (x(u), y(u), z(u)),\ a \leq u \leq b \tag{2.43}$$

Commonly the parameter interval is normalized, such that $[a, b] = [0, 1]$ and unless otherwise stated the normalized interval is used throughout this thesis.

2.3.2 B-Spline Curves

Extensive information about the application of nonrational and rational B-spline curves and surfaces in computational design is available in literature. Comprehensive treatments of the topic is given for example in Farin et al. [28], Hoschek and Lasser [32], Mortensen [55] and Piegl and Tiller [59]. Since this work is mainly related to the application of several techniques, only the most relevant fundamentals and selected methods are briefly described. Because nomenclature can be slightly inconsistent when comparing the different references, the notation of Piegl and Tiller [59] is used throughout this work.

A B-spline curve of degree p can mathematically be expressed as follows:

$$C(u) = \sum_{i=0}^{n} N_{i,p}(u)\, P_i,\ a \leq u \leq b \tag{2.44}$$

The curve is defined by $n+1$ control points P_i and the pth-degree B-spline basis functions

$N_{i,p}$ with $i = 0, \ldots n$. By connecting the control points P_i, also called poles, with straight lines the control polygon is obtained. Computation of the basis-functions requires the specification of the so-called knot-vector. The knot vector U is a sequence of non-decreasing, but not necessarily unique, real numbers u_j for $j = 0, \ldots, m$:

$$U = \{u_0, u_1, \ldots, u_{m-1}, u_m\} \tag{2.45}$$

Between the number of control points $n + 1$, the number of knots $m + 1$ and the degree p the following relation exists:

$$m = n + p + 1 \tag{2.46}$$

By choosing specific values of the knots u_j certain features of the curve can be obtained. This will be addressed in the subsequent section. With the knot vector specified the basis functions $N_{i,p}$ can be calculated recursively according to the following equation [59]:

$$N_{i,0}(u) = \begin{cases} 1 & \text{if} \quad u_i \leq u < u_{i+1} \\ 0 & \text{otherwise} \end{cases} \tag{2.47}$$

$$N_{i,p}(u) = \frac{u - u_i}{u_{i+p} - u_i} N_{i,p-1}(u) + \frac{u_{i+p+1} - u}{u_{i+p+1} - u_{i+1}} N_{i+1,p-1}(u) \tag{2.48}$$

The kth derivatives of the basis function can be computed with the following formula:

$$N_{i,p}^k(u) = p \left(\frac{N_{i,p-1}^{(k-1)}}{u_{i+p} - u_i} - \frac{N_{i+1,p-1}^{(k-1)}}{u_{i+p+1} - u_{i+1}} \right) \tag{2.49}$$

Using equation 2.49 the kth derivative for any curve parameter consequently is given by:

$$\boldsymbol{C}^{(k)}(u) = \sum_{i=0}^{n} N_{i,p}^{(k)}(u) \, \boldsymbol{P_i}, \ a \leq u \leq b \tag{2.50}$$

B-spline curves have many favorable properties, which are discussed in detail in the literature already mentioned above and which make them especially useful for geometrical design. However, since B-spline curves are basically composed of polynomials, they can be considered nonrational (or polynomial) curves. As such they are not capable of representing simple and very common geometrical objects like circles and ellipses. To overcome this limitation nonuniform rational B-spline (NURBS) curves, which can be

understood as a generalization of B-spline curves, have been developed [59]. Introducing the weights $w_i > 0$ associated to the control points $\boldsymbol{P}_i$ the rational basis functions are defined by

$$R_{i,p}(u) = \frac{N_{i,p}(u)\,w_i}{\sum_{j=0}^{n} N_{j,p}(u)w_j}. \tag{2.51}$$

With this the NURBS curve is written analogously to the B-spline curve as follows:

$$\boldsymbol{C}(u) = \sum_{i=0}^{n} R_{i,p}(u)\,\boldsymbol{P_i}, \ a \leq u \leq b \tag{2.52}$$

Because nonrational B-spline curves are used exclusively in the procedures presented in this work an extensive discussion of this type of curves is omitted at this point and the reader is referred to the literature for a comprehensive description of the features of NURBS. Nevertheless, it should be mentioned that if the weights w_i are equal to a non-zero constant for all i it can be shown that $R_{i,p}(u) = N_{i,p}(u)$ and the (nonrational) B-spline curve is obtained.

B-spline or NURBS surfaces can be constructed analogously to B-spline or NURBS curves. A description is not given in this work because the design procedure is completely based on curves and algorithms that operate on these curves. The blade surface construction is only performed in the last step of the design process when the blade is exported for example to the STEP standard. Comprehensive information on the topic of B-spline surfaces and the corresponding algorithms can be found in the literature already cited.
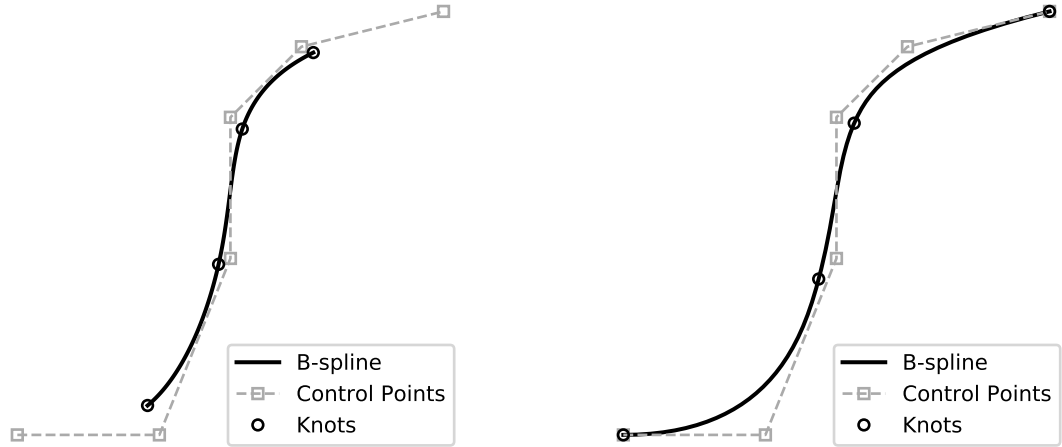
2.3.3 Knot Vectors

Depending on the knot vector used for the computation of the basis functions described in the previous section certain types of curves, which are useful in the geometric design process, can be provided. Retaining the nomenclature of Piegl and Tiller [59] knot vectors are differentiated into *clamped* and *unclamped* versions. Both types can further be subdivided into *uniform* and *nonuniform* knot vectors. In what follows the aforementioned concepts are explained in more detail.

The clamped B-spline curve is obtained by repeating the first and last knots of the knot vector $p+1$ times. Accordingly, the general definition of the clamped knot vector reads as follows:

$$U = \{\underbrace{a,\ldots,a}_{p+1}, u_{p+1}, \ldots, u_{m-p-1}, \underbrace{b,\ldots,b}_{p+1}\} \tag{2.53}$$

Any knot vector without or different multiplicities of first and last knots and the corresponding B-spline curves are denoted unclamped. The reason for this naming convention is that unless the knot vector is chosen as described above, the B-spline curve generally does not reach the first and last control point [32]. If the spacing d between the interior knots is equidistant, that is $u_{i+1} - u_i = d$ for all $p \leq i \leq m - p - 1$, the uniform knot vector is obtained. Usage of this type of knot vector results in the uniform B-spline curve. To illustrate the influence of the different knot vectors Figure 2.9a depicts an

(a) Unclamped, uniform B-spline   (b) Clamped, uniform B-spline

Figure 2.9: Different types of knot vectors and the resulting B-splines

exemplary unclamped B-spline curve of degree $p = 3$ using the uniform knot vector

$$U = \left\{ 0, \frac{1}{9}, \frac{2}{9}, \frac{3}{9}, \frac{4}{9}, \frac{5}{9}, \frac{6}{9}, \frac{7}{9}, \frac{8}{9}, 1 \right\}. \tag{2.54}$$

Besides the B-spline curve, the control polygon as well as the knot locations are indicated in Figure 2.9a and the following figures of this section. Obviously, the curve does not extend to the first and last control point. In contrast, the clamped B-spline curve illustrated in Figure 2.9b starts at the first and ends at the last control point. This curve is defined by the uniform knot vector

$$U = \left\{ 0, 0, 0, 0, \frac{1}{3}, \frac{2}{3}, 1, 1, 1, 1 \right\} \tag{2.55}$$

and uses the same control points as in the previous example of the unclamped curve. If the spacing between the knots is not equal, the nonuniform B-spline is obtained. A

knot vector

$$U = \left\{0, 0, 0, 0, \frac{1}{10}, \frac{9}{10}, 1, 1, 1, 1\right\}. \tag{2.56}$$

leads to the clamped, nonuniform B-spline curve, which is depicted in Figure 2.10a. As can be seen from this figure the knot vector can be used to move parts of the curve closer to the control polygon. For a knot vector without any interior knots
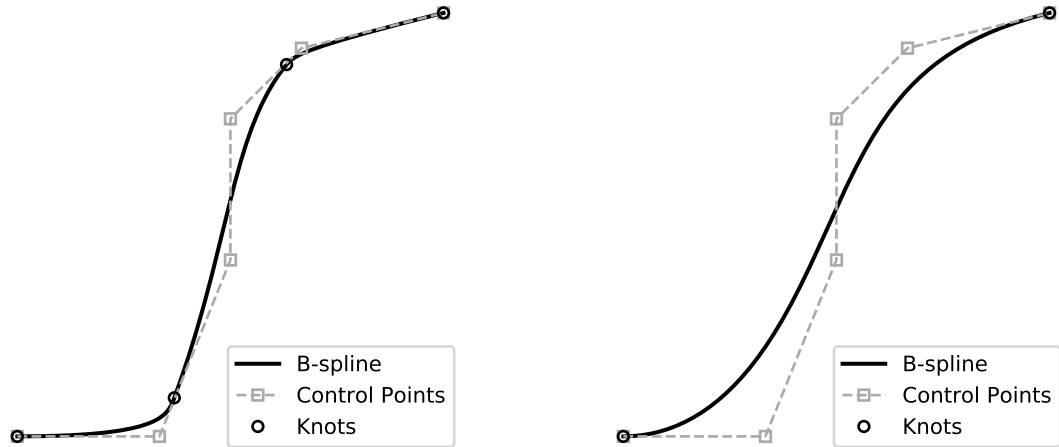
(a) Clamped, non-uniform B-spline   (b) Bézier Curve

Figure 2.10: Different types of clamped B-splines

$$U = \{\underbrace{0, \ldots, 0}_{p+1}, \underbrace{1, \ldots, 1}_{p+1}\} \tag{2.57}$$

the Bézier curve of degree p is obtained [59]. Figure 2.10b shows the Bézier curve, which is generated by using the knot vector

$$U = \{0, 0, 0, 0, 0, 0, 1, 1, 1, 1, 1, 1\} \tag{2.58}$$

and the same control points as before.

Geometrically open and closed curves can be realized by different methods regardless of the usage of a clamped or unclamped type of knot vector [59]. A feature that makes the clamped B-spline curve favorable for geometrical design is the fact that it is tangential to the first and last segments of the control polygon described by the control points. This allows very intuitive curve modification by repositioning of selected control points. Out of these reasons clamped B-splines are exclusively used in the design procedure

presented in this thesis. Furthermore, no distinction is made between nonuniform and uniform B-splines regarding the used algorithms. Unless otherwise stated, the reader can assume that clamped, nonuniform B-splines are used.

2.3.4 Curve Construction by Interpolation

Curves can be constructed straightforwardly by designing a knot vector and specifying the control points as described in the previous section. If a clamped knot vector is used, start and end tangents can be prescribed by choosing the control points appropriately. However, passing of a certain or multiple points is not guaranteed. If on the other hand a curve is needed to pass exactly or approximately through a given set of points, either some sort of interpolation or approximation is required. While approximation tries to fit the B-spline curve as good as possible to a given set of points interpolation forces the curve to pass through the points. In the present implementation only interpolation procedures are used to keep the curve shape as predictable as possible. The interpolation can be performed straightforwardly by solving Equation 2.44 for the unknown control points $\boldsymbol{P_{i,j}}$. Given $\boldsymbol{Q_k}$ interpolation points with $k = 0, \ldots, n$ the corresponding $n + 1$ control points are obtained by solving the following system of equations:

$$\boldsymbol{Q_k} = \boldsymbol{C}(u_k) = \sum_{i=0}^{n} N_{i,p}(u_k)\,\boldsymbol{P_i}, \quad k = 0, \ldots, n \tag{2.59}$$

Obviously this requires the specification of the knot values u_k at the interpolation points. Out of the different methods that are available for this task the three most common are the *equally spaced* (or *uniform*), *chord length* (or *chordal*) and *centripetal* method [59]. Equally spaced knots ranging from 0 to 1 are obtained by simply setting

$$u_k = \frac{k}{n}, \quad k = 0, \ldots, n. \tag{2.60}$$

As this can result in unexpected curve progressions, especially if the data to be interpolated is distributed in an uneven way, this is in general not the recommended method [59]. Better behavior is usually obtained by the *chord length* or *centripetal* methods. Assuming that $u_0 = 0$ and $u_n = 1$ the interior knots of the *chord length* method are calculated as

$$u_k = u_{k-1} + \frac{|\boldsymbol{Q_k} - \boldsymbol{Q_{k-1}}|}{L_{\boldsymbol{Q}}}, \quad k = 1, \ldots, n-1, \tag{2.61}$$

where $L_{\boldsymbol{Q}}$ is the total chord length of the segments joining the interpolation points:

$$L_{\boldsymbol{Q}} = \sum_{k=1}^{n} |\boldsymbol{Q_k} - \boldsymbol{Q_{k-1}}| \tag{2.62}$$

The *centripetal* method can be considered a modification of the chord length method and differs from the *chord length* rule only by taking the square root of the chord-lengths, such that

$$u_k = u_{k-1} + \frac{\sqrt{|\boldsymbol{Q_k} - \boldsymbol{Q_{k-1}}|}}{L_{\boldsymbol{Q}}^*}, \quad k = 1, \ldots, n-1, \tag{2.63}$$

and

$$L_{\boldsymbol{Q}}^* = \sum_{k=1}^{n} \sqrt{|\boldsymbol{Q_k} - \boldsymbol{Q_{k-1}}|} \tag{2.64}$$

According to Piegl and Tiller [59] the *centripetal* method yields better results in case of "sharp turns" in the original data. Unless otherwise stated, the *chord length* method is used throughout this work.

2.3.5 Remarks on Implementation

To avoid the need for a completely new implementation of all the necessary algorithms for e.g. curve construction, interpolation and intersection, the python package `pythonOCC` [57] is used. This library basically provides direct access from python to the 3D modeling framework `Open CASCADE Community Edition` originally written in C++. Besides reducing the development effort, the main advantage of using the `pythonOCC` library lies in the availability of a huge amount of efficient, field-tested and reliable geometrical algorithms, which can be effectively used in the development of the design procedure, and the direct interface to neutral data formats like `STEP` and `IGES`. The latter is especially important when the generated geometry is to be used in a downstream process of the CAE development chain like computational fluid dynamics (CFD) and structural or thermal analysis. Avoiding errors or misunderstandings due to geometry exchange is even more crucial if the geometry has to be prepared for machining or if the geometry simply has to be shared with coworkers for further processing, who may even be using different CAD systems.

2.4 Simple Meridional Flow Analysis (SMA)

2.4.1 Governing Equation

The purpose of the meridional flow analysis is to provide an appropriate estimate of the meridional flow field and a distribution of streamlines in the meridional section of the turbomachine. Streamlines are defined as the curves that in any arbitrary point are tangentially to the meridional flow velocity. A compact description of the meridional flow can be obtained by using Stokes' stream function. For incompressible flow Stokes' stream function Ψ is related to the components of the meridional flow velocities by the following equations:

$$c_z = \frac{1}{r}\frac{\partial \Psi}{\partial r} \tag{2.65a}$$

$$c_r = -\frac{1}{r}\frac{\partial \Psi}{\partial z} \tag{2.65b}$$

The value of Ψ remains constant along a meridional streamline, which means that the streamlines can be obtained by constructing isolines or contour lines of the stream function distribution in the meridional plane.

As shown by Lewis [49] the governing equation for incompressible, rotational, axisymmetric and inviscid flow can be derived with the help of the stream function as defined by Equations 2.65a and 2.65b:

$$\left(\frac{\partial^2 \Psi}{\partial z^2}\right) - \frac{1}{r}\left(\frac{\partial \Psi}{\partial r}\right) + \left(\frac{\partial^2 \Psi}{\partial r^2}\right) = -c_\theta r\frac{(\mathrm{d}c_\theta r)}{\mathrm{d}\Psi} + \frac{r^2}{\rho}\frac{\mathrm{d}p_{tot}}{\mathrm{d}\Psi} \tag{2.66}$$

Blade forces are not incorporated in Equation 2.66 but the distribution of swirl and total pressure could be modelled by the terms on the right hand side. Under the assumption of free-vortex flow, which is an appropriate estimate in the absence of blades, there is no gradient of angular momentum and total pressure across the streamlines:

$$\frac{\mathrm{d}(c_\theta r)}{\mathrm{d}\Psi} = 0 \tag{2.67a}$$

$$\frac{\mathrm{d}p_{tot}}{\mathrm{d}\Psi} = 0 \tag{2.67b}$$

Consequently, Equation (2.66) can be simplified as follows:

$$\left(\frac{\partial^2 \Psi}{\partial z^2}\right) - \frac{1}{r}\left(\frac{\partial \Psi}{\partial r}\right) + \left(\frac{\partial^2 \Psi}{\partial r^2}\right) = 0 \tag{2.68}$$

Equation 2.68 is the basic equation used in the simple meridional flow analysis (SMA).

The numerical solution is obtained by a finite differences method, which is explained in detail in the following section.

Although Equation 2.68 is strictly valid only in the bladeless space (e.g. in the gap between bladerows), it is used to calculate the streamlines that serve as the foundation of the blade design. As a consequence, the streamlines and the corresponding velocity field obtained by solution of above equation must be considered as a first approximation to the real flow. In order to account for the actual spanwise distributions of total pressure rise and blade forces, an iterative procedure combining meridional and blade to blade solutions could be employed. However, since the real flow through a blade row is viscous, turbulent, and three-dimensional by nature this would lead to a solution which would potentially be more precise but would still remain an approximation to the real problem as well. To keep the design method as simple as possible this iterative process is omitted and instead the solution of Equation 2.68 is accepted as reasonable approximation to the meridional flow. Hence, the method proposed in this thesis should rather be understood as a simple design tool, which allows for rapid design iterations, than an exact analysis tool.

2.4.2 Numerical Solution

A finite differences approach is implemented to solve Equation 2.68 for any arbitrarily shaped meridional section in the z, r-plane as described in Section 2.2.1. Obviously a boundary conforming grid is needed to represent the hub and shroud curves adequately. Since simple finite difference formulas are only applicable on equidistant, rectilinear grids, the problem has to be mapped to an equivalent rectangular domain, the so called computational domain. To accomplish this transfer the equations as well as the geometry under consideration have to be transformed into a new set of coordinates ξ, η. This process is depicted in Figure 2.11. In the physical domain the problem is bounded by four curves that are denoted by the corner nodes they are connecting. The lower curve *ab* represents the hub contour, the upper curve *dc* describes the shroud contour and the curves *ad* and *bc* constitute the inlet and the outlet borders respectively (see Figure 2.11a). The basic idea of the transformation procedure is to map the boundary curves to the edges of a rectangle in the computational plane such that the hub and shroud (lower and upper) borders correspond to constant values of the coordinate η, and inlet and outlet (left and right) borders to constant values of the coordinate ξ. By dividing the edges of the rectangle equidistantly as illustrated in Figure 2.11b the computational grid is readily obtained. The indexing of the grid nodes starts for both the physical and the computational domain from the lower left corner with index i increasing in streamwise
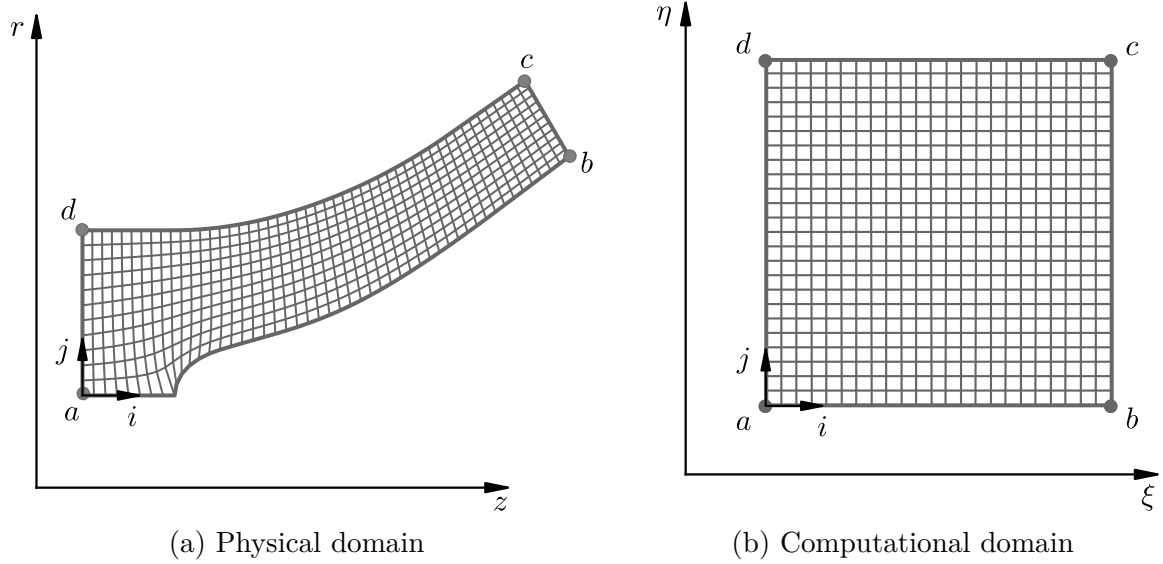
(a) Physical domain   (b) Computational domain

Figure 2.11: Transformation form the physical to the computational domain

direction (from inlet to outlet) and index j increasing in spanwise direction (from hub to shroud). If the number of nodes in streamwise direction is denoted by N_i and the number of nodes in spanwise direction by N_j and the index counting starts from zero, the corresponding index ranges can be specified as $i = 0 \ldots N_i - 1$ and $j = 0 \ldots N_j - 1$. To provide the inverse mapping, that is the mapping of the interior grid nodes from the computational to the physical domain, different methods are available [60]. A very common approach is the usage of differential equations that describe the relation between the two sets of coordinates. In the present work an elliptical grid generation method is chosen. To obtain the mapping relations the following set of inverse Laplace equations is solved:

$$0 = \alpha \left(\frac{\partial^2 z}{\partial \xi^2} \right) - 2\beta \left(\frac{\partial^2 z}{\partial \xi \partial \eta} \right) + \gamma \left(\frac{\partial^2 z}{\partial \eta^2} \right) \tag{2.69}$$

$$0 = \alpha \left(\frac{\partial^2 r}{\partial \xi^2} \right) - 2\beta \left(\frac{\partial^2 r}{\partial \xi \partial \eta} \right) + \gamma \left(\frac{\partial^2 r}{\partial \eta^2} \right) \tag{2.70}$$

The derivation of these formulas and the computation of the geometric coefficients α, β and γ is described in detail in Appendix A.2. Using the index convention as depicted in Figure 2.12 and setting the spacings to $\Delta \xi = \Delta \eta = 1$ central differences are used to discretize the grid generation equations. After rearranging the following formulas can
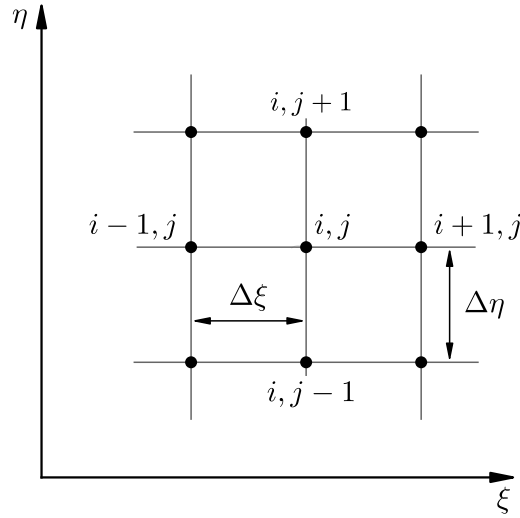
Figure 2.12: Grid index convention

be obtained for the coordinate values at the indices i, j:

$$x_{i,j} = \frac{1}{2\left(\alpha_{i,j} + \gamma_{i,j}\right)} \left[\alpha_{i,j}\left(x_{i+1,j} + x_{i-1,j}\right) \right.$$
$$- \frac{1}{2}\beta_{i,j}\left(x_{i+1,j+1} - x_{i+1,j-1} - x_{i-1,j+1} + x_{i-1,j-1}\right)$$
$$\left. + \gamma_{i,j}\left(x_{i,j+1} + x_{i,j-1}\right) \right] \quad \text{with } x = z, r \tag{2.71}$$

Note that in the above equation x can be substituted by z or r because the equations are identical for both coordinate directions. The geometric coefficients $\alpha_{i,j}, \beta_{i,j}, \gamma_{i,j}$ are analogously approximated by finite differences and the corresponding formulas are provided in Appendix A.2.5, Equation A.21.

Equation 2.71 is solved iteratively using the SOR method, which is also explained in detail in Appendix A.2.5. Taking n as the iteration index the iteration procedure can be formulated as:

$$x_{i,j,\text{SOR}}^{(n+1)} = (\omega - 1)x_{i,j,\text{SOR}}^{(n)} + \omega x_{i,j,\text{GS}}^{(n+1)} \quad \text{with } x = z, r \tag{2.72}$$

The Gauß-Seidel step (GS) is defined as:

$$x_{i,j,\text{GS}}^{(n+1)} = \frac{1}{2\left(\alpha_{i,j}^{(n)} + \gamma_{i,j}^{(n)}\right)} \left[\alpha_{i,j}^{(n)} \left(x_{i+1,j}^{(n)} + x_{i-1,j}^{(n+1)}\right) \right.$$

$$-\frac{1}{2}\beta_{i,j}^{(n)}\left(x_{i+1,j+1}^{(n)} - x_{i+1,j-1}^{(n)} - x_{i-1,j+1}^{(n+1)} + x_{i-1,j-1}^{(n+1)}\right)$$

$$\left. + \gamma_{i,j}^{(n)}\left(x_{i,j+1}^{(n)} + x_{i,j-1}^{(n+1)}\right) \right] \qquad \text{with } x = z, r \qquad (2.73)$$

As indicated in Equation 2.73 the geometric coefficients (α, β, γ) are taken at the last iteration step (iteration index n) because they depend on the grid-coordinates and are therefore not known a priori [56]. Consequently, the values of these coefficients have to be computed after the final iteration loop.

Convergence is assessed based on the relative error in the solution variable. The iteration process is stopped as soon as the maximum relative error is below a specified limit ϵ:

$$\max\left(\frac{|x_{i,j}^{(n+1)} - x_{i,j}^{(n)}|}{\max|x|}\right) < \epsilon \qquad \text{with } x = z, r \qquad (2.74)$$

This condition has to be fulfilled for z and r coordinates simultaneously. However, an upper limit of iterations is considered in order to avoid endless loops. The target value of the convergence limit and the relaxation parameter ω can be set by the user. By default the following values are used:

$$\omega = 1.8 \qquad (2.75)$$

$$\epsilon = 1.0 \times 10^{-6} \qquad (2.76)$$

If no value is provided or an invalid value is specified by the user, the optimum relaxation factor is estimated according to the formula provided by Pletcher et al. [60]:

$$\omega_{opt} = \frac{2}{1 + (1 - \sigma^2)^{1/2}} \qquad (2.77)$$

Considering uniform spacing in ξ and η direction ($\Delta\xi/\Delta\eta = 1$) and denoting the number of nodes along i and j direction by N_j and N_i respectively the factor σ can be calculated as follows:

$$\sigma = \frac{1}{2}\left(\cos\left(\frac{\pi}{N_i - 1}\right) + \cos\left(\frac{\pi}{N_j - 1}\right)\right) \qquad (2.78)$$

Before the grid generation procedure is applied to the real problem of the meridional

(a) Extended physical domain

(b) Boundary nodes

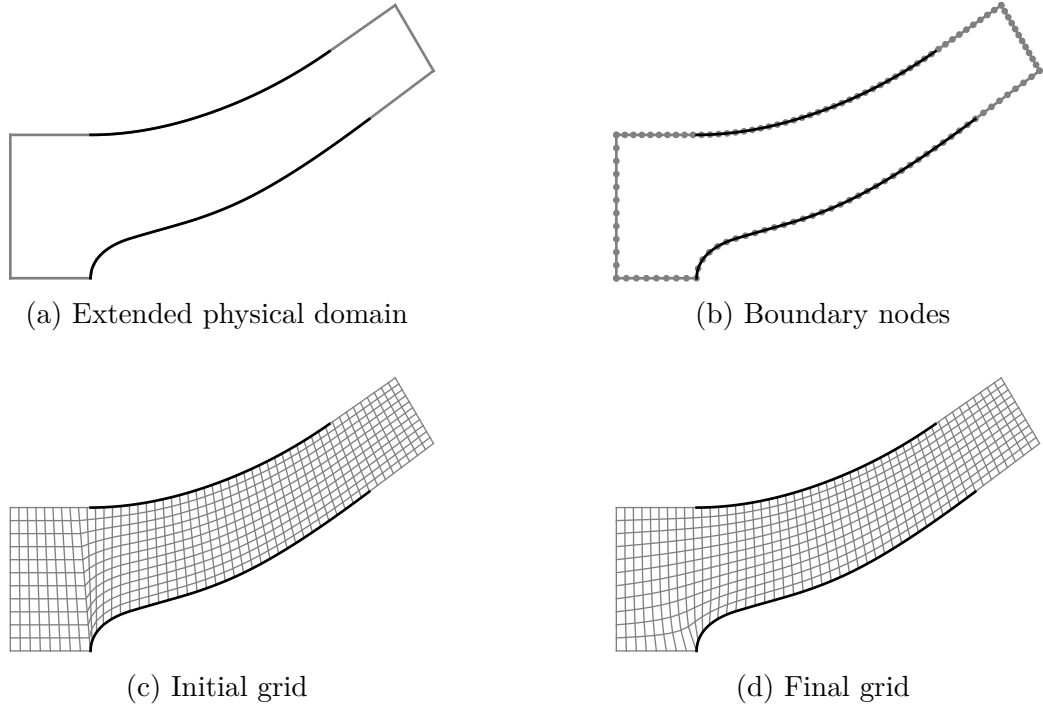(c) Initial grid

(d) Final grid

Figure 2.13: Grid generation procedure

section, the physical domain is extended by a reasonable amount to move the boundaries away from the region of interest (see Figure 2.13a). On the boundary curves the grid nodes are placed equidistantly as depicted in Figure 2.13b. To initialize the interior nodes linear segments are constructed from hub to shroud and divided into equidistant segments. A comparison between the state of the grid after initialization and after the iteration procedure is displayed in Figures 2.13c and 2.13d, respectively.

Once the grid generation is completed, Equation 2.68 can be solved in the computational domain to obtain the stream function distribution. The transformed equation can be written as (see Appendix A.3):

$$\alpha \left(\frac{\partial^2 \Psi}{\partial \xi^2} \right) - 2\beta \left(\frac{\partial^2 \Psi}{\partial \xi \partial \eta} \right) + \gamma \left(\frac{\partial^2 \Psi}{\partial \eta^2} \right) - \frac{\delta}{r} \left(\left(\frac{\partial \Psi}{\partial \eta} \right) \left(\frac{\partial z}{\partial \xi} \right) - \left(\frac{\partial \Psi}{\partial \xi} \right) \left(\frac{\partial z}{\partial \eta} \right) \right) = 0 \quad (2.79)$$

The coefficient δ is equal to the Jacobian J and is computed from the known grid metrics:

$$\delta = \frac{\partial z}{\partial \xi} \frac{\partial r}{\partial \eta} - \frac{\partial z}{\partial \eta} \frac{\partial r}{\partial \xi} = J \quad (2.80)$$

Again central differences are used to discretize the above equation at the interior nodes and the SOR method is used analogously to the grid generation problem. The discretized equations are given in full detail in Appendix A.3. To produce the desired volume flow through the impeller the boundary conditions have to be set adequately. The relation

between the fluid flow through a streamtube bounded by the surfaces that are generated by the contour lines of Stokes' stream function at the values Ψ_2 and Ψ_1 is given as follows:

$$Q_{12} = 2\pi \left(\Psi_2 - \Psi_1 \right) \tag{2.81}$$

Since the hub and shroud boundary curves are streamlines by definition, the value of stream function can be arbitrarily chosen for all the nodes at one of these boundaries. In the current implementation the stream function is set to zero at the hub ($\Psi_h = \Psi_{i,0} = 0$) but any other value would be possible. Considering that the full volume flux Q is passing between hub and shroud the value at the shroud nodes, in the general case, can be obtained from:

$$\Psi_s = \Psi_{i,N_{j-1}} = \frac{Q}{2\pi} + \Psi_h \tag{2.82}$$

To compute suitable values at the grid nodes on the inlet and outlet boundary nodes

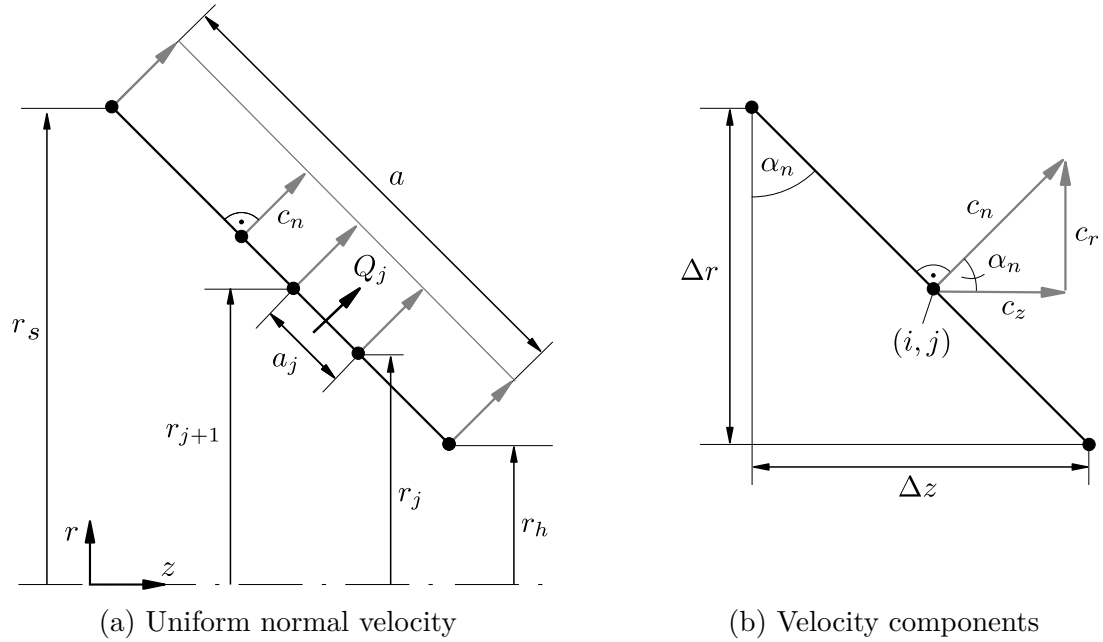(a) Uniform normal velocity　　　　(b) Velocity components

Figure 2.14: Inlet and outlet boundary conditions

a uniform normal velocity profile is assumed. As depicted in Figure 2.14a computation of the normal velocity is accomplished by:

$$c_n = \frac{Q}{\pi \left(r_s + r_h \right) a} \tag{2.83}$$

This relation can be used to calculate the volume flux through the streamtube with

index j bounded by the streamlines of stream function values Ψ_j and Ψ_{j+1}:

$$Q_j = c_n\,\pi(r_j + r_{j+1})\,a_j \tag{2.84}$$

Equation 2.84, in turn, can be used to compute the stream function at the boundary node with index j from Equation 2.81 as follows:

$$\Psi_{j+1} = \frac{Q_j}{2\pi} + \Psi_j = \frac{1}{2}\,c_n\,(r_j + r_{j+1})\,a_j + \Psi_j \tag{2.85}$$

Using Equation 2.85 the stream function values are set for all nodes along the inlet and outlet boundaries. The interior nodes are initialized by copying the values from the inlet nodes to the nodes with the same index j. After initialization the SOR method is used to obtain the solution for Ψ at the interior nodes iteratively. The formal iteration procedure is given in the Appendix A.3. Convergence is judged analogously to the grid generation procedure based on the maximum relative error in the solution variable $(\Delta\Psi)^*_{\max}$ as given in Equation A.29. Once the solution is obtained, the value of stream function is available on all grid nodes including the boundaries. The next section deals with the computation of the velocities and the extraction of streamlines for further usage in the inducer design process.

2.4.3 Velocity and Streamline Computation

Given the values of stream function on the nodes of the grid the velocity components can be computed by solving Equations 2.65a and 2.65b. Again these equations are most conveniently solved in the computational domain. The transformed versions of these equations (see Appendix A.3) read:

$$c_z = \frac{1}{r\delta}\left(\left(\frac{\partial\Psi}{\partial\eta}\right)\left(\frac{\partial z}{\partial\xi}\right) - \left(\frac{\partial\Psi}{\partial\xi}\right)\left(\frac{\partial z}{\partial\eta}\right)\right) \tag{2.86a}$$

$$c_r = \frac{1}{r\delta}\left(\left(\frac{\partial\Psi}{\partial\eta}\right)\left(\frac{\partial r}{\partial\xi}\right) - \left(\frac{\partial\Psi}{\partial\xi}\right)\left(\frac{\partial r}{\partial\eta}\right)\right) \tag{2.86b}$$

Discretization of these equations using central differences is straightforward and the velocities on the interior grid nodes can be readily computed (see Appendix A.3, Equation A.32). Some attention must however be paid to the treatment of the nodes on the boundary curves that represent the inlet and outlet as well as the hub and shroud contours. At the inlet and the outlet borders the velocity is assumed to be normal to the boundary curve. Thus, the components of the velocity are retrieved from the known value of the normal velocity. Given the local inclination of the boundary segment (see

Figure 2.14b) the components at the inlet (index $i = 0$) and the outlet (index $i = N_i - 1$) are set for all nodes in spanwise direction ($0 \leq j \leq N_j - 1$) as follows:

$$c_{z,i,j} = c_{n,i} \cos \alpha_{n,i} \tag{2.87a}$$

$$c_{r,i,j} = c_{n,i} \sin \alpha_{n,i} \tag{2.87b}$$

Since by definition the hub and shroud boundaries are streamlines, the stream function is constant along these curves. Hence, the partial derivatives of stream function with respect to ξ are vanishing along these curves and equations 2.86a and 2.86b are simplified as:

$$c_z = \frac{1}{r\delta} \left(\frac{\partial \Psi}{\partial \eta} \right) \left(\frac{\partial z}{\partial \xi} \right) \tag{2.88a}$$

$$c_r = \frac{1}{r\delta} \left(\frac{\partial \Psi}{\partial \eta} \right) \left(\frac{\partial r}{\partial \xi} \right) \tag{2.88b}$$

The remaining partial derivatives are approximated by forward differences at the hub and backward differences at the shroud boundary. By using the three point formulas [56] for the derivatives normal to the boundaries (in η direction) and central differences along the boundaries (in ξ direction), the following equations are obtained:

$$c_{z,i,j} = \begin{cases} \frac{1}{4r_{i,j}\delta_{i,j}} \left(-3\Psi_{i,j} + 4\Psi_{i,j+1} - \Psi_{i,j+2} \right) \left(z_{i+1,j} - z_{i-1,j} \right) & \text{for } j = 0 \\ \frac{1}{4r_{i,j}\delta_{i,j}} \left(\Psi_{i,j-3} - 4\Psi_{i,j-2} + 3\Psi_{i,j-1} \right) \left(z_{i+1,j} - z_{i-1,j} \right) & \text{for } j = N_j - 1 \end{cases} \tag{2.89a}$$

$$c_{r,i,j} = \begin{cases} \frac{1}{4r_{i,j}\delta_{i,j}} \left(-3\Psi_{i,j} + 4\Psi_{i,j+1} - \Psi_{i,j+2} \right) \left(r_{i+1,0} - r_{i-1,0} \right) & \text{for } j = 0 \\ \frac{1}{4r_{i,j}\delta_{i,j}} \left(\Psi_{i,j-3} - 4\Psi_{i,j-2} + 3\Psi_{i,j-1} \right) \left(r_{i+1,j} - r_{i-1,j} \right) & \text{for } j = N_j - 1 \end{cases} \tag{2.89b}$$

Equations 2.89a and 2.89b are used to compute the velocity components for $1 \leq i \leq N_i - 2$, that is on all nodes on the lower (hub) and upper (shroud) boundaries excluding the corner nodes, which are considered to belong to the inlet and outlet borders. Note that the Jacobion δ has to be computed analogously by forward and backward differences on the hub and shroud boundaries:

$$\delta_{i,j} = \begin{cases} \frac{1}{4} \Big(\left(z_{i+1,j} - z_{i-1,j} \right) \left(-3r_{i,j} + 4r_{i,j+1} - r_{i,j+2} \right) \\ \quad - \left(r_{i+1,j} - r_{i-1,j} \right) \left(-3z_{i,j} + 4z_{i,j+1} - z_{i,j+2} \right) \Big) & \text{for } j = 0 \\ \frac{1}{4} \Big(\left(z_{i+1,j} - z_{i-1,j} \right) \left(r_{i,j-3} - 4r_{i,j-2} + 3r_{i,j-1} \right) \\ \quad - \left(r_{i+1,j} - r_{i-1,j} \right) \left(r_{i,j-3} - 4r_{i,j-2} + 3r_{i,j-1} \right) \Big) & \text{for } j = N_j - 1 \end{cases} \tag{2.90a}$$

Looking at Equations 2.89a and 2.89b it is evident that at nodes on the axis of rotation ($r = 0$) some special treatment is required. This special case is likely to occur on the hub boundary only as can be seen in the example provided in Figure 2.15. The case is treated in the current implementation by copying the z-component of velocity from the neighbor in η direction and setting the r- component to zero. At a stagnation point at zero radius this might locally introduce some unphysical behavior, which, in general, should not disturb the overall result.

Example solutions showing the stream function contours (the streamlines) and the corresponding distribution of meridional velocity for a generic mixed flow impeller are displayed in Figures 2.15a and 2.15b respectively. An overview of the complete meridional
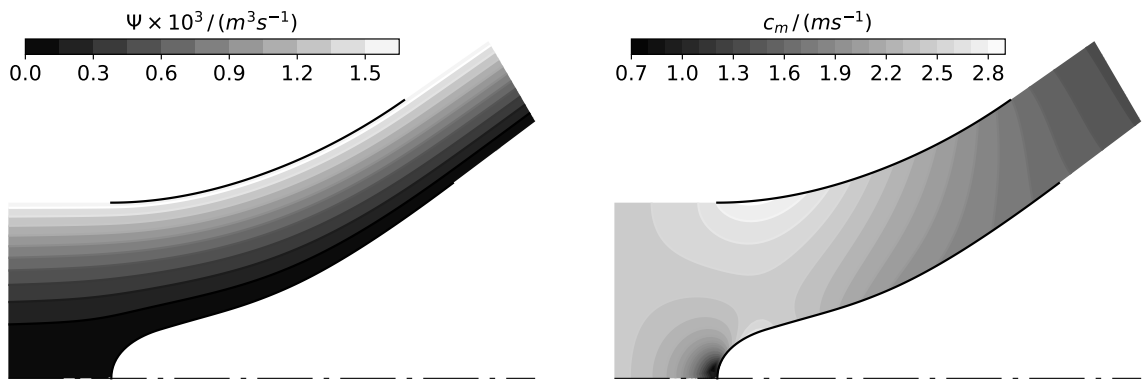
(a) Contours of stream function

(b) Contours of meridional velocity

Figure 2.15: Example solution of the SMA

flow analysis procedure is given in Figure 2.16. Hub, shroud, inlet and outlet curves have to be provided point-by-point. The same number of points has to be specified for hub and shroud and for inlet and outlet respectively. As a result, the grid generation routine stays independent of any geometric algorithms and can in principle be applied to arbitrary, two-dimensional geometries. Furthermore, it is possible to influence the grid distributions on the boundaries by positioning the points appropriately. However, in the developed design procedure this process is automated and the B-spline curves representing the hub and shroud shapes as well as the inlet and outlet segments are sampled equidistantly before they are used as input to the grid generation process. The number of nodes along the grid directions is implicitly set by the number of points provided for the curves.

The iterative routines used for solving the grid and stream function equations are translated to `Cython`-Code [15] in order to reduce the computation time. Both routines expect an equal set of numerical parameters, consisting of relaxation factor, maximum
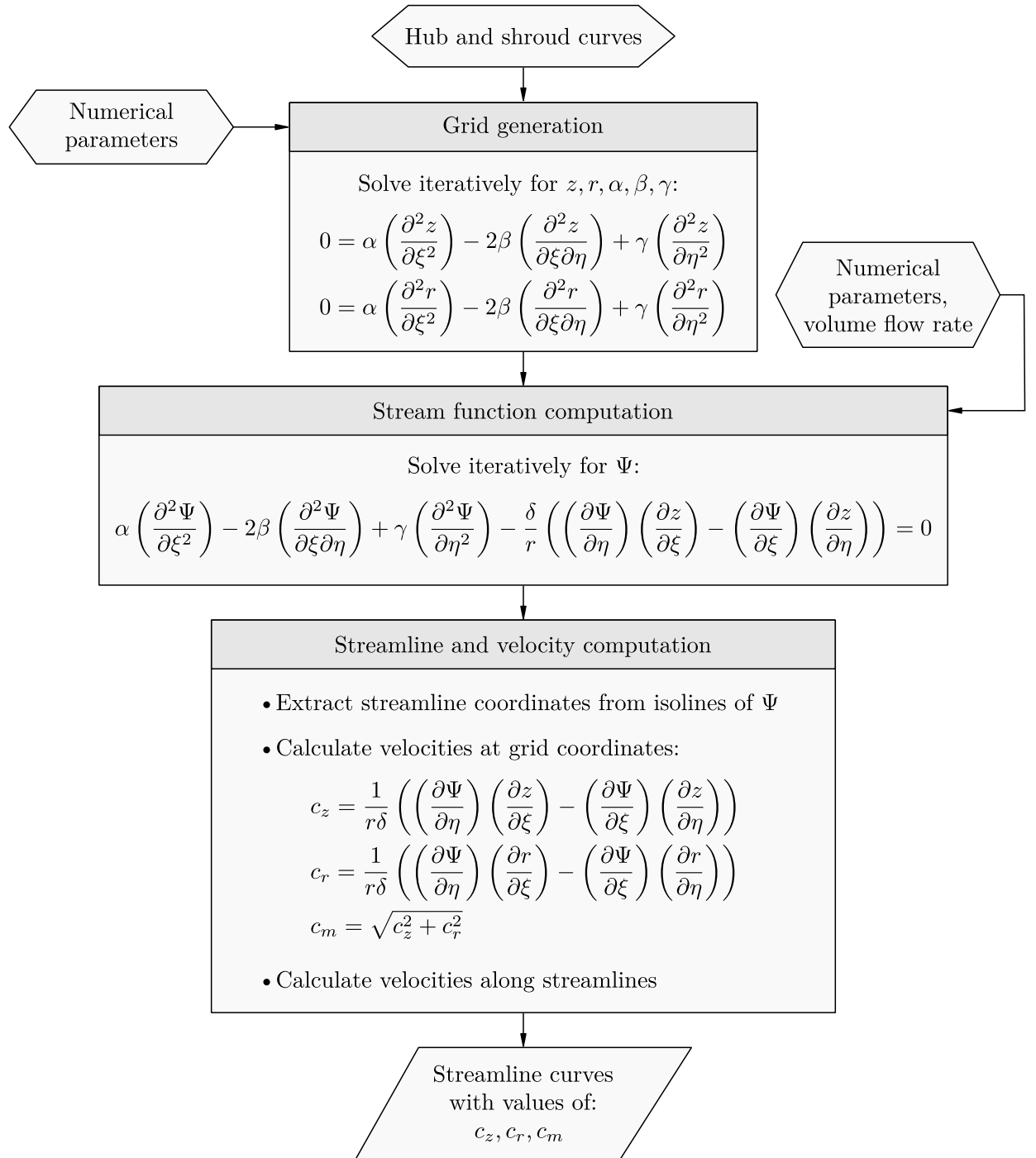
Figure 2.16: Overview of the SMA

number of iterations and convergence tolerance. To set up the stream function solution the volume flow rate has to be provided as well, so that the correct level of velocity is obtained.

The streamline computation is performed with the help of the class `Cntr` of the `matplotlib._cntr` module [33], which is part of the `scipy` package [69] and allows the extraction of the coordinates at constant contour levels. As can be seen from Equation 2.81 the choice of equidistant contour levels leads to streamlines which enclose equal parts of the volume flow rate through the meridional section.

The velocity components along the streamlines are computed by using the class `Clough-Tocher2DInterpolator` of the `scipy.interpolate` module [69]. This method performs interpolation of the data available at the grid nodes. Thus, it is able to deliver the velocities at arbitrary coordinates in the meridional section. If coordinates very close to, or even slightly outside of, the boundaries are specified, the aforementioned method might fail. To avoid invalid or unphysical velocity values the `NearestNDInterpolator` of the `scipy.interpolate` module, which simply uses the value at the closest grid point, is provided as a fallback mechanism [69].

Once the solution is obtained, any desired number of streamlines can be requested. Streamlines are represented by point coordinates and the corresponding velocity components.

2.5 Simple Head Prediction (SHP)

2.5.1 Singularity Method

Basis of the SHP is a classical singularity method applied on the camber curves of two-dimensional blade sections. The singularity method applied in the present thesis was originally proposed by Li [51] and allows to estimate the theoretical head on strictly cylindrical blade sections. In order to apply this method to arbitrarily shaped meridional sections it has to be reformulated in terms of m', θ coordinates and the corresponding velocity components in the conformal cascade plane. Figure 2.17a shows a general meridional configuration containing K streamlines on which the blade geometry is available. The transfer of the corresponding blade sections from the meridional to the cascade plane is achieved by sampling the meridional streamlines at $i = 0 \ldots N - 1$ locations and evaluating the m', θ coordinates of the camber curve at each sampling point. Note that the number of sections K as well as the number of points along each section N is not necessarily equal to the number of design sections N_k and the number of points along the streamlines N_i, respectively (see Section 3.4.4).

An exemplary sketch of the resulting cascade for any $k = 0 \ldots K - 1$ is shown in

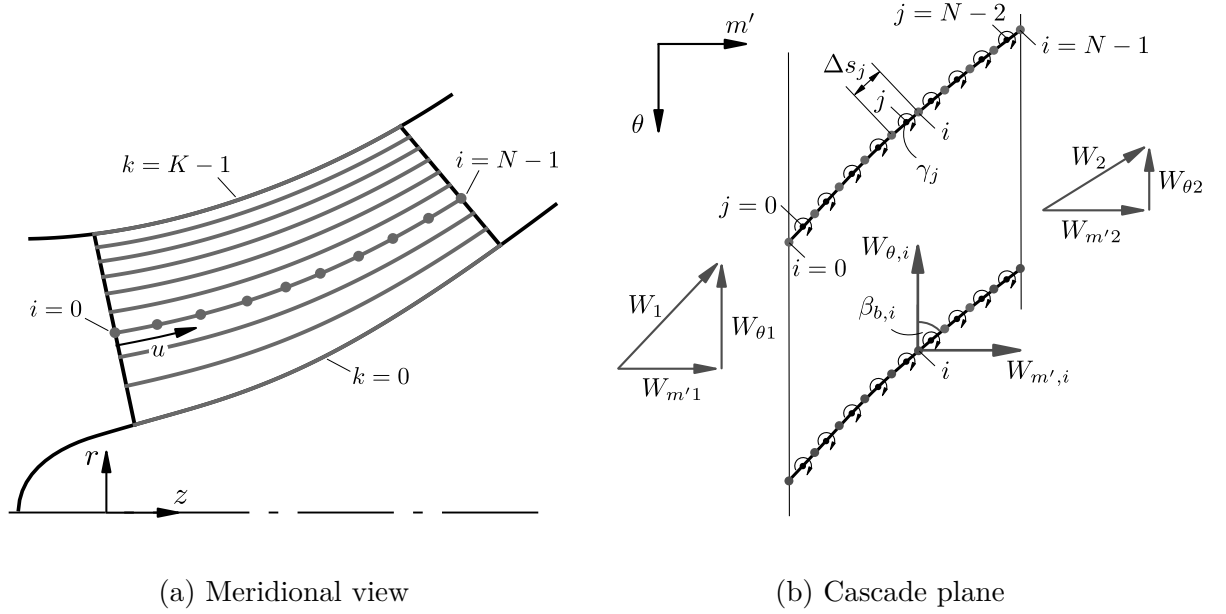(a) Meridional view   (b) Cascade plane

Figure 2.17: Singularity method - mapping from meridional to the cascade plane

Figure 2.17b. Following Lewis [50] the components of the relative velocity components $\boldsymbol{w} = (w_m, w_\theta) = (c_m, \omega r - c_\theta)$ are transformed to the cascade plane by multiplying with the local radius:

$$W_{m'} = r\, w_m \tag{2.91a}$$

$$W_\theta = r\, w_\theta \tag{2.91b}$$

The general approach of the singularity method (as well as the techniques described in references [49] and [50]) is the superposition of a mean translational flow $\bar{\boldsymbol{W}}$ with the flow induced by a singularity distribution located on the blade camber line $\hat{\boldsymbol{W}}$:

$$\boldsymbol{W} = \bar{\boldsymbol{W}} + \hat{\boldsymbol{W}} \tag{2.92}$$

To calculate the induced velocity $\hat{W}$, a potential vortex with an initially unknown local vorticity density (that is the local vorticity strength per unit length) γ_j is placed at the midpoint of each segment ($j = 0 \ldots N - 2$) with length Δs_j between two geometry points i and $i + 1$, as shown in Figure 2.17b. The blade circulation Γ is calculated by summing up all vorticity elements:

$$\Gamma = \sum_{j=0}^{N-2} \gamma_j\, \Delta s_j \tag{2.93}$$

In order to solve for the unknown values of local vorticity density the conformal velocity vector in the cascade plane is required to be tangential to the blade camber line. Formulating this constraint for each segment's end point (i.e. starting from $i = 1$) leads to the following system of equations:

$$\tan\left(\beta_{b,i}\right) = \frac{W_{m',i}}{W_{\theta,i}} = \frac{\bar{W}_{m',i} + \hat{W}_{m',i}}{\bar{W}_{\theta,i} + \hat{W}_{\theta,i}}, \quad i = 1, \ldots, N-1 \tag{2.94}$$

A general derivation of the formulas required to calculate the induced velocity components can be found in Lewis [50]. By application of the coordinate notation of the present thesis the cascade influence factors may be expressed as:

$$F_{m',i,j} = \frac{Z}{4\pi}\left[\frac{\sin\left(Z\left(\theta_i - \theta_j\right)\right)}{\cosh\left(Z\left(m'_i - m'_j\right)\right) - \cos\left(Z\left(\theta_i - \theta_j\right)\right)}\right] \tag{2.95a}$$

$$F_{\theta,i,j} = -\frac{Z}{4\pi}\left[\frac{\sinh\left(Z\left(m'_i - m'_j\right)\right)}{\cosh\left(Z\left(m'_i - m'_j\right)\right) - \cos\left(Z\left(\theta_i - \theta_j\right)\right)}\right] \tag{2.95b}$$

With these formulas the components of the induced velocity can be written in the following compact form:

$$\hat{W}_{m',i} = \sum_{j=0}^{N-2} F_{m',i,j}\,\gamma_j\,\Delta s_j \tag{2.96a}$$

$$\hat{W}_{\theta,i} = \sum_{j=0}^{N-2} F_{\theta,i,j}\,\gamma_j\,\Delta s_j \tag{2.96b}$$

The translational flow has to be modeled in such a way that the correct velocity triangles (see Figure 2.17b) are obtained at the cascade entry (index 1) and cascade exit (index 2). A feature of the method proposed in [51] is the consideration of blade blockage. In the original method the flow velocity on streamsurfaces (that are the surfaces constructed by revolution of the streamlines) are obtained by interpolation and extrapolation of the mean stream tube velocities that are corrected by a blockage factor. Contrary to the original approach the velocities along the streamlines are already known from the previously described meridional flow analysis.

Since the meridional flow is computed without considering the influence of the blades, the local blade blockage is computed according to Equation 2.13:

$$b_i = \left(1 - \frac{t_i\,Z}{2\,\pi\,r_i\,\sin\beta_{b,i}}\right)^{-1} \tag{2.97}$$

Assuming mass conservation along the streamline, the meridional component of the translational flow is defined as:

$$\bar{W}_{m',i} = b_i \, W_{m',i} = W_{m'1} \, \frac{b_i \, W_{m',i}}{W_{m'1}} \tag{2.98}$$

The term $W_{m'1}$ indicates the known meridional flow velocity at the cascade entry location and is directly coupled to the volume flow through the impeller. The term $W_{m',i}$ is the local meridional velocity transferred to the cascade plane. Following Lewis [50] the circumferential component of the translational flow is given by the following equation:

$$\bar{W}_{\theta,i} = W_{\theta\infty} + W_{\omega,i} \tag{2.99}$$

In Equation 2.99 two terms appear that are not that obvious in their meaning. The first term is the circumferential component of the vector mean velocity of the cascade flow, which itself depends on the blade circulation. This fact would require to solve Equation 2.94 separately for each operating point under consideration. How this problem can be resolved quite easily is explained further below in this section. The second term on the right-hand side of Equation 2.99 is related to the influence of the local streamline radius on the relative vorticity strength and is derived in reference [50] as follows:

$$W_{\omega,i} = \omega \left(r_i^2 - \frac{1}{2} \left(r_1^2 + r_2^2 \right) \right). \tag{2.100}$$

After inserting Equations 2.96, 2.98, 2.99 and 2.100 into Equation 2.94 and rearranging the resulting system, the following system of linear equations is obtained for any blade section k:

$$\sum_{j=0}^{N-2} \mathrm{K}_{i,j} \, \gamma_j \, \Delta s_j = \mathrm{R}_i, \tag{2.101}$$

where

$$\mathrm{K}_{i,j} = \tan\left(\beta_{b,i}\right) F_{\theta,i,j} - F_{m',i,j} \tag{2.102}$$

$$\mathrm{R}_i = W_{m'1} \left(b_i \, W_{m',i} / W_{m'1} \right) - W_{\theta\infty} \tan\left(\beta_{b,i}\right)$$

$$- \omega \left(r_i^2 - \frac{1}{2} \left(r_1^2 + r_2^2 \right) \right) \tan\left(\beta_{b,i}\right) \tag{2.103}$$

To avoid solving this system for multiple operating conditions the solution procedure proposed by Lewis [50], based on superposition of so-called unit components, is applied.

If the vorticity distribution is decomposed as follows

$$\gamma_j = W_{m'1}\,\gamma_{m',j} + W_{\theta\infty}\,\gamma_{\theta,j} + \omega\,\gamma_{\omega,j}, \tag{2.104}$$

three independent systems of equations are obtained for unit meridional flow velocity $W_{m'1} = 1$, unit circumferential flow velocity $W_{\theta\infty} = 1$ and unit angular velocity $\omega = 1$, respectively:

$$\sum_{j=0}^{N-2} \mathrm{K}_{i,j}\,\gamma_{m',j}\,\Delta s_j = \frac{b_i\,W_{m',i}}{W_{m'1}} \tag{2.105a}$$

$$\sum_{j=0}^{N-2} \mathrm{K}_{i,j}\,\gamma_{\theta,j}\,\Delta s_j = -\tan\left(\beta_{b,i}\right) \tag{2.105b}$$

$$\sum_{j=0}^{N-2} \mathrm{K}_{i,j}\,\gamma_{\omega,j}\,\Delta s_j = -\tan\left(\beta_{b,i}\right)\left(r_i^2 - \frac{1}{2}\left(r_1^2 + r_2^2\right)\right) \tag{2.105c}$$

Before the systems are solved it is necessary to specify the Kutta condition on the last segment by setting $\gamma_{N-2} = 0$. This reduces the number of equations effectively to $N-2$. Once the unit solutions are obtained, the corresponding circulations are calculated as:

$$\Gamma_{m'} = \sum_{j=0}^{N-1} \gamma_{m',j}\,\Delta s_j \tag{2.106a}$$

$$\Gamma_{\theta} = \sum_{j=0}^{N-1} \gamma_{\theta,j}\,\Delta s_j \tag{2.106b}$$

$$\Gamma_{\omega} = \sum_{j=0}^{N-1} \gamma_{\omega,j}\,\Delta s_j \tag{2.106c}$$

By adequately scaling the unit solutions the actual total circulation can finally be computed as follows:

$$\Gamma = W_{m'1}\,\Gamma_{m'} + W_{\theta\infty}\,\Gamma_{\theta} + \omega\,\Gamma_{\omega} \tag{2.107}$$

2.5.2 Exit Flow

As shown by Lewis [50] the θ-components of the cascade flow at the entry and exit locations can be calculated with the following equations:

$$
\begin{aligned}
W_{\theta 1} = {} & W_{m'1}\left(\frac{Z}{4\pi}\Gamma_{m'}\right) + W_{\theta\infty}\left(1 + \frac{Z}{4\pi}\Gamma_{\theta}\right) \\
& + \omega\left(\frac{Z}{4\pi}\Gamma_{\omega} + \frac{1}{2}\left(r_1^2 - r_2^2\right)\right)
\end{aligned}
\tag{2.108a}
$$

$$
\begin{aligned}
W_{\theta 2} = {} & -W_{m'1}\left(\frac{Z}{4\pi}\Gamma_{m'}\right) + W_{\theta\infty}\left(1 - \frac{Z}{4\pi}\Gamma_{\theta}\right) \\
& - \omega\left(\frac{Z}{4\pi}\Gamma_{\omega} + \frac{1}{2}\left(r_1^2 - r_2^2\right)\right)
\end{aligned}
\tag{2.108b}
$$

Returning to the previously stated problem of the unknown velocity $W_{\theta\infty}$, Equation 2.108a can now be rearranged to obtain:

$$
\begin{aligned}
W_{\theta\infty} = {} & \frac{1}{1 + \frac{Z}{4\pi}\Gamma_{\theta}}\left[W_{\theta 1} - W_{m'1}\left(\frac{Z}{4\pi}\Gamma_{m'}\right)\right. \\
& \left. - \omega\left(\frac{Z}{4\pi}\Gamma_{\omega} + \frac{1}{2}\left(r_1^2 - r_2^2\right)\right)\right]
\end{aligned}
\tag{2.109}
$$

With $W_{\theta\infty}$ provided as a function of the unit solutions the total circulation can directly be computed from Equation (2.107) in a straightforward manner. Likewise the relative flow angle at the cascade exit (or discharge) location can readily be computed with the help of Equation (2.108b):

$$
\beta_2 = \arctan\left(\frac{W_{m'2}}{W_{\theta 2}}\right)
\tag{2.110}
$$

2.5.3 Theoretical Head

In order to calculate the theoretical head produced by the blade section k under consideration Euler's pump equation for the relative system (Equation 2.23) is used:

$$
H_{th,k}^{tot} = \frac{1}{\rho\,g}\left(p_{tot,2} - p_{tot,1}\right) = \omega^2\left(r_2^2 - r_1^2\right) - \omega\left(W_{\theta 2} - W_{\theta 1}\right)
\tag{2.111}
$$

Inserting Equations (2.108a) and (2.108b) leads to:

$$
H_{th,k}^{tot} = \omega\frac{Z}{2\pi g}\left(W_{m'1}\,\Gamma_{m'} + W_{\theta\infty}\,\Gamma_{\theta} + \omega\,\Gamma_{\omega}\right)
\tag{2.112}
$$

Together with Equation (2.107) and using $\omega = 2\pi n$ the following, simple equation for the theoretical head is obtained:

$$H_{th,k}^{tot} = \frac{n\,Z}{g}\,\Gamma_k \tag{2.113}$$

The theoretical total head of the full inducer is finally computed by taking the arithmetic average over all blade sections as proposed by Li [51]:

$$H_{th}^{tot} = \frac{1}{K}\sum_{k=0}^{K-1} H_{th,k}^{tot} \tag{2.114}$$

However, since during standard acceptance tests, the total pressure is not measured, the head is corrected by the fraction caused by the dynamic pressure rise due to the change in circumferential velocity of the absolute flow. Using again Equations (2.108a) and (2.108b) the head associated to this velocity components is expressed as:

$$\begin{aligned}\Delta H_{th,\theta,k} &= \frac{1}{2g}\left[c_{\theta 2}^2 - c_{\theta 1}^2\right]\\ &= \frac{1}{2g}\left[\left(\omega r_2 - \frac{W_{\theta 2}}{r_2}\right)^2 - \left(\omega r_1 - \frac{W_{\theta 1}}{r_1}\right)^2\right]\end{aligned} \tag{2.115}$$

Thus, the corrected theoretical head expected to be a more accurate estimate when comparing with experimental test results is calculated as:

$$H_{th,k} = \frac{n\,Z}{g}\,\Gamma_k - \Delta H_{th,\theta,k} \tag{2.116}$$

To compute the theoretical head of the entire inducer the same method of averaging as in Equation 2.114 is applied:

$$H_{th} = \frac{1}{K}\sum_{k=0}^{K-1} H_{th,k} \tag{2.117}$$

The solution of Equations 2.105a, 2.105b and 2.105c can be obtained by any standard procedure for the solution of linear systems of equations. In the present implementation the `solve` method of the `scipy.linalg` module is used. Consequently, the whole procedure including the inviscid meridional flow calculation provides a result almost instantly if performed on an up-to-date workstation. Due to its simplicity the method can easily be integrated into a preliminary design procedure and can be used in an interactive environment delivering feedback on the influence of geometry changes on the inducer performance.

2.5.4 Loss Model

The singularity method described in the previous section is an idealized, two-dimensional and inviscid approximation to the real flow conditions in the blade passages. Losses that occur due to viscous effects have therefore to be considered by a loss model. In the current work the very simple model developed by Li [51] is used. Because this model was derived from experimental data, it should also include the influence of tip clearance. The head loss predicted with this model is related to the mean inflow velocity at the root mean square (rms) radius $r_{1,\mathrm{rms}} = \sqrt{\frac{1}{2}(r_{1h}^2 + r_{1s}^2)}$ as follows:

$$H_{loss} = f_c \xi \frac{w_{1,\mathrm{rms}}^2}{2g} \tag{2.118}$$

As can be seen from Fig. 2.18a the loss coefficient ξ can be expressed as a function of
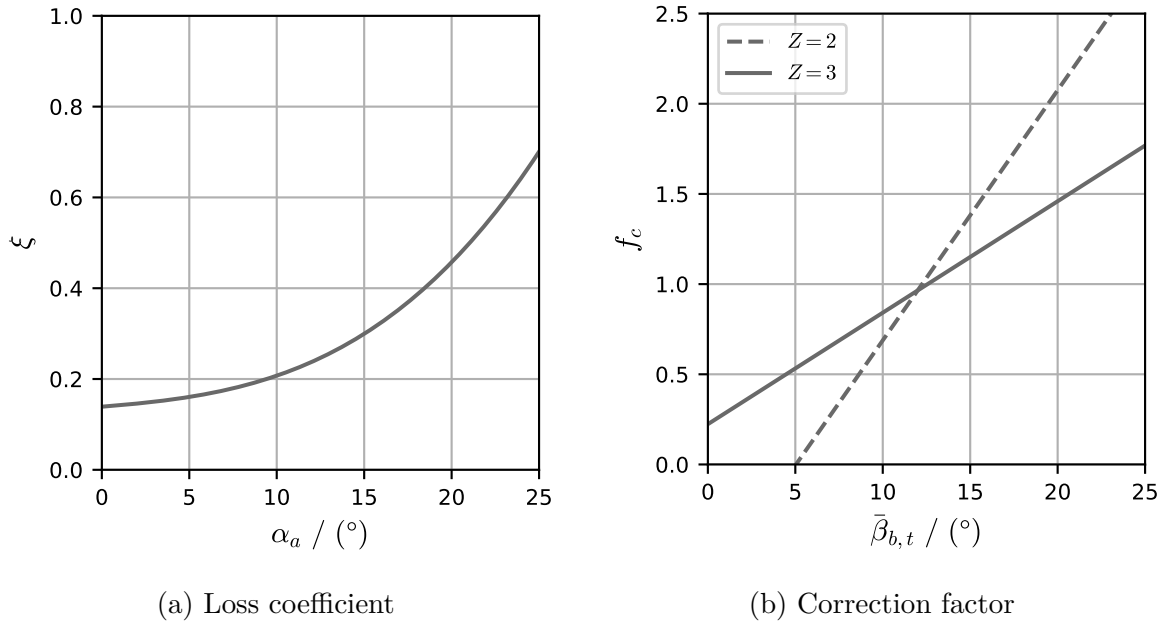
(a) Loss coefficient

(b) Correction factor

Figure 2.18: Loss model, reproduced from Li [51]

angle of attack α_a at the rms-radius. Because the camber of inducers is comparatively low and the blades are very long, no distinction is made between incidence and angle of attack, and the latter is calculated as:

$$\alpha_a = \beta_b - \beta \tag{2.119}$$

The factor f_c is a correction factor derived by Li [51] that is correlated to the number of blades and the mean blade angle at the tip radius according to Figure 2.18b. The head of the inducer is finally calculated by subtracting the head loss (Equation 2.118) from

the mean theoretical head (Equation 2.117):

$$H = H_{th} - H_{loss} \tag{2.120}$$

Analogously, the total head is calculated as follows:

$$H^{tot} = H_{th}^{tot} - H_{loss} \tag{2.121}$$

2.5.5 Overview

With the loss model presented in the previous section the proposed method for head prediction of non-cavitating inducers is complete. An overview of the SHP is given by the flow chart in Figure 2.19, which also includes the most important formulas. An intrinsic weakness of the method clearly is the one-way coupling of meridional and cascade flow. This could lead to inaccurate predictions of the exit flow conditions. Another problem that might restrict the application of the method is the fact that the loss model is applied to the entire inducer only. As a result, there's no information of the loss distribution among the individual blade sections. A similar problem exists with the calculation of the total head, which is simply assumed to be the arithmetic average of the blade section heads. Nevertheless, these basic assumptions effectively reduce the complexity of the method and help to provide a very simple and fast method for the overall head prediction. Furthermore, the SHP alone does not require any iteration procedure and consequently is fast in terms of computation time.

2.5.6 Limitations

At this point some remarks on important limitations of the method as proposed in the previous sections are appropriate.

The first limitation concerns the treatment of the two-dimensional camber curve. In the present implementation of the method the camber curve is directly used as the geometrical foundation for the singularity method. Hence, the flow is constraint to follow the angle distribution prescribed by the camber curve. The basic assumption, which justifies this constraint, is that the blade is comparatively thin (or at least of constant thickness), such that the camber line, the mean camber line as well as the blade suction and pressure sides collapse into the same line (or can be considered of same shape). Thus, a major drawback of the approach chosen in the current implementation is that the actual profile design cannot be included in the cascade analysis. Only the blockage effect is considered irrespective of the actual asymmetry of the underlying thickness distributions.
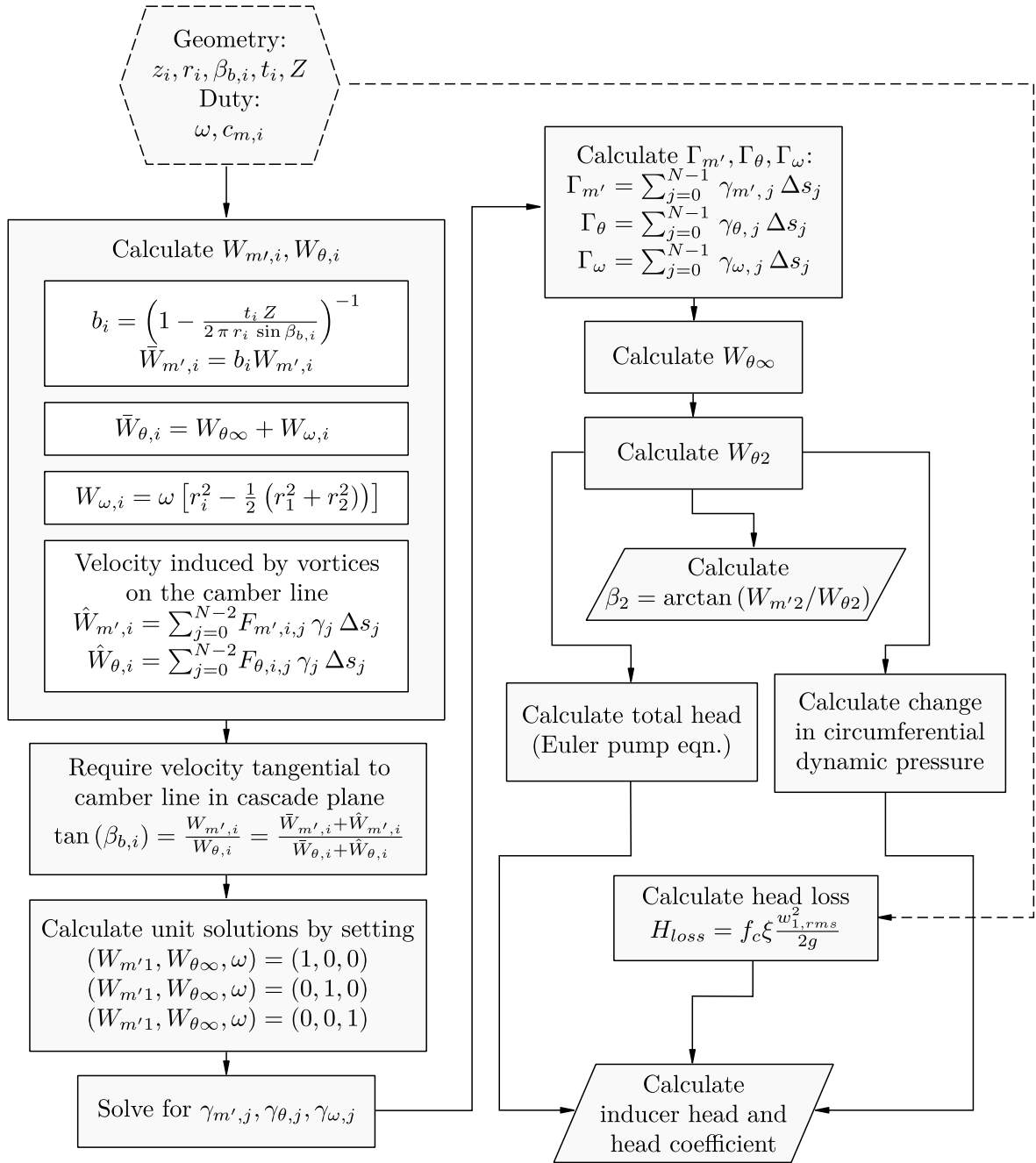
Figure 2.19: Overview of the SHP

A possible alternative, without transitioning to a more advanced analysis method, might be to compute the mean camber line under consideration of the actual blade profiles and to use this mean camber line to set up the singularity method. As a result, the asymmetry of thickness distributions would be reflected by the angle distribution of the mean camber line. However, unexpected blade angle distributions could be obtained along the mean camber line by this approach, especially for blades with substantially asymmetric thickness distributions.

Furthermore, for truly single sided thickness distributions, where either suction or pressure side thickness are set to zero, the camber curve effectively represents the suction or pressure side of the blade. Application of the singularity method to this camber curves might even provide a more direct feedback to the designer. Since the inducers investigated in this thesis (see Section 4.2.3) are designed with a suction side thickness distribution only, no recomputation of the camber curve is performed such that the pressure side blade angle progression as intended by the designer is used as the input for the singularity method.

The second restriction lies in the two-dimensional nature of the singularity method described above. Three-dimensional effects due to the three-dimensional blade shape (e.g. at the swept leading edge) simply cannot be reflected correctly by the two-dimensional approach, since the flow is limited to the two-dimensional streamsurfaces. Furthermore, three-dimensional flow features due to viscous effects are not considered in the present model. Viscous effects are only introduced in an integral fashion for the whole inducer, by means of a very simple loss model.

The third restriction concerns the computation of the average total head produced by the complete blade by averaging over the single blade sections. This approach could be seen as problematic or even questionable in so far as the average value of total head is identical to the head produced on each streamline only in case of true free vortex flow. In this case the streamline shape and velocity distributions computed with the SMA are consistent with the cascade solution of the SHP. For any other distribution of head predicted with the SHP the free vortex assumption is not strictly fulfilled anymore and the previously computed streamline and velocity distributions are no longer valid from a theoretical point of view. However, from a practitioner's point of view this inaccuracy could be accepted as long as the average value of head given by Equation 2.114 is reasonable and reflects changes in blade geometry.

As a consequence of the points discussed above, the SHP can of course only be considered a preliminary design tool, which produces an initial approximation to the head produced by the inducer. To adequately describe the distribution of flow variables three-dimensional, viscous methods have to be employed.

2.6 Computational Fluid Dynamics

2.6.1 Fundamental Equations

The commercial CFD code ANSYS CFX applied in this thesis uses a finite volume method to solve the governing equations of fluid mechanics. In the incompressible case, which is assumed for the flow through the inducers investigated, only the equations of

mass and momentum conservation are considered. Since Direct Numerical Simulations (DNS) are still not feasible for the majority of turbomachinery flows, turbulence has to be modeled. A very common approach to handle this issue, is the combination of the Reynolds-Averaged Navier Stokes (RANS) equations with a two-equation turbulence model. In what follows, the corresponding equations are discussed shortly. More details can be found in textbooks (e.g. Pletcher et al. [60], Versteeg and Malalasekera [68]) or the documentation of ANSYS CFX [5].

Making use of index notation and neglecting density fluctuations as well as momentum sources the conservation equations of mass and momentum can be written as follows:

$$\frac{\partial \bar{\rho}}{\partial t} + \frac{\partial}{\partial x_j} \left(\bar{\rho}\, \bar{u}_j \right) = 0 \tag{2.122}$$

$$\frac{\partial \bar{\rho}\, \bar{u}_i}{\partial t} + \frac{\partial}{\partial x_j} \left(\bar{\rho}\, \bar{u}_i \bar{u}_j \right) = -\frac{\partial \bar{p}}{\partial x_j} + \frac{\partial}{\partial x_j} \left(\bar{\tau}_{ij} - \bar{\rho}\, \overline{u_i' u_j'} \right) \tag{2.123}$$

The overline indicates time (or ensemble) averaged quantities and is usually dropped from all terms but the product of fluctuating velocity components $\overline{u_i' u_j'}$. For highly compressible flows density or mass weighted averaging (Favre-averaging) has to be performed [68]. In the incompressible case the equations above can be formulated as follows [60]:

$$\frac{\partial u_j}{\partial x_j} = 0 \tag{2.124}$$

$$\rho \left(\frac{\partial u_i}{\partial t} + \frac{\partial}{\partial x_j} \left(u_i\, u_j \right) \right) = -\frac{\partial p}{\partial x_j} + \frac{\partial}{\partial x_j} \left(\tau_{ij} - \rho\, \overline{u_i' u_j'} \right) \tag{2.125}$$

The terms τ_{ij} represent the components of molecular stress tensor and the terms $\rho\, \overline{u_i' u_j'}$ are the so-called Reynolds stresses. For a Newtonian fluid the former can be expressed as:

$$\tau_{ij} = \mu \left[\left(\frac{\partial u_i}{\partial x_j} + \frac{\partial u_j}{\partial x_i} \right) - \frac{2}{3} \delta_{ij} \frac{\partial u_k}{\partial x_k} \right] \tag{2.126}$$

Making use of Equation 2.124, the second term in the square brackets vanishes and Equation 2.126 is simplified to:

$$\tau_{ij} = \mu \left(\frac{\partial u_i}{\partial x_j} + \frac{\partial u_j}{\partial x_i} \right) \tag{2.127}$$

According to the Boussinesq hypothesis the Reynolds stresses can be modeled analo-

gously by introducing turbulent viscosity μ_t and using the following approach:

$$-\rho\, \overline{u_i' u_j'} = \mu_t \left(\frac{\partial u_i}{\partial x_j} + \frac{\partial u_j}{\partial x_i} \right) - \frac{2}{3}\delta_{ij} \left(\rho k + \mu_t \frac{\partial u_k}{\partial x_k} \right) \tag{2.128}$$

Again, for incompressible flows this can be simplified as follows:

$$-\rho\, \overline{u_i' u_j'} = \mu_t \left(\frac{\partial u_i}{\partial x_j} + \frac{\partial u_j}{\partial x_i} \right) - \frac{2}{3}\delta_{ij}\rho k \tag{2.129}$$

The effective viscosity is computed by adding molecular and turbulent viscosity:

$$\mu_{\text{eff}} = \mu + \mu_t \tag{2.130}$$

With this assumption, also called the eddy viscosity hypothesis, the momentum equations solved by ANSYS CFX can be written as:

$$\rho \left(\frac{\partial u_i}{\partial t} + \frac{\partial}{\partial x_j}(u_i\, u_j) \right) = -\frac{\partial p'}{\partial x_j} + \frac{\partial}{\partial x_j}\left[\mu_{\text{eff}} \left(\frac{\partial u_i}{\partial x_j} + \frac{\partial u_j}{\partial x_i} \right) \right] \tag{2.131}$$

In ANSYS CFX the term $\frac{2}{3}\delta_{ij}\rho k$ is integrated into pressure by setting:

$$p' = p + \frac{2}{3}\rho k \tag{2.132}$$

How this expression for pressure is treated by the solver is described in the documentation of the code [5]. The turbulent kinetic energy k appearing in above equations is defined as:

$$k = \frac{1}{2}\overline{u_i' u_i'} \tag{2.133}$$

A related quantity often used for boundary value specification and initialization is turbulence intensity I. It is defined as the ratio of the rms value of average fluctuating velocity components and a reference velocity u_{ref} [68]:

$$I = \frac{\sqrt{\frac{1}{3}\overline{u_i' u_i'}}}{u_{\text{ref}}} = \frac{\sqrt{\frac{2}{3}k}}{u_{\text{ref}}} \tag{2.134}$$

In order to solve Equation 2.131 suitable values of turbulent viscosity have to be determined with the help of a model. For turbomachinery flows typically two-equation turbulence models are used for this purpose. The shear stress transport (SST) k-omega model has gained high popularity because it provides a blending from the k-omega model

at locations close to the wall to the k-epsilon model outside of the boundary layer. Depending on the distance from the wall the model thereby can make use of the beneficial properties of both turbulence models . Hence, this model is chosen for the simulations performed in the course of this thesis. However, recent investigations of inducers indicate that the use of other models might be equally reasonable [41]. As the SST model belongs to the $k - \omega$ type of turbulence models, turbulent viscosity is calculated by:

$$\mu_t = \rho \frac{k}{\omega} \tag{2.135}$$

Thus, two additional equations are introduced; one for turbulent kinetic energy k and one for turbulent frequency ω. These equations are described in detail in ANSYS, Inc. [5] and read:

$$\frac{\partial (\rho k)}{\partial t} + \frac{\partial}{\partial x_j} (\rho u_j k) = \frac{\partial}{\partial x_j} \left[\left(\mu + \frac{\mu_t}{\sigma_{k3}} \right) \frac{\partial k}{\partial x_j} \right] + P_k - \beta' \rho k \omega \tag{2.136}$$

$$\frac{\partial (\rho \omega)}{\partial t} + \frac{\partial}{\partial x_j} (\rho u_j \omega) = \frac{\partial}{\partial x_j} \left[\left(\mu + \frac{\mu_t}{\sigma_{\omega 3}} \right) \frac{\partial \omega}{\partial x_j} \right] + (1 - F_1) 2 \rho \frac{1}{\sigma_{\omega 2} \omega} \frac{\partial k}{\partial x_j} \frac{\partial \omega}{\partial x_j}$$
$$+ \alpha_3 \frac{\omega}{k} P_k - \beta_3 \rho \omega^2 \tag{2.137}$$

The coefficients with index 3 are obtained by application of the formula

$$\phi_3 = F_1 \phi_1 + (1 - F_1) \phi_2, \tag{2.138}$$

where ϕ represents any of the model coefficients. These coefficients are given in the documentation [5] as follows:

$$\alpha_1 = 5/9 \tag{2.139a}$$

$$\beta_1 = 0.075 \tag{2.139b}$$

$$\sigma_{k1} = 1.176 \tag{2.139c}$$

$$\sigma_{\omega_1} = 2 \tag{2.139d}$$

$$\alpha_2 = 0.44 \tag{2.139e}$$

$$\beta_2 = 0.0828 \tag{2.139f}$$

$$\sigma_{k2} = 1 \tag{2.139g}$$

$$\sigma_{\omega 2} = 1/0.856 \tag{2.139h}$$

The remaining coefficient β' is specified as:

$$\beta' = 0.09 \tag{2.140}$$

To avoid overprediction of turbulent viscosity the limiter

$$\mu_t = \frac{\rho a_1 k}{\max\left(a_1 \omega, S F_2\right)} \tag{2.141}$$

is employed, where $a_1 = 0.031$ and S is called invariant measure of strain rate. This quantity is defined as

$$S = \sqrt{2 S_{ij} S_{ij}}, \tag{2.142}$$

where the components of strain rate are given by

$$S_{ij} = \frac{1}{2}\left(\frac{\partial u_i}{\partial x_j} \frac{\partial u_j}{\partial x_i}\right). \tag{2.143}$$

The blending functions F_1 and F_2 are defined as:

$$F_1 = \tanh\left(\left\{\min\left(\max\left(\frac{\sqrt{k}}{\beta'\omega y}, \frac{500\mu}{\rho\omega y^2}\right), \frac{4\rho k}{CD_{k\omega}\sigma_{\omega 2}y^2}\right)\right\}^4\right) \tag{2.144}$$

$$F_2 = \tanh\left(\left\{\max\left(\frac{s\sqrt{k}}{\beta'\omega y}, \frac{500\mu}{\rho\omega y^2}\right)\right\}^2\right) \tag{2.145}$$

They are functions of the distance to the nearest surface y, the turbulence quantities k and ω and the viscosity μ. The coefficient $CD_{k\omega}$ is calculated as follows:

$$CD_{k\omega} = \max\left(2\rho\frac{1}{\sigma_{\omega 2}\omega}\frac{\partial k}{\partial x_j}\frac{\partial \omega}{\partial x_j}, 1.0 \times 10^{-10}\right) \tag{2.146}$$

More details about e.g. the near-wall treatment and the numerical discretization can be found in the solver documentation [5].

2.6.2 Inviscid, Two-Dimensional Axisymmetric Flow

To validate the SMA introduced in Section 2.4 a comparison with three-dimensional, viscid flow is not appropriate since the method models inviscid, two-dimensional, axisymmetric flow. Consequently a different set of equations is to be solved in order to produce the validation data. ANSYS Fluent is chosen for this task due to its ability to solve the Euler equations for two-dimensional axisymmetric geometries [8]. In this case

and under the assumption of incompressible, steady-state flow without sources Fluent solves the following equations (in cylindrical coordinates z, r):

$$\frac{\partial u_z}{\partial z} + \frac{\partial u_r}{\partial r} + \frac{u_r}{r} = 0 \tag{2.147}$$

$$\frac{1}{r}\frac{\partial}{\partial z}\left(ru_z u_z\right) + \frac{1}{r}\frac{\partial}{\partial r}\left(ru_r u_z\right) = -\frac{1}{\rho}\frac{\partial p}{\partial z} \tag{2.148}$$

$$\frac{1}{r}\frac{\partial}{\partial z}\left(ru_z u_r\right) + \frac{1}{r}\frac{\partial}{\partial r}\left(ru_r u_r\right) = -\frac{1}{\rho}\frac{\partial p}{\partial r} \tag{2.149}$$

Details about the solver theory are included in the code documentation [8].

3 Development and Implementation

3.1 Development Philosophy

The target of the newly developed program is to provide a comprehensible design system that is independent of commercial software. All libraries used are free of cos, open source and without dependencies on proprietary software. Nevertheless, interfaces to common engineering software products are provided allowing for further processing of the designed geometry in the CAE-process. Especially a smooth transition to grid generation and computational fluid dynamics (CFD) is required. Since the program is entirely developed in Python, it is laid out as a single python package. This package itself consists of a set of modules containing the whole design functionality. The Python programming language is mainly selected because of the availability of packages for scientific computing and GUI development, which facilitate the extension and continued development of the code by engineering students and researchers.

3.2 Design Overview

An overview of the design work flow is depicted in Figure 3.1 by means of a flow chart. Starting from the basic parameters, which cover the fluid properties and the operating conditions, the meridional shape of the inducer is designed. This design step includes the calculation or specification of the basic dimensions constraining the final shape of hub and shroud. Of particular importance in this early state of design is the dimensioning of the inlet eye, as it has great impact on suction performance. Besides the diameters at the inlet also the outlet dimensions and the axial extent of the inducer have to be defined. These mainly depend on higher level requirements like the dimensions of already existing downstream components or the mechanical connection to the pump assembly.

Once the basic dimensions are fixed, the hub and shroud curves as well as the leading and trailing edge shape are designed by configuring and manipulating the corresponding B-spline curves. Based on hub and shroud shapes two-dimensional streamlines are computed and the meridional blade sections are extracted by intersecting with the leading and trailing edges. These blade sections are mapped to the cascade plane and are subsequently used in the blade design step.

Before the blade shape is designed the number of blades and a certain type of blade is chosen. In the present implementation two different blade types, which consider the special demands of inducers, are provided. Furthermore blade sweep at the leading edge can be configured. Depending on the choice of blade type, leading and trailing edge
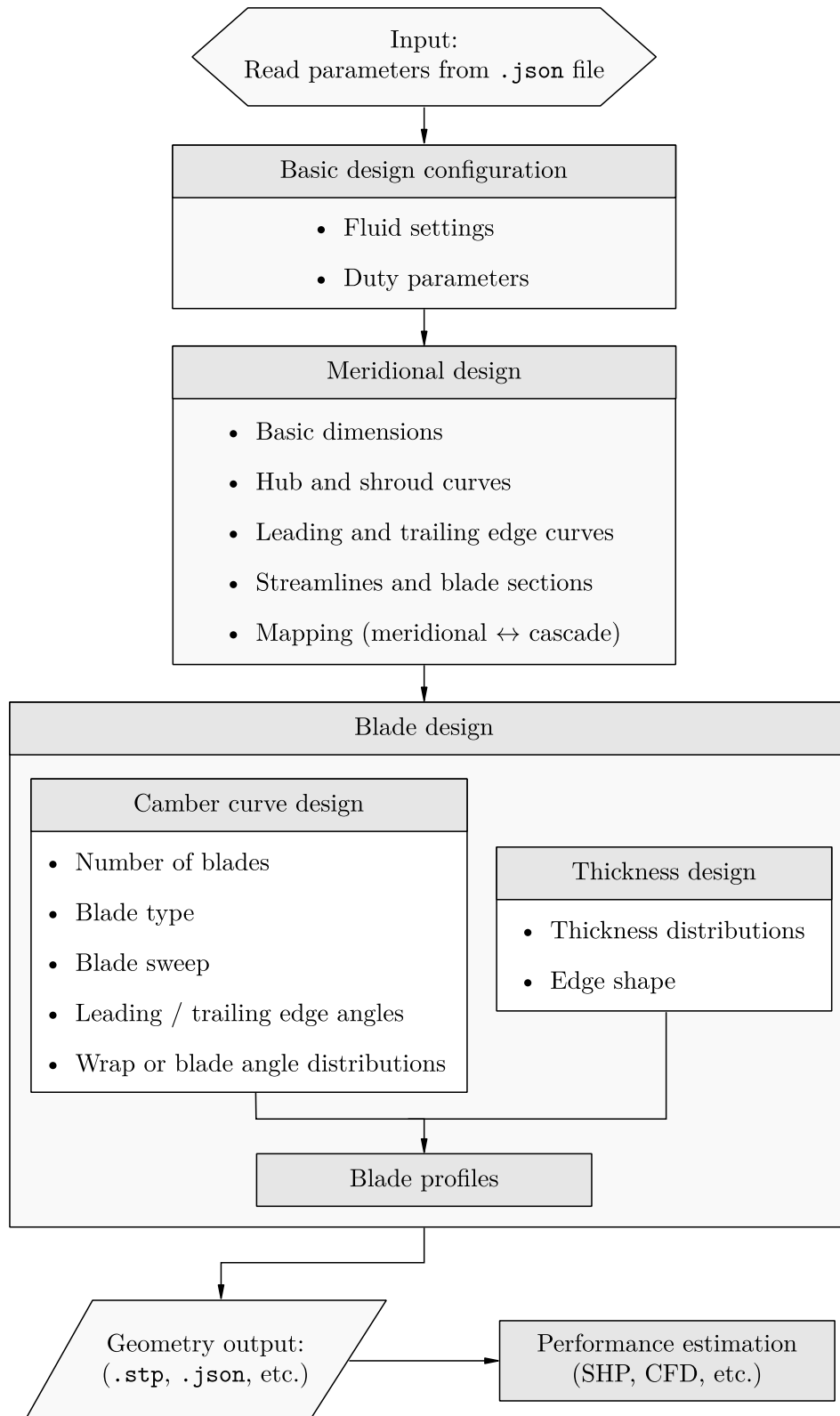
Input:
Read parameters from `.json` file

Basic design configuration

- Fluid settings
- Duty parameters

Meridional design

- Basic dimensions
- Hub and shroud curves
- Leading and trailing edge curves
- Streamlines and blade sections
- Mapping (meridional $\leftrightarrow$ cascade)

Blade design

Camber curve design

- Number of blades
- Blade type
- Blade sweep
- Leading / trailing edge angles
- Wrap or blade angle distributions

Thickness design

- Thickness distributions
- Edge shape

Blade profiles

Geometry output:
(`.stp`, `.json`, etc.)

Performance estimation
(SHP, CFD, etc.)

Figure 3.1: Overview of the design steps

blade angles are determined and used to produce the camber curves of two-dimensional blade sections in the cascade plane.

In the final step of blade design, thickness distributions are used to create the blade profiles. These profiles can be exported directly to different data formats or be used internally to create a three-dimensional blade surface, which is easily transferable to a 3D-CAD via a `.step` file. Furthermore the present implementation provides export capability for file formats used by the commercial turbomachinery grid generation software ANSYS TurboGrid [7] and the commercial blade generation software BladeGen [4]. The final blade shapes can then be used to predict the non-cavitating inducer head with the integrated simple head prediction (SHP) method or for more complex investigations with CFD codes.

Input and output of design parameters are realized with the `.json` file format, which is a standard to convert human-readable text files to programming language specific data formats [35].

In the following section the design steps mentioned before are discussed in-depth and parametrization and implementation details are presented.

3.3 Basic Design Parameters

The basic design parameters are divided into fluid parameters and duty parameters. Since the fluid is considered to be incompressible, the only fluid properties that have to be specified are density and saturation pressure. These values are mainly used to convert pressure values to head values and vice versa. By specification of the rotational speed n, the volume flow rate Q and the Head H the design point of the inducer is fixed. The range of operation to be considered in the head estimation routine can already be set at this point by choosing values of the maximum and minimum volume flow rate. Furthermore, the direction of rotation has to be specified in order to obtain the proper blade orientation. According to the coordinate convention (see Section 2.2.2) the direction of rotation can be right (positive) or left (negative). As already indicated in Section 2.5 only the static part of the head effectively increases the $\mathrm{NPSH_a}$ of the downstream pump impeller. Hence, a parameter is provided, which allows the designer to toggle the usage of the corrected head, i.e. the head reduced by the amount of circumferential dynamic head. This setting influences the calculation of the trailing edge blade angle as will be described in Section 3.5.6. Further parameters required to perform the velocity triangle and energy transmission computation are estimates of the hydraulic efficiency and the swirl number. The latter can be specified at the hub and at the shroud section, respectively, and interpolated values are used at the intermediate

sections. In the common case of axial inflow conditions both values are set to one.

At this point one of the main problems of inducer design (see also Japikse [38]) is already obvious: Can the inducer be considered as a separate component or should it be designed together with the impeller as one unit? If the target head of the inducer is prescribed, the blade angle is effectively determined by the design rule that is applied. If the inducer is intended for an existing pump application with an already designed impeller and already fixed inlet dimensions, then two options will arise. Either the impeller has to be modified to account for the inlet swirl or the impeller is kept as it is and a decreased efficiency or a shift of best efficiency point (BEP) is accepted. If on the other hand a new design is attempted from scratch, a similar problem arises. In addition to the exit flow conditions in this case also the discharge dimensions of the inducer are unknown. Thus, multiple iterations of inducer and impeller design are very likely to be required until an acceptable solution is achieved. In both cases an efficient and parametric design system, which in a first step covers only the inducer, is a valuable tool for the designer. Nevertheless, the option of a coupled or combined inducer-impeller design could be of interest in the future. This is why the essential methodology for geometry generation developed in the following sections is not strictly limited to inducers and can be extended in a straightforward way to any type of pump impeller.

3.4 Meridional Section

The starting point for the meridional design is an adequate choice of the basic dimensions of the impeller. These dimensions are used to constrain the shape of the meridional section by initially fixing four control points as indicated in Figure 3.2. In the z, r-coordinate system of the meridional plane the control points defined by the basic dimensions can be specified as follows:

$$p_{1h} = (z_{1h}, r_{1h})$$
$$p_{1s} = (z_{1s}, r_{1s})$$
$$p_{2h} = (z_{2h}, r_{2h})$$
$$p_{2s} = (z_{2s}, r_{2s})$$

The problem of finding or choosing the basic dimensions of the inducer thus reduces to setting the coordinates of these four points. To obtain optimum suction performance, the inlet eye, which is described by $d_{1h} = 2\,r_{1h}$ and $d_{1s} = 2\,r_{1s}$, that is by the points p_{1h} and p_{1s}, has to be designed carefully and based on physical reasoning. This will be dealt with in the following section. Since the inflow is assumed to be aligned axially, the
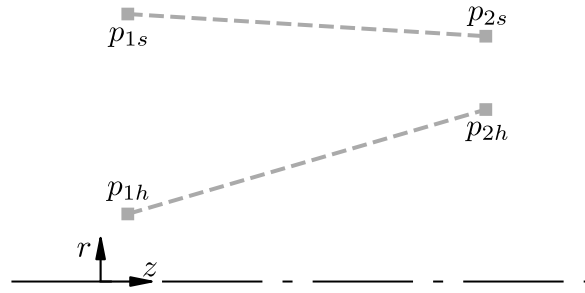
Figure 3.2: Initial meridional section

inlet location (index 1) is orientated perpendicular to the axis of rotation. This means that the z-coordinates at the hub and shroud are set to equal values ($z_{1h} = z_{1s}$). The dimensions at the outlet location (index 2) on the other hand can be designed more freely by specification of the z, r coordinates at hub and shroud. Using this direct approach the geometrical matching of the inducer to an existing pump inlet is facilitated and the axial length of the inducer can be directly controlled by the designer.

Once inlet and outlet dimensions are fixed, the curves representing the hub and shroud contours have to be constructed. A flexible way of describing these curves is necessary to allow for almost arbitrary shaped geometries of hub and shroud. While smooth contours are typically used for the hub curve, straight and simple tapered shroud configurations are prevalent in practice. The reason for this is that tight clearances have to be guaranteed and contact of the blade tip with the casing has to be avoided.

In the last step of meridional section design the leading and trailing edges have to be defined. In general they can be positioned freely along the hub and shroud curves but their design already has influence on the final blade shape. Particularly the axial extent of the blade is determined and the more subtle parameter of blade sweep can be affected by the position and shape of the leading and trailing edge.

3.4.1 Inlet Eye Design

Defining the inlet eye requires the specification of the hub and shroud diameters at the inducers inlet. The hub diameter d_{1h} usually is limited by mechanical reasons, that is for example the minimum shaft diameter required or the dimensions of a bolt or a nut needed to axially secure the inducer on the shaft. Therefore, it is either specified directly or it is specified indirectly by setting a fixed value of hub to shroud diameter ratio $\nu_1 = d_{1h}/d_{1s}$. What remains is the problem of finding the appropriate shroud diameter to obtain a desired value of suction specific speed Ω_{ss}.

The inlet eye design is performed based on the so-called *Brumfield Criterion* [36], which basically leads to the same conclusion as the reasoning of Dixon [27].

(a) Constant meridional velocity   (b) Velocity triangle at the shroud (s)
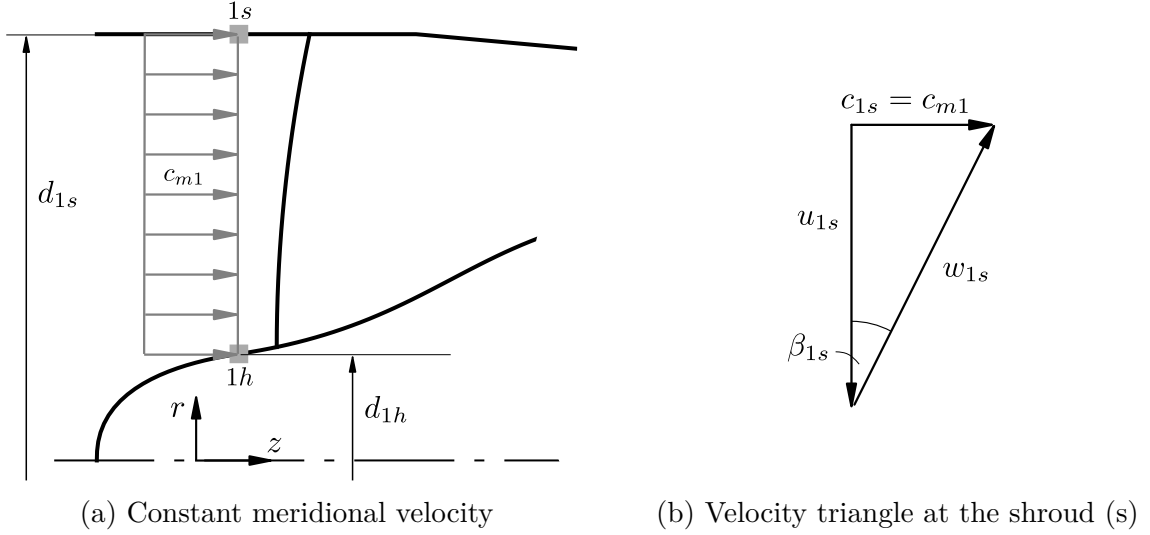
Figure 3.3: Brumfield Criterion - inlet conditions

In Figure 3.3a the meridional flow approaching the inducer (or any other type of impeller) is depicted. The flow is assumed to be inviscid and swirl-free such that the velocity diagram displayed in Figure 3.3b is obtained immediately in front of the impellers leading edge. A generalized derivation of the equations including the effect of swirl is provided in Appendix B. Independent of the swirl of the inflow angular speed of the blade may be expressed in terms of circumferential velocity at the outer diameter as follows:

$$\omega = 2\pi n = \frac{2\,u_{1s}}{d_{1s}} \tag{3.1}$$

Supposing that the meridional velocity c_{m1} is uniformly distributed in the cross sectional area at location 1 and introducing the hub blockage factor $k = 1 - \nu_1^2$ the volume flow can be expressed as:

$$Q = c_{m1}\frac{\pi}{4}(d_{1s}^2 - d_{1h}^2) = c_{m1}\frac{\pi}{4}d_{1s}^2(1 - \nu_1^2) = c_{m1}\frac{\pi}{4}kd_{1s}^2 \tag{3.2}$$

The total pressure along the streamline at the outer diameter can be calculated according to:

$$p_{tot,1s} = p_{1s} + \frac{1}{2}\rho c_{1s}^2 \tag{3.3}$$

Due to the acceleration of the fluid caused by the rotating blades the local pressure p close to the blades is reduced [27]. Cavitation inception occurs when the pressure p at some location is decreased to vapor pressure p_v. With the blade cavitation coefficient

defined as

$$\sigma_b = \frac{p_{1s} - p_v}{\frac{1}{2}\rho w_{1s}^2},$$
(3.4)

the pressure p_{1s} can be expressed as:

$$p_{1s} = \sigma_b \left(\frac{1}{2}\rho w_{1s}^2\right) + p_v$$
(3.5)

The blade cavitation coefficient is an empirical factor, which relates the inflow conditions to a certain level of cavitation observed during experiments. Typical values corresponding to the cavitation inception point, which is the point where the first occurrence of cavitation is detected during suction performance test runs, lie in the range of $\sigma_b = 0.2\ldots0.4$ for standard pump impellers [27]. According to Japikse et al. [39] this range is extended to $\sigma_b = 0.1\ldots1$ in industrial practice and to values of $\sigma_b < 0.1$ for rocket turbopumps. For carefully designed inducers even lower values of $\sigma_b < 0.001$ are indicated by Japikse [38] but the corresponding levels of cavitation are not clear. Assuming the velocity triangle as depicted in Figure 3.3b the net positive suction head H_s or NPSH can be written in terms of blade cavitation number:

$$H_s = \text{NPSH} = \frac{(p_{tot,1s} - p_v)}{g\rho} = \frac{1}{2g}\left[\sigma_b\, w_{1s}^2 + c_{1s}^2\right]$$
$$= \frac{1}{2g}\left[(1 + \sigma_b)c_{m1}^2 + \sigma_b u_{1s}^2\right]$$
(3.6)

Typically suction performance of pumps is expressed by means of the suction specific speed, which can be defined in a dimensionless way as follows [27]:

$$\Omega_{ss} = 2\pi n \frac{Q^{1/2}}{(g\text{NPSH})^{3/4}}$$
(3.7)

When comparing values of suction specific speed, it has to be considered that there exist different unit conventions. In Appendix C the conversion factors from the dimensionless version to the European and US-American unit conventions are provided. Furthermore, the level of head drop at which NPSH is evaluated in the experiment has to be specified. In practice, usually NPSH_3 at 3 % head drop of the whole pump is used in the above equations. For inducers also different values ranging from 10 % [36] to 30 % [2] or even 50 % [38] are documented.

By substitution of the net positive suction head H_s, the volume flow Q and the angular velocity ω in the definition of suction specific speed, as given in Equation 3.7, by

Equations 3.6, 3.2 and 3.1 respectively the following equation is obtained:

$$\Omega_{ss} = \frac{\left(\pi k u_{1s}^2 c_{m1}\right)^{1/2}}{\left(\frac{1}{2}\left[(1+\sigma_b)c_{m1}^2 + \sigma_b u_{1s}^2\right]\right)^{3/4}} \tag{3.8}$$

Introduction of the flow coefficient $\varphi_1 = c_{m1}/u_{1s}$ finally leads to:

$$\Omega_{ss} = \frac{\left(\pi k \varphi\right)^{1/2}}{\left(\frac{1}{2}\left[(1+\sigma_b)\varphi^2 + \sigma_b\right]\right)^{3/4}} \tag{3.9}$$

Equation 3.9 represents the general relation between suction specific speed, flow coefficient and the blade cavitation coefficient. Following Dixon and Hall [27], the maximum theoretically achievable suction specific speed can be derived from this equation by computing $(\mathrm{d}\Omega_{ss}/\mathrm{d}\varphi) = 0$. As a result, the optimum flow coefficient depending only on the blade cavitation number can be obtained by:

$$\varphi = \left(\frac{\sigma_b}{2(1+\sigma_b)}\right)^{1/2} \tag{3.10}$$

Of course, the inverse relationship can equally be determined and reads as follows:

$$\sigma_b = \frac{2\varphi^2}{1 - 2\varphi^2} \tag{3.11}$$

Elimination of σ_b in Equation 3.9 with the help of Equation 3.11 on the other hand gives the optimum suction specific speed for fixed hub blockage factor k as a function of flow coefficient:

$$\Omega_{ss}^* = \frac{\Omega_{ss}}{k^{1/2}} = \left(\frac{\pi \left(\frac{2}{3}\right)^{3/2} \left(1 - 2\varphi^2\right)^{3/2}}{\varphi^2}\right)^{1/2} \tag{3.12}$$

The value denoted by Ω_{ss}^* is also called *corrected suction specific speed*. Equation 3.12, which is known as Brumfield's criterion [36], can be used to calculate the flow coefficient which would be required to provide optimum suction performance. Computation of the corresponding optimum shroud diameter then is straightforward:

$$d_{1s} = \left(\frac{4Q}{\pi^2 \varphi n k}\right)^{1/3} \tag{3.13}$$

It has to be noted that both Equations 3.12 and 3.13 are solved by iterating towards a satisfying solution because the hub blockage factor k is not known a priori. In the

current design procedure the design for maximum suction specific speed is accomplished by a combined iterative procedure, which updates k at the beginning of every iteration step. The updated k is then kept constant to solve Equation 3.12 for the flow coefficient φ, which in turn is used to compute an update of d_{1s} from 3.13. Of course, it is
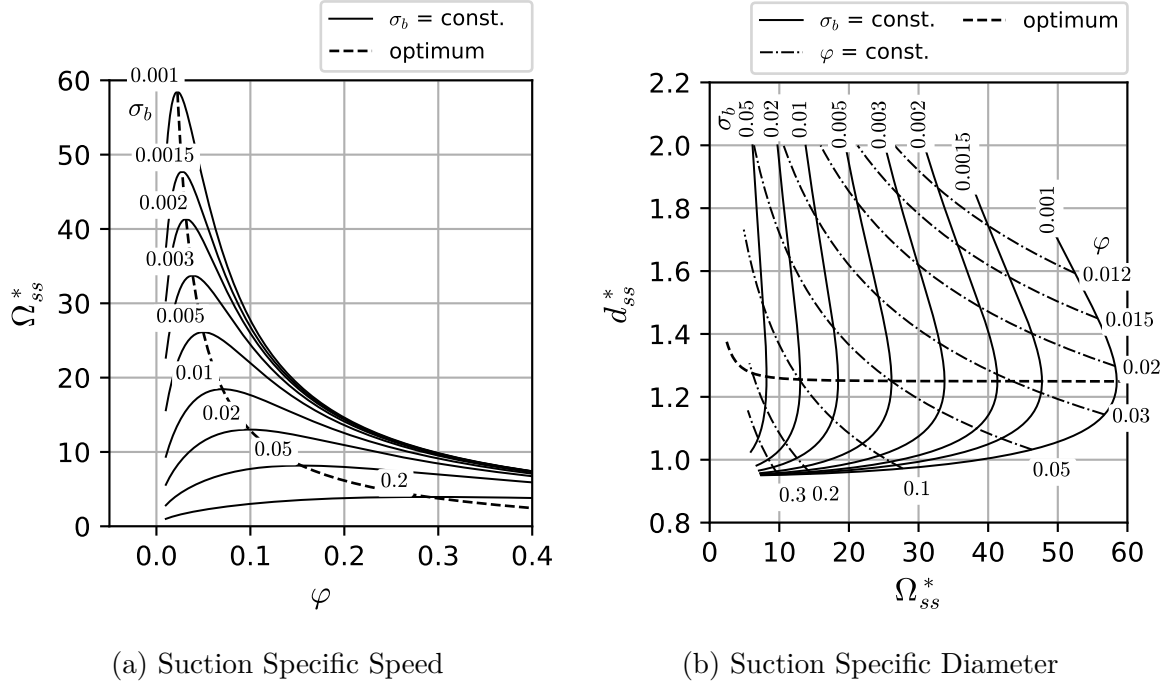

(a) Suction Specific Speed

(b) Suction Specific Diameter

Figure 3.4: Theoretical tendencies of inducer inlet design

also possible to choose the inlet diameter manually without maximizing suction specific speed. Figure 3.4a shows the theoretical relationship between corrected suction specific speed Ω_{ss}^* and flow coefficient φ, which is a direct result of the chosen inlet dimensions. If a certain value of blade cavitation coefficient is assumed the discrepancy to the optimally achievable values of suction specific speed according to Brumfield's criterion, displayed as a dashed line, can directly be retrieved from this diagram.

Figure 3.4b, which is adapted from Jakobsen [36], can either be used to check the suction specific speed that is theoretically achievable with a set of chosen design parameters or to select a diameter suitable to obtain a desired level of suction specific speed. The *corrected suction specific diameter d_{ss}^** is obtained by expressing speed n in Equation 3.13 in terms of corrected suction specific speed:

$$d_{ss}^* = d_{1s} \frac{k^{1/2} \left(gH_s \right)^{1/4}}{Q^{1/2}} = \left(\frac{2}{\pi^2 \varphi \Omega_{ss}^*} \right)^{1/3} \tag{3.14}$$

3.4.2 Hub and Shroud Design

The hub and shroud curves are designed by one or multiple segments, which are represented by uniform B-spline curves. By default the B-spline curves are cubic (of degree 3) as long as at least four control points are given. If less control points are given, the degree is reduced. Piecewise linear curves are obtained by setting the degree of the B-spline to 1. In this case, the B-spline curve is equivalent to the control polygon.

The curves are directly constructed from the control points specified by the user and the corresponding uniform knot vector (see Section 2.3). In case of multiple curve segments, the start and end points of joining segments have to be identical to ensure a valid curve without interruptions (G^0 continuity). Furthermore, the tangential direction can be forced to be equal at the joining point of two segments (G^1 continuity). In this case, the control points are shifted accordingly. Figure 3.5a depicts the control polygons of the hub and shroud section of an generic inducer with tapered shroud and smooth hub section. Both hub and shroud section consist of three curve segments. At the hub B-spline curves are used and at the shroud piecewise linear curves are employed as described above. By fixing the starting point of one segment at the inlet and the end point of the same or any other segment at the outlet it is ensured that the main dimensions are respected by the meridional shape design. This is indicated by the filled gray square marker. The curve progression upstream, downstream and in-between these points can be designed without constraints. Evaluation of the B-spline curves resulting from the control polygon leads to the curves shown in Figure 3.5b. If either no control points are specified or

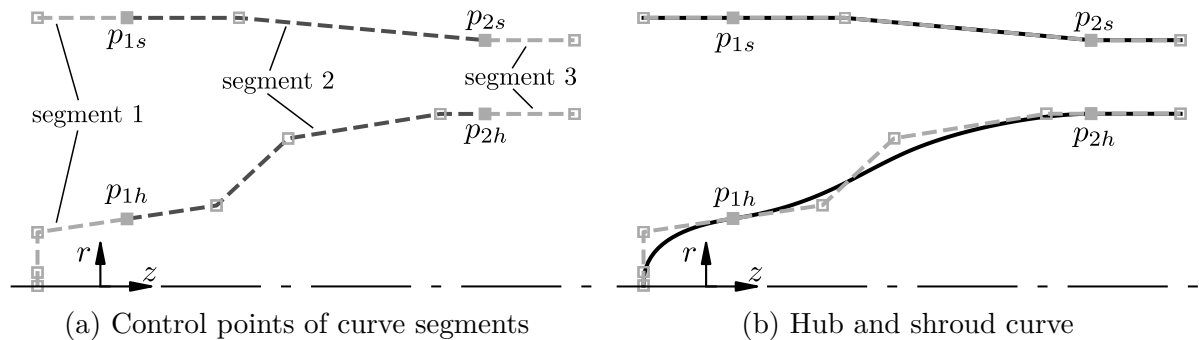(a) Control points of curve segments   (b) Hub and shroud curve

Figure 3.5: Meridional curve design - consideration of basic dimensions

the provided control points are inconsistent with the basic dimensions, a default curve construction method is provided for the hub and the shroud as illustrated in Figure 3.6a. Given the straight line connecting the points defined by the basic dimensions at the hub the z-coordinates of three points distributed equidistantly are used as initial values. The r-coordinate of the first and last of these points is replaced by the radius of the inlet or outlet point respectively to obtain horizontal tangents at the entry and discharge

69

(a) Default control points of hub and shroud curve
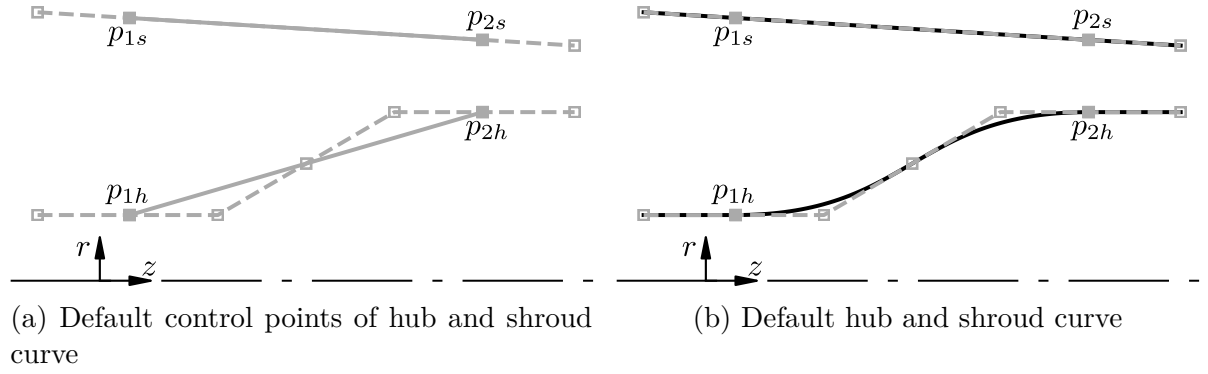
(b) Default hub and shroud curve

Figure 3.6: Meridional curve design - default curve construction

locations. At the shroud the straight segment connecting the already available points is used. Both hub and shroud are extended tangentially to provide some space for the leading and trailing edge positioning and the meridional flow analysis. The resulting curves for the example under consideration are depicted in Figure 3.6b

On top of the simple meridional analysis (SMA), which is performed on every change of the underlying meridional curves and provides a visualization of the meridional velocity field, a method to compute the meridional area as well as the mean velocity progression is implemented. The method is based on a geometrical procedure developed by Krämer [44], who also used it to generate streamtubes of equal flow in the meridional section. Hence, this method, which is described shortly in the remainder of this section, could alternatively be used to obtain streamlines in the meridional section. In the first step the meridional section is triangulated (see Figure 3.7a) by equidistantly sampling the hub and shroud curve and then finding the closest connections from hub to shroud as explained in detail by Krämer [44]. As a result, straight lines linking hub and shroud are obtained. On these lines the midpoint of a circle, which is tangentially to both the hub and shroud curve is computed iteratively. The contact points of the circle with the hub and shroud curves are used together with the midpoint as the control points of a parabolic (degree two) B-spline reaching from hub to shroud (see Figure 3.7b). Because of this construction method the B-splines are perpendicular to the hub and shroud sections and are well suited to be used as quasi-normals of the meridional flow field. The midpoints of the circles, that are the central points of the control polygons defining the quasi-normals, are directly used to compute the midline by means of interpolation with a cubic B-spline curve. The meridional velocity can subsequently be sampled from the flow field computed with the SMA as described before. To compute the cross-sectional area distribution along the midline integration along the quasi-normals has to be performed. Supposing that n is the curve parameter of the quasi normal i as depicted in Figure 3.7c the corresponding cross sectional area is obtained by integration
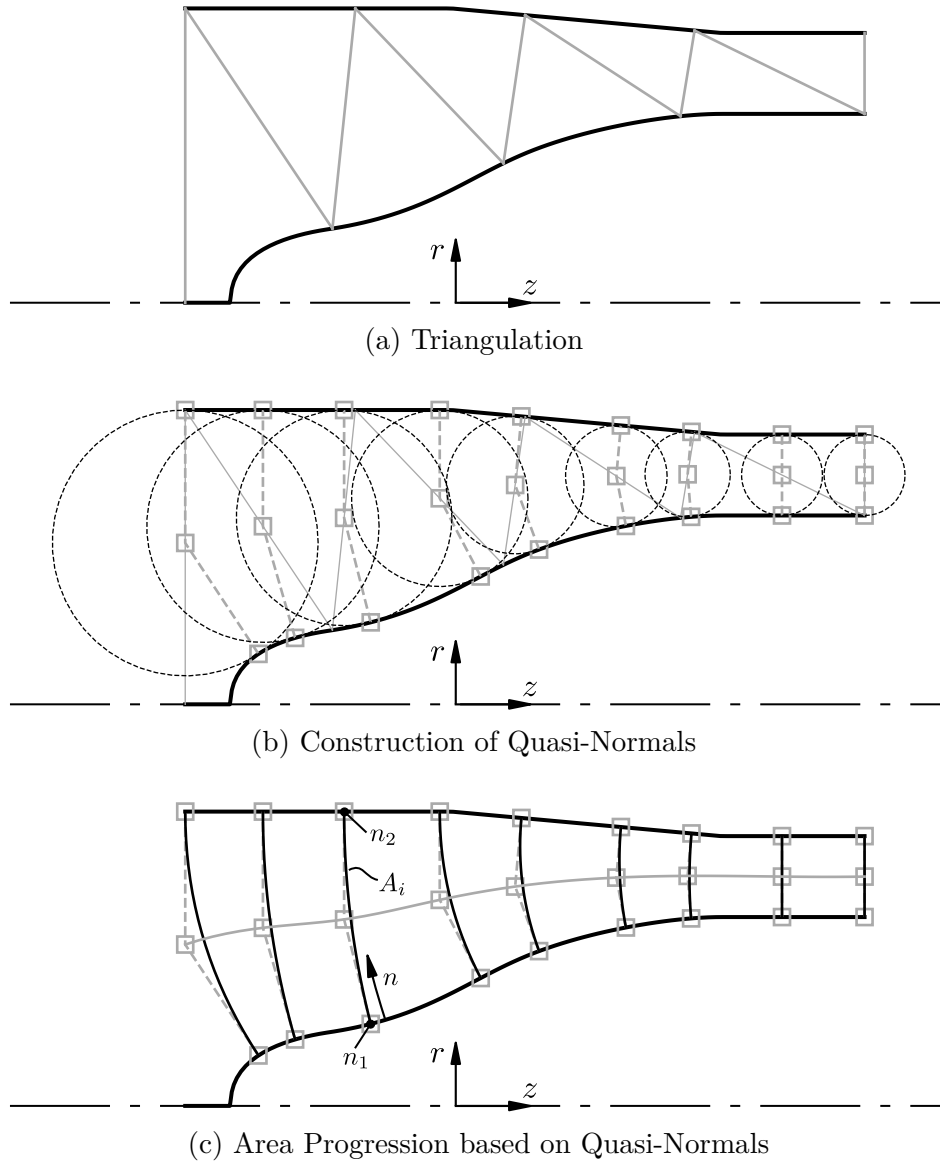
(a) Triangulation

(b) Construction of Quasi-Normals

(c) Area Progression based on Quasi-Normals

Figure 3.7: Meridional area progression

as follows:

$$A_i = \int_{n_1}^{n_2} 2\pi r(n)\, \mathrm{d}n \tag{3.15}$$

Under the assumption of constant meridional flow velocity along the quasi-normals, segments of equal flow can be computed, which, as already mentioned, might be used to construct an alternative set of streamlines. Another set of less physical streamlines could also be obtained by simply computing equidistantly spaced segments along the quasi normals. Although in principle any arbitrary set of streamlines could be used to derive the blade sections, the major drawback of these two alternative sets of streamlines

is, that there is no physical relation between the velocity field and the streamline shape.

3.4.3 Leading and Trailing Edge Design

The leading and trailing edges are positioned by specification of the control points $p_{le,h}$, $p_{te,h}$ on the hub and $p_{le,s}$, $p_{te,s}$ on the shroud curve. These control points can be moved along the curves by modification of their length coordinate l_h and l_s respectively. As indicated in Figure 3.8a the length coordinate is defined as the arc length evaluated along the hub or shroud curve. To make the specification more intuitive for the designer the percentage of curve length, which is obtained by normalizing the arc length with respect to the total curve length, is used.

By default, a straight segment obtained by using only the two control points at hub and shroud is used. Additional intermediate control points can be specified in a non-dimensional way, by considering the hub point with coordinates (0,0) and the shroud point with coordinates (1,1). Figure 3.8b shows the leading and trailing edge represented by B-spline curves of degree two (parabolic) using one additional intermediate control point. If more than three control points are specified, cubic B-spline curves are generated in the same fashion as already explained in Section 3.4.2 for the hub and shroud curves.

(a) Defining control points   (b) Curves
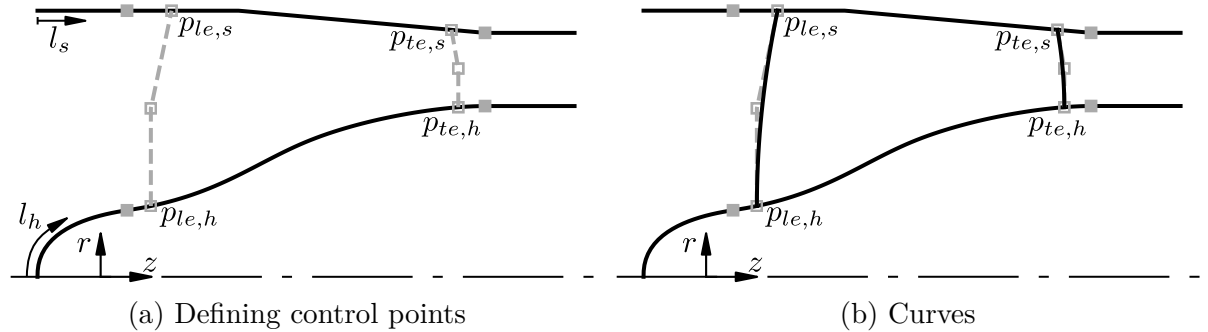
Figure 3.8: Leading and trailing edge design

As an alternative approach of parametrization, the inclination angles ε_{le} and ε_{te} measured against the radial direction can be used to construct the shroud points of leading and trailing edges. With these angles a straight line is constructed and the intersection point of this line with the shroud curve is used as the shroud point of the leading or trailing edge as indicated in Figure 3.9. By convention, the angles are considered positive if counter-clockwise rotation would be required to align the edge with the radial direction with the minimum amount of rotation. Thus, in Figure 3.9 the leading edge inclination would be considered positive and the trailing edge inclination negative, i.e. $\varepsilon_{le} > 0$ and $\varepsilon_{te} < 0$.

Note that both approaches mentioned so far do not require the leading and trailing edges to be coincident with the inlet and outlet points defined by the basic dimensions (plotted as gray squares). However, a setting is provided to fix the control points of the edges at the hub and shroud section independently to the corresponding points determined from the basic dimensions. By not constraining the positions of the edges a great degree of freedom is given to the designer and the design of the meridional shape is decoupled from the leading and trailing edge design. Nevertheless, the designer should tend to position the blades edges close to the inlet and outlet locations to avoid unexpected performance behavior.
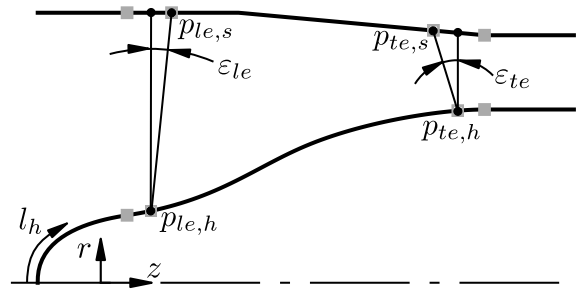
Figure 3.9: Alternative parametrization of leading and trailing edge

3.4.4 Transformation to the Cascade Plane

With the meridional section readily laid out the SMA is used to compute any desired number of streamlines from the inlet to the outlet, which are subsequently used to construct the blade sections. Compared to conventional centrifugal pump impellers a higher number of sections can be necessary for inducers to correctly represent the swept and therefore the highly three-dimensional leading edge shape (see Section 3.5.4). To develop the blade sections in the cascade plane a mapping of coordinates allowing the transfer from the three-dimensional z, r, θ (or x, y, z) space to the m', θ plane and vice versa has to be provided. The procedure developed in this thesis is based on the approach of Miller [54] and makes use of B-splines to accomplish the mapping. At the beginning of the mapping procedure the streamlines, which are available as a discrete set of points on the meridional grid (see Section 2.4.3), are interpolated using chord-length parametrization. By splitting the resulting B-spline curves at their intersections with the leading and trailing edge, three curve segments are obtained. These segments are sampled equidistantly with a specified number of points. By default, 100 points are used for the blade section between leading and trailing edge and 10 points are used upstream and downstream of the blade edges. The three sets of points are then interpolated again using uniform parametrization ranging from $u_0 = -1$ to $u_1 = 0$ for the upstream part
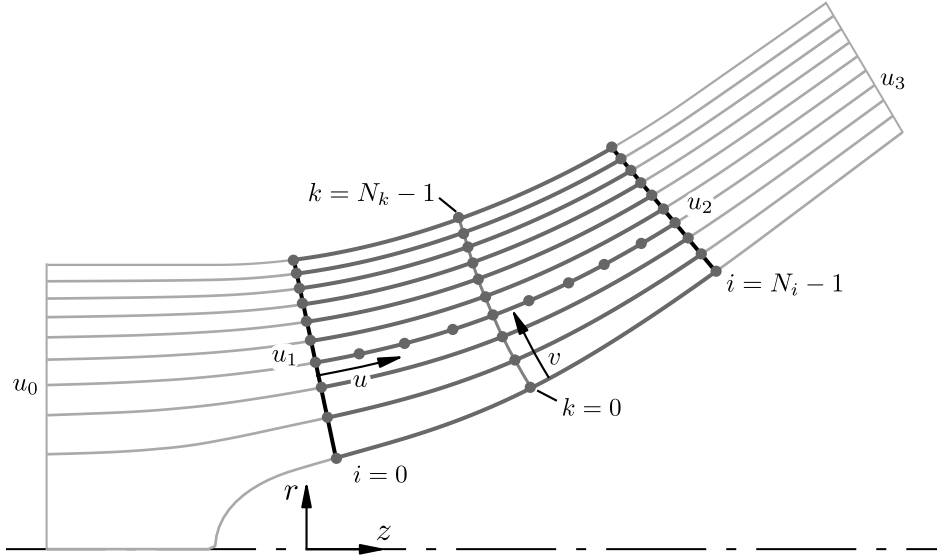
Figure 3.10: Curve parametrization and index convention

of the streamline, from $u_1 = 0$ to $u_2 = 1$ for the blade section and from $u_2 = 1$ to $u_3 = 2$ for the downstream part of the streamline. With this convention the leading and trailing edge locations can always be identified by the curve parameters $u_1 = 0$ and $u_2 = 1$, respectively. Figure 3.10 illustrates the parameter convention for the example of a generic mixed-flow impeller. Along the streamline curves the meridional and radius normalized meridional coordinates m and m' are computed and the four following B-spline curves are generated by interpolation:

$$\boldsymbol{C}_{zrm}(u) = \begin{bmatrix} z(u) \\ r(u) \\ m(u) \end{bmatrix} \longleftrightarrow \begin{bmatrix} z(m) \\ r(m) \\ u(m) \end{bmatrix} = \boldsymbol{C}_{zru}(m) \tag{3.16}$$

$$\boldsymbol{C}_{zrm'}(u) = \begin{bmatrix} z(u) \\ r(u) \\ m'(u) \end{bmatrix} \longleftrightarrow \begin{bmatrix} z(m') \\ r(m') \\ u(m') \end{bmatrix} = \boldsymbol{C}_{zru}(m') \tag{3.17}$$

The curves used for the direct mapping, that is for the mapping to the cascade plane, are called $\boldsymbol{C}_{zrm}(u)$ and $\boldsymbol{C}_{zrm'}(u)$ and use the parameter u along the streamlines introduced before. With the help of these curves the coordinates z, r, m and m' can be computed conveniently for any parameter u in the valid parameter range. By reversing the roles of the curve parameter u and the m and m' coordinates, which is completely legitimate since they are both increasing by definition (see Section 2.2.2), the inverse mappings $\boldsymbol{C}_{zru}(m)$ and $\boldsymbol{C}_{zru}(m')$ are obtained. Thus, the curve parameter u can be computed for

any value of m or m' by simply evaluating the corresponding B-splines. No mapping is required for the circumferential coordinate θ because it directly translates from the three-dimensional z, r, θ to the m', θ coordinate system. Using the above mappings it is a straightforward process to transfer a blade section developed in the cascade plane to the three-dimensional space.

To facilitate storage, access and manipulation of the data along the blade sections it is organized in a three-dimensional array $\boldsymbol{B}$:

$$\boldsymbol{B}^{N_k \times N_i \times N_d} = \begin{bmatrix} \boldsymbol{D}_0 & \dots & \boldsymbol{D}_{N_k-1} \end{bmatrix} \tag{3.18}$$

The first dimension is of size N_k and represents the sections along the spanwise direction. For each blade section a two-dimensional array $\boldsymbol{D}_k$ of size $N_i \times N_d$ is stored, where N_i is the number of points and N_d is the number of quantities stored along the blade section:

$$\boldsymbol{D}_k^{N_i \times N_d} = \begin{bmatrix} u_0 & v_0 & m_0 & m'_0 \dots \\ \vdots & \vdots & \vdots & \vdots & \dots \\ u_{N_i-1} & v_{N_i-1} & m_{N_i-1} & m'_{N_i-1} & \dots \end{bmatrix}_k \tag{3.19}$$

In principle N_d can be extended to accommodate the desired number of quantities of interest. In the current implementation N_d is of size 13 and at the section k the following quantities are stored for every index i:

$$D_{k,i} = [u, \, v, \, z, \, r, \, m, \, m', \, \theta, \, \beta_b, \, t, \, c_z, \, c_r, \, c_m, \, l_{3d}]_{k,i} \tag{3.20}$$

Similar to the streamwise curve parameter u the spanwise parameter v is provided to allow for simple interpolation along the spanwise direction (from hub to shroud). This parameter could be chosen in different ways (e.g. by chord-length or centripetal method) and independently at every streamwise location i to achieve the desired interpolation results. However, a more convenient approach using uniform parametrization is implemented, such that the blade sections are treated as curves of constant span coordinate. Besides the wrap angle θ, the blade angle β_b, the thickness t and the velocity components of the meridional flow c_z, c_r and c_m, the length coordinate in the three-dimensional space l_{3d} is stored. These values are necessary for the construction of the blade profile, as will be explained in Section 3.5.9.

3.5 Blade Design

3.5.1 Number of Blades

Common inducer designs have two to four blades, where three seems to be the most widely spread number of blades [31, 36]. There's no correlation known that could be used to select the optimum number of blades for a new inducer design. This parameter therefore has to be selected out of experience or by a trial-and-error approach. Besides the best trade-off between flow guidance and friction losses also more system related aspects can be important when choosing the blade number Z. As indicated by Jakobsen [36] having a common denominator of the number of inducer and impeller blades is supposed to be advantageous. Another parameter, which is not well documented but directly coupled to the used number of blades of the inducer and the downstream impeller, is the relative positioning between these two components.

3.5.2 Helical Blade

The helical blade type is the classical version of the inducer blade. Helical inducers can be further divided into constant and variable pitch (or lead) versions. In case of constant or approximately constant blade thickness the most basic version of the inducer, the so called *flat plate* inducer, is obtained. These types of inducers have been extensively studied in the past (see e.g. Acosta [1]) and were favored because of their comparably easy manufacturing [36].

The basic equation describing the helical blade shape (in terms of the blade lead per radian λ) relates the radii r at any axial location z to the blade angle β_b and reads as follows:

$$\lambda(z) = r(z)\tan(\beta_b(z)) = \text{const.} \tag{3.21}$$

As described by Jakobsen [36] the wrap angle can be computed by solving the following equation numerically for θ:

$$\mathrm{d}z = \tan(\beta_b)\,\mathrm{d}(r\theta) \tag{3.22}$$

By specification of the blade angle distribution $\beta_{b,\text{ref}}(z)$ at some reference radius r_{ref} the blade angle can be computed at arbitrary coordinates (z, r) using the equations above. A common choice for the reference radius is the rms-radius r_{rms} [36]. Since the leading and trailing edges are in general no straight radial lines, the z-coordinate range varies on the different blade sections. Thus, the reference blade angle distribution is expressed

with respect to the normalized axial coordinate z^*:

$$z^* = \frac{z - z_{te}}{z_{le} - z_{te}} \tag{3.23}$$

With the blade angle distribution available at the reference radius (e.g. at r_{rms}) the blade angle at any location given by z, r coordinates is computed as follows:

$$\beta_b(z^*, r) = \arctan\left(\frac{\lambda(z^*)}{r}\right)$$

$$= \arctan\left(\frac{r_{\text{ref}}}{r} \tan(\beta_{b,\text{ref}}(z^*))\right) \tag{3.24}$$

Equation 3.24 is particularly useful to calculate the blade angle at the leading and trailing edge and could be employed to solve Equation 3.22 directly (e.g. by using a finite differences method) as proposed by Jakobsen [36]. However, this approach could lead to inconsistency in the blade angle values, which are alternatively recomputed from Equation 2.17, i.e. by differentiation of the θ curve. To avoid this inconsistency Equation 2.17 is used instead to compute the wrap angle $\theta(m')$ along the blade section by integration of the blade angle:

$$\theta = \theta(m'_{le}) + \int_{m'_{le}}^{m'} \frac{\mathrm{d}m'}{\tan\beta_b} \tag{3.25}$$

In the current implementation linear and parabolic blade angle progressions are provided by setting the exponent p in the following equation either 1 or 2:

$$\beta_{b,\text{ref}}(z^*) = \beta_{b,le} + (\beta_{b,te} - \beta_{b,le})(z^*)^p \tag{3.26}$$

For both types of progression the specification of a constant angle segment starting from the leading edge is possible. This is realized by providing a threshold value z^*_{const} and defining the angle distribution as follows:

$$\beta_{b,\text{ref}}(z^*) = \begin{cases} \beta_{b,le} & , z^* \leq z^*_{\text{const}} \\ \beta_{b,le} + (\beta_{b,te} - \beta_{b,le})z^{*p} & , z^* > z^*_{\text{const}} \end{cases} \tag{3.27}$$

Figure 3.11 depicts the two different blade angle distributions comparing the versions with and without a constant angle section starting from the blade leading edge. The linear version is shown in Figure 3.11a, the parabolic in Figure 3.11b.
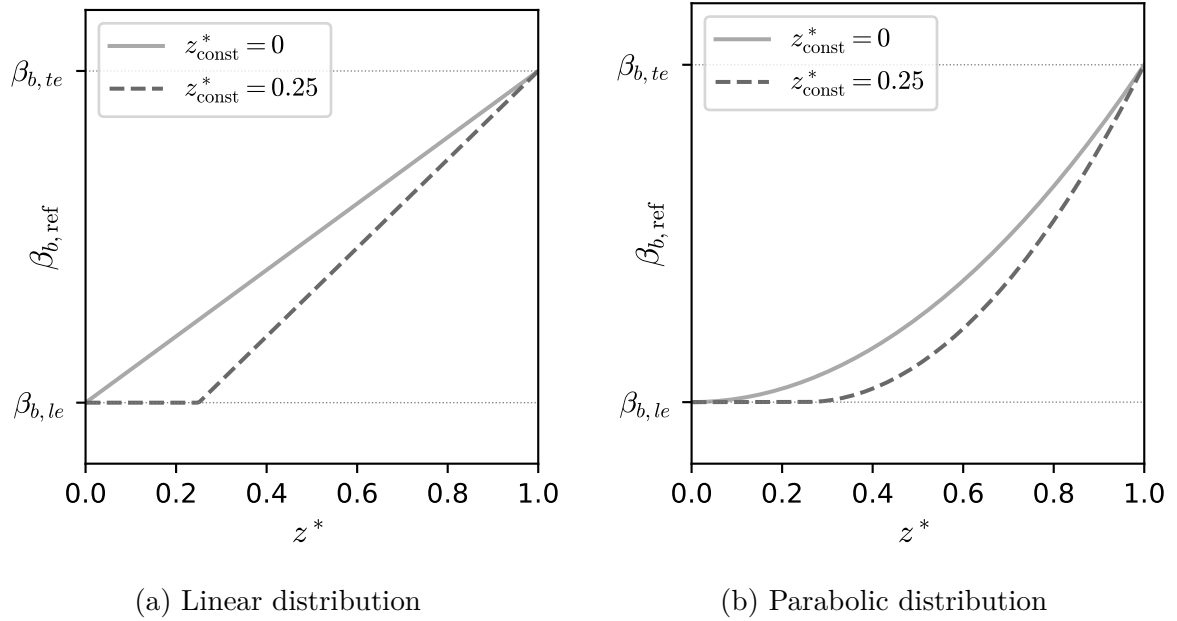
(a) Linear distribution

(b) Parabolic distribution

Figure 3.11: Blade angle distributions at reference radius

3.5.3 General Blade

Since the helical blade is mostly fixed by specification of the angle distribution on the reference radius, the designer's freedom in shaping the other blade sections is limited. Towards the hub sections undesirably large blade angles can result from this design rule and a careful matching of meridional shape and blade angle has to be performed. Hence, the designer could prefer a distinct and less restricting way of prescribing the blade angle progression in such kind of situations. Furthermore, the designer might be used to the procedure commonly applied in the design of conventional centrifugal pump impeller design where the blade mean line can be specified either by prescribing the blade angle (β_b) or the wrap angle (θ) progression freely on different blade sections running from leading to trailing edge. Out of these reasons a different blade type, the general blade, is introduced. Two different design modes have been implemented, called the *Theta* and the *Beta* design mode. In both cases angle distributions are described by means of the control points of uniform B-splines of degree three, to allow for a comparatively simple parametrization of the curves. Although exactly the same set of parameters is used to define the control points for both the Theta and the Beta design modes, the interpretation of the parameters naturally differs slightly. This will be explained in more detail below, considering first the Theta design mode.

In the current implementation only the hub and the shroud sections are used to define the entire blade but an extension to more blade sections would be straightforward. The

advantage of a reduced number of blade sections, on which design manipulations are manually performed, is that a smooth blade is obtained by linearly interpolating the control points of the intermediate sections. Figure 3.12a shows the parametrization of
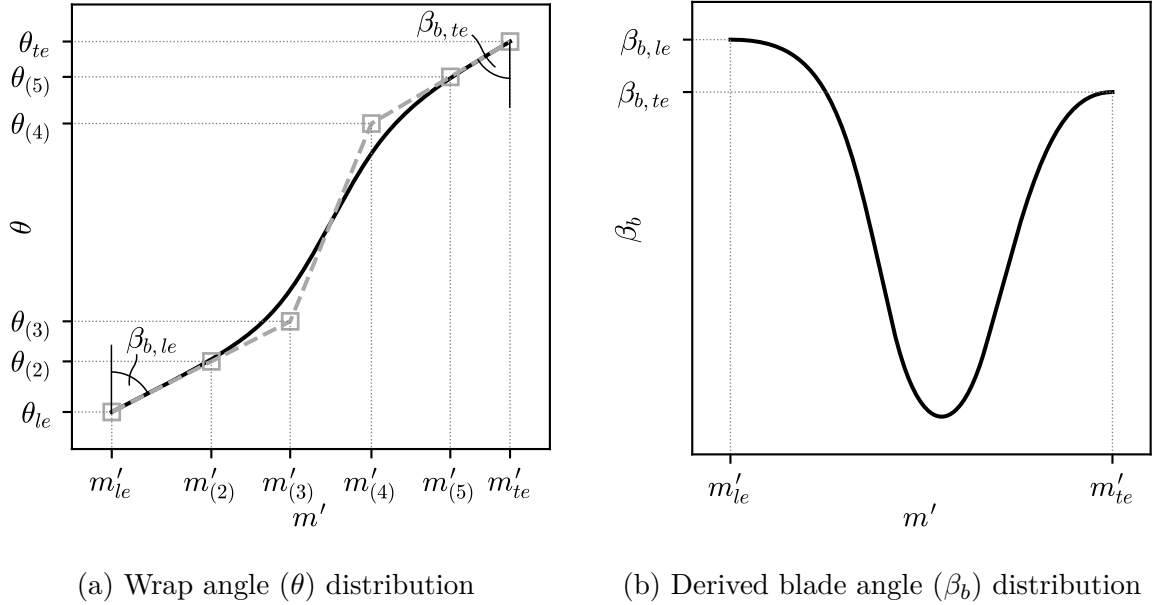

(a) Wrap angle (θ) distribution   (b) Derived blade angle (β_b) distribution

Figure 3.12: General blade design (Theta design mode)

the wrap angle (θ) progression on the hub section of an exemplary high head inducer. The θ curve (or camber curve) is parametrized by six control points $p_{(1)}$ to $p_{(6)}$. To avoid confusion with the indices previously used for the inlet and outlet locations and the indices commonly used for the velocity triangles at the leading and trailing edge (see Section 2.2.2), the indices of the coordinates of the control points are written in round brackets. Because the first and the last points are constraint by the leading and trailing edge coordinates they can be equivalently expressed by different indices:

$$p_{(1)} = (m'_{(1)}, \theta_{(1)}) = (m'_1, \theta_1) = (m'_{le}, \theta_{le}) \tag{3.28}$$

$$p_{(6)} = (m'_{(6)}, \theta_{(6)}) = (m'_2, \theta_2) = (m'_{te}, \theta_{te}) \tag{3.29}$$

The last notation is the one which will be used in the remainder of this section as it prevents the indices from being mistaken. In the θ design mode, the control points $p_{(2)}$, $p_{(3)}$ and $p_{(4)}$, $p_{(5)}$ have to be positioned in such a way that the blade angles at the leading and trailing edge are realized as desired. Supposing the blade angles at the leading and trailing edges are fixed (see Sections 3.5.5 and 3.5.6), the corresponding control points have to be located along the ray at the corresponding angle (see Figure 3.12a). Four parameters are used to define the locations of the four remaining control points. They

are called $m'^*_{(2)}$, $m'^*_{(5)}$, $m'^{**}_{(3)}$ and $m'^{**}_{(4)}$ and are specified in a normalized way as follows:

$$m'^*_{(2)} = \frac{m'_{(2)} - m'_{le}}{m'_{te} - m'_{le}} \tag{3.30}$$

$$m'^{**}_{(3)} = \frac{m'_{(3)} - m'_{(2)}}{m'_{(5)} - m'_{(2)}} \tag{3.31}$$

$$m'^{**}_{(4)} = \frac{m'_{(4)} - m'_{(2)}}{m'_{(5)} - m'_{(2)}} \tag{3.32}$$

$$m'^*_{(5)} = \frac{m'_{(5)} - m'_{le}}{m'_{te} - m'_{le}} \tag{3.33}$$

This means that the meridional position of the second point and the second last point are specified as a percentage of the total meridional length (radius normalized) and the third point and the third last point as a percentage of the remaining distance in-between the second and second last points. Thus, the m' coordinates of the control points are calculated with the help of the following formulas:

$$m'_{(2)} = m'_{le} + (m'_{te} - m'_{le})m'^*_{(2)} \tag{3.34}$$

$$m'_{(3)} = m'_{le} + (m'_{(5)} - m'_{(2)})m'^{**}_{(3)} \tag{3.35}$$

$$m'_{(4)} = m'_{te} - (m'_{(5)} - m'_{(2)})m'^{**}_{(4)} \tag{3.36}$$

$$m'_{(5)} = m'_{te} - (m'_{te} - m'_{le})m'^*_{(5)} \tag{3.37}$$

The corresponding θ-coordinates are then set as follows:

$$\theta_{(2)} = \theta_{le} + (m'_{(2)} - m'_{le})/\tan(\beta_{b,le}) \tag{3.38}$$

$$\theta_{(3)} = \theta_{le} + (m'_{(3)} - m'_{le})/\tan(\beta_{b,le}) \tag{3.39}$$

$$\theta_{(4)} = \theta_{te} - (m'_{te} - m'_{(4)})/\tan(\beta_{b,te}) \tag{3.40}$$

$$\theta_{(5)} = \theta_{te} - (m'_{te} - m'_{(5)})/\tan(\beta_{b,te}) \tag{3.41}$$

By computing the derivative along the camber curve the blade angle distribution is obtained. As can be seen from Figure 3.12b the s-shaped camber curve at the hub section results in a smooth progression of blade angle with a distinct local minimum, which in this case is displayed in an exaggerated way due to the unequal scaling of the axes. Although the blade angle at the blade edges is ensured by this method, it has to be noted that due to the underlying properties of the uniform B-spline curves the extent of the constant blade angle section cannot be controlled precisely. This is

becoming especially clear by looking at the change in slope of the blade angle curve in Figure 3.12b close to the blade edges. The easiest way to obtain a curve that passes the second or second last control point would be to add a fourth control point along the ray at the leading or trailing edge angles, respectively. Nevertheless, this is not considered by default and the parameters provided can be used to obtain a desired progression very conveniently. Similar to the normalization used for the leading and trailing edge curve parametrization additional interior control points, between $p_{(3)}$ and $p_{(4)}$, can be specified. The normalization in this case is performed with respect to the third and the third from last control point. Although this provides some additional degree of freedom, it should normally not be necessary to include more control points, all the more, as a smooth transition from the leading edge to the trailing edge angle is generally desired.
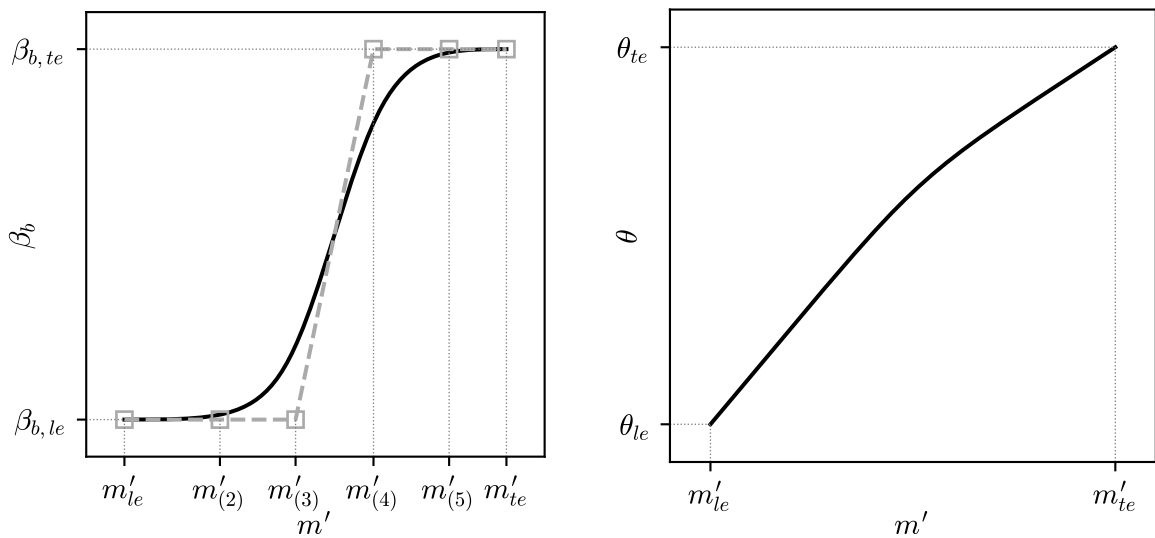
(a) Blade angle (β_b) distribution   (b) Derived wrap angle (θ) distribution

Figure 3.13: General blade design (Beta design mode)

In case of the Beta design mode, the blade angle progression at the hub and shroud sections is prescribed instead of the wrap angle by using the same set of parameters. Consequently, the same formulas 3.34 to 3.37 are applied to obtain the m' coordinates of the control points. Constant blade angle sections at the leading and trailing edge of

the blade are obtained by simply setting:

$$\beta_{b,(2)} = \beta_{1b} = \beta_{b,le} \tag{3.42}$$

$$\beta_{b,(3)} = \beta_{1b} = \beta_{b,le} \tag{3.43}$$

$$\beta_{b,(4)} = \beta_{2b} = \beta_{b,te} \tag{3.44}$$

$$\beta_{b,(5)} = \beta_{2b} = \beta_{b,te} \tag{3.45}$$

The resulting distribution is illustrated in Figure 3.13a, this time for the shroud section of the exemplary high head inducer. As before the actual meridional length (in terms of m' coordinate) of the constant angle segment is not enforced by the current parametrization because preference is given to a smooth (C^2 continuous) curve shape with a minimum number of control points.

(a) Theta curves (camber curves)   (b) Blade angle distributions
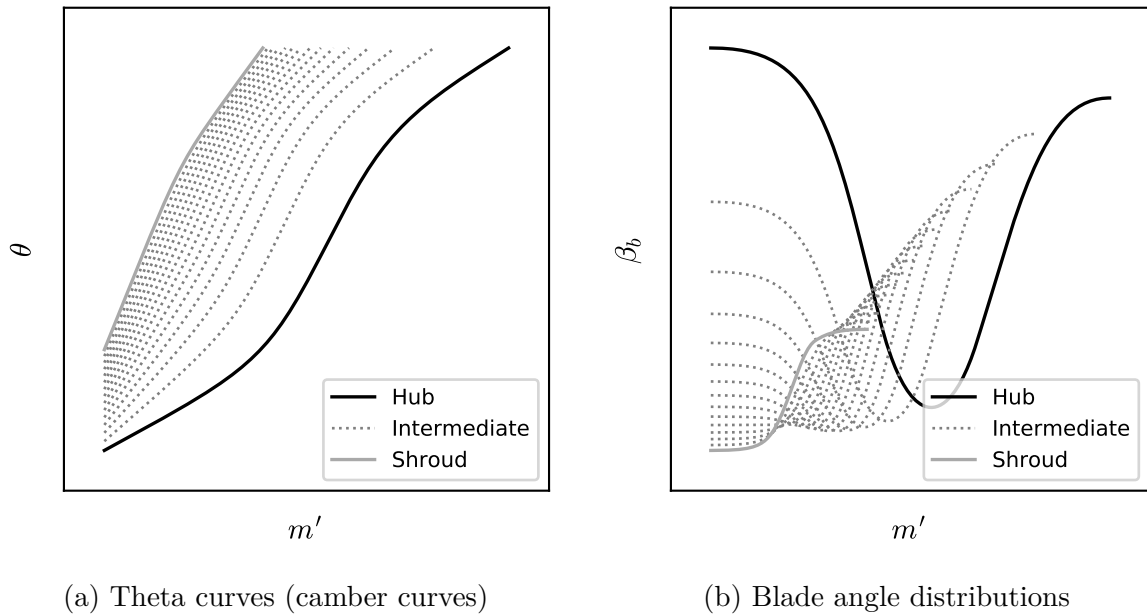
Figure 3.14: Result of Theta design mode

While the blade angle prescription might seem like a very intuitive and convenient way to obtain the desired flow turning, it is not guaranteed that a valid blade shape is obtained from this method. The reason for this is that the control over the wrap angle is effectively lost by directly designing the blade angle progression. In fact the wrap angle progression is obtained by integration of the β_b curve as already seen in case of the helical blade type. Since there is no coupling between the m' coordinates of the different blade sections, the wrap angle resulting from this angle can vary drastically along the spanwise direction and highly twisted blades with strong lean could be obtained. Nevertheless,

the resulting camber curve derived from the specified blade angle distribution is depicted in Figure 3.13b. A very careful adjustment of the blade angle in streamwise as well as in spanwise direction is necessary to generate a valid blade shape. This can be a very time consuming trial and error process which is why the Theta design mode is generally preferred.

As already mentioned only the hub and shroud sections are prescribed in the current implementation. The intermediate sections are obtained by linear interpolation of the parameters introduced above. By application of the same construction procedure as previously used for the hub and shroud sections the B-spline curves on the intermediate sections are assembled. With this procedure it is ensured that the blade angles comply with the desired angles already computed on all the blade sections. Figures 3.14a and 3.14b show the theta curves and the blade angle progressions for the hub, shroud and the intermediate blade sections of the exemplary inducer.

3.5.4 Blade Sweep

It is commonly accepted that a certain amount of backward- or forward-sweep has positive influence on the suction performance and stability under cavitating conditions without decreasing the head rise significantly. Several studies have been performed in the past. Investigations on this topic are documented for example in references [3, 13, 37]. Therefore, a design procedure for inducers should enable the designer to define the sweep angle of the leading edge in a parametrical way.

The definition of sweep angle used in this thesis is depicted in Figure 3.15. The sweep angle $\Delta\theta_{1s}$ is measured against the positive rotating direction such that a positive sweep angle corresponds to a backward sweep design and a negative sweep angle to a forward
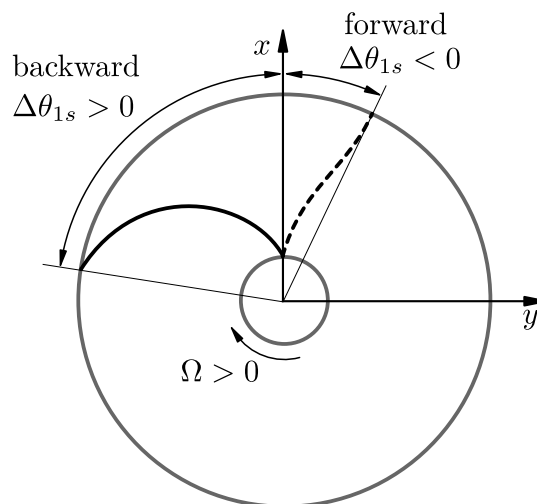

Figure 3.15: Definition of blade sweep in front view

sweep design. Both designs are reported in the open literature [17, 36] but the backward swept design is the predominant one in unshrouded inducers, due to structural advantages [22].

Acosta et al. [3] developed a theoretical model to investigate the effect of swept leading edges on the cavitation behavior of an inducer. The investigations performed with this model indicate improved cavitation behavior for both backward and forward sweep designs. However, the inducer geometries used are very specific and extracting some design advice from these results is hardly possible (and not intended by the authors). Very little information is available in the open literature on how exactly the sweep angle progression from hub to shroud should be designed. Acosta et al. [3] used an involute curve to define the leading edge shape in the front view (looking from inlet to outlet) but no detailed information about the construction of the main blade geometry is provided. Bakir et al. [13] investigated the effect of successively increasing the backward sweep of a cylindrical inducer from 29° to 101°. While suction performance and cavitation stability could be improved substantially by increasing the backward sweep, a shift of best efficiency point to higher flow rates was observed. At the same time the slope of the head characteristic curve was reduced. Based on these results a backward sweep angle between 65 and 90° is recommended by Gülich [31]. As was already stated above these recommendations are again based on specific investigations and any generalization is subject of a certain degree of uncertainty. However, good initial designs are very likely if sweep angles are chosen in this range.

Choi et al. [22] performed another specific study of the effect of blade sweep on the hydraulic performance of an inducer. Numerical and experimental investigations of a backward and a forward sweep inducer designed for the same application are performed in this study. Interestingly the results indicate that a forward swept design can even improve efficiency and the leading edge tip backflow pattern while suction performance is maintained. This advantage is attributed to the fact that a smaller inlet diameter and a reduced axial length could be used for the forward sweep design. Although generalization of these results is equally arguable, it clearly shows that there is still potential for optimizing every individual application. The procedure developed in this thesis therefore wants to provide a flexible way to design the leading edge shape and leave room even for unconventional design solution.

In the current procedure the blade sweep is parametrized by means of the sweep angle $\Delta\theta_{1s}$ at the leading edge shroud position as depicted in Figure 3.15. A linear progression of wrap angle from zero at the hub to the specified value at the shroud is realized by interpolation with the spanwise parameters at the leading edge. By default, a uniform parametrization is used along the blade section as described in Section 3.4.4 and the

sweep back angle at any spanwise location $v = 0 \ldots 1$ is calculated as:

$$\Delta\theta_1(v) = (\Delta\theta_{1s} - \Delta\theta_{1h})\, v + \Delta\theta_{0h} = \Delta\theta_{1s}\, v \tag{3.46}$$
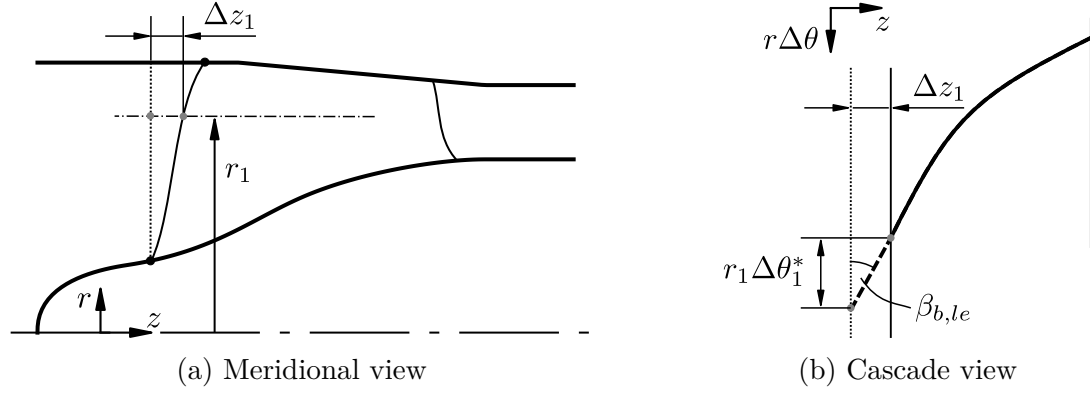

(a) Meridional view   (b) Cascade view

Figure 3.16: Cut back of leading edge

An alternative option is provided to perform a cut of a virtual straight radial leading edge before the additionally specified sweep back is realized. With this procedure the sweep angle is also controlled by the meridional leading edge curve, which can be advantageous for the overall blade wrap distribution. Figure 3.16a depicts a meridional section with the virtual radial leading edge indicated by a dotted line. The final leading edge curve is obtained by virtually cutting away the excessive material over an axial length of $\Delta z_1 = z_1(v) - z_{1h}$ while assuming a constant radius $r_1(v)$ and a blade angle at each blade section close to the leading edge. Developing the cascade view at this radius the geometric properties of the cut can be derived as shown in Figure 3.16b. Thus, the virtual cut is considered by increasing the starting value of wrap angle θ at each section by

$$\Delta\theta_1^*(v) = \frac{z_1(v) - z_{1h}}{r_1(v)\tan(\beta_{b,le})}. \tag{3.47}$$

The total leading edge wrap angle then is computed by

$$\Delta\theta_1(v) = \Delta\theta_1^*(v) + \Delta\theta_{1s}'\, v, \tag{3.48}$$

where $\Delta\theta_{1s}'$ is the additionally specified sweep angle. Of course any other progression of sweep angle with respect to spanwise parameter v or an alternative parameter like radius r is easily implemented within this structure. In the current work only the linear progression is used as it does not further increase the number of design parameters.

3.5.5 Leading Edge Blade Angle

The selection of the entry blade angle is critical to guarantee the required operational range on the one hand and the suction performance on the other hand. According to Acosta [2] typical values of blade angle range from 7 to 15°. This coincides with the historical study of blade angles presented by Japikse [38], which includes blade angles between 5 and 15°.

In the present design method two options are provided to specify the blade angle. It is either specified directly or it is determined based on the incidence to blade angle ratio. In the latter case the inlet flow angle is computed for any radius r_1 from the following equation:

$$\beta_1 = \arctan\left(\frac{c_{m1}}{2\pi r_1 n \delta_r}\right) \tag{3.49}$$

At this point blockage can either be neglected or included by replacing c_{m1} with $c_{m1}' = b_1 c_{m1}$. Consequently, β_1 should be replaced by β_1':

$$\beta_1' = \arctan\left(\frac{c_{m1}'}{2\pi r_1 n \delta_r}\right) \tag{3.50}$$

Furthermore, it is very common to assume a constant mean velocity at the inlet such that $c_{m1} = \bar{c}_{m1}$, where $\bar{c}_{m1}$ is taken as the arithmetic average of the meridional velocity along the leading edge. However, it is also possible to use the local meridional velocity which is provided by the SMA. For the typical assumption of swirl free inlet conditions δ_r is set to 1.

If the blade angle is specified directly, the resulting incidence angle can be checked by using Equations 2.27 or 2.28. If the second approach is used, that is, the incidence to blade angle ratio i/β_{1b} is prescribed, the following equation will have to be solved for β_{1b}

$$\beta_{1b} = \frac{\beta_1}{1 - (i/\beta_{1b})} \tag{3.51}$$

While this is straightforward when blockage is neglected, an iterative solution is necessary when blockage is to be included, since the blockage factor (see Equation 2.13) depends on the blade angle. Thus, Equation 3.51 is modified to

$$\beta_{1b}\left(1 - (i/\beta_{1b})\right) = \arctan\left(\frac{b_1 c_{m1}}{2\pi r_1 n \delta_r}\right) \tag{3.52}$$

with

$$b_1 = \left(1 - \frac{t_1 \, Z}{2 \, \pi \, r_1 \, \sin \beta_{b1}} \right)^{-1} .$$

(3.53)

Computation of the leading edge blade angle β_{1b} is performed for all desired locations along the leading edge.

Recommendations on how to choose the incidence or the incidence to blade angle ratio can be found in the literature. Depending on the blade thickness Jakobsen [36] proposes values between 0.35 for thin and 0.5 for thick blades with the mean value of 0.425 being the generally preferred value. He suggests that higher values than 0.425 should also be chosen if a wide range of flow rate is desired. The reasoning behind this is, that zero incidence should not be obtained at the maximum required flow rate. A similar guideline is provided by Gülich [31], who states that the incidence should not fall below 1° at the maximum desired flow rate.

Depending on the blade type according to Sections 3.5.2 and 3.5.3 different options are provided to determine the leading edge blade angle β_{1b} along the spanwise direction. For the helical blade only one parameter, either blade angle or incidence to blade angle ratio, has to be specified to fix the inlet blade angle at the reference radius. In case of the general blade type the same helical blade angle progression along the leading edge can be used, or instead the parameters may be set independently for the hub and shroud sections. Linear interpolation then is used to compute the blade angle at the points along the leading edge directly or the incidence to blade angle ratio, which in turn is used to calculate the blade angle with the help of Equation 3.51 or 3.52.

3.5.6 Trailing Edge Blade Angle

Similar to the blade entry angle design different methods to determine the exit blade angle are provided. For both the helical and the general blade type the exit blade angle can either be determined by specification of the blade camber angle or by using Euler's equation (Equation 2.22). While the application of the first option is straightforward, the latter requires further assumptions and some more input. As can be seen from the velocity triangle in Figure 2.8b the exit blade angle is equal to the flow angle under the assumption of blade congruent flow. This can be expressed as:

$$\tan \beta_{2b} = \frac{c_{m2}{}'}{u_2 - c_{\theta 2 \infty}}$$

(3.54)

To avoid writing all the relations twice blade blockage is included in the above equation and in the following equations as well without loss of generality. If blade blockage is to

be neglected, the correct equations are obtained by simply setting the blockage factor to one.

The relation between the perfectly guided flow and the velocity triangle for a finite number of blades is expressed by the slip factor concept introduced in Section 2.2.3. Thus, with the help of Equation 2.32 the velocity component $c_{\theta 2 \infty}$ can be replaced with

$$c_{\theta 2 \infty} = c_{\theta 2} + u_2(1 - \gamma), \tag{3.55}$$

which leads to the following expression for the trailing edge blade angle:

$$\beta_{2b} = \arctan\left(\frac{c_{m2}{}'}{\gamma u_2 - c_{\theta 2}}\right) \tag{3.56}$$

From Euler's pump equation (Equation 2.22) the circumferential component of the absolute flow velocitiy $c_{\theta 2}$ is computed by:

$$c_{\theta 2} = \frac{1}{u_2}\left(\frac{y}{\eta_h} + u_1 c_{\theta 1}\right) \tag{3.57}$$

The circumferential velocity at the inlet can be expressed by using the swirl number as follows:

$$c_{\theta 1} = u_1(1 - \delta_r) \tag{3.58}$$

Introducing Equations 3.55, 3.57 and 3.58 into Equation 3.54 the following expression for the exit blade angle is obtained:

$$\beta_{2b} = \arctan\left(\frac{c_{m2}{}' u_2}{y/\eta_h - \gamma u_2^2 + u_1^2(1 - \delta_r)}\right) \tag{3.59}$$

Obviously, two estimates for hydraulic efficiency η_h and slip factor γ have to be provided at this point. According to Jakobsen [36] a hydraulic efficiency of 0.85 can be applied. Gülich [31] suggests a range of 0.7 to 0.9, which is why a default value of 0.8 is defined. As already indicated earlier in Section 2.2.3 no slip factor correlations have been established yet for inducers. Hence, the task of choosing the slip factors is passed to the designer. Depending on the blade type, that is helical or general, either one value for the reference radius has to be specified or the values, which are to be used at the hub and shroud sections. Linearly interpolated values of the slip factor are then used at the intermediate blade sections.

In case of swirl free inflow conditions ($\delta_r = 1$), which are typically assumed, the last term

of the denominator in Equation 3.59 vanishes. Analogously to the leading edge angle computation an iterative solution of Equation 3.59 is only required if blade blockage is considered, since the blade blockage factor depends on the blade angle itself.

The specific work y included in Equation 3.59 is generally assumed to be equal on all the blade sections. Since the specific work is directly related to the total pressure rise caused by the inducer blades (see Equation 2.24), this complies with the free vortex assumption used in the meridional flow analysis. However, in conventional pump acceptance tests usually only static pressures are measured and used to specify the pumps performance and suction capability. For inducer applications this means that only the static pressure rise effectively increases the $\mathrm{NPSH_a}$ of the downstream impeller, and as a consequence decreases the $\mathrm{NPSH_r}$ of the whole pump unit. Therefore, it can be seen as a valid option to exclude the circumferential dynamic pressure rise due to swirl generated by the inducer from the design considerations.

Subtracting the fraction y_θ due to swirl from the specific work y, the corrected specific work, denoted by y_c, is derived as follows:

$$y_c = y - y_\theta = y - \frac{1}{2}\left(c_{\theta 2}^2 - c_{\theta 1}^2\right) = \frac{1}{\rho}\left(p_2 - p_1\right) + \frac{1}{2}\left(c_{m2}^2 - c_{m1}^2\right) \qquad (3.60)$$

Making use of Euler's pump equation the following relation is obtained:

$$y_c = \eta_h\left(u_2 c_{\theta 2} - u_1 c_{\theta 1}\right) - \frac{1}{2}(c_{\theta 2}^2 - c_{\theta 1}^2) \qquad (3.61)$$

The solution of this quadratic equation in $c_{\theta 2}$ is given by:

$$c_{\theta 2} = \eta_h u_2 - \sqrt{(\eta_h u_2)^2 - (2y_c + u_1^2(1 - \delta_r)(2\eta_h - (1 - \delta_r)))} \qquad (3.62)$$

Equation 3.62 can now be used in conjunction with Equation 3.56 to calculate the trailing edge blade angle. However, if the radicand in the above equation gets negative, there's no valid solution for the above procedure. To avoid failure of the whole design program the blade angle is limited to $\beta_{2b} = 90°$ in this case. Thus, the option of applying the correction of the specific work as explained above should be used carefully.

3.5.7 Solidity

Typical values found in the literature range from 1.5 to 3 at tip section for two- to four-bladed inducers [1]. Jakobsen [36] argued that a solidity from 2.0 to 2.5 might be necessary to achieve optimum suction performance. More recent tendencies seem to indicate that also smaller values of solidity of around 1 might be sufficient for low

performance applications [39]. Gülich [31] claims that optimum values of solidity lie in the range of 1.4 and 1.8. He further states that solidity values larger than 2.5 aren't advantageous. Other references alternatively provide values of wrap angle. According to Lakshminarayana [46] rocket turbopump inducers feature wrap angles of around 360°. In the work of Bakir et al. [13] solidity at the tip of a three-bladed inducer was gradually reduced from 2.95 to 2.35 by successively cutting back the leading edge. This was equal to a reduction of wrap angle from 339° to 267°. The results of this investigations showed that the reduction of wrap angle had no substantial effect on overall performance. In fact, the cutting of the leading edge improved the suction performance and reduced pressure fluctuations during cavitation tests (see also Section 3.5.4). Since solidity in the current implementation is practically fixed by defining the camber curves, the wrap angle is used as an input parameter where applicable. However, solidity is computed in the cascade view of the hub and the shroud section as c'/s' (see Figure 2.3b). In the design work flow the value is provided to the designer in order to support the camber curve design.

3.5.8 Thickness Distribution

The thickness distribution is used to add the desired amount of material to the already designed camber curves. In this way the final blade profile, which should guide the flow in the expected way is obtained. Thus, an appropriate way of shaping the thickness distribution is needed.

Different two- and three-dimensional methods of adding the thickness distribution to the blade camber are compiled by Miller [54] but normally not much detail is provided about this step in the open literature, especially for mixed-flow and radial impellers.

In the current work the three-dimensional approach proposed by Miller [54] is adopted to provide a general method to construct symmetric as well as asymmetric profiles. The latter is of huge interest when designing inducers since the thickness is usually added only in the direction pointing to the suction side of the blade camber line [31]. This means that the blade camber line is effectively interpreted as the blade's pressure side. Furthermore, a specific wedge-shaped sharpening of the suction side leading edge is usually performed to improve the suction performance of inducers [36]. It is therefore desirable to include this geometrical detail in a parametrical way into the blade profile design.

Similar to the blade camber line or blade angle definition, the thickness distribution is represented by a uniform B-spline curve of degree three describing the progression of blade thickness along the length of the three-dimensional camber curve. Both co-
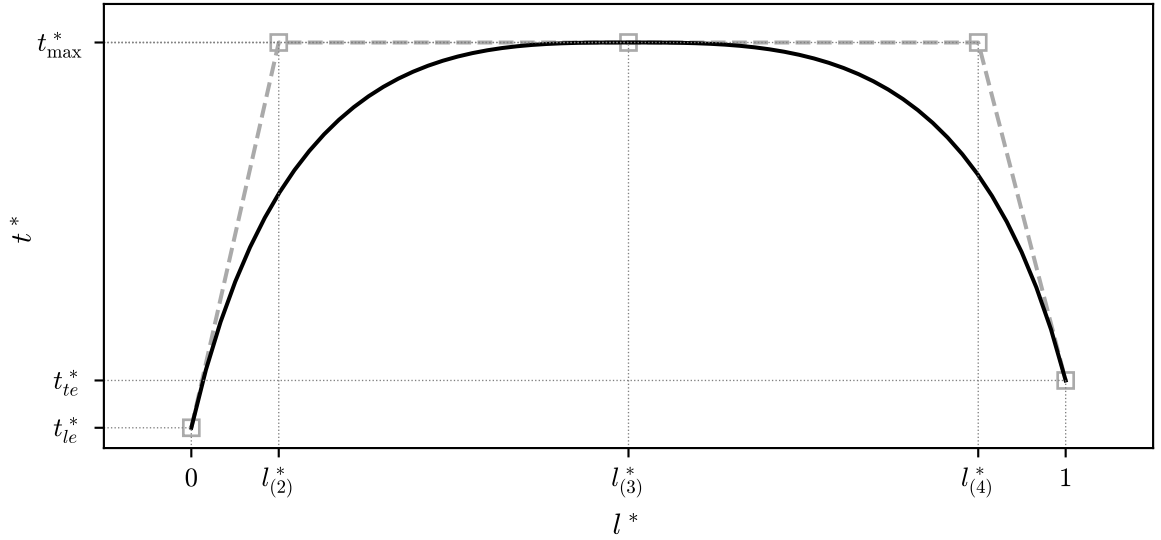
(a) Default thickness distribution
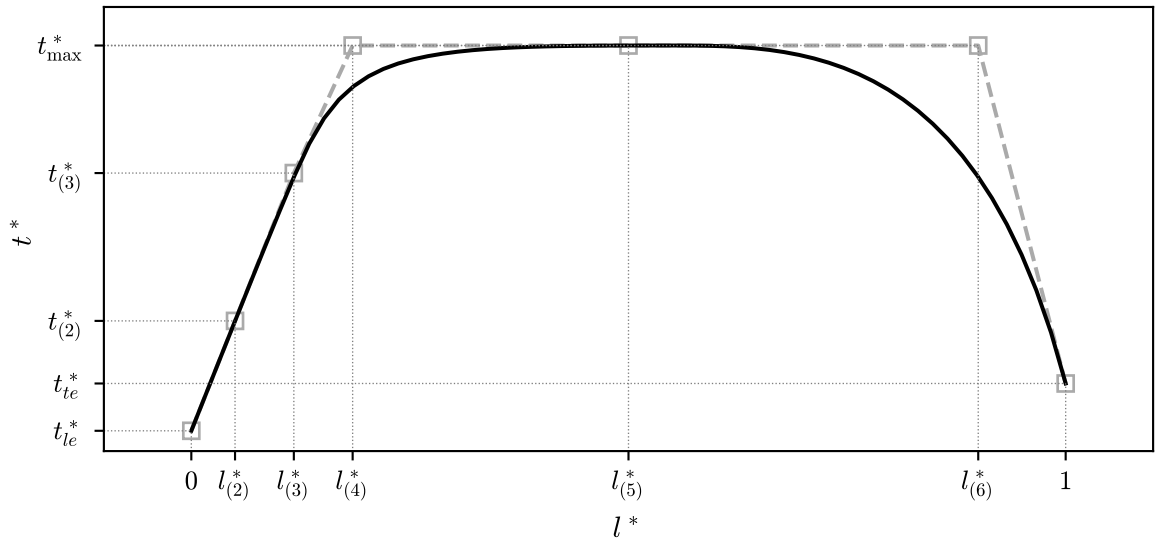
(b) Default thickness distribution with parametric leading edge sharpening

Figure 3.17: Exemplary thickness distributions

ordinates are normalized by the total camber curve length $l_{\max}$ (see Figure 2.4a) as follows:

$$l^* = l/l_{\max} \tag{3.63}$$

$$t^* = t/l_{\max} \tag{3.64}$$

Exemplary progressions of the thickness distributions ($t^*(l^*)$ progressions) are depicted in Figure 3.17. Similar to the camber curve design procedure the curve is controlled

by positioning the control points. By default five control points $p_{(1)} \ldots p_{(5)}$ are used to generate a smooth progression of thickness as illustrated in Figure 3.17a. Their locations can be specified by the user based on only few input parameters. Since the first and the last control points are fixed by the specification of the leading and trailing edge thickness, the three interior control points remain to be defined. If no user input is provided, they are preset as follows:

$$p_{(2)} = (0.1, t^*_{\max}) \tag{3.65}$$

$$p_{(3)} = (0.5, t^*_{\max}) \tag{3.66}$$

$$p_{(4)} = (0.9, t^*_{\max}) \tag{3.67}$$

This means that control points with a user-specified maximum thickness value $t_{\max}$ are provided at $10\,\%$, $50\,\%$ and $90\,\%$ of the total camber curve length.

(a) Leading edge sharpening   (b) Elliptical edge rounding

Figure 3.18: Detailed edge design

An additional setting is provided that facilitates the leading edge sharpening already mentioned above. If a distribution including the sharpening is requested, the default thickness distribution is defined by seven control points $p_{(1)} \ldots p_{(7)}$ where, like before, only the interior points have to be specified. This is illustrated in Figure 3.17b. The two additional control points are used to generate a wedge-shaped thickness progression starting from the leading edge thickness. A sketch of the desired wedge-shaped leading edge geometry is shown in Figure 3.18a. In this two-dimensional view the blade is imagined as being unwrapped from the surface of revolution (the streamsurface) and flattened out into the plane, which of course results in a simplification of the real three-dimensional blade shape. However, since the change in radius along the streamlines in the entry region close to the leading edge can be assumed as being small, the angle distortion can also be expected to be small and thus of little influence. Furthermore, this geometric description can merely be seen as a tool for the designer to manipulate

the leading edge shape of the final blade in a parametrical way. The real value of the (three-dimensional) wedge angle is hardly measurable such that the distortion resulting from this simplified parametrization is of minor importance.

To accomplish the leading edge sharpening two additional parameters, the wedge length l_w and the wedge angle α_w have to be provided. Using the normalized version of the wedge length l_w^*, the first two of the interior control points are fixed by the following default values:

$$l_{(2)}^* = l_w^* \tag{3.68}$$

$$t_{(2)}^* = t_{le}^* + l_w^* \tan \alpha_w \tag{3.69}$$

$$l_{(3)}^* = \frac{1}{2} \left(l_w^* + \max \left(0.1, t_{\max}^* / \tan \alpha_w \right) \right) \tag{3.70}$$

$$t_{(3)}^* = \min \left(t_{le}^* + l_{(3)}^* \tan \alpha_w, t_{\max}^* \right) \tag{3.71}$$

While the second control point $p_{(2)}$ is directly determined by the wedge parameters, the third control point $p_{(3)}$ is chosen such that it is located midway between the point of $10\,\%$ camber length and the point where the wedge-shape would first reach the maximum thickness value $t_{\max}$. The thickness value at this length coordinate then is either the thickness resulting from the wedge-shape or the maximum thickness, whichever value is smaller. Thus, the control points are fixed as follows:

$$p_{(2)} = (l_{(2)}^*, t_{(2)}^*) \tag{3.72}$$

$$p_{(3)} = (l_{(3)}^*, t_{(3)}^*) \tag{3.73}$$

$$p_{(4)} = (\max \left(0.1, t_{\max}^* / \tan \alpha_w \right), t_{\max}^*) \tag{3.74}$$

$$p_{(5)} = (0.5, t_{\max}^*) \tag{3.75}$$

$$p_{(6)} = (0.9, t_{\max}^*) \tag{3.76}$$

Once the control points are initially defined, the designer can move them freely and add additional or remove intermediate control points. However, the already set values of the input parameters are ignored in that case.

As a final step of thickness distribution design treatment of the edges is considered. This edge treatment is incorporated into the thickness distribution in order to obtain properly rounded edges of the three-dimensional blade profile. In the current implementation elliptical arcs are used at both ends of the thickness distribution. The elliptical round off is constructed separately for suction and pressure sides by an iterative algorithm, which is explained exemplarily for the situation at the leading edge as depicted in Figure

3.18b. Goal of the algorithm is the construction of an elliptical arc (gray), which starts tangentially to the thickness axis (t or t') from the leading edge point p_{le} and connects smoothly to the thickness distribution (black). The arc is derived from an ellipse with user specified aspect ratio a/b. It is found by searching for the boundary point p_b, where the ellipse and the thickness distribution share their tangential direction.

To achieve zero thickness at the leading edge of the final profile the ellipse major axis is shifted by $t_{le}/2$ such that the center point $p_m = (l_m, t_m) = (a, t_{le}/2)$. From the tangent equation of the shifted ellipse

$$\frac{(l - l_m)(l_b - l_m)}{a^2} + \frac{(t - t_m)(t_b - t_m)}{b^2} = 1 \tag{3.77}$$

an expression for the unknown value of l_m can be retrieved by differentiation and rearranging as follows:

$$l_m = \frac{\partial t}{\partial l}\left(\frac{a}{b}\right)^2 (t_b - t_m) + l_b \tag{3.78}$$

(a) Leading edge, two-sided　　　　　(b) Trailing edge, single-sided
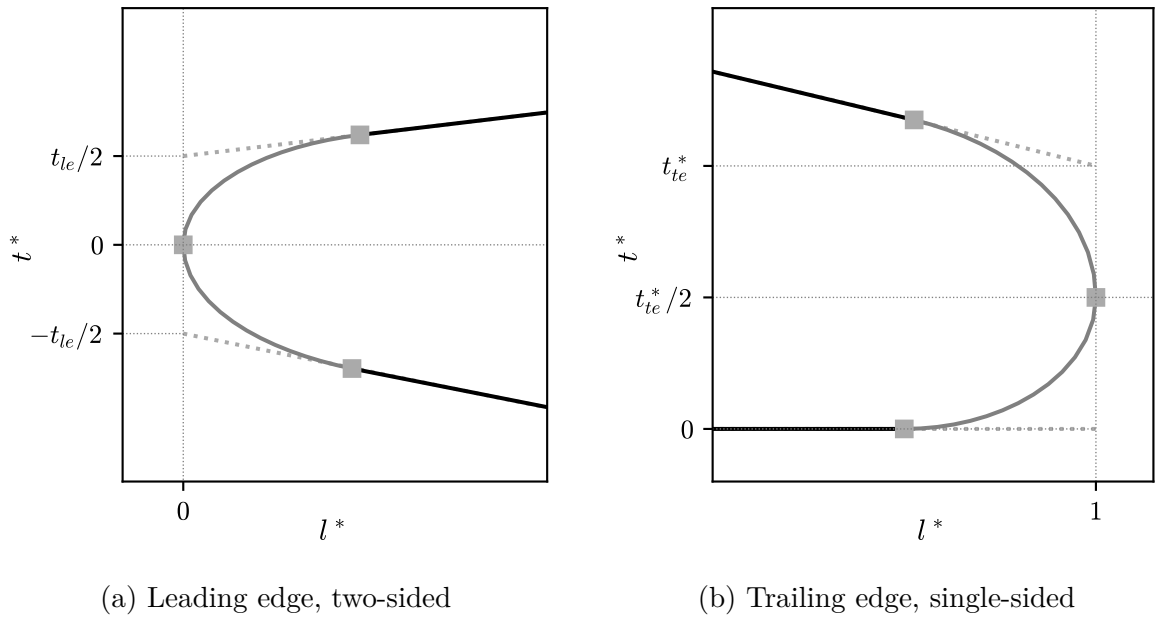
Figure 3.19: Elliptical rounding

The algorithm now iteratively evaluates the thickness distribution curve to obtain the coordinates and the slope of the potential boundary point. At every iteration step it checks whether the ellipse equation is satisfied at the current boundary point by

computing the error

$$\frac{(l_b - l_m)^2}{a^2} + \frac{(t_b - t_m)^2}{b^2} - 1 = \epsilon_e \tag{3.79}$$

Since the thickness curve is a parametric curve, the target value is the curve parameter u_b. The parameter search is constrained by bracketing the solution inside the interval $[u_1, u_{b,\max}]$, that is between the leading edge curve parameter and a certain maximum parameter. By default the maximum parameter is set to $10\,\%$ of the whole parameter range between leading edge and trailing edge:

$$u_{b,\max} = 0.1\,(u_2 - u_1) + u_1 \tag{3.80}$$

Once the error ϵ_e is below a certain tolerance value, the algorithm stops and the parameter at which the boundary point is found is used to trim the thickness curve appropriately. Only slight modifications are necessary to adopt this procedure to the geometric situation at the trailing edge. The resulting elliptical shapes are depicted in Figure 3.19a for a two-sided but asymmetric thickness distribution and in Figure 3.19b for a single-sided thickness distribution. As already mentioned in Section 2.2.1 the pressure side thickness distributions are assigned a negative sign just to provide a clear presentation of both thickness distributions in a single illustration.

(a) Two-sided
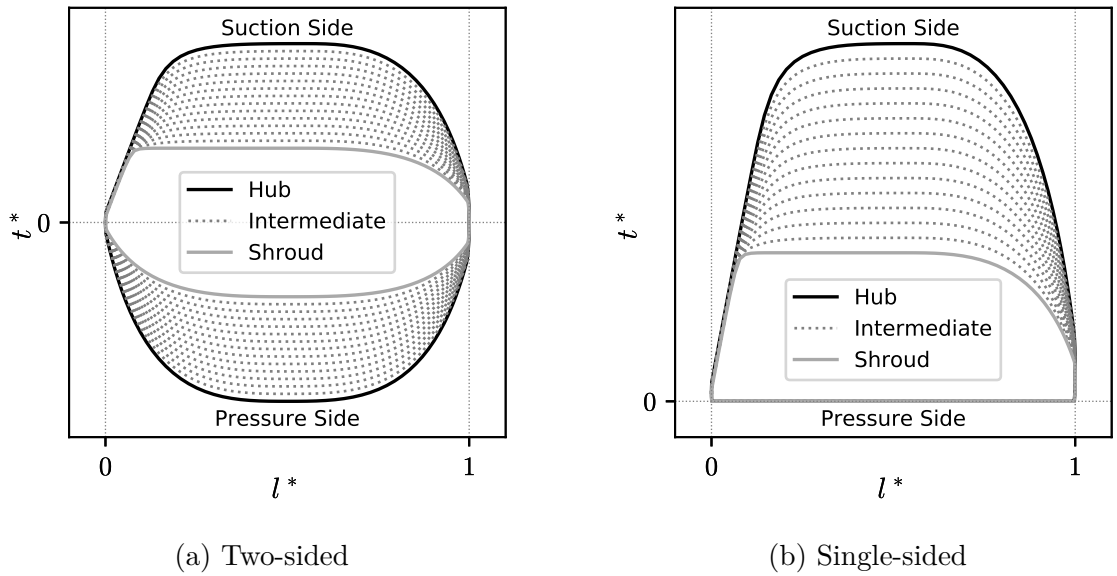
(b) Single-sided

Figure 3.20: Two- and single-sided thickness distributions

Similar to the blade camber line design only the thickness distributions belonging to the hub and shroud sections of the blade are prescribed directly by the designer. On both of

these sections two thickness distributions are required to provide the necessary thickness data for the completion of the suction side and the pressure side of the profile. The intermediate sections are obtained by linear interpolation in the spanwise direction on a point-by-point basis. As a result, two series of thickness distributions are obtained as illustrated in Figure 3.20a. For single sided, asymmetric profiles one of the distributions is simply set to a straight line with zero thickness on all of the blade sections (Figure 3.20b).

In contrast to the approach of Miller [54] the curves representing the leading edge, main blade and trailing edge segments are not merged in the current implementation but are stored separately in order to keep control over the curve parametrization and the number of nodes used for the profiles at the leading and trailing edges. This is particularly important if the blade edges are very thin compared to the maximum blade thickness and only take up a very small part of the total blade length, which is normally the case for inducers. By using a single parametrized curve one could risk that the blade edges are not represented adequately, when evaluating points along the curves. Therefore, the number of points used for the blade profile generation are provided as input parameters, which can be specified by the user. How the thickness distributions are finally used to construct the final blade profile is described in detail in the following section.

3.5.9 Blade Profile

The blade profile is composed of the camber (or theta) curve and the thickness distributions on the suction and pressure sides. Again there are several possible methods to construct the profiles from these ingredients. Since a very precise representation of the blade is desired, especially due to the importance of the edge shape design, the three-dimensional method proposed by Miller [54] is adopted in the present implementation. The first step of this method consists of the construction of the three-dimensional camber curve, which is a matter of simple mapping of coordinates. In the next step three-dimensional normals are computed at the parametrical locations used for the corresponding thickness distribution. Because the normal construction is computational expensive, due to the interpolation steps involved, the same normals are used to apply the suction side and the pressure side thickness to the camber curve. This requires a sampling of the thickness distributions so that thickness values on suction and pressure side are available at the same length coordinates. The sampling is performed separately for each of the three segments of the thickness distributions, that is the leading edge, main blade and the trailing edge segment, to ensure that the desired number of nodes
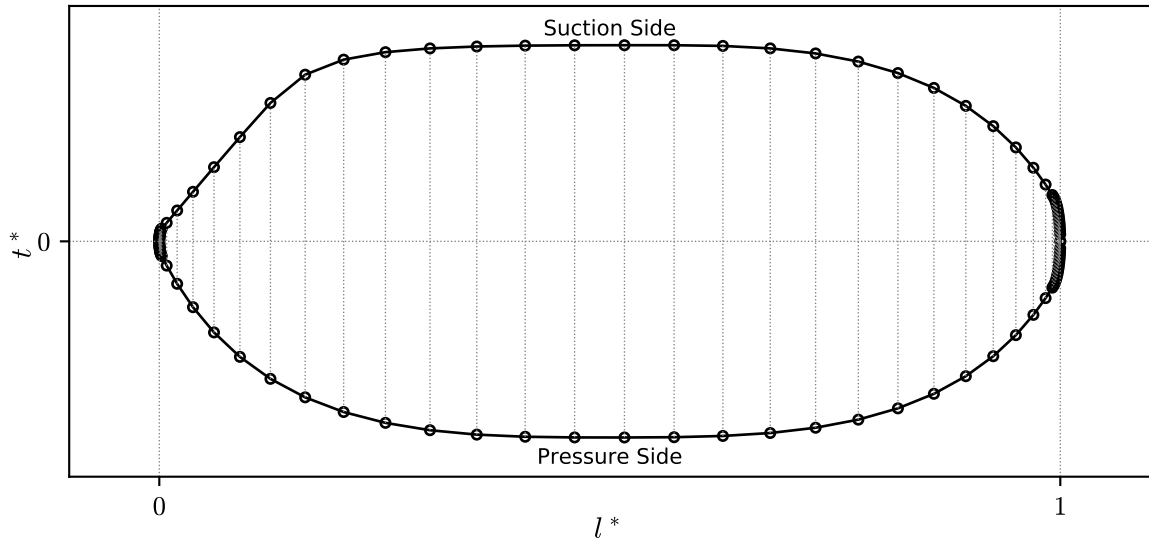
(a) Total view
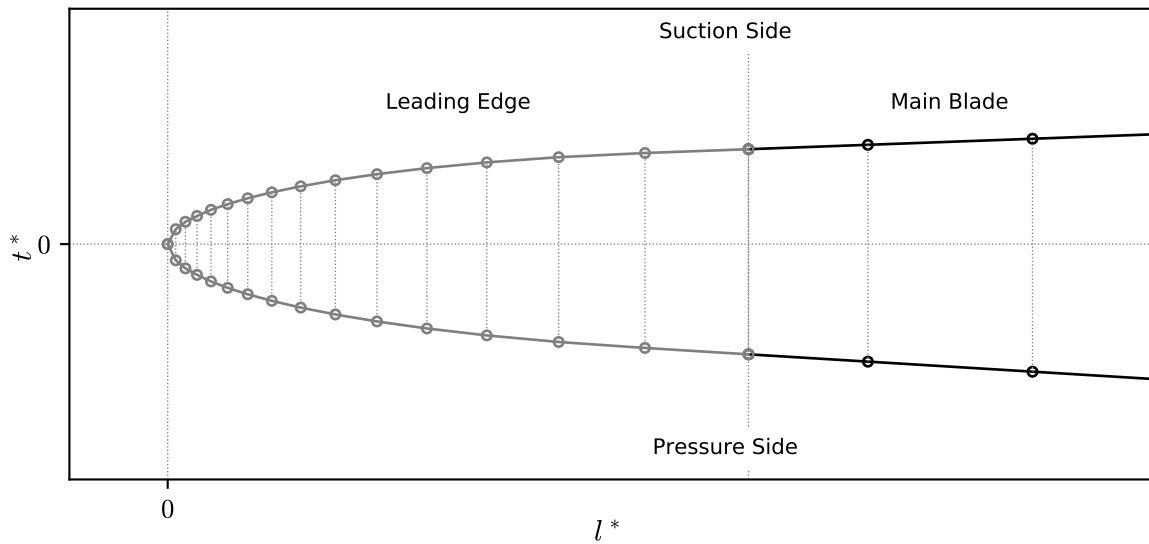
(b) Detailed view of leading edge

Figure 3.21: Sampling of the thickness distributions

is returned. Furthermore, the curvature of the thickness distributions at the edge segments require a reduction of node spacing in order to adequately represent the edge shape. This is realized by a geometrical node spacing, which is applied to the edge segments. If the total number of nodes of the segment under consideration is denoted by n_i, the geometrical spacing of the nodes is prescribed by the following formula:

$$l_i = l_{i-1} + f^{i-1} \frac{l_{n_i-1} - l_0}{\sum_{j=0}^{n_i-1} f^j}, \quad i = 1, \ldots n_i - 1 \tag{3.81}$$

The rate of growth of the spacing can be controlled by the factor f, which by default is set to a value of 1.2. To obtain a smooth transition from the edge segments the nodes of the main blade segment are distributed by means of a cosinus function [6]:

$$l_i = \frac{(1 - \cos \phi_i)}{2}(l_{n_i-1} - l_0) + l_0, \quad i = 1, \ldots n_i - 1 \tag{3.82}$$

The ϕ_i are obtained by dividing the interval $[\phi_0, \phi_{n_i-1}]$ equidistantly. The limits of the interval are calculated by:

$$\phi_0 = \arccos \left(1 - 2 \left[\frac{\Delta l_0}{l_{n_i-1} - l_0} \right] \right) \tag{3.83}$$

$$\phi_{n_i-1} = \arccos \left(1 - 2 \left[1 - \frac{\Delta l_{n_i-1}}{l_{n_i-1} - l_0} \right] \right) \tag{3.84}$$

Similar to the geometrical node distribution used for the edge segments the spacing at the transition to the edges is controlled by the values used for Δl_0 and Δl_{n_i-1}. By default they are set as 1.2 times the distance to the last node of the edge distribution at the leading edge and 1.2 times the distance to the first node of the distribution at the trailing edge, respectively. An exemplary sampling of the entire thickness distribution is shown in Figure 3.21a. The total number of nodes was reduced to improve the visualization of the increase in node density towards the blade edges. A detailed view of the leading edge sampling is provided in Figure 3.21a. As already mentioned before the numbers used for the edge segments and the main blade segments can be specified

(a) Normals in cascade plane   (b) Sampling of normals
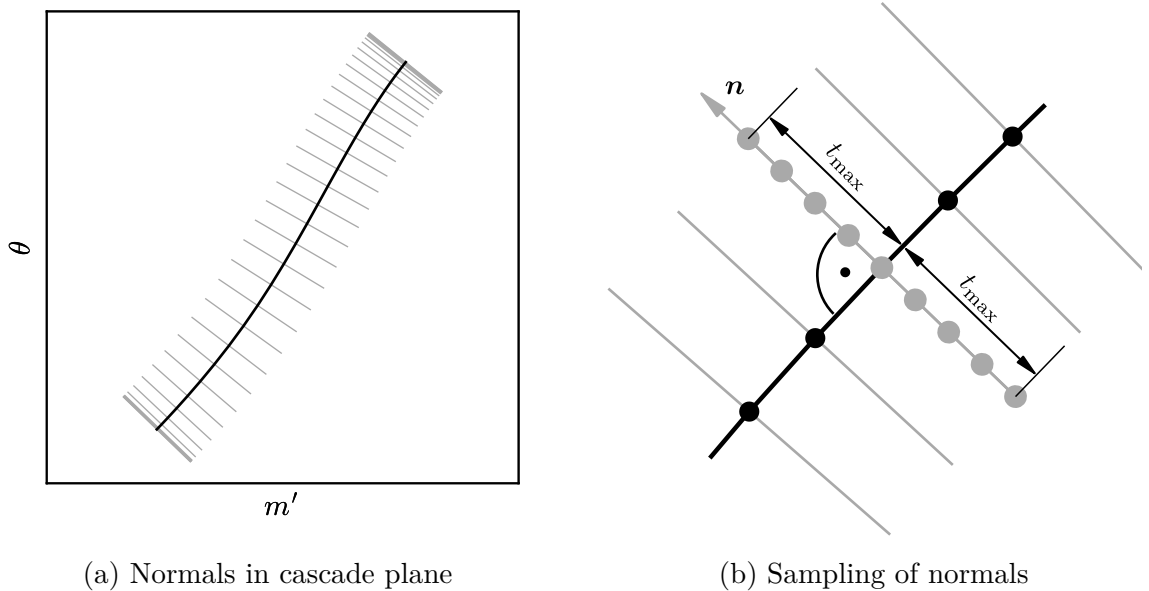
Figure 3.22: Normal directions along blade camber curve

(a) Three-dimensional normals

(b) Construction of profile points
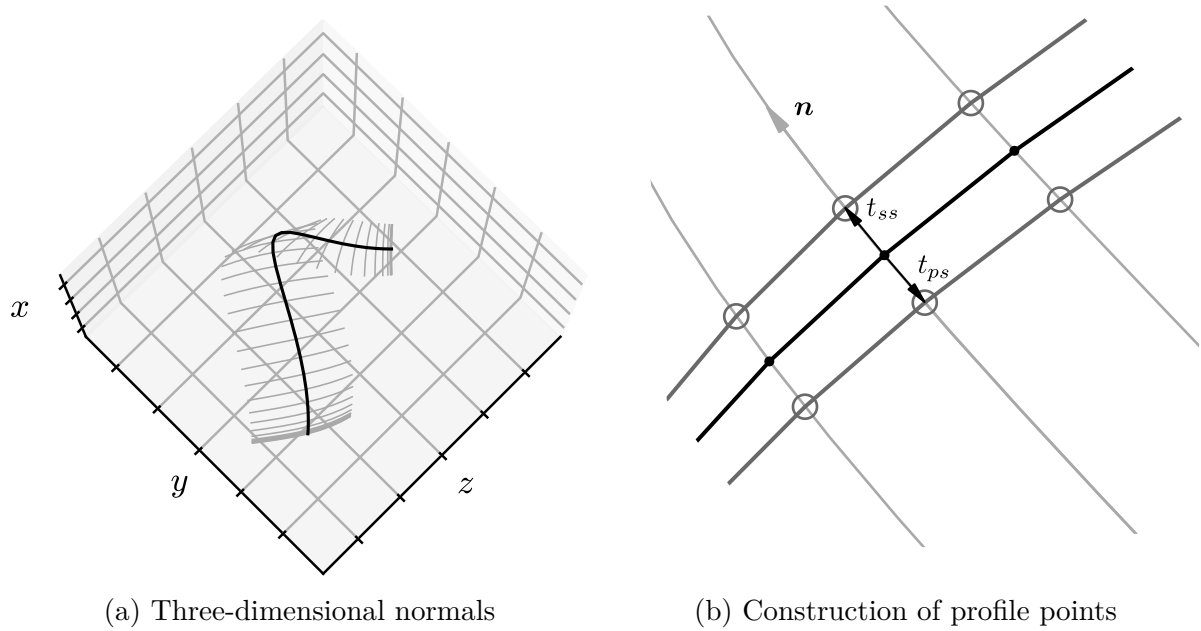
Figure 3.23: Three-dimensional blade profile construction

by the user. By default 15 nodes are used for the edge segments and 60 for the main blade segment. Since the boundary nodes are included in both the edge and the main blade segment, this leads to a total of 88 points used for each profile side. The process of final profile construction is depicted in Figure 3.22, 3.23 and 3.24. In these figures also a reduced number of points is used to improve the visualization of the procedure. First the two-dimensional normals are created at the parametric locations of the points along the thickness distribution. In the blade-to-blade view, as depicted in Figure 3.22a, the normals are straight lines perpendicular to the camber curve, since the cascade view is angle conserving as explained earlier. However, the real thickness cannot be applied without distortion effects in this view [54]. Because of this, the normals are transferred on a point-by-point basis to the three-dimensional space. As indicated in Figure 3.22b the sampling of the normals is limited to a reasonable length $t'_{\max}$ to both sides of the camber curve. This length is estimated by dividing local thickness by radius and searching the maximum value on any of the blade sides. To guarantee that the real thickness is reached on the three-dimensional normals the maximum value found is corrected by a factor of 1.1. This estimation process can be expressed by the following formula:

$$t'_{\max} = 1.1 \times \max\left(\max\left(t_{ss}/r\right), \max\left(t_{ps}/r\right)\right) \tag{3.85}$$

An adequate number of points has to be sampled from the segment of the normal limited

(a) 3D-Profile

(b) 2D-Profile (cascade plane)
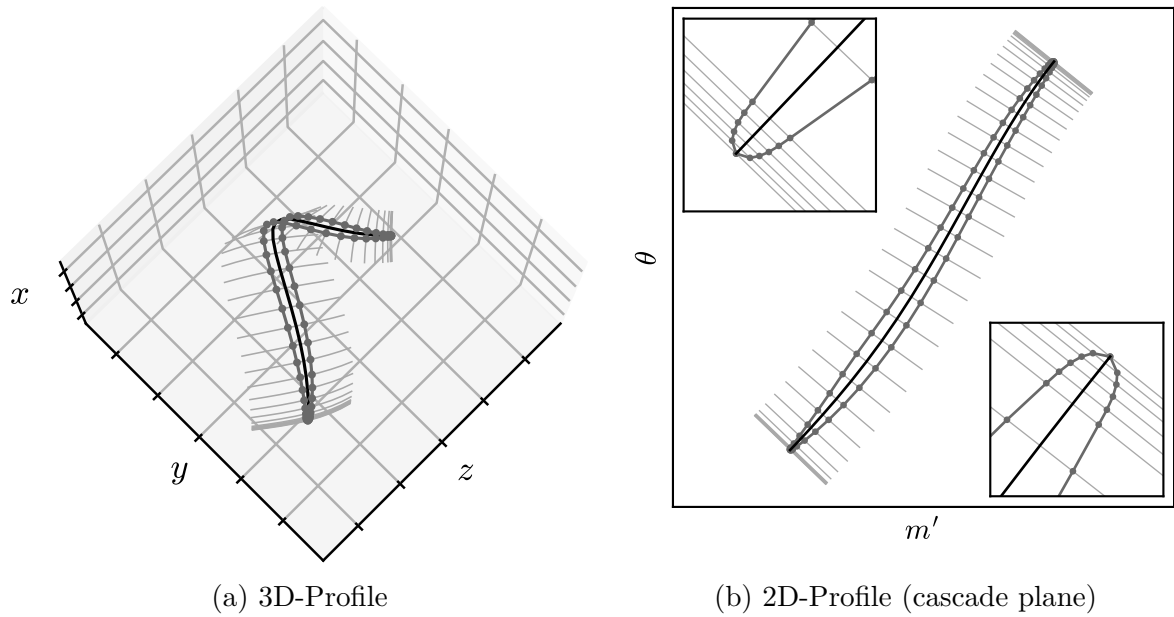
Figure 3.24: Blade profile

by $t'_{\max}$ to both sides of the camber curve to ensure a smooth normal curve in three-dimensions. In the current implementation 5 points on each side of the camber curves are used by default. Parametrization of the curves ensures that evaluation of the normals at a parameter value of 0 results in a point on the camber curve. Once the mapping to the three-dimensional space is completed the sampled points are interpolated by a uniform B-spline of degree three to obtain normal curves lying in the surface of revolution representing a streamsurface. Along these curves, which are illustrated exemplarily in Figure 3.23a, the real thickness can be used to fix the point of the blade surface. This is depicted in more detail in Figure 3.23b. At each point of the three-dimensional camber curve the points on the corresponding normal at a distance of t_{ss} and t_{ps} are set (and stored) as the points constituting the suction side and pressure side profile, respectively (see Figure 3.24a). Although not necessary for the construction of the final blade surface, the blade profile points can be mapped back to the cascade plane. As a result, the two-dimensional blade profile is obtained as depicted in Figure 3.24b. In the boxes at the lower left and upper right corners of this figure detail views are provided, which illustrate the increase of node density at leading and trailing edge, respectively. The process described above is performed for all streamlines so that multiple blade sections are obtained between hub and shroud. These blade sections are used to construct the blade surface. Several export options are provided to export the generated blade geometry into different data formats to facilitate, for example, the grid generation process in the CFD work flow.

4 Verification and Validation

4.1 Overview

Two test cases are used to demonstrate the functioning of the components of the implemented design procedure. In Section 4.2 the two designs are discussed and compared in detail. Since both test cases are chosen with the ultimate target to fit them to an existing experimental pump unit investigated by Knapp [43], they are developed using the same meridional section.

Verification and validation of the simple meridional flow analysis (SMA) introduced in Section 2.4 is of particular importance because the streamlines provided by this method are the foundation of the blade design, and thus should be physically reasonable. Furthermore, a realistic estimate of meridional velocity should be obtained in order to appropriately represent the velocity triangles involved in the blade angle design. Finally, the meridional velocity distributions along the streamlines are used as input to the simple head prediction method (SHP) and consequently have an impact on the quality of head prediction. In a first step of verification the simple case of a cylindrical meridional section is considered in order to prove correct implementation of the numerical scheme. Due to the assumption of inviscid, free-vortex flow, it is not possible to perform validation based on experimental data. Instead, the SMA is tested on the meridional section of the final inducer test cases mentioned above and the results are compared with the solution of a two-dimensional, inviscid numerical simulation employing a commercial CFD code. Accuracy of both the SMA and the reference CFD solutions is analyzed and discussed. A similar procedure of verification and validation is performed for the simple head prediction method (SHP) described in Section 2.5. To make sure that the singularity method, which is the main component of the SHP, is implemented correctly, a comparison with an analytical solution of a cascade of flat plates is performed. Proceeding with the design process, two different blades are created, one for each of the blade types described in Sections 3.5.2 and 3.5.3. Since no flow field measurements of these inducers are available, these prototypes are used to test the SHP against the results of three-dimensional, viscous CFD simulations of the blade passage. After an analysis of the uncertainty of the results the outcome of this comparisons is discussed in Section 4.4.

To validate and evaluate the developed design procedure, the prototypes generated are eventually investigated experimentally in conjunction with the already mentioned single stage volute pump. A detailed description of the real pump setups as well as the measurement procedures and a discussion of the results of the investigations are given in Section 4.5.

4.2 Test Cases

4.2.1 Basic Design Considerations

To obtain a similar hydraulic design fitting to the existing pump assembly, the design point of the entire pump is kept unchanged and is defined as:

$$Q = 100\,\mathrm{m^3 h^{-1}} \tag{4.1a}$$

$$H_P = 30\,\mathrm{m} \tag{4.1b}$$

$$n = 3000\,\mathrm{min^{-1}} \tag{4.1c}$$

Based on the reasoning of Janigro and Ferrini [37] the inducers are designed for approximately $10\,\%$ of the whole stage head H_P. Using this percentage, the inducers design head is set as

$$H = 3\,\mathrm{m}. \tag{4.2}$$

This head is assumed to be the corrected head neglecting the circumferential dynamic pressure rise due to the swirl produced by the inducer, as discussed in Section 3.5.6. Thus, the total head rise of the inducer is expected to be higher than the above design value. Since the inducer is operating in series with the impeller and is mounted on the same shaft, volume flow rate Q and speed n can be adopted from the pump and applied to the inducers as well.

However, several modifications of the original pump were necessary to employ an inducer impeller configuration in the original pump unit. A new impeller is designed to provide space for mounting the inducer on the original shaft. Furthermore, an additional pressure tap is provided to judge the static pressure rise generated by the inducer during operation of the entire inducer-pump stage. Further details about this impeller design are given in Appendix D. The whole pump stage is described in Section 4.5.1.

In the design steps that are described in the following sections the inflow to the pump is assumed to be swirl free (swirl number $\delta_r = 1$). The working fluid is supposed to be pure water at $25\,^\circ\mathrm{C}$ with constant density and vapor pressure:

$$\rho = 997\,\mathrm{kg/m^3} \tag{4.3a}$$

$$p_v = 3170\,\mathrm{Pa} \tag{4.3b}$$

To obtain a uniform representation of the non-dimensional characteristic values, flow coefficient, head coefficient and cavitation coefficient are computed based on the di-

mensions of the experimental setup (see Section 4.5.1). Hence, flow coefficient and cavitation coefficient are computed with respect to the diameter at the suction pressure tap $d_{p1} = 97\,\text{mm}$ and head coefficient with respect to the main impellers outer diameter $D_2 = 163\,\text{mm}$ using the following formulas:

$$\varphi = \frac{4Q}{\pi^2 n d_{p1}^3} \tag{4.4a}$$

$$\psi = \frac{2gH}{(\pi n D_2)^2} \tag{4.4b}$$

$$\sigma = \frac{2g\text{NPSH}}{\left(\pi n d_{p1}^2\right)^2} \tag{4.4c}$$

Consequently, design flow and head coefficient denoted by subscript d are given as follows:

$$\varphi_d = 0.247 \tag{4.5}$$

$$\psi_d = 0.09 \tag{4.6}$$

4.2.2 Meridional Design

Due to space limitations and the need to match the inducer to the existing pump assembly the meridional shape of the inducers is confined to certain dimensions. This is illustrated in Figure 4.1, which shows a sketch of the meridional section of the inducer. The dashed lines indicate the (virtual) inducer inlet and outlet planes, where the latter is identical to the impeller inlet plane. A convenient feature of the design program is that arbitrary meridional shapes can be represented. Therefore, although not necessary in general, the rounding at the upstream end of the inducer hub (also called inducer nose) and the downstream transition to the radial section of the main impeller is already considered during inducer design. The smallest possible hub diameter is chosen based on structural and mechanical considerations. Sufficient hub wall thickness as well as sufficient clearance for the bolt securing the inducer on the shaft have to be provided. As can be seen from Table 4.1 the final inlet hub diameter is fixed as $d_{1h} = 20\,\text{mm}$. Choosing a design suction specific speed of $\Omega_{ss} = 9.35$, which corresponds to $n_{ss} \approx 495\,\text{min}^{-1}$ or $N_{ss} \approx 25\,550\,\text{min}^{-1}$, the inlet diameter d_{1s} is estimated as $d_{1s} = 120\,\text{mm}$ by using Equations 3.12 and 3.13 with the known inlet hub diameter. Using this diameter should theoretically permit to reach NPSH $\approx 1\,\text{m}$, which is equal to a cavitation coefficient of $\sigma \approx 0.084$ according to Equation 4.4c. Note that the optimum flow coefficient for the inducer amounts to $\varphi_{opt} = 0.134$, if computed for the inlet geometry of the inducer
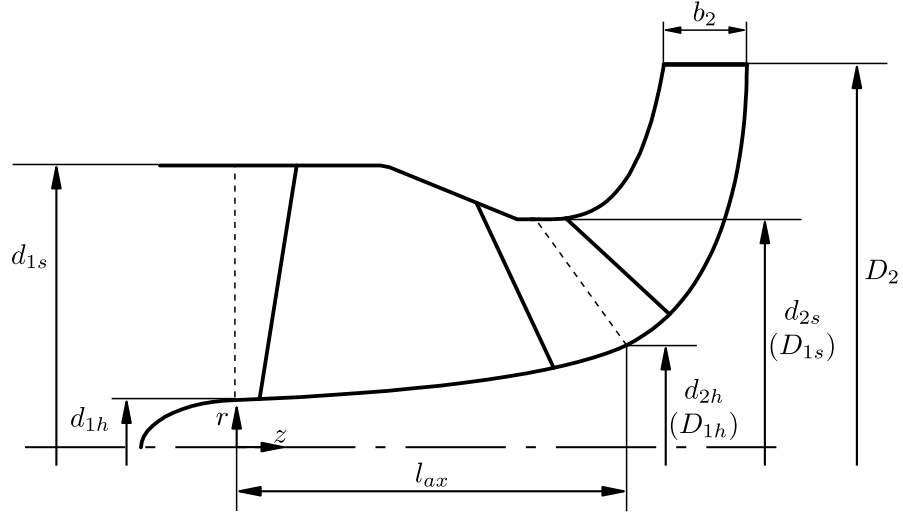
Figure 4.1: Meridional view with basic dimensions

defined by d_{1s} and d_{1h}.

The hub and shroud diameter at the inducer exit d_{2h} and d_{2s} are determined by the impeller inlet diameters. These are denoted by upper case letters so that $d_{2h} = D_{1h} = 41.9 \, \text{mm}$ and $d_{2s} = D_{1s} = 97 \, \text{mm}$. In general, the axial length l_{ax} of the inducer is a result of the desired blade wrap angle (or solidity). However, in the current case it is also limited by the increased overhang of the inducer-pump assembly. While at the hub

Table 4.1: Basic dimensions of test cases

Dimension	Value	Unit
d_{1h}	20	mm
d_{1s}	120	mm
$d_{2h}(D_{1h})$	41.9	mm
$d_{2s}(D_{1s})$	97	mm
l_{ax}	81.4	mm
D_2	163	mm
b_2	17.6	mm

a smooth transition towards the impeller is realized by a single B-spline curve, multiple linear curve segments are used at the shroud section. As a result, a cylindrical segment at the inlet of the inducer is obtained before the diameter is decreased towards the impeller inlet. A further advantage of the straight curve segments is that the (normal) clearance between inducer tip and the casing wall (shroud), which is chosen as $0.5 \, \text{mm}$, can be achieved more easily in the manufacturing process. Figure 4.2a shows the area circles and the geometrical midline constructed with the algorithm explained in Section 3.4.2. The circles are used to compute the quasi-normals that are employed to calculate the

(a) Area circles

(b) Area and velocity distribution
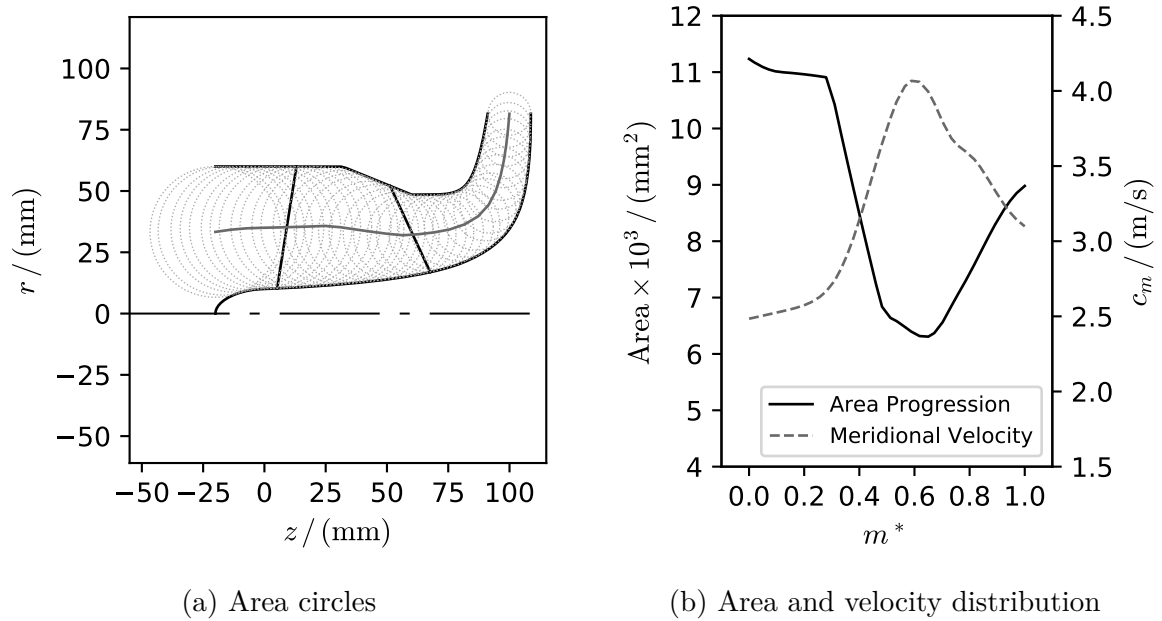
Figure 4.2: Analysis of meridional area distribution

area distribution. In Figure 4.2b this area distribution is displayed along the normalized length of the midline. The SMA is applied to this meridional section in order to compute

(a) Streamlines
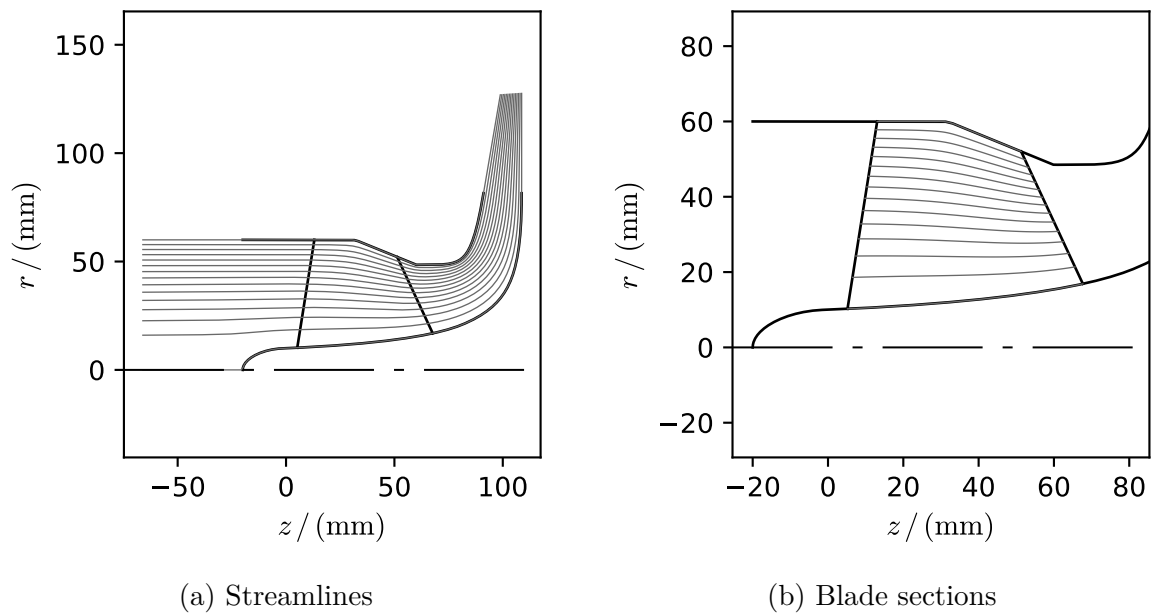
(b) Blade sections

Figure 4.3: Generation of blade sections

streamlines and the meridional velocity field. By evaluating the velocity field at the midline coordinates the velocity distribution as shown in Figure 4.2b is obtained. Figure 4.3a displays the 15 streamlines used for the test case designs. This comparatively

high number of streamlines is needed to adequately represent the three-dimensional leading edge shape resulting from the backward sweep, as will be described below. The computation domain is automatically extended upstream and downstream of the meridional curves in order to guarantee smooth streamlines, which are not influenced by the boundary conditions. Trimming of the streamlines at the intersection points with the leading and trailing edge curves delivers the blade section curves as shown in Figure 4.3. These curves are the foundation of the blade design of both test cases presented in the following section.

4.2.3 Blade Design

Table 4.2 gives an overview of the essential properties of the two inducer test cases designed to validate the design procedure developed in this thesis. The first test case

Table 4.2: Basic properties of the test cases

	HEL	**GEN**
Number of blades	3	3
Blade type	Helical	General
Angle distribution	Parabolic	B-spline (Theta Mode)
Thickness type	Suction Side Only	Suction Side Only

is a helical design, in the following denoted by the acronym HEL, which stands for the helical blade type described in Section 3.5.2. The second test case, analogously denoted by GEN, is an inducer with the general blade type. While inducer HEL employs a parabolic angle distribution at the reference radius, the Theta design mode is used for inducer GEN to define the angle distribution based on a B-spline curve. For both inducers thickness is added only to the suction side of the three-dimensional camber curve, such that the pressure side of the final blade effectively represents the angle distribution.

A more detailed collection of the geometrical features of the blade designs is summarized in Table 4.3. Following Jakobsen [36] the leading edge blade angle is computed based on the ratio of incidence to leading edge blade angle for both design examples. For the helical inducer HEL the ratio $(i/\beta_{b,le})_{\mathrm{rms}} = 0.425$ is used at the reference diameter r_{rms}. In case of inducer GEN the ratio is varied from 0.425 at the shroud to 0.325 at the hub in order to avoid overly large blade angles at the hub section. Although the effect is small due to small leading edge blade thickness (see Table 4.3), blade blockage is considered in the computation of the leading edge blade angles by application of Equation 3.52. The equation is solved under the assumption of a mean meridional velocity that is equal

Table 4.3: Geometrical details of the test cases

Parameter	Unit	HEL		GEN	
		Hub	Shroud	Hub	Shroud
t_{le}	mm	0.1	0.1	0.1	0.1
t_{te}	mm	0.5	0.5	0.5	0.5
θ_{le}	°	0	76.3	0	76.7
θ_{te}	°	221.5	215.8	230.0	216.7
$\beta_{b,le}$	°	54.6	13.5	56.9	13.4
$\beta_{b,te}$	°	54.4	24.4	71.9	22.4
σ'	–	3.03	1.21	3.07	1.21

to the arithmetic mean of the meridional velocity at the leading edge points. For the helical blade this equation only has to be solved once for the reference radius. The blade angle values at the leading edge coordinates of the real blade sections shown in Figure 4.3 are then obtained with the help of Equation 3.24. For inducer GEN, by contrast, Equation 3.52 is solved for each blade section individually.

(a) Leading edge

(b) Trailing dge
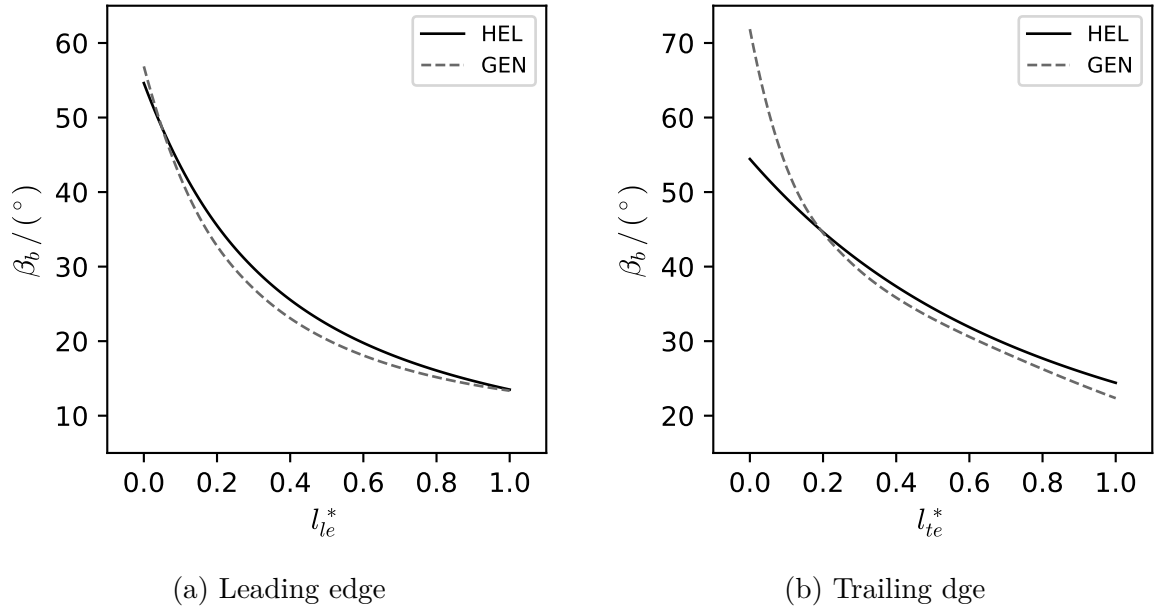
Figure 4.4: Comparision of blade angle distribution along LE and TE

To visualize the differences of both design approaches Figure 4.4a depicts the blade angle distributions along the normalized leading edge length for both inducers. As can be seen from this figure almost identical blade angles are obtained at the shroud section, whereas bigger differences are achieved around the mid of the leading edge. In this region the general blade type uses smaller leading edge blade angles. However, the increase

in blade angle is steeper towards the hub, such that eventually a higher blade angle is obtained at the hub. As for the leading edge blade angle the trailing edge angle is computed differently for both cases. For the helical inducer HEL only the blade angle at the reference radius r_{rms} has to be computed. This is achieved by application of Equations 3.56 and 3.62 assuming a slip factor of $\gamma = 0.8$ and a hydraulic efficiency of $\eta_h = 0.8$, which is a reasonable estimate according to Gülich [31]. Inducer GEN on the other hand uses a prescribed camber angle at the hub and shroud blade sections. As can be extracted from Table 4.3 camber angles are $\Delta\beta_b = 15°$ at the hub and $\Delta\beta_b = 9°$ at the shroud section. Inducer HEL employs a parabolic angle distribution at the

(a) Inducer HEL   (b) Inducer GEN
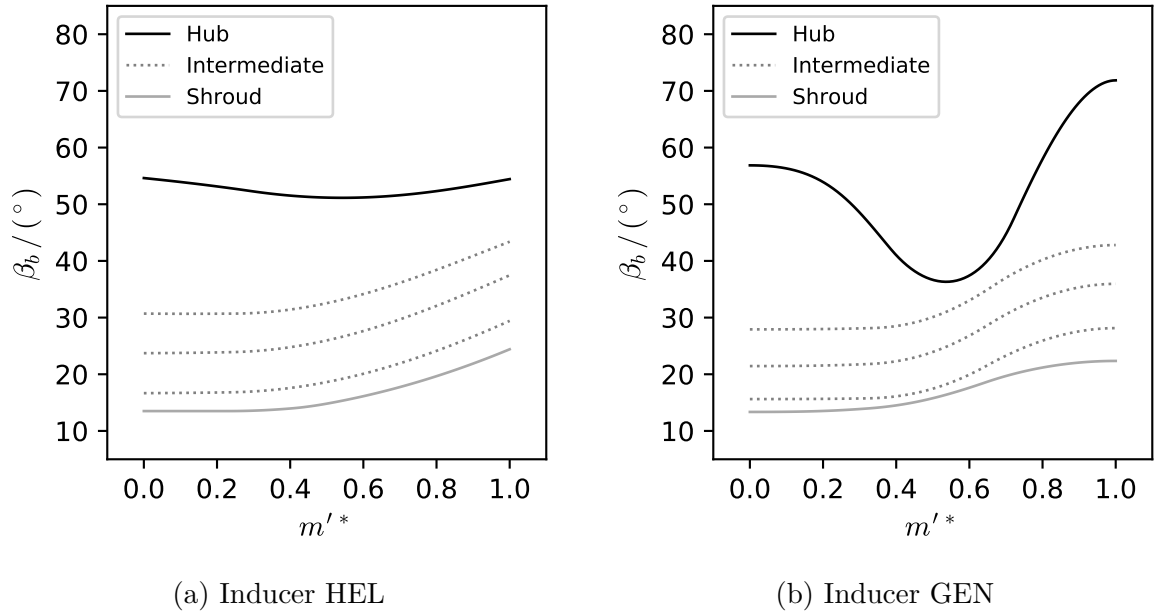
Figure 4.5: Blade angle distribution along blade sections

reference radius with a constant angle section ranging from the leading edge to 25 % of axial length. In case of Inducer GEN the blade angle is retrieved from a B-spline curve prescribing the wrap angle distribution. This results in the angle distributions depicted in Figure 4.5a and 4.5b, respectively. For the sake of clarity only three of the thirteen intermediate angle distributions are displayed in these figures. It should also be noted that the blade angle is plotted against the normalized m' coordinates along the individual blade sections, which is why the leading edge corresponds to an abscissa value of 0 and the trailing edge to a value of 1. In Figures 4.6a and 4.6b, on the other hand, the wrap angle θ is plotted against the actual m' coordinate of each blade section. This leads to the conformal representation of the camber curves displaying the true blade angle (see Section 2.2.2). Figures 4.6a and 4.6b clearly show that the two design examples provide completely different blade shapes. A direct comparison of the blade

(a) Inducer HEL

(b) Inducer GEN
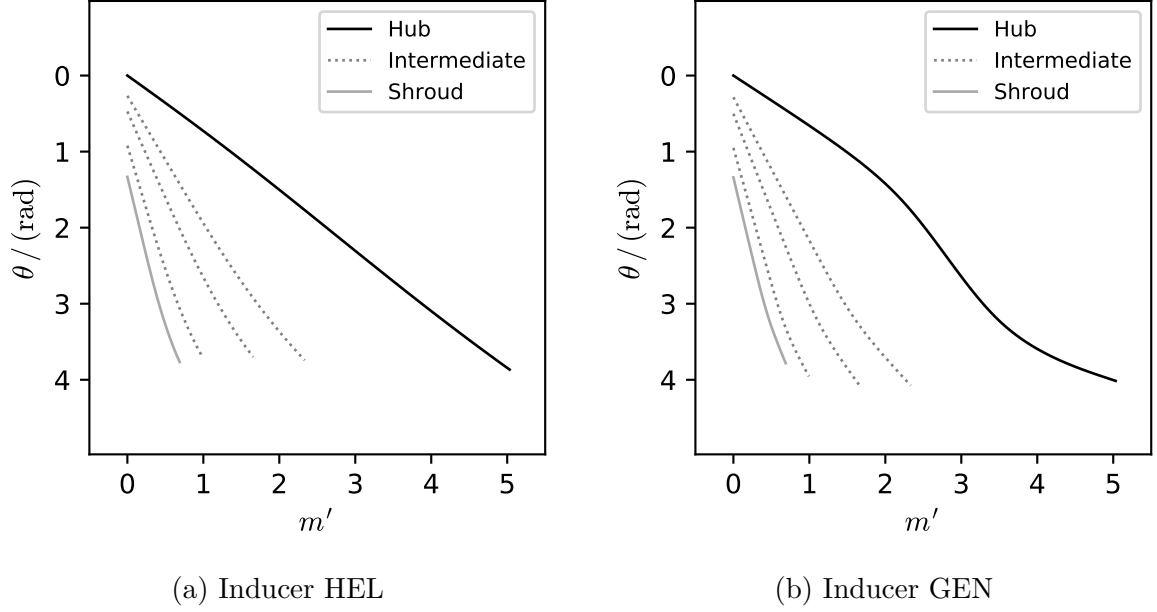
Figure 4.6: Wrap angle distribution along blade sections

angle distributions on hub and shroud as depicted in Figures 4.7a and 4.7b points this out even more. The distinctive difference between the two blades is that in the case of the general blade the angle distribution blends smoothly and with zero slope (tangential to the horizontal direction) into the leading and trailing edge angle. This is achieved by setting the control point parameters introduced in Equations 3.30 - 3.32 as follows:

$$m'^{*}_{(2)} = 25\,\% \tag{4.7a}$$

$$m'^{**}_{(3)} = 33\,\% \tag{4.7b}$$

$$m'^{**}_{(4)} = 66\,\% \tag{4.7c}$$

$$m'^{*}_{(5)} = 90\,\% \tag{4.7d}$$

For the helical blade a constant angle segment of blade angle distribution is only realized where the meridional sections are cylindrical (with constant radius). This is approximately true at the outer sections (see Figures 4.3b and 4.5a). Due to the parabolic angle distribution defined on the reference radius the trailing edge angle is generally reached with significant, nonzero slope.

A backward swept leading edge is designed for both cases by application of Equation 3.48 and by adding a sweep angle of

$$\Delta\theta'_{1s} = 45°. \tag{4.8}$$

(a) Hub section

(b) Shroud section
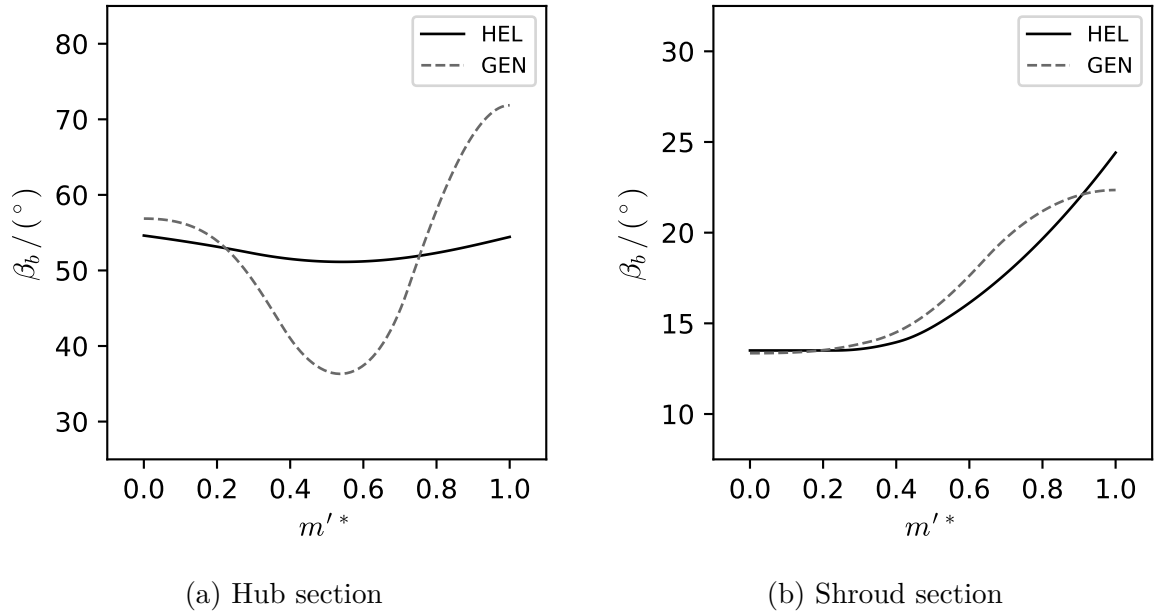
Figure 4.7: Comparison of blade angle distribution along blade sections

As a result, a backward sweep angle of approximately 76° is obtained for both inducers (see Table 4.3). The final leading edge shapes are depicted in Figure 4.8a. Clearly, very similar leading edge shapes are obtained for both test cases. At the trailing edge, as can be seen from the rear view displayed in Figure 4.8b, bigger differences between the two designs exist. This is due to the distinct wrap angle distributions shown in Figures 4.6a and 4.6b.

(a) Front view

(b) Rear view
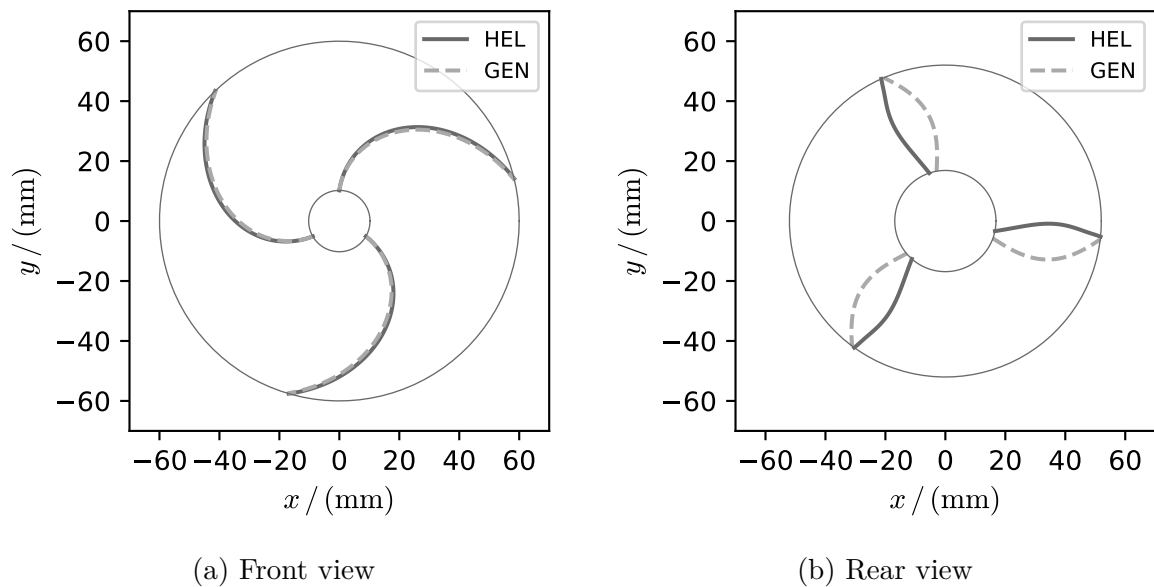
Figure 4.8: Leading and trailing edge shape
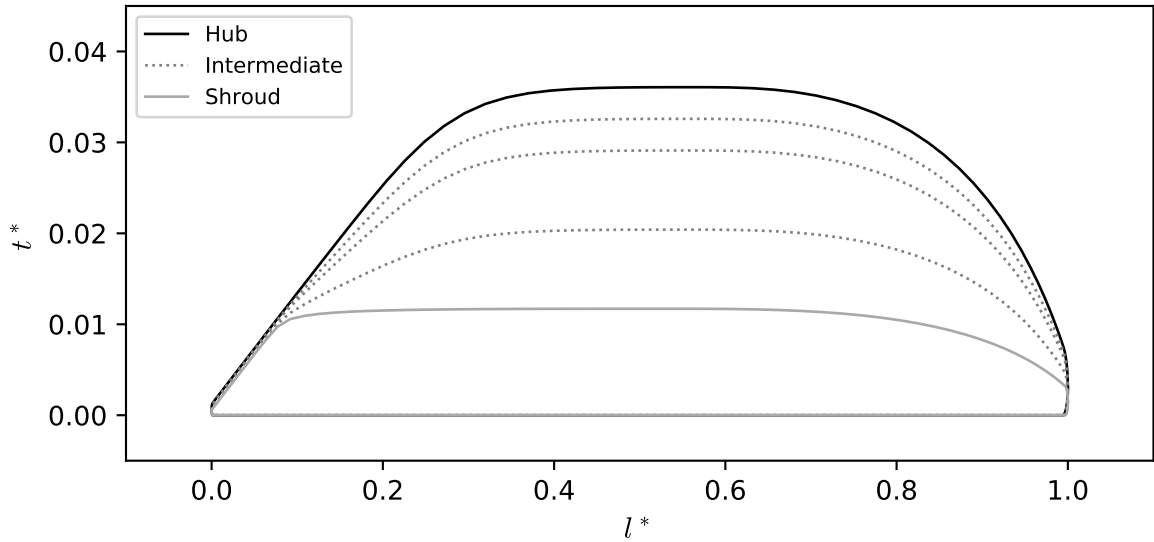
Figure 4.9: Thickness distributions

Blade thickness is specified equally for both inducer designs. A maximum thickness of 3 mm at the hub and 2 mm at the shroud is prescribed. The suction side leading edge sharpening was performed with a wedge angle of 7° and a wedge length of 5 % of the three-dimensional camber curve length. By default this sharpening is applied uniformly from hub to shroud in order to obtain a smooth blade surface. The ellipse ratio is set to a value of $a/b = 2$ at leading and trailing edge. Since the blade length is similar for both
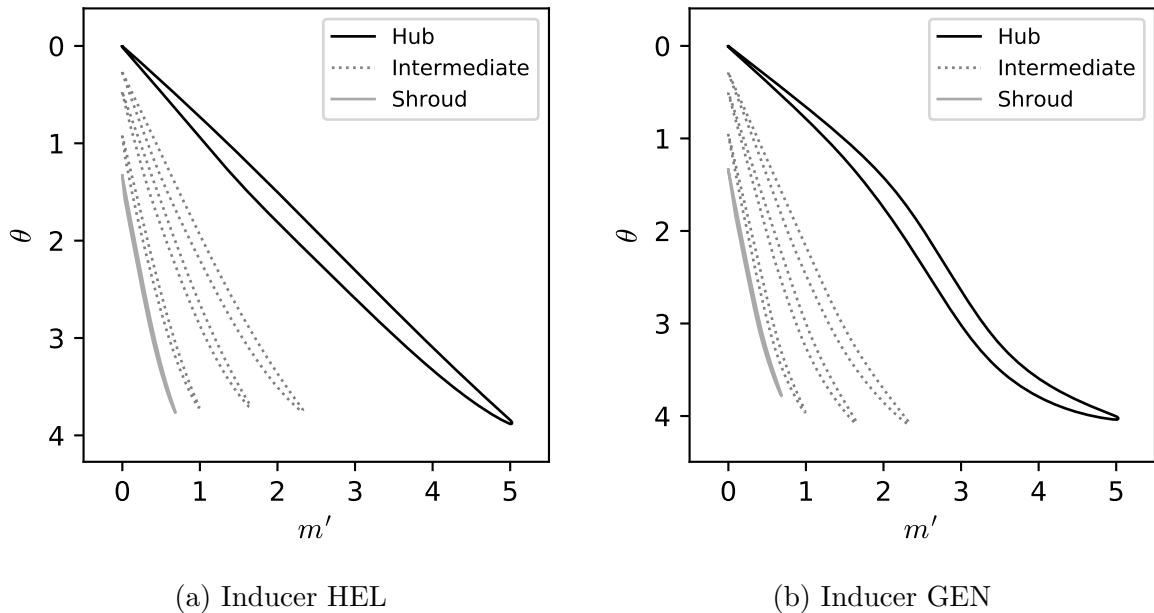
(a) Inducer HEL

(b) Inducer GEN

Figure 4.10: Blade profiles in cascade view

inducers, due to nearly equal values of solidity, the normalized thickness distributions are almost identical. Hence, the thickness distribution shown in Figure 4.9 qualitatively applies to both inducer variants discussed in this section.

The final blade profiles are depicted in the conformal cascade plane in Figures 4.10a and 4.10b for inducers HEL and GEN, respectively. Again, only three intermediate sections between hub and shroud are displayed. However, all fifteen blade sections including hub and shroud sections are used to construct the final blade surface. The plots of the profiles clearly show that despite similar total wrap angles at the shroud and hub sections very different blade shapes are created especially at the inner sections. While the shroud sections are almost identical, the trailing edge shapes due to the different wrap angle distributions at the intermediate sections differ significantly. The most obvious difference, however, is found in the s-shaped profile at the hub section, which is a direct result of the around 17.5° higher trailing edge blade angle of inducer GEN.

4.3 Verification and Validation of the SMA

4.3.1 Cylindrical Meridional Section

As a test case to verify the implementation of the SMA the most simple cylindrically shaped meridional section depicted in Figure 4.11a is considered. For this geometry the radial locations r_k of K streamlines can be expressed analytically by basic application of the continuity equation as done by Li [51]. According to the continuity equation the

(a) Description of geometry
(b) SMA vs. analytical result
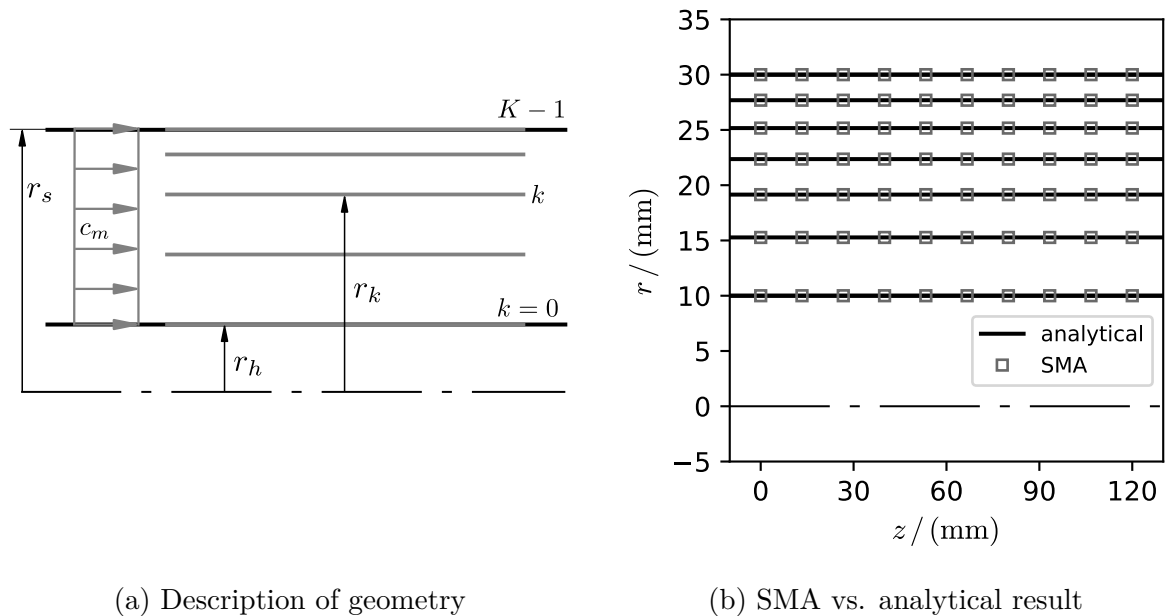
Figure 4.11: Verification of the SMA

volume flow rate Q is related to the mean axial velocity by

$$Q = c_m \pi \left(r_{K-1}^2 - r_0^2 \right),\tag{4.9}$$

where index $k = 0$ corresponds to the hub radius r_h and $k = K - 1$ to the shroud radius r_s. If the mean axial velocity c_m is assumed to be constant, the same relation can be formulated for the flow rate Q_k between two adjacent streamlines:

$$Q_k = c_m \pi \left(r_{k+1}^2 - r_k^2 \right)\tag{4.10}$$

Supposing equal flow rates between each pair of adjacent streamlines, the flow rate Q_k is related to the total flow rate by:

$$Q_k = \frac{Q}{K-1}\tag{4.11}$$

Combination of the equations above leads to the following recursion formula for the radial streamline locations:

$$r_{k+1} = \sqrt{\frac{r_{K-1}^2 - r_0^2}{K-1} + r_k^2}, \quad k = 0, \dots, K-1\tag{4.12}$$

To compare this result with the streamlines computed by the SMA an arbitrary cylindrical meridional shape is considered and the coordinates of seven streamlines ($K = 7$) are computed. A grid with $n_i \times n_j = 150 \times 30$ nodes is used and the convergence tolerance is set to 1×10^{-6}. The dimensions of the meridional can be extracted from Figure 4.11a. Along each streamline computed with the SMA 10 points are evaluated equidistantly. As can be seen from Figure 4.11b, the implemented method reproduces the analytical result very well. Since this case is the most simple one, the more complex meridional geometry of the inducer test cases presented earlier is investigated in the next section.

4.3.2 Inducer Test Cases

An extended version of the original meridional section of the experimental pump unit is used to validate the simple meridional flow analysis developed to generate streamlines and the corresponding velocity distributions. Since the meridional flow analysis is limited to inviscid, free-vortex flow, validation is performed against the commercial CFD solver Fluent (Version 18.2), which provides the possibility to model inviscid, axisymmetric flow. The numerical setup of the case in the SMA and Fluent is described shortly in what follows. In a first step grid dependency of the solution is investigated separately for both methods. Following this, qualitative comparisons of the streamline distributions

and the velocity fields as well as a quantitative assessment of the predicted velocities along selected evaluation lines are presented and a discussion of the results is provided.

Numerical Setup - SMA

Grid influence on the solution is studied by application of the Grid Convergence Index (GCI) methodology [11, 21], which is based on generalized Richardson Extrapolation. To estimate the uncertainty attributed to discretization, three successively refined grids are used with the grid refinement factor defined as

$$r_{k+1,k} = \left(\frac{n_k}{n_{k+1}} \right)^{1/2}, \tag{4.13}$$

where n_k is the number of cells used at grid size index k. Table 4.4 lists the grid properties used for the study of grid convergence. Refinement is performed by doubling the number of nodes in both grid directions. As a result, refinement factors of approximately 2 are obtained. The quantity ϕ_k denotes the variable of interest computed on the grid with

Table 4.4: Grid sizes used in the grid convergence study of the SMA

Grid Size Index	$N_i \times N_j$	No. of Nodes	No. of Cells n_k	Refinement Factor r
1	300×60	18000	17641	$r_{21} = 2.02$
2	150×30	4500	4321	$r_{32} = 2.04$
3	75×15	1125	1036	$-$

index k. With the differences between the solutions computed on the different grids denoted by $\varepsilon_{21} = \phi_1 - \phi_2$ and $\varepsilon_{32} = \phi_2 - \phi_3$, respectively, the apparent order p is computed with the formulas given by Celik et al. [21]:

$$p = \frac{1}{\ln(r_{21})} \left| \ln \left(|\varepsilon_{32}/\varepsilon_{21}| \right) + q(p) \right| \tag{4.14}$$

$$q(p) = \ln \left(\frac{r_{21}^p - s}{r_{32}^p - s} \right) \tag{4.15}$$

$$s = 1 \cdot \text{sgn} \left(\varepsilon_{32}/\varepsilon_{21} \right) \tag{4.16}$$

A fixed point iteration method with the initial guess

$$p^{(0)} = 1/\ln(r_{21}) \left| \ln \left(|\varepsilon_{32}/\varepsilon_{21}| \right) \right| \tag{4.17}$$

is used to solve Equation 4.14 for p. Extrapolated values of the solution variable are then computed as follows:

$$\phi_{\text{ext}}^{21} = \left(r_{21}^p \phi_1 - \phi_2\right) / \left(r_{21}^p - 1\right) \tag{4.18}$$

According to the procedure described by Celik et al. [21] the approximate relative error e_a, the estimated extrapolated error e_{ext}, and the grid convergence index GCI are calculated and reported:

$$e_a^{21} = \left|\frac{\phi_1 - \phi_2}{\phi_1}\right| \tag{4.19}$$

$$e_{\text{ext}}^{21} = \left|\frac{\phi_{\text{ext}}^{21} - \phi_1}{\phi_{\text{ext}}^{21}}\right| \tag{4.20}$$

$$\text{GCI}^{21} = \frac{F_s \cdot e_a^{21}}{r_{21}^p - 1} \tag{4.21}$$

A factor of safety $F_s = 1.25$ is chosen as recommended for three-grid studies [11]. By replacing indices 2 and 1 with 3 and 2 in above relations the extrapolated value and the error estimates for grid size index 2 can be obtained as well. The GCI method is
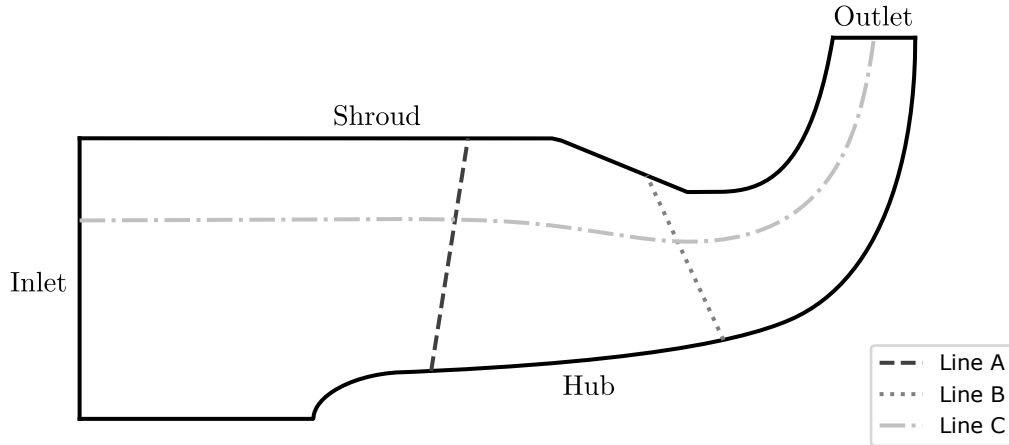
Figure 4.12: Test case setup and evaluation lines

applied to the stream function Ψ, which is the solution variable directly obtained from the implemented numerical scheme of the SMA, and the meridional velocity c_m. Both variables are evaluated and averaged along three lines in the meridional sections. These lines are displayed in Figure 4.12 and are denoted with Line A, Line B and Line C. Line A represents the inducer leading edge curve, Line B the trailing edge curve and Line C the middle streamline extracted from the SMA solution on the finest grid (grid

size index 1). Before the results of the GCI method are presented, the iteration error is investigated by looking at the convergence of the scheme. The convergence behavior of the different grids measured by the tolerance level $(\Delta\Psi)_{\mathrm{max,rel}}$ as defined in Equation A.29 is depicted in Figure 4.13a. As expected, convergence to machine accuracy is achieved with less iterations on the smaller grids. In practice this level of convergence is not required, such that substantially less iterations are needed. This is demonstrated by evaluation of the mean values of meridional velocity along Line C at solution tolerance levels ranging from 10^{-4} to the lowest value achievable, which is approximately 10^{-15}. The trend of the mean value of meridional velocity along Line C is depicted in Figure

(a) Convergence
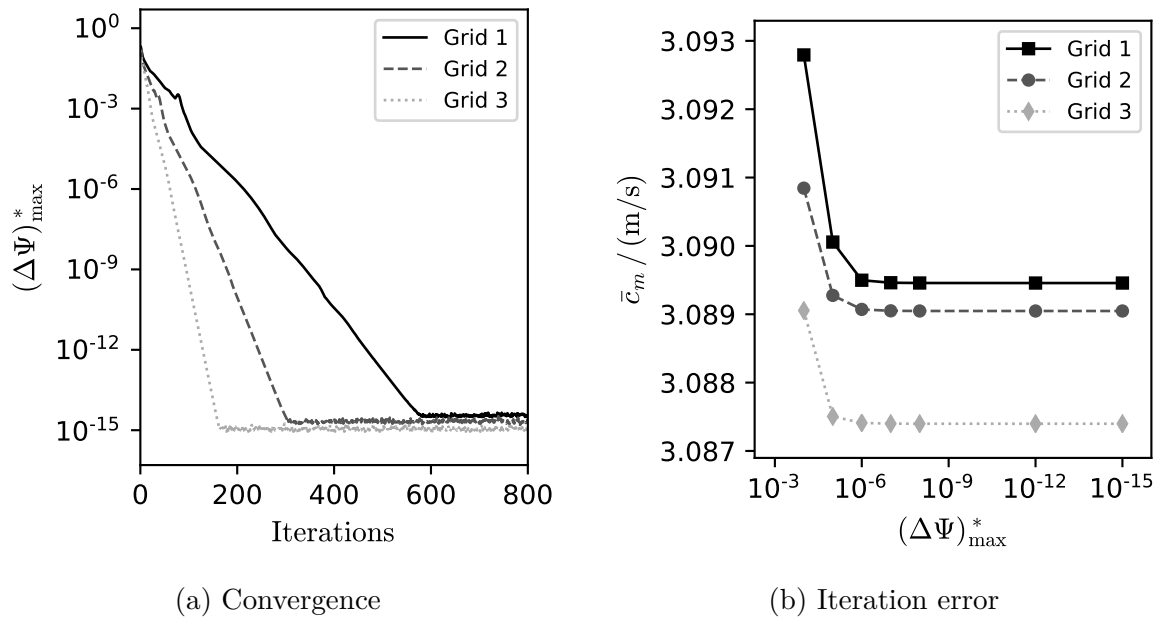
(b) Iteration error

Figure 4.13: Convergence on different grids

4.13b. This result clearly indicates that for all grids under consideration a tolerance below 10^{-5} to 10^{-6} is sufficient to reduce the iteration error to an acceptable level. Limiting the tolerance to a value of this range has the advantage that the computation time needed by the solution procedure is kept low, while maintaining high accuracy. Looking at the absolute values of velocity on the ordinate of Figure 4.13b it can already be noticed that the actual value of the target quantity only depends slightly on the grid resolution. As already mentioned this is further investigated by means of the GCI method introduced above. Table 4.5 reports the most important quantities obtained with the help of this method for the mean values of stream function and meridional velocity along the evaluation lines A, B and C. The apparent order p of the scheme reflects the expected order of the implementation, which should theoretically be around 2, very well, especially if it is considered, that interpolation is involved in the evaluation

Table 4.5: Results of the uncertainty analysis with the GCI method

		Ψ^A	c_m^A	Ψ^B	c_m^B	Ψ^C	c_m^C
p		1.67	2.87	1.88	1.96	2.08	1.89
e_a^{21}	(%)	0.001 42	0.002 95	0.029 46	0.058 15	0.007 02	0.013 82
e_a^{32}	(%)	0.004 72	0.022 99	0.113 33	0.238 24	0.031 30	0.053 76
e_{ext}^{21}	(%)	0.000 63	0.000 45	0.010 74	0.019 50	0.002 11	0.004 96
e_{ext}^{32}	(%)	0.002 05	0.003 41	0.040 19	0.077 64	0.009 13	0.018 78
$\mathbf{GCI^{21}}$	(%)	0.000 79	0.000 57	0.013 43	0.024 38	0.002 63	0.006 20
$\mathbf{GCI^{32}}$	(%)	0.002 57	0.004 26	0.050 26	0.097 13	0.011 42	0.023 48

of the variables along the lines. Approximate errors and extrapolated errors are at a very low level, even for the mid-size grid with index 2. The same is true for the actual values of GCI. For the fine grid (index 1) the GCI^{21} values calculated for the different variables are below 0.03 %, for the coarser grid (index 2) the values of GCI^{32} are already below 0.1 %. This indicates that grid size 2 is already sufficient to obtain appropriate results. To illustrate the findings of the GCI method, a slightly modified version of the

(a) Stream function

(b) Meridional velocity
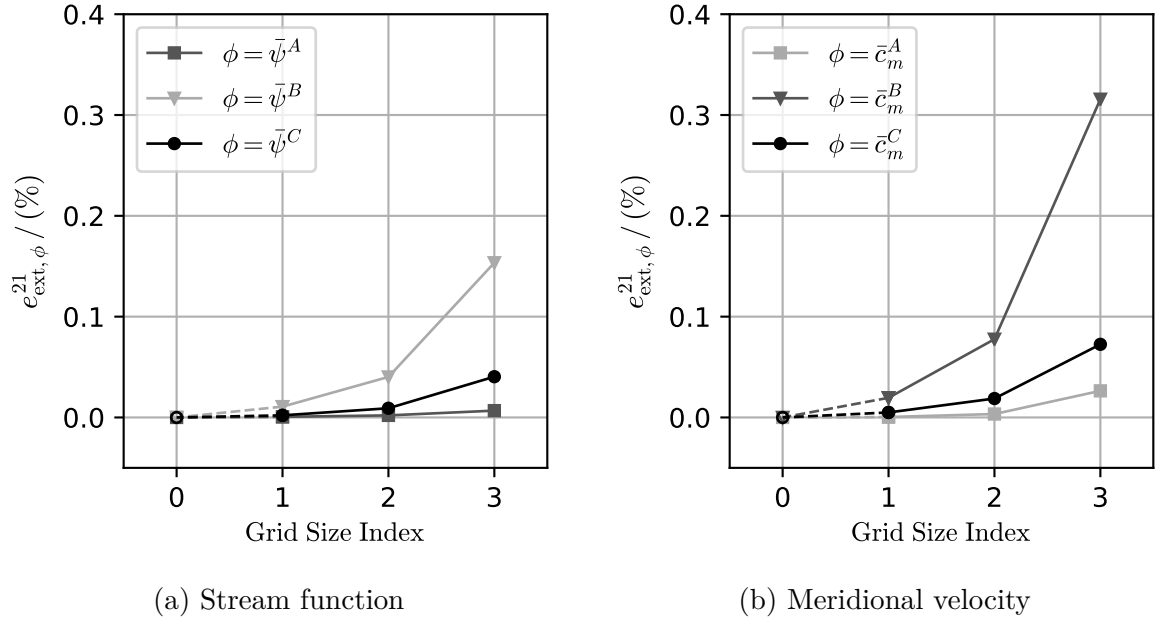
Figure 4.14: Influence of grid size on solution variables

estimated extrapolated error is used:

$$e_{\text{ext},\phi}^{21} = \left(1 - \left|\frac{\phi}{\phi_{\text{ext}}^{21}}\right|\right) \tag{4.22}$$

This error basically represents the normalized difference between the solution variable ϕ obtained on any of the grids and the corresponding extrapolated value. Figures 4.14a and 4.14b depict the trend of this error measure with the decrease in grid spacing. The dashed lines indicate the extrapolation towards zero grid spacing, which is assigned to a grid spacing index of 0. Although this assignment is arbitrary, the curve trends can help to estimate the influence of the grid refinement on the approximate error. As already indicated, low values of error are already obtained for grid size index 2. This is the reason why the results of this grid are used in the comparison with the CFD simulations.

Numerical Setup - CFD

To compare the results of SMA and CFD, identical boundary curves are used for the SMA and the Fluent simulation. In the latter case, the meridional section is discretized with an unstructured, quadrilateral dominant mesh, which is automatically generated by the ANSYS Workbench mesher. Analogously to the the previous section the GCI method is applied to gauge the grid influence on the solution variables. Three different grid sizes are used to evaluate the uncertainty attributed to discretization. The node

Table 4.6: Grid sizes used in the grid convergence study of the 2D CFD setup

Grid Size Index	No. of Nodes	No. of Cells n_k	Refinement Factor r
1	35117	34664	$r_{21} = 2.00$
2	8896	8665	$r_{32} = 1.98$
3	2324	2206	$-$

and cell numbers as well as the corresponding refinement factors are listed in Table 4.6. Grid refinement factors close to 2 are realized for both levels of refinement. Figure 4.15 displays the coarsest mesh (index 3). Fluent's two-dimensional coupled solver with second order discretization of pressure and momentum is used to compute the inviscid axisymmetric flow. The boundary conditions are defined as depicted in Figure 4.15.

Since the problem is considered axisymmetric, the segment of the hub line at zero radius is defined as axis boundary. The remaining part of the hub curve and the shroud curve are set as walls. At the inlet a uniform velocity according to the mass flow rate is prescribed. The outlet is defined as outflow boundary [8]. In order to provide accurate reference solutions and ensure little influence of iteration error, computations are performed until very low values of residuals (below 10^{-10}) are obtained for all of the grids.

The same evaluation lines as depicted in Figure 4.12 are imported into the post-processor and the solution variables are extracted from the CFD data on the grid. Again, stream
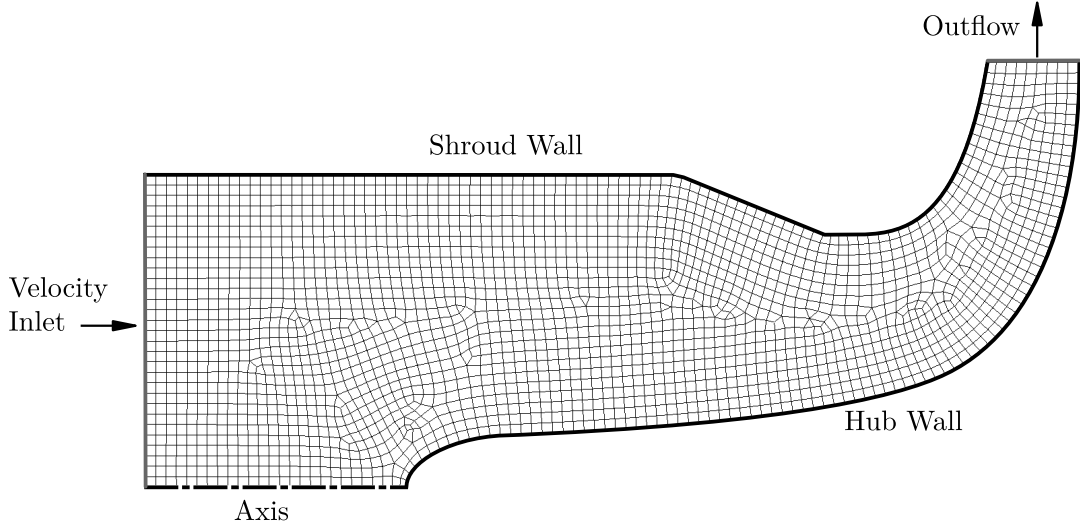
Figure 4.15: 2D Grid (Grid 1) and boundary conditions used for the CFD simulation

function and meridional velocity are averaged along these lines and the GCI method is applied. The results are summarized in Table 4.7. All variables under investigation reveal an apparent order above 1, the only exception being the mean meridional velocity $\bar{c}_m^A$ along Line A. However, the computed apparent order is used to estimate the uncertainty as recommended by Celik et al. [21]. As can be seen from the tabulated data, approximate relative and estimated extrapolated errors are below 1 % even for the coarse grid. Grid convergence indices for the fine and the medium grids are below 0.4 % and 0.75 %, respectively.

Analogously to the previous section, the estimated extrapolated error according to Equation 4.22 is computed and the results are plotted against the grid size index in Figures 4.16a and 4.16b. The trend towards the extrapolated values are again indicated by dashed lines. Similar degressive progressions with increasing number of cells, can be observed for both parameters. Contrary to the results of the SMA the average values along Line C exhibit the biggest dependency on the grid. For the solutions on the finest

Table 4.7: Results of the GCI method for the CFD case

		$\bar{\Psi}^A$	$\bar{c}_m^A$	$\bar{\Psi}^B$	$\bar{c}_m^B$	$\bar{\Psi}^C$	$\bar{c}_m^C$
p		1.80	0.12	3.47	4.99	1.13	1.24
e_a^{21}	(%)	0.035 82	0.025 98	0.021 45	0.002 56	0.237 96	0.341 37
e_a^{32}	(%)	0.121 52	0.027 92	0.230 34	0.077 59	0.510 70	0.789 13
e_{ext}^{21}	(%)	0.014 49	0.289 74	0.002 12	0.000 08	0.199 89	0.250 55
e_{ext}^{32}	(%)	0.050 31	0.315 64	0.023 57	0.002 65	0.438 33	0.592 77
$\mathbf{GCI}^{21}$	(%)	0.018 12	0.363 23	0.002 65	0.000 10	0.249 36	0.312 41
$\mathbf{GCI}^{32}$	(%)	0.062 92	0.395 80	0.029 46	0.003 31	0.545 52	0.736 60

(a) Stream function

(b) Meridional velocity
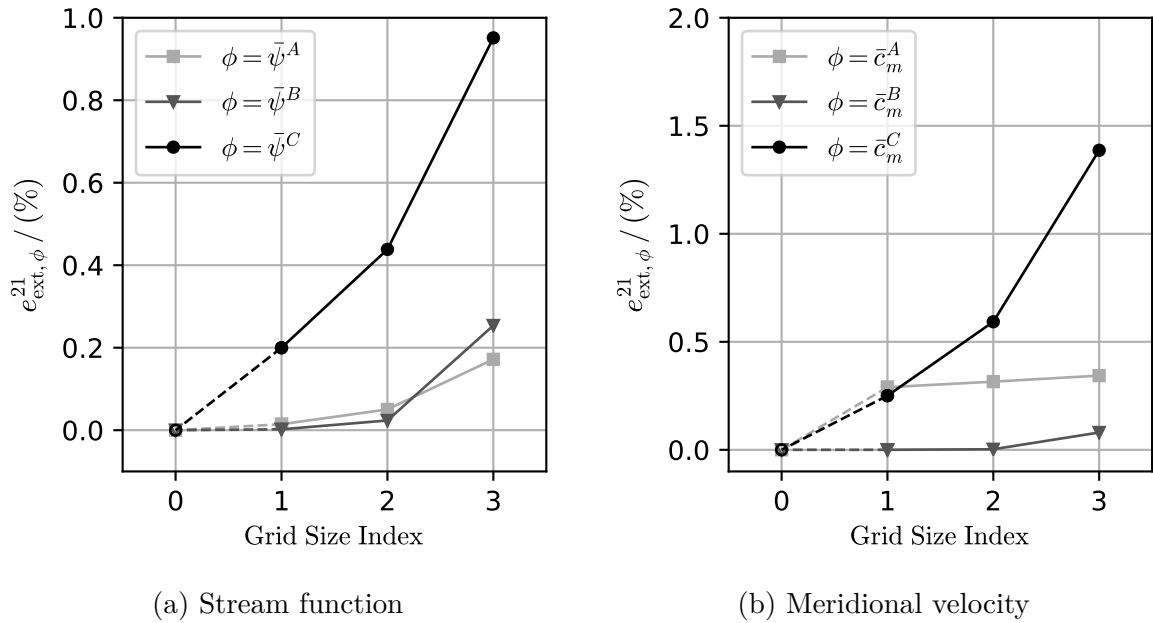
Figure 4.16: Influence of grid size on solution variables (CFD)

grid (index 1) the estimated extrapolated errors are below $0.5\,\%$ for all the solution variables. This is why the fine grid solutions are used as reference for the validation presented in the next section.

Results

The meridional flow analysis has two major goals. First, smooth meridional streamlines are needed as a foundation of blade section design. Second, an estimate of meridional flow velocity is needed as input for the singularity method used in the head prediction method. Thus, the method should produce reasonable estimates of the stream function levels as well as an approximation of the velocity field. The first point is validated by comparing the isolines of stream function of the SMA and the CFD solution. Three intermediate levels of stream function are extracted and plotted together in Figure 4.17. As can be seen from this figure, almost indistinguishable streamline progressions are obtained. Only small differences of streamline slope can be observed when closely examining the region at the exit boundary. Since the exit boundary is usually placed at some distant downstream of the region of interest, this can be considered a minor issue. The second point, that is the estimation of meridional velocity, is assessed based on the progressions along the evaluation lines. Figures 4.18a, 4.18b and 4.18c depict these values along the normalized meridional length coordinate m^*, which is computed independently for each of the three lines. In case of Line A and Line B this coordinate runs from hub to shroud. Since Line C represents a streamline, the meridional curve
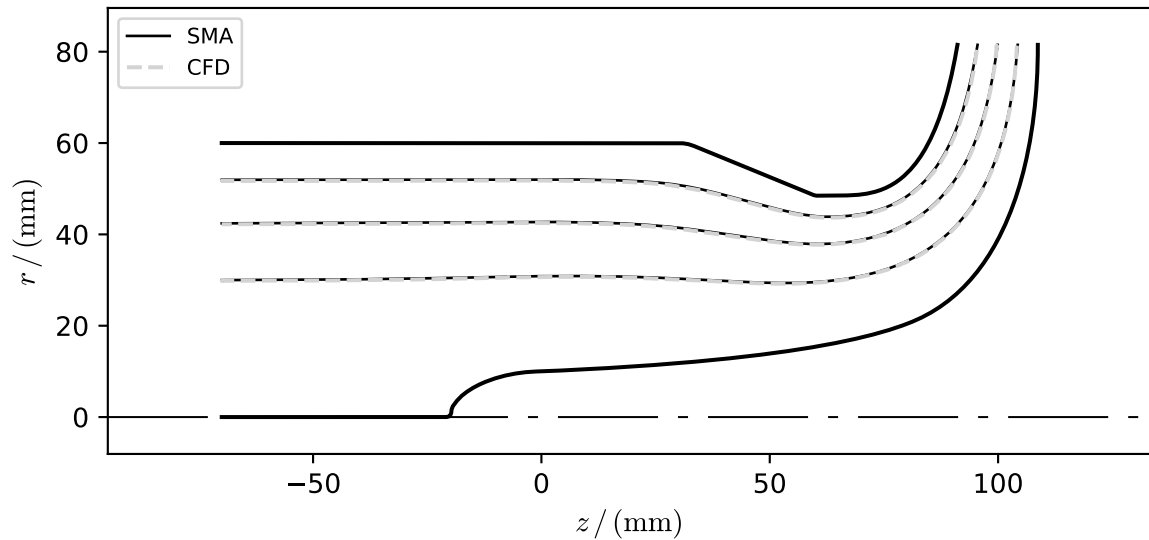
Figure 4.17: Isolines of stream function - SMA vs. CFD

length is measured from the inlet to the outlet. For all three lines very good agreement of the velocity profiles is observable. Discrepancies mainly exist close to the boundaries at hub and shroud. Especially for Line A, which represents the leading edge location, the influence of the upstream stagnation point at the hub is visible. It can be assumed that this is caused by the special treatment of the nodes at zero radius in the velocity computation as described in Section 2.4.3. In fact, in case of the SMA a very fine grid would be necessary to resolve the smooth progression of velocity at the stagnation point at zero radius, as it occurs at the inducer nose. However, the overall shape of the curve matches the result of the CFD simulation reasonably well and the quantitative prediction of the velocity level is satisfying. This is even more true for the other two evaluation lines. Looking at Line C (Figure 4.18c) small discrepancies are only visible towards the outlet boundary. In the region between the dotted lines, which indicate the leading and trailing edge points found at the intersections of Line A and B with Line C, almost perfectly matching velocity distributions are obtained. This is of particular interest because the velocity data on this range of the streamline is used as input for the SHP.

To gain a more complete and illustrative impression of the computed velocity fields, Figures 4.19a and 4.19b show contour plots of the meridional velocity distribution. The same number of contour levels and the same legend limits are used to produce these figures. Notable differences mainly exist at the hub stagnation point, as already discussed above, and towards the exit boundary. These discrepancies can be expected because the free-vortex assumption is not made in the commercial code and a different

(a) Line A

(b) Line B

(c) Line C
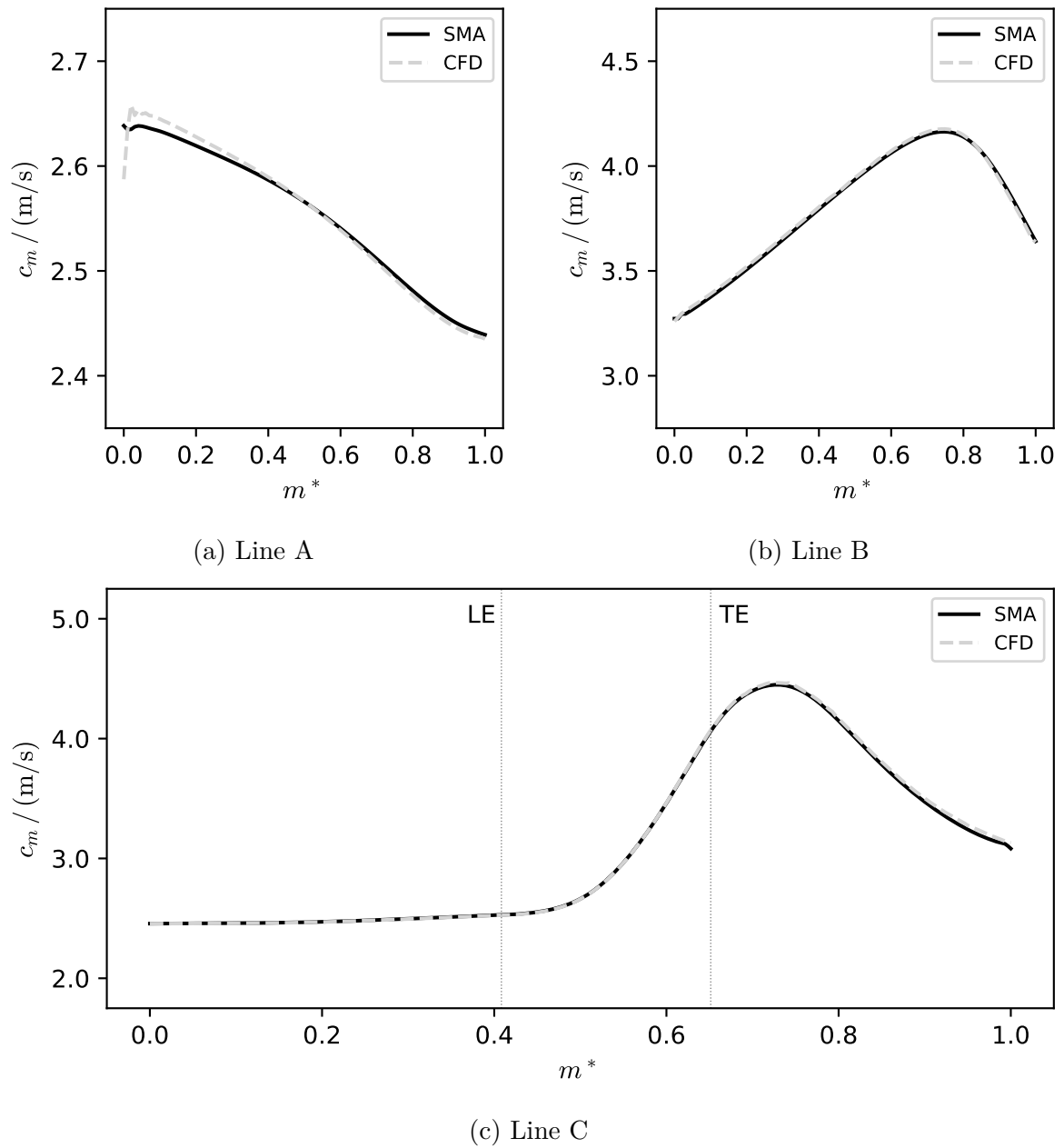
Figure 4.18: Meridional velocity along evaluation lines - SMA vs. CFD

set of equations with different boundary conditions is solved (see Section 2.6.1). Despite this fact, very good agreement of the contour shapes and levels generated by the two different solution methods can be observed.

(a) SMA

(b) CFD
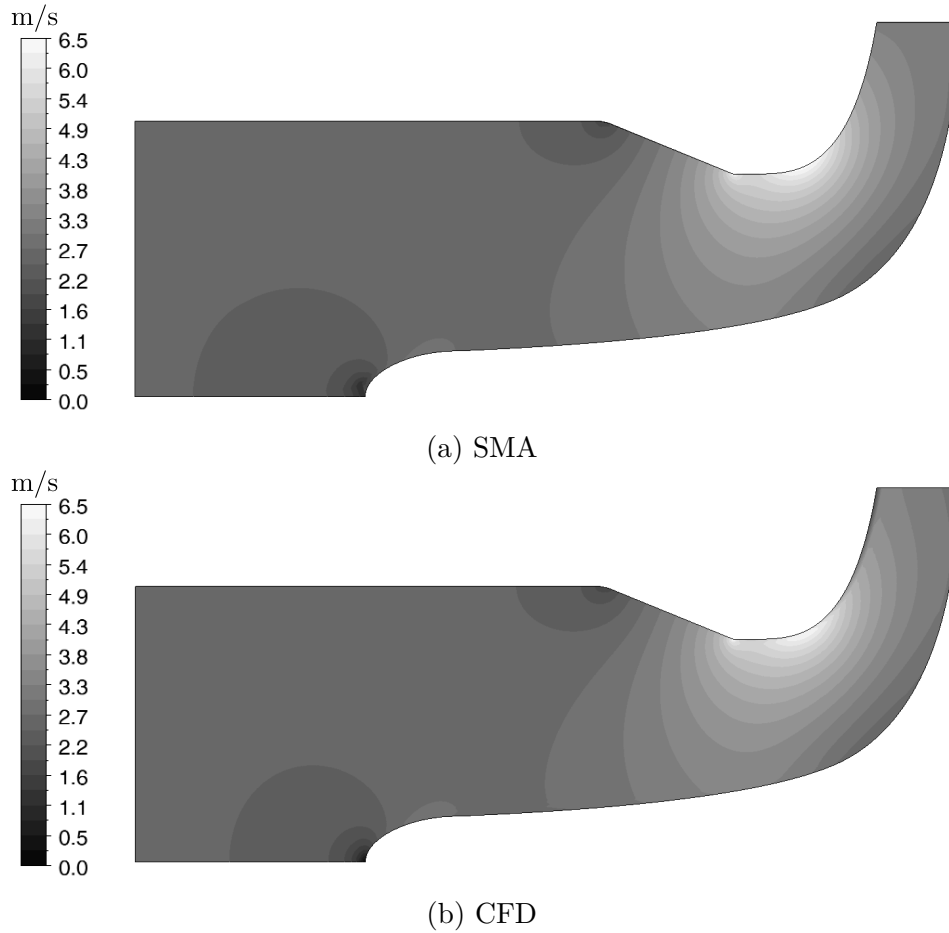
Figure 4.19: Contours of meridional velocity - SMA vs. CFD

4.4 Verification and Validation of the SHP

4.4.1 Cascade of Flat Plates

Implementation of the singularity method described in Section 2.5.1 is verified with the help of the analytical solution of a non-staggered cascade of flat plates with infinitesimal thickness. The analytical solution is given by Scholz [64] and reads

$$\frac{\gamma(x)}{w_\infty} = \frac{2\sin\alpha_\infty}{\cosh\left(\frac{\pi}{2}\frac{l}{t}\right)} \sqrt{\frac{\sinh\left(\pi\frac{l}{t} - \pi\frac{x}{t}\right)}{\sinh\left(\pi\frac{x}{t}\right)}}, \tag{4.23}$$

where nomenclature is adapted so that x is the coordinate along the plate starting from the leading edge, l the total (chord) length, t the spacing of the cascade and α_∞ the angle of attack. The equation above is applied to the cascade configuration depicted in

Figure 4.20a by setting $r = 1\,\mathrm{m}$. As a consequence, the following relations are obtained:

$$m' = \frac{x}{r} \tag{4.24}$$

$$l' = \frac{l}{r} \tag{4.25}$$

$$t' = \frac{t}{r} = \frac{2\pi}{Z} \tag{4.26}$$

With $\frac{l}{t} = \frac{l'}{t'} = \frac{Zl}{2\pi}$ and $C_1 = r\,w_\infty$, Equation 4.23 can be written as:

$$\frac{\gamma(m')}{C_1} = \frac{2\sin\alpha_\infty}{\cosh\left(\frac{Z\,l'}{4}\right)} \sqrt{\frac{\sinh\left(\frac{Z\,l'}{2} - \frac{Z}{2}m'\right)}{\sinh\left(\frac{Z}{2}m'\right)}} \tag{4.27}$$
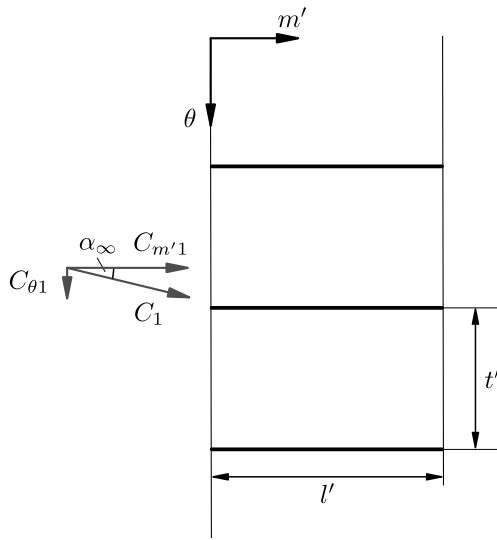
(a) Cascade geometry
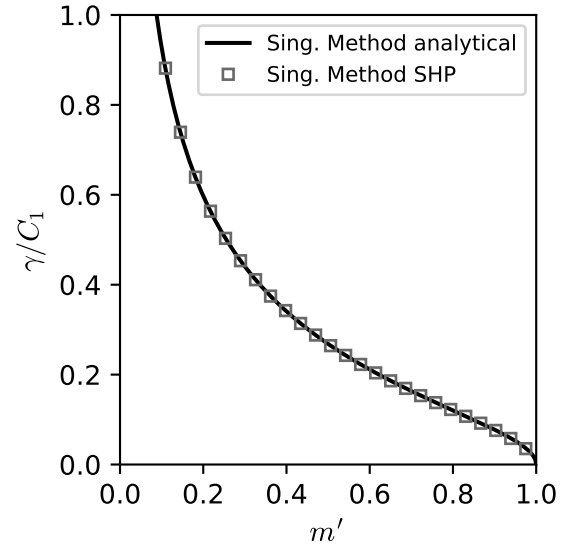
(b) Singularity method vs. analytical result

Figure 4.20: Verification of the singularity method of the SHP

Vorticity density distribution γ is computed for $C_1 = 1\,\mathrm{m^2/s}$ and $l' = 1$ using $N_i = 500$ points along the plates. Displaying only a reduced number of points, the result is shown together with the corresponding analytical solution in Figure 4.20b. As can be seen, excellent agreement between the result of the implemented singularity method and the analytical solution is achieved. Although effects due to thickness are not included, this proves that implementation at least in the limiting case of zero thickness was successful.

4.4.2 Inducer Test Cases

Numerical Setup - SHP

The result of the SHP, which is used to predict the head of the inducers under consideration, is influenced only by the number of blade sections N_k and the number of points used along the blade camber line N_i (see Figure 2.17b). In all cases an equidistant distribution of nodes is used. Before a comparison with the CFD results is attempted, the influence of these parameters on the predicted head value is investigated. The sensitivity of the solution to these parameters is determined by the relative difference to a reference solution, which is defined as:

$$\Delta \psi_{th}^* = \left| \frac{\psi_{th} - \psi_{th,ref}}{\psi_{th,ref}} \right| \times 100\,\% \tag{4.28}$$

The number of sections used varied between one and fifteen. In the former case only the middle blade section is used, while in the latter all blade sections are used to obtain the mean head generated. Figure 4.21a shows the relative difference of theoretical head
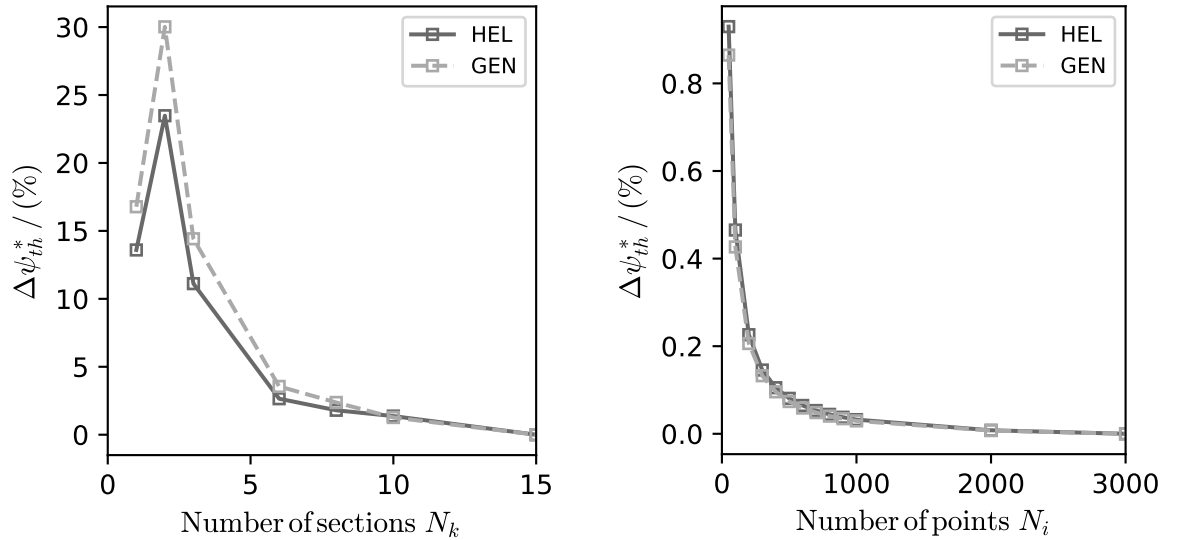
(a) Number of blade sections   (b) Number of nodes along camber curve

Figure 4.21: Investigation of the numerical parameters of the SHP

coefficient with respect to the head coefficient obtained with all the blade sections:

$$\psi_{th,ref} = \psi_{th,N_k=15} \tag{4.29}$$

The trends indicate that at least five sections are required to obtain results within a relative difference of 5 %. However, since the solution of the systems of linear equations

is very fast on a modern workstation, all fifteen sections are used to compute the head curves discussed in the remainder of this thesis. Although the curves depicted in Figure 4.21a behave similar for both test cases, there is very likely a significant influence of the geometry on the result. Considering that the total head is calculated by averaging over all included blade sections it is quite obvious that an adequate number of blade sections is needed to correctly represent the blade geometry. This might be especially true if there are stronger variations of blade angle distribution in spanwise direction (from hub to shroud), as it is the case for inducer GEN. The sensitivity of the solution depending on the number of blade sections included also indicates that the method of averaging the heads of the individual blade sections to compute the total head might be a critical weakness of the current method. To investigate the influence of the number of nodes along the blade sections this number is varied from 50 to 3000. The relative difference of head coefficient in this case is defined with respect to the solution obtained with the highest node number, that is:

$$\psi_{th,ref} = \psi_{th,N_i=3000} \tag{4.30}$$

Looking at the progression of this value as a function of node number as depicted in Figure 4.21b, it can be seen quite clearly that the solution is considerably less sensitive to this parameter. Again, inducer GEN exhibits a stronger sensitivity to the parameter under investigation. This might as well be due to the distinct blade angle progression used for this variant. However, a number of nodes of 500 already yields differences below 0.1% for both geometries under consideration. This is why $N_i = 500$ is used to compute the results presented within this thesis.

Numerical Setup - CFD

In order to judge the head prediction computed by the SHP it is compared with CFD results. The latter are obtained by employing a reduced simulation model that considers only one blade channel of the inducer. Nevertheless, the real three-dimensional blade geometry including the tip gap is represented in these simulations. Since the inducer is modeled without the downstream pump components, the outflow section is modified. This was done by extending the original meridional section radially. A three-dimensional view of the passage model of inducer HEL, is depicted in Figure 4.22. The model consists of three domains, called inflow, inducer and outflow. While the inflow domain is stationary, the inducer and outflow domains are modeled as rotating. To connect the domains and allow for frame and pitch change Frozen Rotor interfaces are used. Rotational periodicity is set up on the periodic faces. All walls are modeled as non-

slip walls and are considered as adiabatic and smooth. The shroud walls are set as stationary. As a consequence, the corresponding boundaries in the rotating domains have to be defined as counter-rotating. The hub walls as well as the inducer blades are defined as rotating. Incompressible and isothermal single phase flow of water at $25\,°\text{C}$ is assumed in all simulation runs. Turbulence is modeled with the SST-Turbulence model and the automatic wall function provided by ANSYS CFX for omega-based turbulence models (see reference [5] for more details) is used. The node spacing at the walls is chosen so that average values of around $y^+ \approx 30$ are obtained in all the domains. At the inlet boundary the total pressure and at the outlet the mass flow is specified. Inlet turbulence level is set by using the Medium Intensity option, which is equal to a specification of a turbulence intensity of $5\,\%$ and $\mu/\mu_t = 10$ [5]. Steady state simulations are performed for different flow rates in order to obtain the head curve for the two inducer variants. The High Resolution option is chosen for Advection Scheme and Turbulence Numerics Settings. A physical timescale equal to $1/\omega$ is set for all simulation runs. Flow coefficient is varied from $140\,\%$ to $50\,\%$ of design flow coefficient. This is equal to a variation of volume flow rate from $140\,\text{m}^3/\text{h}$ to $50\,\text{m}^3/\text{h}$. RMS residuals of mass and momentum below 1×10^{-4} are ensured for all simulated points. However, most of the simulations reach much smaller residuals and almost constant progressions of characteristic values after less than 300 iterations, which is the maximum number of iterations performed for each flow rate. Final evaluation of the characteristic values is performed in the post-processing at evaluation planes upstream and downstream of the inducer (see Figure 4.22). The upstream evaluation plane is moved axially away from the inducer leading edge in order to avoid interference of the head evaluation by possible backflow due to inlet recirculation. Its axial position is chosen identical to the pressure tap location in the experimental setup. Different methods of averaging are applied to the CFD result in order to obtain results that are comparable to the SHP. The actual averaging method used is described together with the presentation of the corresponding results.

Table 4.8: Grid sizes used in the grid convergence study for inducers HEL and GEN

Grid Size Index	No. of Cells n_k		Refinement Factor r	
	HEL	GEN	HEL	GEN
1	960860	919970	$r_{21} = 1.45$	$r_{21} = 1.46$
2	315640	297434	$r_{32} = 1.37$	$r_{22} = 1.35$
3	123220	119778	–	–

Grid influence is studied by means of the GCI methodology already introduced. A three-grid study with the grids listed in Table 4.8 is performed for both inducers under
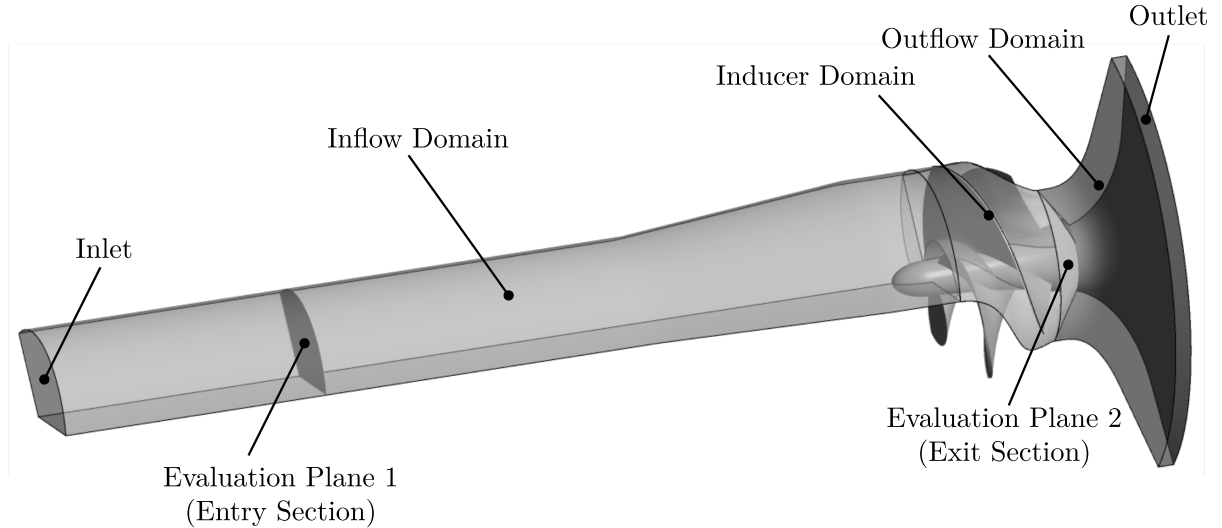
Figure 4.22: Simulation model

consideration. The table also includes the refinement factors, which are above the recommended minimum value of 1.3. While the grids for inflow and outflow domains are created manually with the grid generation software ANSYS ICEM CFD [6], the inducer blade passage domain is discretized with ANSYS TurboGrid [7]. Independent of the grid size index ten cells are used to resolve the tip clearance.

Mass flow averaged values of total pressure evaluated at the inlet and exit sections (see Figure 4.22) are used to compute head coefficient and efficiency at the design flow coefficient ($\varphi/\varphi_d = 1$). The results of the GCI method applied to these variables are summarized in Table 4.9. Although the inducers are similar in dimension and shape

Table 4.9: Results of the GCI method for the 3D-CFD cases

		ψ		η	
		HEL	GEN	HEL	GEN
p		1.02	5.14	3.64	1.38
e_a^{21}	(%)	0.281 73	0.246 21	0.309 64	0.397 54
e_a^{32}	(%)	0.335 70	1.077 24	0.893 76	0.512 02
e_{ext}^{21}	(%)	0.618 04	0.041 58	0.108 05	0.579 76
e_{ext}^{32}	(%)	0.901 51	0.287 90	0.417 36	0.975 00
$\mathbf{GCI^{21}}$	(%)	0.767 81	0.051 95	0.135 21	0.728 93
$\mathbf{GCI^{32}}$	(%)	1.116 82	0.358 84	0.523 88	1.230 75

and the same numerical setup is used for both variants, different trends of the apparent order as well as the uncertainty due to discretization can be observed. While the results

of inducer HEL indicate a higher apparent order and smaller values of uncertainty in efficiency than the results of inducer GEN, it is the other way around for head coefficient. However, the GCI lies below $0.8\,\%$ for the fine grid and below $1.25\,\%$ for the medium grid for both variables under consideration. To illustrate the influence of the grid refinement on the uncertainty in the solution variables, the estimated extrapolated error according to Equation 4.22 is depicted in Figures 4.23a and 4.23b for head coefficient and efficiency, respectively. As can be seen from the figures, the estimated extrapolated error lies below $1\,\%$ for both solution values. Because of this and the advantage of having a substantially reduced computation time the medium grid (grid size index 2) is used for the investigations in this thesis.

(a) Head coefficient

(b) Efficiency
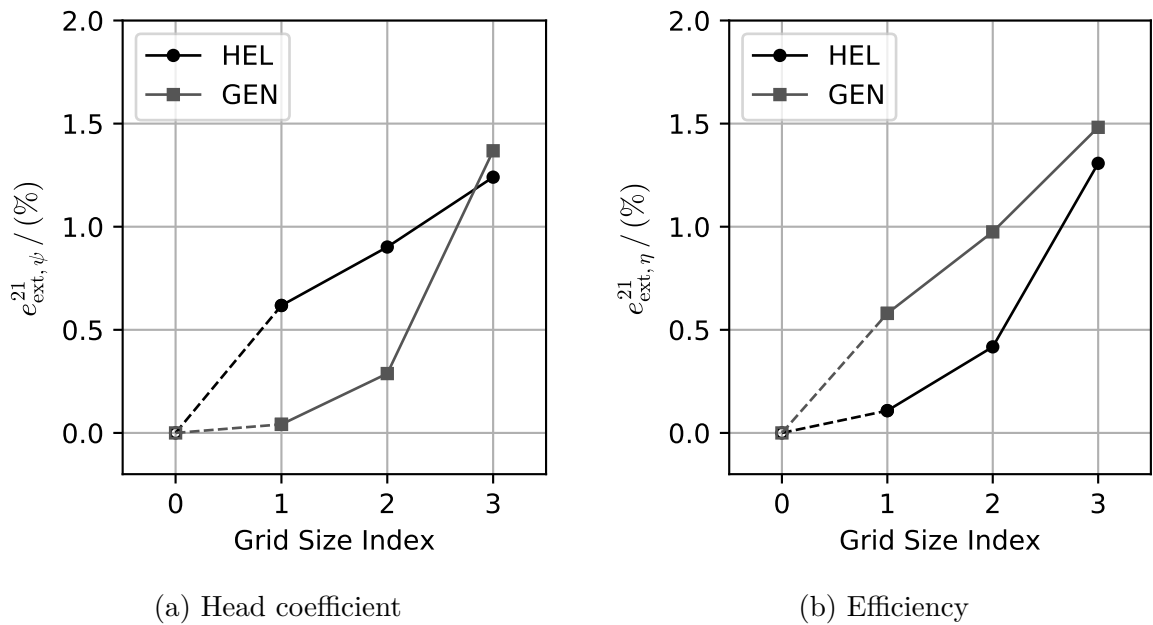
Figure 4.23: Influence of grid size on solution variables (3D-CFD)

Results

Comparisons of total head rise computed with the SHP and CFD are depicted in Figures 4.24a and 4.24b for inducers HEL and GEN, respectively. Besides the total head coefficient (based on total head, see Equation 2.121) also the theoretical head coefficient obtained with the SHP (based on Equation 2.114) is displayed. The head coefficients are plotted against normalized flow coefficient $\varphi^* = \varphi/\varphi_d$, where φ_d is the flow coefficient at the design flow rate. As already mentioned, head coefficient is computed with respect to the outer diameter D_2 of the main pump impeller, although not present in the current study. In case of the CFD results the mass flow weighted average of total pressure in the entry and exit planes is used for the computation of total head coefficient. Evidently,

(a) Inducer HEL
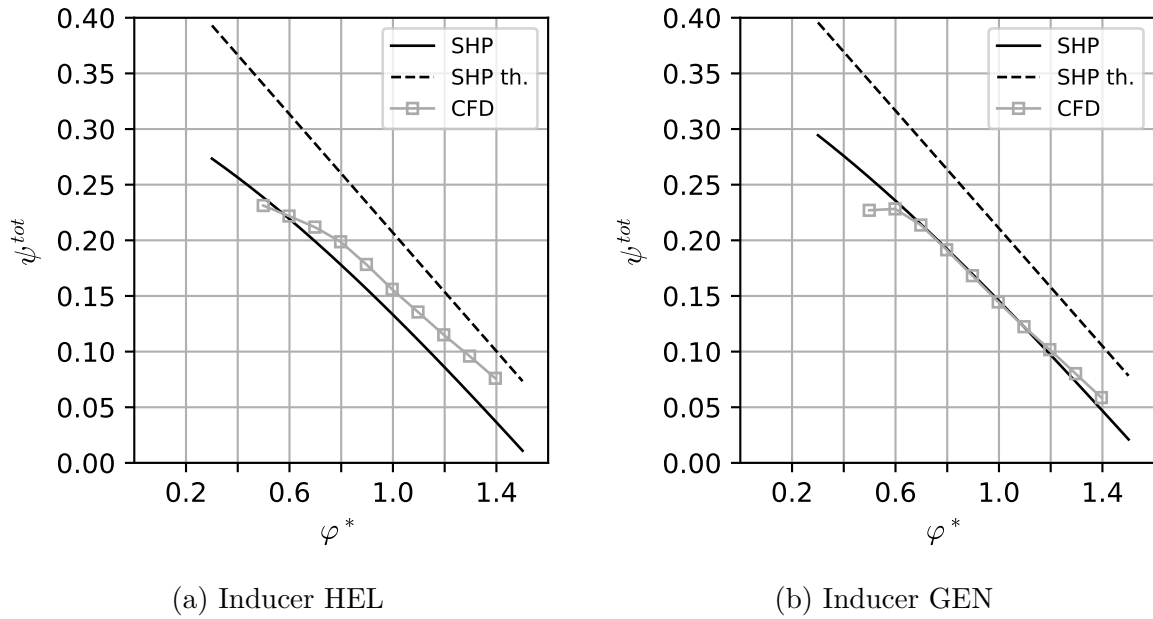
(b) Inducer GEN

Figure 4.24: Head coefficient characteristics (based on total head H^{tot})

the head prediction underestimates the head for Inducer HEL, while for Inducer GEN very good agreement is achieved close to the design flow rate and even at weak part-load and overload. The result of the CFD simulation predicts significantly higher head coefficients for Inducer HEL than for inducer GEN. Comparing the theoretical head curves it can be seen that the difference in the total head estimated by the SHP is mainly caused by the loss model. However, in both cases a good approximation to the head curve slope is provided by the simple model approach.

Since the total head is usually not the quantity that is of the biggest interest to the engineer (because it cannot be measured with a simple pressure tap), the head coefficient based on corrected head according to Equation 2.117 is investigated as well. Different to the total head calculation, the sum of area weighted average of static pressure and of dynamic pressure based on the meridional velocity component in the evaluation planes is used to compute this head from the CFD results. The curves displayed in Figures 4.25a and 4.25b indicate similar trends for both solutions. Again for inducer GEN quite good agreement of the head coefficient close to design flow rate is achieved. In contrast to the CFD results the head of inducer GEN at design conditions is predicted by the SHP to be higher than that produced by Inducer HEL. The simple method as well as the CFD simulation predict an unstable head characteristic around 60 % of design flow rate. A further parameter of interest during design iterations is the discharge flow angle of the inducer. This angle can be computed by evaluating formula 2.110 in case of the SHP. It is assumed that this angle is equal to the vane discharge angle, which is achieved

(a) Inducer HEL

(b) Inducer GEN
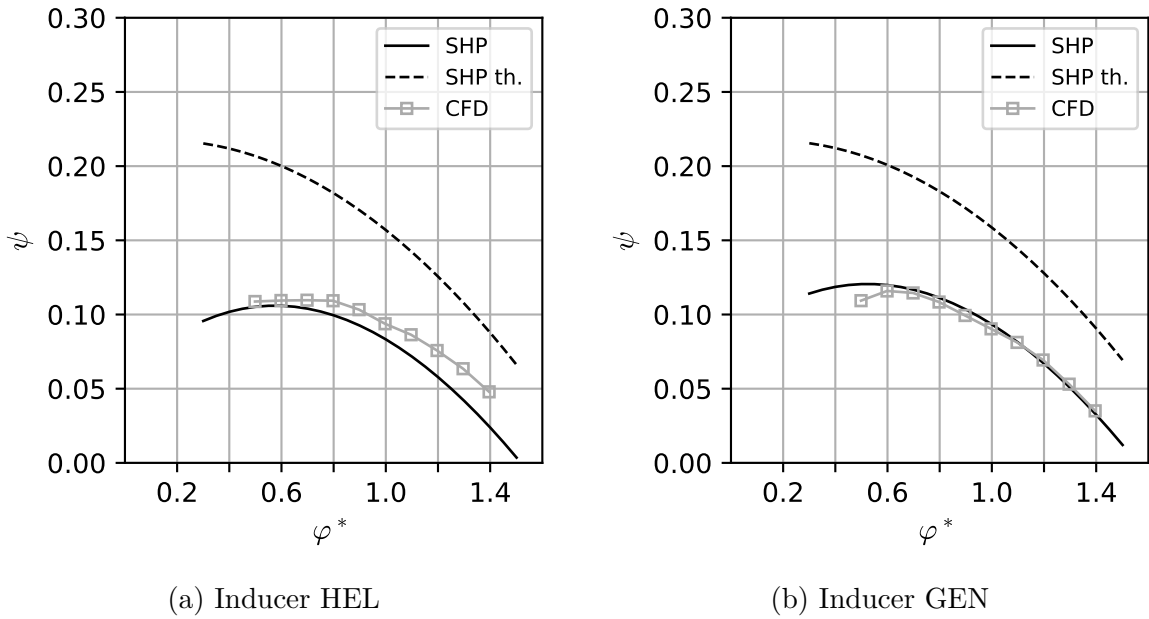
Figure 4.25: Head coefficient characteristics (based on corrected head H)

immediately at the blade trailing edge location. To extract the equivalent angle from the result of the three-dimensional CFD simulation circumferentially averaged values of the flow angle at equidistant radial positions are calculated on a surface immediately downstream of the trailing edge. Figures 4.26a and 4.26b depict the distribution of the discharge angle at design flow rate plotted against the normalized meridional coordinate measured from hub to shroud. From these figures it becomes clear, that the three-dimensional CFD simulation predicts a much more complex discharge flow pattern than suggested by the simplified flow model. Strong deviation from the blade angle can be observed close to hub and shroud, where the influence of the wall friction and the tip clearance in case of the shroud section is evident. At the hub the SHP also predicts the highest deviation but the distribution of flow angle is completely different and much simpler in shape. According to the CFD result the flow is well guided by the blade from around 30 % to 75 % of the trailing edge length. In this region slightly negative deviation angles are predicted (flow angle greater than blade angle), which is most probably caused by an increased meridional through-flow velocity in this region. The simple head prediction method also indicates flow angles greater than the blade angle at the upper region of the blade trailing edge. This indicates that the method can only deliver an idealized concept of the real flow through the inducer. It is expected that a coupling between the cascade flow (singularity method) and the meridional flow solution could improve the prediction of flow features. However, viscous effects, which are known to heavily influence the flow field of inducers [46], are not considered by

(a) Inducer HEL

(b) Inducer GEN
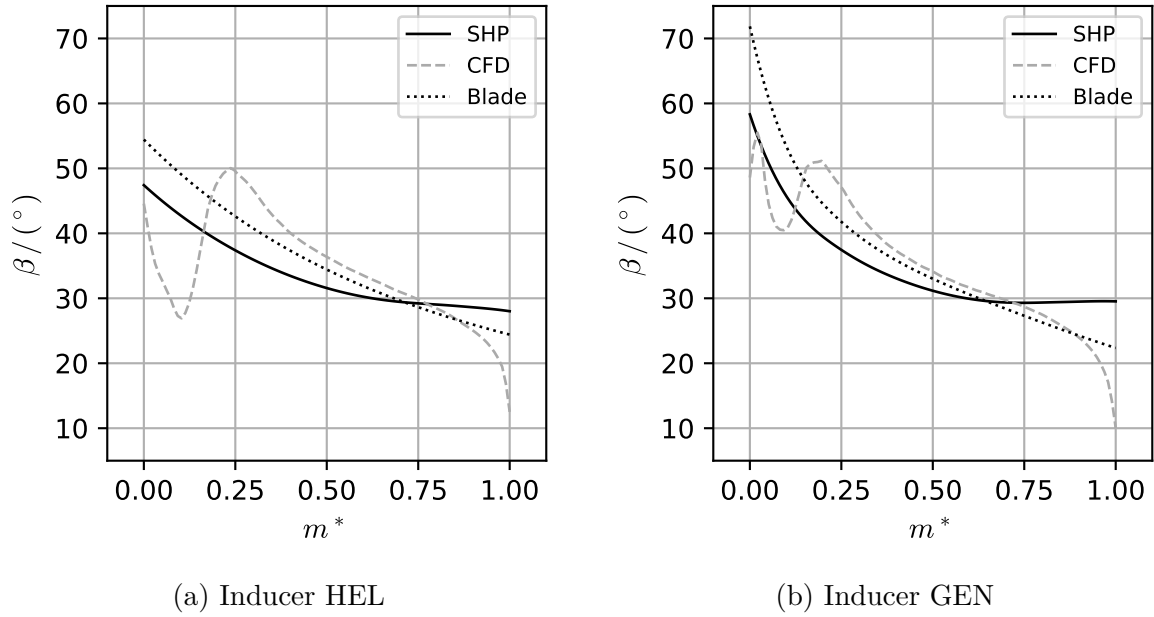
Figure 4.26: Exit flow angle (along trailing edge, from hub to shroud), $\varphi^* = 1$

either the singularity method of the SHP or the meridional flow analysis of the SMA. Furthermore, the tip leakage and secondary flows caused by the interaction with the blade surfaces are not included in the current method. Nevertheless, reasonably good agreement between arithmetically averaged discharge flow angle extracted from CFD can be obtained, as is demonstrated by the values in Table 4.10.

Table 4.10: Average discharge flow angle

Inducer	$\overline{\beta}_{2,CFD}$	$\overline{\beta}_{2,SHP}$	$\overline{\beta}_{2b}$
HEL	34.02°	32.79°	34.39°
GEN	32.75°	33.79°	34.47°

The exit flow patterns are investigated in more detail by comparing the circumferentially averaged meridional velocity component in the discharge section as depicted in Figures 4.27a and 4.27b. Clearly, the trend of the velocity profiles is only roughly represented by the meridional velocity, which is a direct result of the SMA. Because the influence of the blade is neglected in this simplified analysis both velocity profiles are identical and predict the maximum velocity at 75 % of meridional trailing edge length. Compared to the CFD results huge differences in the absolute values of velocities and their location along the trailing edge exist. The global peak of meridional velocity computed by CFD is significantly higher and located at around 60 % for inducer HEL and 75 % for inducer GEN. The maximum values of meridional velocity are similar for both inducers. Towards

(a) Inducer HEL   (b) Inducer GEN
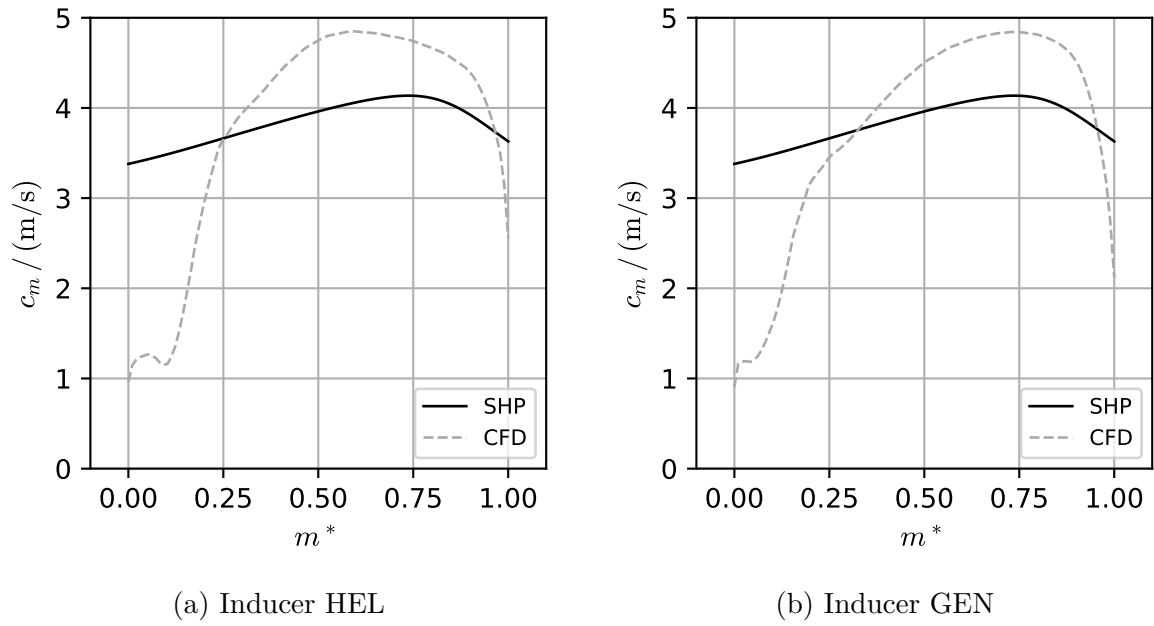
Figure 4.27: Meridional velocity (along trailing edge, from hub to shroud), $\varphi^* = 1$

the hub and shroud walls a reduction of meridional velocity can be observed for both inducers. Due to the shift of velocity maximum towards the shroud the drop in velocity is steeper for inducer GEN. Close to the hub both inducers show a small fluctuation of meridional velocity, with a local peak of velocity that is more developed in case of inducer HEL. According to Euler's pump equation (Equation 2.22) head generation of

(a) Inducer HEL   (b) Inducer GEN
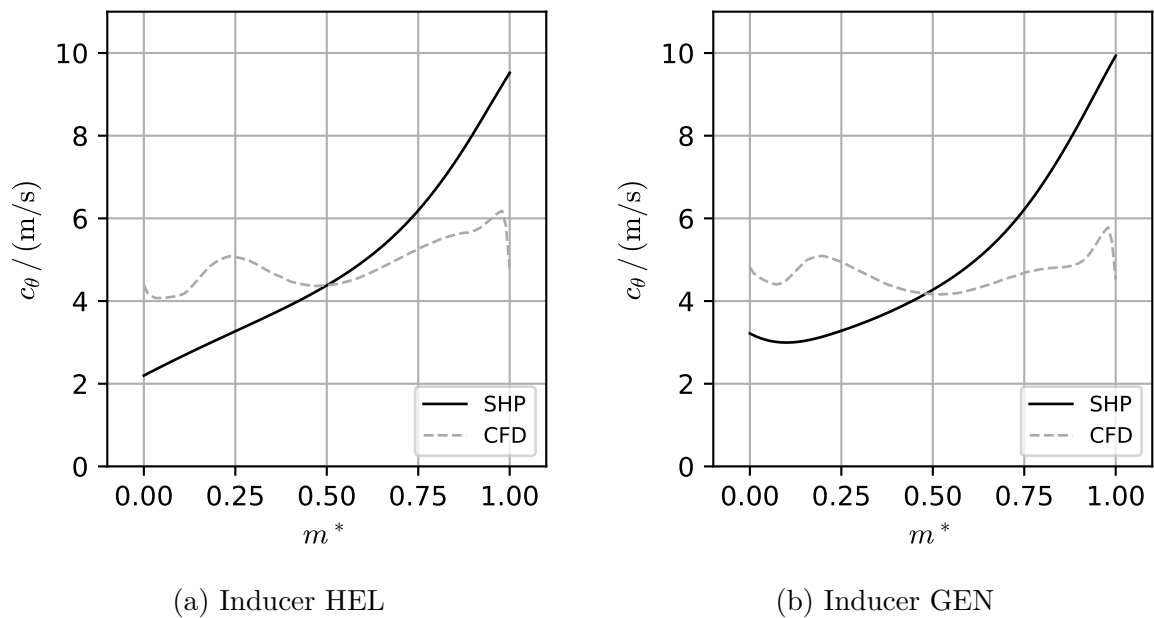
Figure 4.28: Circumferential velocity (along trailing edge, from hub to shroud), $\varphi^* = 1$

the inducers is directly related to the change of the circumferential velocity component of the absolute flow. Assuming swirl free inflow and considering that the change in radius along the blade section is small for the inducers under investigation, the generated circumferential velocity can be seen as the main reason for head rise. Figures 4.28a and 4.28b depict the circumferentially averaged distributions of this velocity component in the discharge section for both inducers. Compared to the results of the CFD simulation, the distributions predicted by the SHP reach significantly higher values at the shroud. While for inducer HEL the value of circumferential velocity rises continuously from hub to shroud, there is a soft decrease starting from the hub for inducer GEN. From approximately 15 % of meridional trailing edge length the velocity rises even stronger and reaches a higher value at the shroud. Completely different and more complicated distributions are predicted by the CFD simulations. This indicates that viscous effects, which are not included in the singularity method of the SHP, cause a very different flow pattern at the inducer's discharge. For both inducers a softly oscillating distribution can be observed from hub to approximately 50 % of trailing edge length. Starting from there, especially for inducer GEN a much weaker increase of the circumferential velocity component compared to the SHP prediction is found. Interestingly, for both inducers the intersection point of the inviscid prediction by the SHP and the CFD result lies close to 50 % of the meridional trailing edge length. This might be a reason why, despite the huge differences in the discharge flow patterns, the average head is quite well predicted. At this point it should be remarked that the above investigations are performed without considering the effect of the impeller or other downstream components on the inducer discharge flow. To validate the results above with experimental data, elaborate and costly flow field measurements would be required on an especially designed test bench for inducers. Although such investigations have been performed, the question remains if the findings are representing the actual flow pattern in the real inducer application together with an impeller.

In addition to the already discussed results the singularity method adopted in the SHP also allows to evaluate the head produced by the single blade sections. The head rise produced by the fifteen blade sections from hub to shroud ($k = 0 \ldots 14$) is displayed in Figure 4.29a. According to this figure the SHP predicts higher theoretical total head coefficients for inducer HEL on the interior sections ($k = 2 \ldots 9$). On the inner and outer sections higher head coefficients are estimated for inducer GEN. The figure clearly demonstrates that, according to the SHP, most of the the head is produced at the outer sections for both test-cases and the head decreases continuously towards the hub section. Furthermore, each single blade section can be judged by analyzing the head rise along the blade section from leading to trailing edge. This is depicted for hub, shroud and
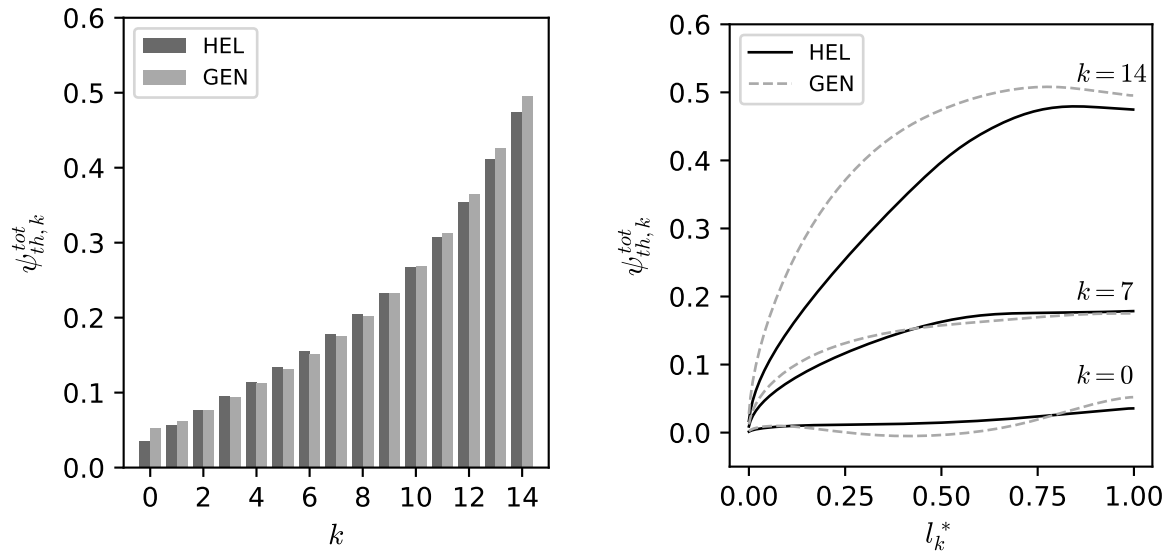
(a) Theoretical total head coefficient on blade sections

(b) Theoretical total head coefficient along selected blade sections

Figure 4.29: Theoretical head coefficient distribution, $\varphi^* = 1$

a middle section ($k = 7$) in Figure 4.29b, where the theoretical total head coefficient is plotted against normalized three-dimensional camber curve length (corresponding to section k). As already observed before, the head rise is highest at the shroud (or tip) sections and significantly lower at the hub section. At the shroud and mid section a steeper head rise is predicted for inducer GEN. For both test cases there is no more head rise after approximately 75 % of the blade length at the outer section. In fact, a small decrease of head coefficient can be observed in both cases along the remaining part of this section. It can be assumed that this effect is due to reduction in diameter caused by the contraction of the meridional shroud contour on the one hand and due to the decrease in blade thickness towards the trailing edge on the other hand. The hub section of variant GEN contributes slightly more to the total head, although negative head coefficients are predicted for up to 75 % of blade length. This indicates that the blade shape could be optimized in this region.

4.5 Validation of Inducer Designs

4.5.1 Experimental Setup

An experimental test bench developed at the institute's laboratories is used to validate the designed prototypes in conjunction with a real pump unit. The test bench, originally setup and used in the investigations carried out by Knapp [43], is modified to incorporate

the newly developed inducer pump. A new impeller that has to comply with two main requirements is designed. First, it was reduced in axial length to create space for the inducer. This is done by adapting the meridional section and the positioning of the leading edge. Second, the impeller still needs to operate appropriately with the original volute to avoid excessive material and manufacturing costs for a new volute design. This is achieved by adapting the blade angle distributions accordingly. Details about the impeller design are provided in Appendix D. Since the test rig was formerly used to

Figure 4.30: Schematic of the pump loop

investigate different volute design criteria, multiple volute configurations are available. The volute selected for the current investigations was designed and investigated together with the original impeller by Knapp [43]. The volute is named *Alpha* because of the underlying design rule prescribing the volute angle α as a function of wrap angle. Further details about the volute design and numerical as well as test results of the original pump configuration are reported in [43]. Several modifications of the original test bench have been made in order to realize the investigations described in this thesis. Figure 4.30 depicts a schematic drawing of the pump loop including auxiliary devices and sensors. An overview of the used sensors, including measurement ranges and accuracies is provided in Table 4.11.

Following the recommendations of Knapp [43] a torquemeter with appropriate range and integrated speed sensor to automatically acquire torque and speed signals is installed. Furthermore, a differential pressure probe is used for the measurement of the head. However, the originally used absolute pressure sensors are not removed but are used in parallel to the differential pressure probe in order to keep results comparable to earlier

Table 4.11: Sensors

Quantity (Symbol)	Sensor	Range	Unit	Accuracy
Absolute pressure (p_1)	E+H Cerabar M	$0\ldots10$	bar	$0.2\,\%$
Absolute pressure (p_2)	E+H Cerabar M	$0\ldots10$	bar	$0.2\,\%$
Absolute pressure (p_3)	E+H Cerabar M	$0\ldots10$	bar	$0.2\,\%$
Absolute pressure (p_{tank})	E+H Cerabar M	$0\ldots10$	bar	$0.2\,\%$
Difference pressure (Δp_{12})	ABB 266MST	$0\ldots2.5$	bar	$0.04\,\%$
Difference pressure (Δp_{13})	ABB 266MST	$0\ldots20$	bar	$0.04\,\%$
Volume flow rate (Q)	E+H Promag 50W80	$0\ldots180$	m^3/h	$0.4\,\%$
Temperature (T)	E+H TST414	$223\ldots673$	K	$0.5\,\%$
Torque (M)	KTR Dataflex 16/50	$-50\ldots50$	Nm	$0.1\,\%$
Speed (n)	KTR Dataflex 16/50	$0\ldots4000$	rpm	(-)

investigations. The locations of the pressure taps are indicated in the section view of

(a) Full measurement section

(b) Detail view
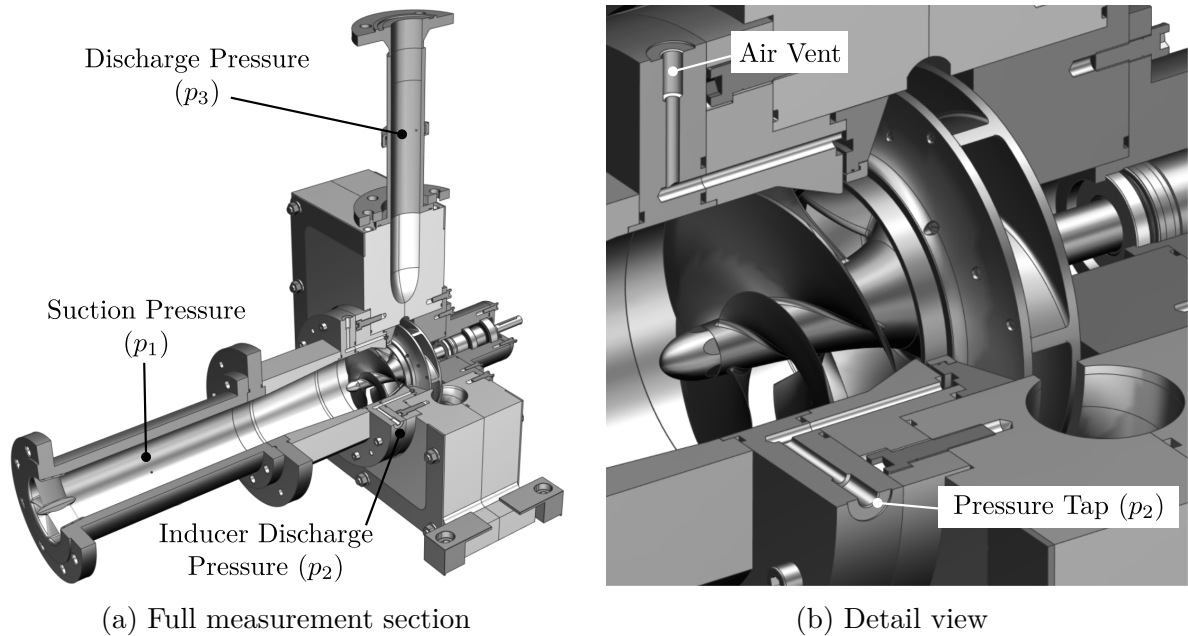
Figure 4.31: Experimental pump unit

the inducer-pump assembly displayed in Figure 4.31a. An additional pair of differential and absolute pressure sensors is installed to estimate the head rise generated by the inducer. To achieve this, a new casing is designed that allows to measure the pressure between inducer and impeller at the outer diameter directly in front of the wear ring of the impeller. As can be seen from Figure 4.31b the pressure is measured from the plenum that results out of the grooves in the wear ring seat and the inducer casing. Since this location cannot be accessed easily by drilling in radially, the plenum is connected axially to a flange protruding from the volute block. Additional o-ring seals are required

to seal the system. A second tap, used as air vent, is provided at the top of this flange. The whole inflow section was made out of PMMA to obtain visual access to the inducers leading edge during test runs. This is not only helpful while measuring NPSH characteristics but can also be an advantage when measuring head curves at higher inlet pressures because small amounts of vapor can develop even under normal operation [18].

4.5.2 Pump configurations

Three pump configurations are investigated to judge the influence of the inducers on the performance. As a reference the pump impeller is investigated without mounting one of the inducers. A special nut was created for this purpose.

Figure 4.32a shows a section view of this configuration, which is called Pump IMP. The other two configurations are named according to the inducer prototype that is used, i.e. Pump HEL and Pump GEN. An exemplary section view of inducer pump HEL is depicted in Figure 4.32b. Both pumps use the same inflow and outflow configuration, such that the differences in measurement results can be fully attributed to the inducers and the interaction with the impeller.

The hardware was manufactured in the universities workshops by CNC-machining. A high-strength aluminum alloy EN AW 7022 (AlZn5Mg3Cu) was employed for the impeller and the inducers because of its good machinability. The impeller hub and blades were produced from one piece and the shroud was fixed to it with three bolts per blade. Figure 4.33a shows a top view of the impeller, Figure 4.33b shows the two inducers from a lateral view.

(a) Pump IMP   (b) Pump HEL
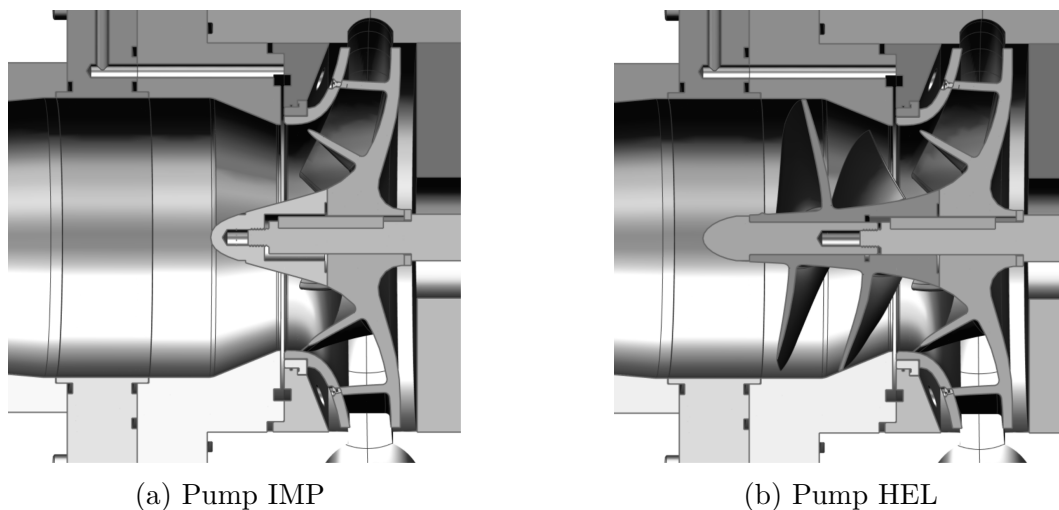
Figure 4.32: Pump configurations

(a) Impeller

(b) Inducers GEN (left) and HEL (right)

Figure 4.33: Test hardware

4.5.3 Measurement Procedure

Two different measurement types are conducted for each of the pump configurations; Head and NPSH measurements. During a head measurement rotational speed is kept constant by fixing the frequency of the frequency converter. The signals of the sensors are acquired with a National Instruments NI USB-6259 data acquisition device and are processed in a custom built LabView software. This program is also used to regulate the volume flow rate through the test bench by controlling the valve. Starting from the highest possible flow rate, which is around $130 \, \text{m}^3/\text{h}$ in the current configuration, the flow rate is reduced successively, while keeping the inlet total pressure approximately constant at $2 \, \text{bar}$. For each flow rate ten repeated measurements of the signals are performed. In every measurement loop the mean value of continuously acquired data over $1 \, \text{s}$ of measurement time is stored in an output file. The sampling rate is set to $10 \, \text{kS/s}$ on all analogue channels. The only digital signal, the frequency of the speed sensor, is captured continuously and is stored together with the averaged analogue data. In the case of NPSH measurements speed and flow rate are kept as constant as possible, while the tank pressure is reduced step by step. This is achieved by lowering the tank pressure by venting or by evacuating with the help of a vacuum pump. The signal acquisition procedure is identical to the head measurements.

During all measurements visualization is realized by means of two network cameras that are mounted close to the pump inlet. A freeze image of the inducer or impeller is generated by synchronizing a stroboscope with the frequency signal of the speed sensor.

4.5.4 Characteristic values

The data acquired from the sensors is used to compute the characteristic values of the pump. By neglecting any possible amount of swirl and assuming uniform pressure in the measurement sections the head of the inducer is computed according to Equation 2.25 as follows:

$$H_{12} = \frac{\Delta p_{12}}{\rho\, g} + \frac{\bar{c}_{m2}^2 - \bar{c}_{m1}^2}{2\, g} \tag{4.31}$$

Analogously, the pump head is calculated by:

$$H = H_{13} = \frac{\Delta p_{13}}{\rho\, g} + \frac{\bar{c}_{m3}^2 - \bar{c}_{m1}^2}{2\, g} \tag{4.32}$$

Alternatively, the signals of the absolute pressure sensors could be used to calculate the head as follows:

$$H_{12,abs} = \frac{p_2 - p_1}{\rho\, g} + \frac{\bar{c}_{m2}^2 - \bar{c}_{m1}^2}{2\, g} \tag{4.33}$$

$$H_{abs} = H_{13,abs} = \frac{p_3 - p_1}{\rho\, g} + \frac{\bar{c}_{m3}^2 - \bar{c}_{m1}^2}{2\, g} \tag{4.34}$$

Although the absolute pressures are acquired during measurements, they are not used in the evaluation of the results presented in this thesis. Since the pressure taps are connected to differential pressure sensors ($\Delta p_{12}, \Delta p_{13}$) and the absolute pressure sensors (p_1, p_2, p_3) are mounted at equal horizontal level, the hydrostatic head components ($z_2 - z_1$) and ($z_3 - z_1$) are equal to zero and consequently do not appear in the above equations. With the cross sectional areas at the pressure tap locations (see Figure 4.34) denoted by A_{p1}, A_{p2}, and A_{p3} the mean meridional velocities at these points are computed by

$$\bar{c}_{m1} = Q/A_{p1} = 4Q/(\pi d_{p1}^2) \tag{4.35a}$$

$$\bar{c}_{m2} = Q/A_{p2} = 4Q/(\pi d_p^2) \tag{4.35b}$$

$$\bar{c}_{m3} = Q/A_{p3} = 2Q/(\pi b_{p_2}(D_{1s} + D_{1h})) \tag{4.35c}$$

The corresponding values of power and efficiency are computed according to Equations 2.36 and 2.37. Because shaft power is measured for the entire inducer-impeller assembly,
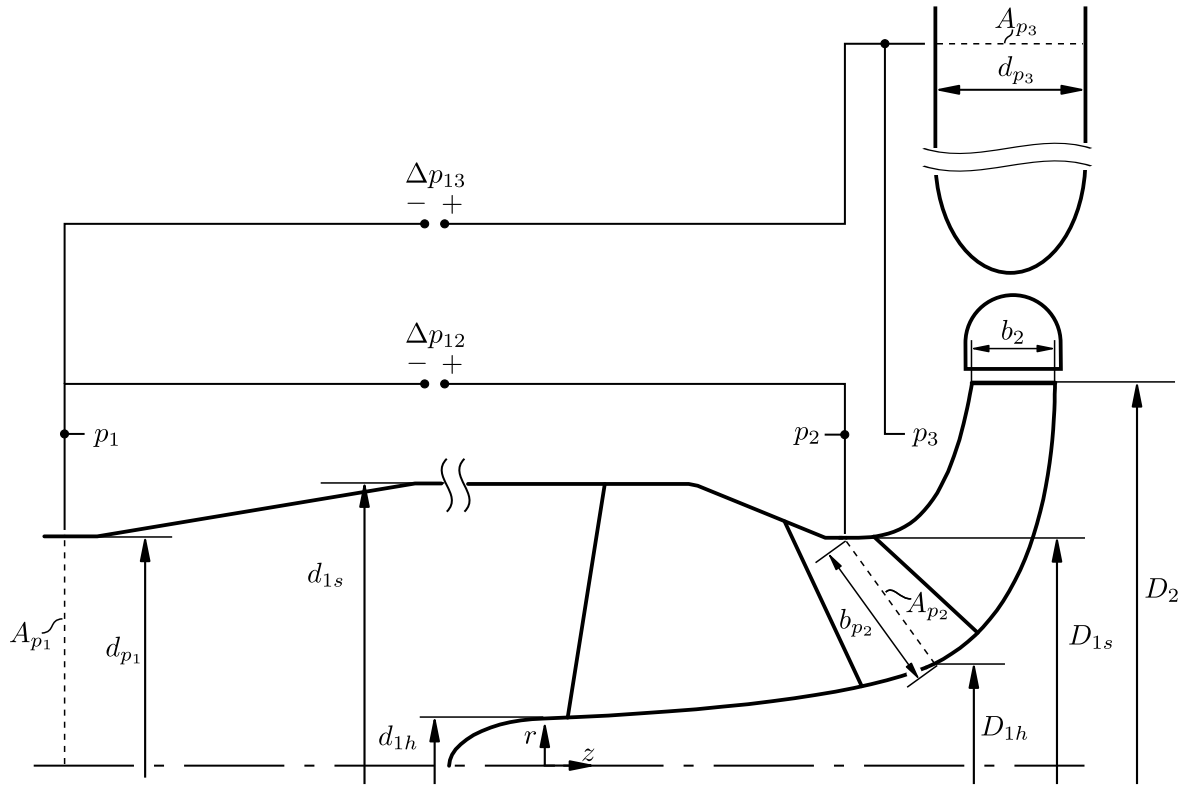
Figure 4.34: Schematic of the measurement section

these values can only be provided for the whole pump:

$$P_h = P_{h,13} = \rho g Q H_{13} \tag{4.36}$$

$$\eta = \eta_{13} = \frac{\rho g Q H_{13}}{M \omega} \tag{4.37}$$

Under the same assumptions as above NPSH is calculated based on the suction pressure and the mean inlet velocity according to Equation 2.38:

$$\text{NPSH} = \frac{p_1 - p_v(T)}{\rho g} + \frac{\bar{c}_{m1}^2}{2g} \tag{4.38}$$

Saturation pressure is considered to be a function of temperature T only, which is evaluated during measurement and evaluation.

Because the maximum speed of the frequency controlled motor used at the test bench is limited to a value slightly below the nominal speed of $n = 3000\,\text{rpm}$ a conversion of the characteristic parameters is performed based on the affinity laws as given in DIN EN ISO 9906:2012 [26]. If the data measured at the speed n_m is indicated by index m

the conversion to nominal speed n is applied as follows:

$$Q = Q_m \left(\frac{n}{n_m} \right) \tag{4.39a}$$

$$H = H_m \left(\frac{n}{n_m} \right)^2 \tag{4.39b}$$

$$P = P_m \left(\frac{n}{n_m} \right)^3 \tag{4.39c}$$

$$\eta = \eta_m \tag{4.39d}$$

$$\text{NPSH} = \text{NPSH}_m \left(\frac{n}{n_m} \right)^2 \tag{4.39e}$$

The dimensionless characteristic parameters as defined in Section 2.2.4 are computed by the following equations:

$$\varphi = \frac{\bar{c}_{m1}}{u_{p_1}} \tag{4.40}$$

$$\psi = \frac{2gH}{u_2^2} \tag{4.41}$$

$$\lambda = \frac{\phi\psi}{\eta} \tag{4.42}$$

$$\sigma = \frac{2g\text{NPSH}}{u_{p_1}^2} \tag{4.43}$$

In order to provide a uniform representation of the dimensionless characteristics, flow coefficient φ as well as the cavitation coefficient σ are computed with respect to the diameter at the inlet pressure tap, and the head coefficient ψ is computed with respect to the impeller outlet diameter. The circumferential velocities at these locations are computed by:

$$u_{p1} = \pi n d_{p_1} \tag{4.44}$$

$$u_2 = \pi n D_2 \tag{4.45}$$

Head coefficients corresponding to the head measurements H_{12} and $H = H_{13}$ are calculated according to Equation 4.41:

$$\psi_{12} = \frac{2gH_{12}}{u_2^2} \tag{4.46}$$

$$\psi = \psi_{13} = \frac{2gH_{13}}{u_2^2} \tag{4.47}$$

142

A discussion of uncertainty analysis and an evaluation of uncertainty for the actual measurement data is provided in Appendix E.

4.5.5 Experimental Results

Non-Cavitating Characteristic Curves

Characteristic curves are obtained at an inlet total pressure level of 2 bar and at the maximum rotational speed realizable with the available equipment (motor and frequency converter). By application of the affinity laws given in Equations 4.39 the results are converted to nominal speed of 3000 rpm. Figure 4.35 depicts a comparison of head coefficient, efficiency and performance coefficient curves for the three pump configurations. All points represent the mean values of 10 repeated measurements at approximately constant operating conditions. Quantitative analysis of the characteristic coefficients at 50 %, 80 %, 100 %, 120 % of the design flow rate are summarized in Table 4.12. By

Table 4.12: Experimental results - characteristic coefficients

φ^*	Pump	ψ_{13}	ψ_{12}	η	λ
	IMP	1.005	0.182	0.603	0.603
0.50	HEL	1.035	0.278	0.593	0.593
	GEN	1.033	0.273	0.597	0.597
	IMP	0.966	0.098	0.739	0.739
0.80	HEL	0.977	0.210	0.735	0.735
	GEN	0.979	0.207	0.743	0.743
	IMP	0.907	0.048	0.781	0.781
1.00	HEL	0.919	0.155	0.779	0.779
	GEN	0.919	0.148	0.784	0.784
	IMP	0.806	0.018	0.778	0.778
1.20	HEL	0.826	0.108	0.784	0.784
	GEN	0.825	0.096	0.788	0.788

adding the inducers the characteristic curves are not altered significantly for the operating points close to design flow rate. Head coefficient is increased only slightly in this range of operation. In part-load, starting from around 60 % of design flow rate, a stronger influence of the inducers can be observed. Head coefficient rises faster with decreasing flow rate for pump configurations HEL and GEN and then becomes instable at approximately 40 % of nominal flow rate. In comparison to this, the base pump configuration IMP does not exhibit this behavior and provides an almost horizontal head coefficient characteristic towards shut-off head. However, shut-off head is not measured, such that it cannot be ruled out that any instability exists for this pump configuration
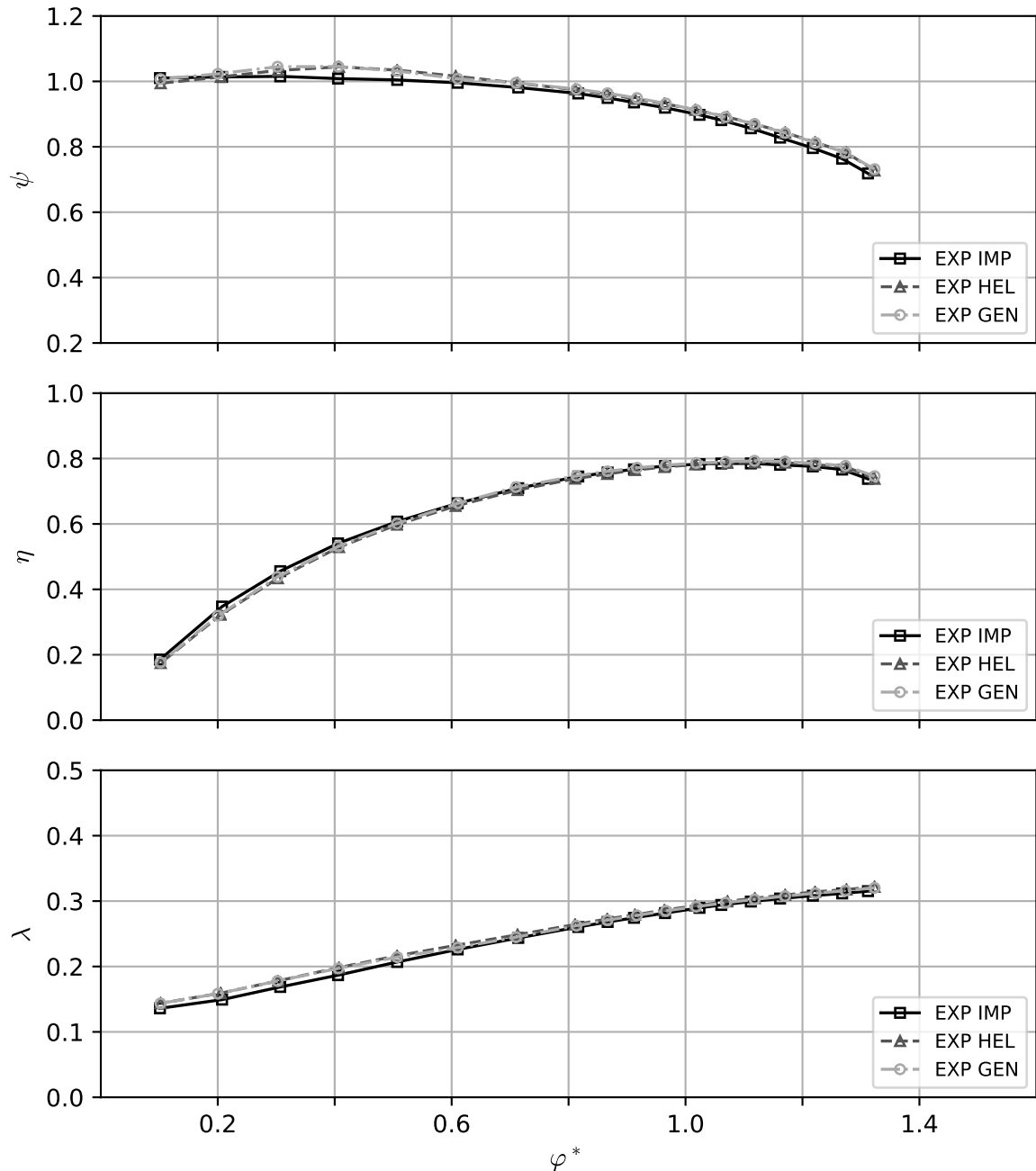
Figure 4.35: Characteristic curves

at lower flow rates (between $\varphi^* = 0.1$ and $\varphi^* = 0.0$). The reason for the instability occurring with the inducer configurations might be that the inducer head breaks down at a certain flow rate as was already indicated by the results presented in Section 4.4.2. The underlying flow mechanism is not completely understood but it can be assumed that increased part load recirculation leading to vortex breakdown are causing the drop in head coefficient [31]. However, since the instability is weak in terms of drop in head

coefficient and occurs first at strong part-load, it does not prevent the application of the inducers.

Analyzing the experimental results quantitatively, it can be found that at design flow the head coefficient of the whole pump (ψ_{13}) rises from 0.907 to 0.917, which is approximately equal to 1.3 % of the head of pump IMP without any inducer. This clearly indicates that there is interaction between inducer and the subsequent impeller since the heads do not simply add up. In fact, the swirl produced by the inducer effectively reduces the head of the impeller, such that the pump head remains almost unaltered.

Looking at the efficiency characteristic curve, it can be seen that the influence of the inducers is rather small. This indicates that a good matching between inducer and impeller could be achieved. In fact, the inducer-impeller configuration GEN operates at slightly higher efficiencies from about 60 % of design flow rate. However, efficiency is reduced at smaller flow rates for both inducer configurations. Furthermore, the point of best efficiency (BEP) is shifted to approximately 110 % - 115 % of nominal flow rate. Without changing the inducer-impeller combination a redesigned volute with a smaller cross sectional area could be developed to match the BEP to the desired design values. Other possibilities involve changes to the impeller like changing outlet width or blade number [31].

Performance coefficient λ, also shown in Figure 4.35, is a measure for the input power required to drive the pump unit. While the rise in performance coefficient caused by the inducers is only marginally at design and overload, it is higher at part load. Due to increased surface friction, tip leakage and other secondary flow losses, an increase in input power and a decrease in efficiency is expected over the entire operating range. However, this is not observable. In fact, the result is in accordance with the observations made for efficiency. An implication of this finding is once more, that the impeller is well adapted to work in combination with both of the inducers. On the other hand it can be assumed that the impeller design is very tolerant of varying inflow conditions (with and without pre-swirl).

Investigation of the head generation of the inducers is done by evaluating the head coefficient ψ_{12}. This head coefficient is depicted again for all pump configurations in Figure 4.36. In case of pump configuration IMP no inducer is present, such that the pressure difference measured might be explained by the leakage flow through the wear ring gap (see Figure 4.31b). Furthermore, the pressure measurement at this position close to the impeller inlet could be influenced by recirculation from the impeller leading edge. This recirculation process, which intensifies with increasing part load, would increase the pressure measured at the outer diameter. By computing the difference between the interpolated data of head coefficient ψ_{12} of the measurements with inducer
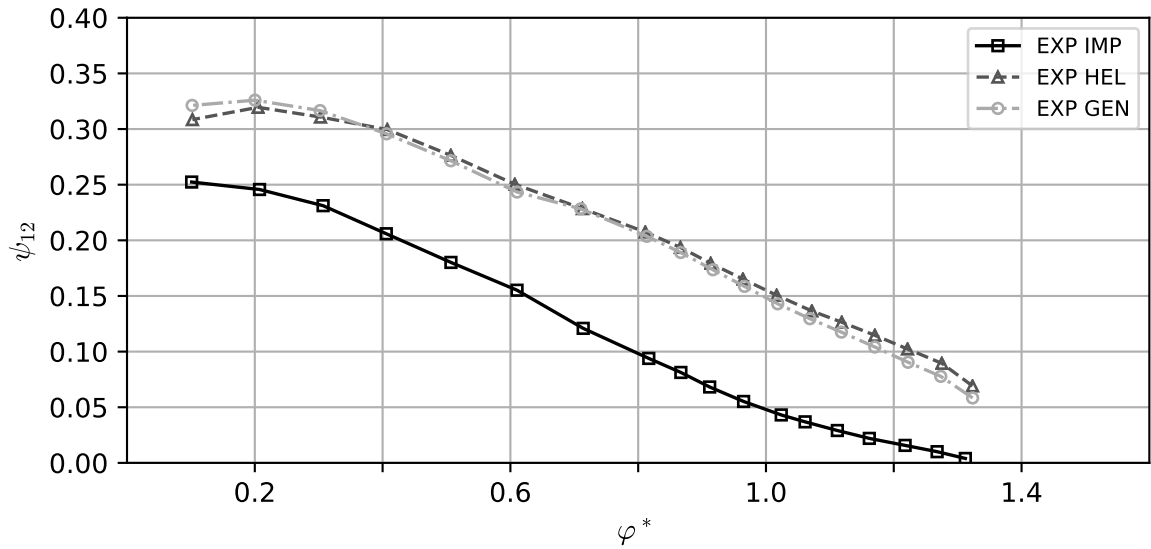
Figure 4.36: Inducer head coefficient (ψ_{12})

(pump configurations HEL and GEN) and without inducer (pump configuration IMP) an estimate of the influence of the inducers is obtained. This difference of head coefficients
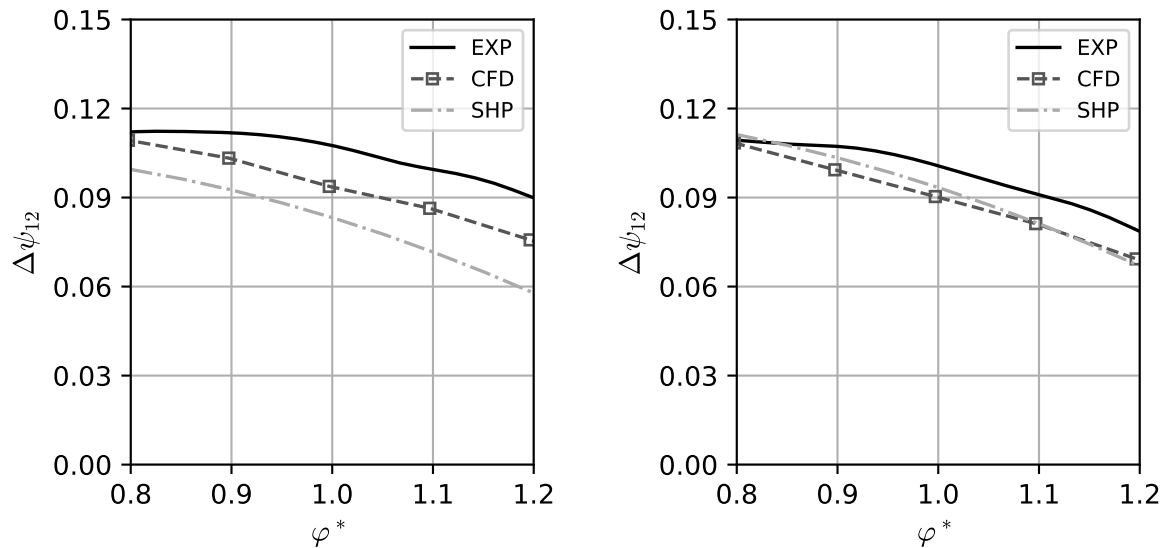
(a) Inducer HEL

(b) Inducer GEN

Figure 4.37: Inducer head coefficient ($\Delta\psi_{12}$)

is defined as $\Delta\psi_{12} = \psi_{12} - \psi_{12}^{\mathrm{IMP}}$ and is depicted in Figures 4.37a and 4.37b from 80 % to 120 % of design flow coefficient together with the data of the SHP and the CFD simulations presented previously in Chapter 4.4.2 for both inducer prototypes. Of course, the results of SHP and CFD are not directly comparable with the measured values because the pressure evaluation method is different. While in the SHP and CFD

the averaged static pressures at the inducer discharge are used, the circumferentially averaged static pressure at the outer diameter between inducer and impeller is measured in the experiment. Furthermore, effects due to interaction between inducer and impeller cannot be removed by the simple subtraction of head coefficients. For the SHP the difference relative to the corresponding measurement value is found to be around 23 % for Inducer HEL and 7 % for inducer GEN. In case of the CFD simulation the equivalent differences are approximately 13 % and 10 % for inducer HEL and GEN, respectively. Taking into account the huge differences in effort required to produce these results and considering the simplifications included in the SHP as well as in the CFD simulation, which only models a single blade channel, the agreement can be rated as good. The experimental data based on the static pressure at the outer diameter confirms that the helical inducer provides a higher head than the general blade design. This cannot be reproduced by the SHP and the amount of difference is underpredicted also by the CFD result. A deeper investigation of the distribution of flow, especially at the inducer's discharge, is needed to understand the origin of this behavior.

Cavitating Performance

While the results discussed so far are obtained under non-cavitating conditions, the influence on suction performance has yet to be addressed. Hence, suction performance is evaluated by performing head drop measurements to obtain NPSH as described in Section 4.5.3. NPSH measurements are performed for 80 %, 100 %, 120 % of design flow rate. Figure 4.38 depicts the head drop curves at design flow rate ($\varphi^* \approx 1$) for all pump
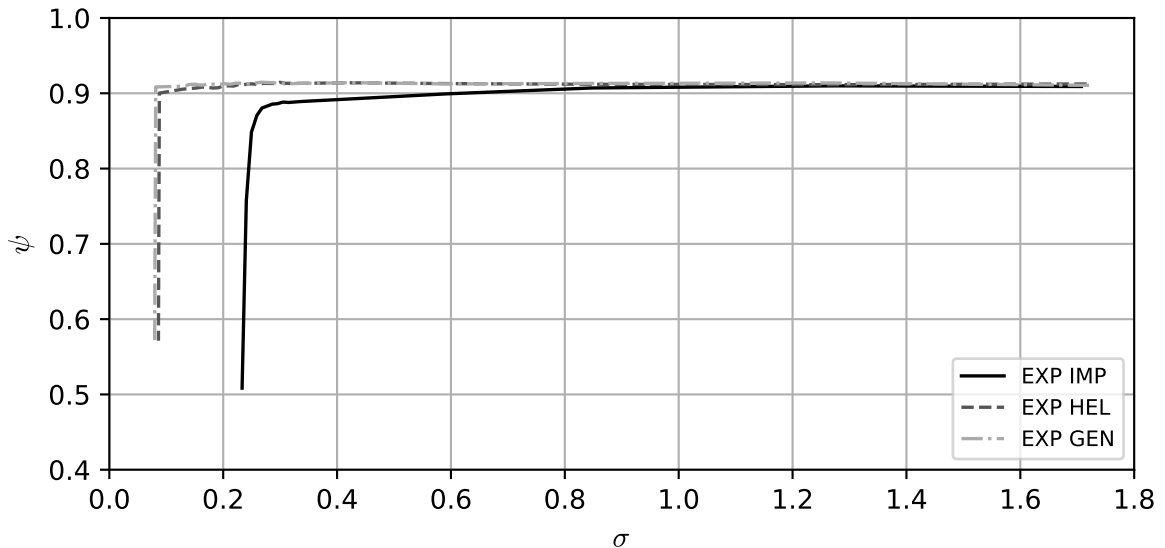
Figure 4.38: Pump head coefficient (ψ) at design flow rate ($\varphi^* \approx 1$)

configurations. The effect of adding the inducers is clearly visible; significantly lower cavitation coefficients are achieved with pump configuration HEL and GEN. Furthermore, the head drop occurs more abruptly for the inducer pumps, whereas a comparatively soft drop of head is observed for pump IMP. This is the reason why with the current test bench configuration tank pressure has to be reduced very carefully and in small steps when approaching the head drop condition. Hence, a comparably high number of measurement points is necessary for the inducer configurations. This is why markers are omitted for the individual measurement points in the figures displaying the head drop curves. Evaluating the cavitation coefficient at a 3% drop of head leads to the

Table 4.13: Experimental results - suction performance ($\varphi^* \approx 1$)

Pump	$\sigma_{3\%}$	$n_{ss}/(\text{rpm})$	$N_{ss}/(\text{rpm})$	Ω_{ss}
IMP	0.273	207.63	10723.04	3.92
HEL	0.088	485.86	25092.19	9.18
GEN	0.081	514.27	26559.83	9.72

values summarized in Table 4.13. Head drop is computed with respect to the head measured at the highest value of cavitation coefficient. Since inlet pressure is lowered successively, this is equal to the head measured at the first measurement point of the head drop measurement run. Computation of the cavitation coefficient is performed by interpolating the measured data linearly and then searching for the desired drop in head numerically. The tabulated values indicate that cavitation coefficient is reduced by more than two thirds at design flow coefficient ($\varphi^* \approx 1$). Although not explicitly listed, similar reductions of the cavitation coefficient can be found in case of the measurement at part-load ($\varphi^* \approx 0.8$) and overload ($\varphi^* \approx 1.2$).

Suction specific speed, calculated for design flow rate $Q = 100\,\text{m}^3/\text{h}$ and rotational speed $n = 3000\,\text{rpm}$, is more than doubled as can be seen from Table 4.13. Besides the non-dimensional version Ω_{ss} also the European (n_{ss}) and US-American version of suction specific speed are provided as they might be more common to the reader. Conversion factors are provided in Appendix C.

The values obtained in the measurements at design flow coefficient are slightly lower than the design value of $n_{ss} \approx 495\,\text{min}^{-1}$ for inducer HEL and moderately higher than the design value for inducer GEN. This might be caused by the small differences in leading edge blade angle design of the two inducers (see Figure 4.4a) and points out how important an exact control of the leading edge shape is for the designer of inducers. It should also be considered that measurement uncertainty rises with decreasing values of cavitation coefficient (see Appendix E). Nevertheless, both inducer designs provide

a very good initial design, which could be used to refine the design parameters and produce an improved design.
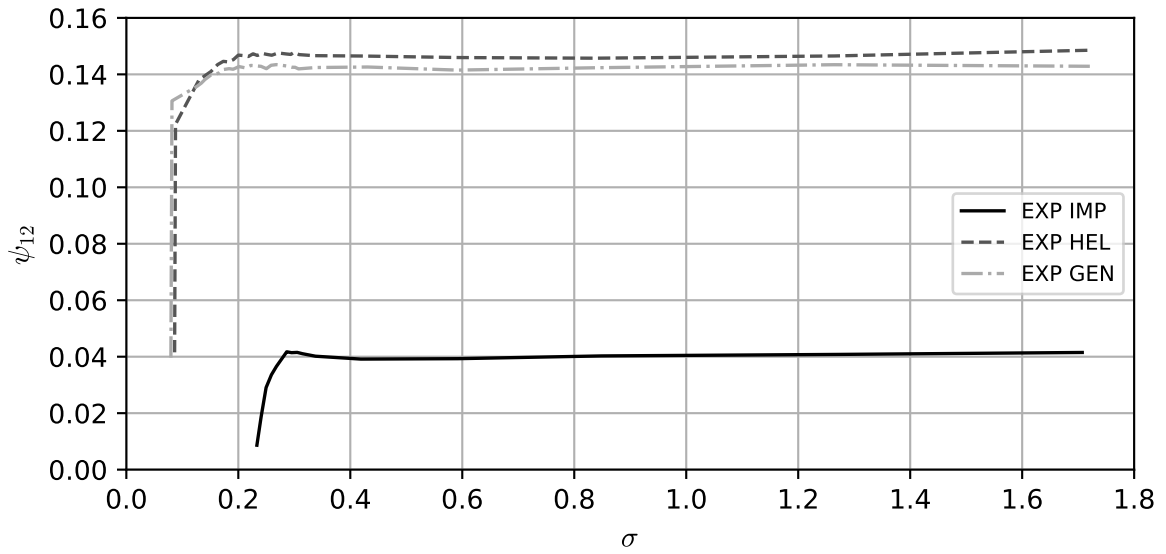
Figure 4.39: Inducer head coefficent (ψ_{12}) at design flow rate ($\varphi^* \approx 1$)
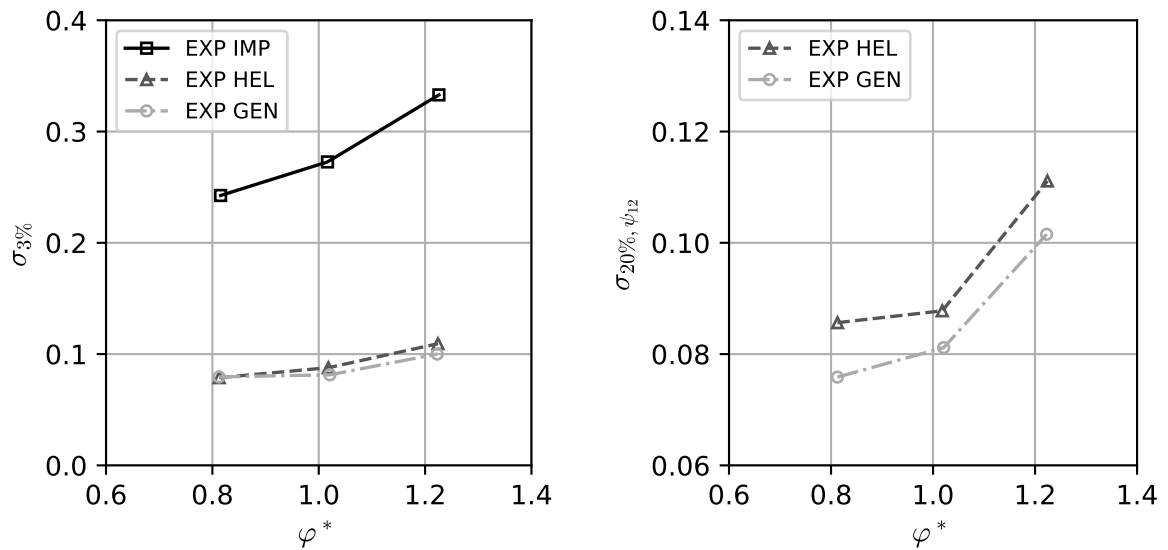
(a) Cavitation coefficient at 3 % head drop ($\sigma_{3\%}$) for all pump configurations

(b) Cavitation coefficient at 20 % of inducer head drop ($\sigma_{20\%,\psi_{12}}$) for inducer pumps

Figure 4.40: Cavitation coefficient characteristic curves

Analogously to the non-cavitating case, the inducer head coefficient ψ_{12} is used to investigate the influence of the inducers. At the design flow coefficient the head drop curves depicted in Figure 4.39 are obtained. As expected, the head coefficient of the pump

configuration IMP is substantially lower than the head coefficients of the other configurations. Comparing the curves of the inducer pumps (HEL and GEN) to the curves for the whole pump (Figure 4.38) the drop of inducer head coefficient ψ_{12} appears a lot softer.

If ψ_{12} is now evaluated at $\sigma_{3\%}$ of the whole pump, it becomes clear, that the inducer is already operating with a substantially higher decrease of head coefficient. In fact, the inducer head coefficient is already reduced by approximately $15\,\%$ - $20\,\%$ at this operating point.

The cavitation coefficient characteristics of the pump configurations are obtained by plotting $\sigma_{3\%}$ against normalized flow coefficient φ^* in the measured range from $80\,\%$ to $120\,\%$ (Figure 4.40a). Both inducers significantly reduce cavitation coefficient at all three operating points. Inducer GEN reaches slightly lower values at $100\,\%$ and $120\,\%$ of design flow coefficient. A similar trend can be observed if cavitation coefficient at $20\,\%$ of drop of inducer head coefficient, denoted by $\sigma_{20\%,\psi_{12}}$, is evaluated at the different flow rates. Figure 4.40b shows these progressions for both pump configurations HEL and GEN.

Of course this reflects only an excerpt of the full cavitation characteristic of the pump. Further measurements at part-load and overload are required to investigate the full range of operation and to detect possible instabilities due to cavitation. Nevertheless, the present investigation confirms the intended reduction in cavitation coefficient for the design point of the pump.

5 Conclusions and Perspective

An integral inducer design procedure was developed and tested on a real experimental pump unit. Making use of B-splines the geometric design steps provide a parametrical way of controlling and manipulating blade shape, opening the door to optimization methods. The meridional section can be designed freely, allowing for arbitrary hub and shroud shapes. This is not only of interest for high head inducers, which use a tapered hub contour to support the pressure rise process, but also for inducers with converging shroud shapes. The latter can be necessary to match the inducer with a large inlet diameter to an impeller with a smaller suction diameter.

A two-dimensional, inviscid flow computation method is integrated in the design procedure to generate physically motivated streamlines in the meridional plane. These streamlines are used as the basis of the blade section design. In the present thesis two different blade shapes are implemented; the helical and the general blade. While the helical blade design can be considered the classical method, the general blade shape offers greater design flexibility because the blade angle distributions can be designed more freely. Both methods provide the possibility to create a blade with specified amount of backward or forward sweep in a parametrical way. Emphasis is also placed on the development of a three-dimensional method to generate the blade profile in an asymmetric manner. Two thickness distributions can be designed independently, and the corresponding thicknesses are added on the opposite sides of the three-dimensional camber curve. This is especially useful if the profiling is performed only for the suction side (or the pressure side) of the blade. A parametric approach of wedge-shaped leading edge sharpening is incorporated into the thickness distribution design. However, the method can be easily extended to other sharpening or other profile shapes. To generate manufacturing-ready blade surfaces an elliptical rounding of the blade edges is provided operating at the thickness distribution level. With this approach an undistorted mapping of the profile to the three-dimensional space is achieved. However, different edge types and various other ways to apply them to the blade profile are imaginable.

The blade sections can finally be used in a simple head prediction procedure. This procedure is based on a singularity method that only operates on the two-dimensional blade camber curves in the cascade plane and delivers estimates of theoretical head and discharge flow conditions. Changes of meridional flow velocity as well as blade blockage are considered by the method. Viscous effects are introduced into the method by a very simple loss model giving an estimate of the total head loss.

In order to test the design method two inducers with different blade types were designed and manufactured. Verification and validation of both, the meridional flow analysis and

the head prediction method, were performed based on simple analytical solutions and with the help of numerical simulations of the two inducer prototypes. The meridional flow analysis provided a quite good agreement with the numerical solutions computed by a commercial CFD code. Although reasonable estimates for the head of the inducers were observed, the limitations of the head prediction method are revealed by investigation of the discharge velocity profiles of the inducers. However, rough estimates of head and average discharge angles can still be useful in the early design stage. In the last step the inducer prototypes were examined experimentally. The results show that the inducer designs reduce cavitation coefficient at three percent of head drop by a factor of around three and more than double suction specific speed of the pump unit. Furthermore, the efficiency of the pump is not altered significantly by application of the inducers.

This successful application of the design method does not only demonstrate the functionality of the developed procedure but also indicates the potential for future inducer developments. Since the design method does not rely on any commercial software, its extension and further development are feasible without limitations. Future steps could include the design of inducers featuring splitter or tandem blades as well as the unified design of inducer and impeller. A different direction of research could address more advanced performance analysis methods like quasi three-dimensional or full three-dimensional codes, which also consider the cavitating performance of the inducer. Application of these methods could be used to produce far more optimized inducer geometries in the future.

Bibliography

[1] A. J. Acosta. An experimental study of cavitating inducers. *Second Symposium on Naval Hydrodynamics*, 1958.

[2] A. J. Acosta. Flow in inducer pumps, an aperçu. *Proceedings of the 4th International Symposium on Transport Phenomena and Dynamics of Rotating Machinery*, 1992.

[3] A. J. Acosta, Y. Tsujimoto, Y. Yoshida, S. Azuma, and C. Paul. Effects of leading edge sweep on the cavitating characteristics of inducer pumps. *International Journal of Rotating Machinery*, 7(6):397–404, 2001.

[4] ANSYS, Inc. Bladegen user's guide, 2017.

[5] ANSYS, Inc. CFX Documentation, 2017.

[6] ANSYS, Inc. ICEM CFD Documentation, 2017.

[7] ANSYS, Inc. TurboGrid Documentation, 2017.

[8] ANSYS, Inc. Fluent Documentation, 2018.

[9] K. Ashihara, A. Goto, K. Kamijo, H. Yamada, and M. Uchiumi. Study on turbopump inducers designed by 3-d inverse design method. *Proceedings of the AFI-2001 The First International Symposium on Advanced Fluid Information*, 2001.

[10] K. Ashihara, A. Goto, K. Kamijo, H. Yamada, and M. Uchiumi. Improvements of inducer inlet backflow characteristics using 3-d inverse design method. *American Institute of Aeronautics and Astronautics AIAA 2002-4158*, 2002.

[11] ASME, V&V 20-2009. Standard for verification and validation in computational fluid dynamics and heat transfer, 2009.

[12] F. Bakir, S. Kouidri, R. Noguera, and R. Rey. Design and analysis of axial inducers performances. *ASME FEDSM 98-5118*, 1998.

[13] F. Bakir, S. Kouidri, R. Noguera, and R. Rey. Experimental analysis of an axial inducer influence of the shape of the blade leading edge on the performances in cavitating regime. *Journal of Fluids Engineering*, 125(2):293–301, 2003. doi: 10.1115/1.1539872.

[14] F. Bakir, R. Rey, A. Gerber, T. Belamri, and B. Hutchinson. Numerical and experimental investigations of the cavitating behavior of an inducer. *Int J Rotating Machinery*, 10:15–25, 2004.

[15] S. Behnel, R. Bradshaw, C. Citro, L. Dalcin, D. S. Seljebotn, and K. Smith. Cython: The best of both worlds. *Computing in Science & Engineering*, 13(2):31–39, Mar 2011. doi: 10.1109/mcse.2010.118.

[16] C. Bramanti, A. Cervone, and L. d'Agostino. A simplified analytical model for evaluating the noncavitating performance of axial inducers. *43rd AIAA/AS-ME/SAE/ASEE Joint Propulsion Conference & Exhibit*, 2007.

[17] C. Brennen. *Hydrodynamics of Pumps*. Oxford University Press, 1994. ISBN 0198564422.

[18] A. R. Budris and P. A. Mayleben. Effects of entrained air, NPSH margin, and suction piping on cavitation in centrifugal pumps. In *Proceedings of the 15th International Pump Users Symposium*. Texas A&M University. Turbomachinery Laboratories, 1998.

[19] S. H. Carpenter. Performance of cavitating axial inducers with varying tip clearance and solidity. Master's thesis, California Institute of Technology, 1957.

[20] A. D. S. Carter and H. P. Hughes. A theoretical investigation into the effect of profile shape on the performance of aerofoils in cascade. *British A.R.C.*, R&M 2384, 1946.

[21] I. B. Celik, U. Ghia, P. J. Roache, C. J. Freitas, H. Coleman, and P. E. Raad. Procedure for estimation and reporting of uncertainty due to discretization in cfd applications. *Journal of Fluids Engineering*, 130(7), 07 2008. ISSN 0098-2202. doi: 10.1115/1.2960953. 078001.

[22] C.-H. Choi, J.-S. Kim, and J. Kim. Study on the forward-sweep inducer for lre turbopumps. *Acta Astronautica*, 65:214 – 220, 2009.

[23] P. Cooper. Analysis of single- and two-phase flows in turbopump inducers. *Journal of Engineering for Power*, 89(4):577–586, 1967. doi: 10.1115/1.3616742.

[24] O. Coutier-Delgosha, R. Fortes-Patella, J. L. Reboud, N. Hakimi, and C. Hirsch. Numerical simulation of cavitating flow in 2d and 3d inducer geometries. *International Journal for Numerical Methods in Fluids*, 48:135–167, 2005. doi: 10.1002/fld.820.

[25] L. d'Agostino, L. Torre, A. Pasini, and A. Cervone. On the preliminary design and noncavitating performance prediction of tapered axial inducers. *Journal of Fluids Engineering*, 130(11):111303–1–111303–8, 2008. doi: 10.1115/1.2979007.

[26] DIN EN ISO 9906:2012. Rotodynamic pumps - hydraulic performance acceptance tests, 2012.

[27] S. L. Dixon and C. A. Hall. *Fluid Mechanics and Thermodynamics of Turbomachinery.* Butterworth-Heinemann, Elsevier Inc., 2010.

[28] G. E. Farin, J. Hoschek, and M.-S. Kim. *Handbook of computer aided geometric design.* Elsevier, Amsterdam, 2002. ISBN 0-444-51104-0.

[29] M. Farrashkhalvat and J. P. Miles. *Basic Structured Grid Generation.* Butterworth Heinemann, 2003.

[30] R. Furst and J. Desclaux. A simple procedure for prediction of npsh required by inducers. *Pumping Machinery*, 1989.

[31] J. F. Gülich. *Kreiselpumpen.* Springer Vieweg, 4th edition, 2013. ISBN 978-3-642-40031-5. doi: 10.1007/978-3-642-40032-2.

[32] J. Hoschek and D. Lasser. *Fundamentals of Computer Aided Geometric Design.* A. K. Peters, Ltd., Natick, MA, USA, 1993. ISBN 1-56881-007-5.

[33] J. D. Hunter. Matplotlib: A 2d graphics environment. *Computing in Science & Engineering*, 9(3):90–95, 2007. doi: 10.1109/MCSE.2007.55.

[34] IEC 60193. Hydraulic turbines, storage pumps and pump-turbines - model acceptance tests, 1999.

[35] ISO/IEC 21778:2017. The json data interchange syntax, 2017.

[36] K. J. Jakobsen. *Liquid Rocket Turbopump Inducers.* NASA SP-8052, 1971.

[37] A. Janigro and F. Ferrini. Inducer pumps. *Recent Progress in Pump Research*, von Karman Institute for Fluid Dynamics Lecture Series 61, 1973.

[38] D. Japikse. Overview of industrial and rocket turbopump inducer design. *Fourth International Symposium on Cavitation, California Institute of Technology, Pasadena, CA USA*, 2001. CAV2001:sessionB7.001.

[39] D. Japikse, W. D. Marscher, and R. B. Furst. *Centrifugal Pump Design and Performance.* Concepts ETI, Inc., 1997. ISBN 9780933283091.

[40] JCGM. Evaluation of measurement data - guide to the expression of uncertainty in measurement, 2008.

[41] E. S. Karakas, H. Watanabe, M. Aureli, and C. A. Evrensel. Cavitation performance of constant and variable pitch helical inducers for centrifugal pumps: Effect of inducer tip clearance. *Journal of Fluids Engineering*, 142(2), 10 2019. doi: 10.1115/1.4044629. 021101.

[42] Y. Kita, K. Furusho, T. Yoshida, K. Hirose, and K. Yamamoto. Overall performance of flat-plate helical inducers. *JSME Trans.*, Ser. B:3324–3329, 1992.

[43] A. Knapp. *Numerische und experimentelle Untersuchung der Auswirkungen von Auslegungsmethoden für Spiralgehäuse auf die Performance einer Kreiselpumpe.* PhD thesis, Technische Universität Kaiserslautern, 2019.

[44] S. Krämer. *Entwurf von Beschaufelungen hydraulischer Maschinen mit Hilfe neuronaler Netze.* PhD thesis, Technische Universität München, 2006.

[45] B. Lakshminarayana. Three-dimensional flow field in rocket pump inducers part 1: Measured flow field inside the rotating blade passage and at the exit. *Journal of Fluids Engineering*, 95(4):567–578, 1973. doi: 10.1115/1.3447071.

[46] B. Lakshminarayana. Fluid dynamics of inducers - a review. *Journal of Fluids Engineering*, 104:411–427, 1982.

[47] B. Lakshminarayana. *Fluid Dynamics and Heat Transfer of Turbomachinery.* John Wiley & Sons, New York, 1995. ISBN 9780471855460.

[48] B. Lakshminarayana and C. A. Gorton. Three dimensional flow field in rocket pump inducers part 2: Mean flow and turbulence characteristics inside the rotor passage, and theoretical analysis. Technical report, Pennsylvania State University, 1975.

[49] R. Lewis. *Turbomachinery Performance Analysis.* Butterworth-Heinemann, 1996. ISBN 1850655758.

[50] R. Lewis. *Vortex Element Methods for Fluid Dynamic Analysis of Engineering Systems.* Cambridge University Press, 2005. ISBN 9780521017541.

[51] W.-G. Li. Head curve of noncavitating inducer. *Journal of Fluids Engineering*, 133 (2), 2011. doi: 10.1115/1.4003504. 024501.

[52] S. Lieblein. Incidence and deviation-angle correlations for compressor cascades. *Journal of Basic Engineering*, 82(3):575–584, 09 1960. doi: 10.1115/1.3662666.

[53] E. J. Logan. *Handbook of Turbomachinery.* Marcel Dekker, Inc., 2nd edition, 2003.

[54] P. L. I. Miller. *Blade geometry description using B-splines and general surfaces of revolution.* PhD thesis, Iowa State University, Ames, Iowa, 2000.

[55] M. E. Mortensen. *Geometric Modeling.* John Wiley and Sons, Inc., 2nd edition, 1997.

[56] M. Necati Özisik. *Finite Difference Methods in Heat Transfer.* CRC Press, 1994. ISBN 0-8493-2491-2.

[57] T. Paviot. pythonOCC - A 3D CAD/CAE/PLM development framework for the Python programming language, Version 0.18.1, December 2017. `https://github.com/tpaviot/pythonocc`, accessed April 16, 2019.

[58] C. Pfleiderer and H. Petermann. *Strömungsmaschinen.* Springer, Berlin/Heidelberg, 2005. ISBN 3-540-22173-5.

[59] L. Piegl and W. Tiller. *The NURBS Book.* Springer-Verlag, Berlin, Heidelberg, 1997. ISBN 3-540-61545-8.

[60] R. H. Pletcher, J. C. Tannehill, and D. A. Anderson. *Computational Fluid Mechanics and Heat Transfer.* CRC Press, 2013.

[61] X. Qiu, C. Mallikarachchi, and M. R. Anderson. A new slip factor model for axial and radial impellers. *Proceedings of the ASME Turbo Expo*, 2007.

[62] X. Qiu, D. Japikse, J. Zhao., and M. R. Anderson. Analysis and validation of a unified slip factor model for impellers at design and off-design conditions. *Proceedings of ASME Turbo Expo*, 2010.

[63] C. C. Ross and G. Banerian. Some aspects of high-suction specific-speed pump inducers. *Transactions of the American Society of Mechanical Engineers*, 78:1715–1721, 1956.

[64] N. Scholz. *Aerodynamik der Schaufelgitter.* G. Braun GmbH, Karlsruhe, 1965.

[65] L. B. Stripling. Cavitation in turbopumps - part 2. *Journal of Fluids Engineering*, 84(3):339–350, 1962. doi: 10.1115/1.3657315.

[66] L. B. Stripling and A. J. Acosta. Cavitation in turbopumps - part 1. *Journal of Fluids Engineering*, 84(3):326–338, 1962. doi: 10.1115/1.3657314.

[67] J. F. Thompson, B. K. Soni, and N. P. Weatherhill. *Handbook of Grid Generation.* CRC Press, 1999.

[68] H. K. Versteeg and W. Malalasekera. *An Introduction to Computational Fluid Dynamics*. Pearson Education Limited, Harlow, 2007. ISBN 978-0-13-127498-3.

[69] P. Virtanen, R. Gommers, T. E. Oliphant, M. Haberland, T. Reddy, D. Cournapeau, E. Burovski, P. Peterson, W. Weckesser, J. Bright, S. J. van der Walt, M. Brett, J. Wilson, K. Jarrod Millman, N. Mayorov, A. R. J. Nelson, E. Jones, R. Kern, E. Larson, C. Carey, İ. Polat, Y. Feng, E. W. Moore, J. Vand erPlas, D. Laxalde, J. Perktold, R. Cimrman, I. Henriksen, E. A. Quintero, C. R. Harris, A. M. Archibald, A. H. Ribeiro, F. Pedregosa, P. van Mulbregt, and SciPy 1.0 Contributors. SciPy 1.0–Fundamental Algorithms for Scientific Computing in Python. *arXiv e-prints*, art. arXiv:1907.10121, Jul 2019.

[70] H. Watanabe and H. Tsukamoto. Design optimization of cryogenic pump inducer. *Proceedings of 2010 International Conference on Pumps and Fans*, 2010.

[71] G. F. Wisclicenus. Preliminary design of turbopumps and related machinery. Reference Publication 1170, NASA, 1986.

List of Figures

List of Tables

A Meridional Flow Computation

A.1 Governing Equation

The governing equation of simplified meridional flow (Equation 2.68) has to be solved numerically for arbitrary shaped meridional sections. A finite difference method is applied in this thesis, which itself depends on the usage of an appropriate grid. Thus, the next section deals with the grid generation problem before the solution procedure of Equation 2.68 is discussed.

The formulas provided in the following two sections are based on the explanations and mathematical derivations available in the open literature, e.g. [29, 56, 60, 67]. They are included in this appendix in order to serve as a compact reference for readers that may be confronted with similar problems.

A.2 Elliptical Grid Generation

A.2.1 Transformation of Partial Derivatives

The two-dimensional flow domain of arbitrary shaped meridional sections can hardly be represented by a Cartesian or rectilinear grid. Hence, the grid lines are generally curved in the physical space. Unfortunately, calculation of derivatives by means of finite differences along these curved grid lines is difficult. To circumvent this problem a coordinate transformation is performed leading to a rectilinear or a Cartesian representation of the physical grid in the computational domain.

If the physical coordinates in two dimensions are given as (x, y), which can simply be replaced by (z, r) in case of the meridional section discussed in Section 2.4.2, then the equivalent points in the computational domain are described by (ξ, η) coordinates as follows [56]:

$$\xi = \xi(x, y) \tag{A.1}$$

$$\eta = \eta(x, y). \tag{A.2}$$

Accordingly, the inverted procedure is written as:

$$x = x(\xi, \eta) \tag{A.3}$$

$$y = y(\xi, \eta) \tag{A.4}$$

Considering these relations the partial derivatives have to be transformed to the com-

putational coordinate system according to the chain rule. The first partial derivatives read:

$$\left(\frac{\partial}{\partial x}\right) = \left(\frac{\partial}{\partial \xi}\right)\left(\frac{\partial \xi}{\partial x}\right) + \left(\frac{\partial}{\partial \eta}\right)\left(\frac{\partial \eta}{\partial x}\right)$$

$$\left(\frac{\partial}{\partial y}\right) = \left(\frac{\partial}{\partial \xi}\right)\left(\frac{\partial \xi}{\partial y}\right) + \left(\frac{\partial}{\partial \eta}\right)\left(\frac{\partial \eta}{\partial y}\right)$$

Analogously, the second order partial derivatives can be formulated as:

$$\left(\frac{\partial^2}{\partial x^2}\right) = \left(\frac{\partial}{\partial x}\right)\left(\frac{\partial}{\partial x}\right) = \left(\frac{\partial}{\partial x}\right)\left[\left(\frac{\partial}{\partial \xi}\right)\left(\frac{\partial \xi}{\partial x}\right) + \left(\frac{\partial}{\partial \eta}\right)\left(\frac{\partial \eta}{\partial x}\right)\right]$$

$$= \left(\frac{\partial^2}{\partial x \partial \xi}\right)\left(\frac{\partial \xi}{\partial x}\right) + \left(\frac{\partial}{\partial \xi}\right)\left(\frac{\partial^2 \xi}{\partial x^2}\right) + \left(\frac{\partial^2}{\partial x \partial \eta}\right)\left(\frac{\partial \eta}{\partial x}\right) + \left(\frac{\partial}{\partial \eta}\right)\left(\frac{\partial^2 \eta}{\partial x^2}\right)$$

$$\left(\frac{\partial^2}{\partial y^2}\right) = \left(\frac{\partial}{\partial y}\right)\left(\frac{\partial}{\partial y}\right) = \left(\frac{\partial}{\partial y}\right)\left[\left(\frac{\partial}{\partial \xi}\right)\left(\frac{\partial \xi}{\partial y}\right) + \left(\frac{\partial}{\partial \eta}\right)\left(\frac{\partial \eta}{\partial y}\right)\right]$$

$$= \left(\frac{\partial^2}{\partial y \partial \xi}\right)\left(\frac{\partial \xi}{\partial y}\right) + \left(\frac{\partial}{\partial \xi}\right)\left(\frac{\partial^2 \xi}{\partial y^2}\right) + \left(\frac{\partial^2}{\partial y \partial \eta}\right)\left(\frac{\partial \eta}{\partial y}\right) + \left(\frac{\partial}{\partial \eta}\right)\left(\frac{\partial^2 \eta}{\partial y^2}\right)$$

For the mixed partial derivatives the following expressions can be obtained:

$$\left(\frac{\partial^2}{\partial x \partial \xi}\right) = \left(\frac{\partial}{\partial x}\right)\left(\frac{\partial}{\partial \xi}\right) = \left[\left(\frac{\partial}{\partial \xi}\right)\left(\frac{\partial \xi}{\partial x}\right) + \left(\frac{\partial}{\partial \eta}\right)\left(\frac{\partial \eta}{\partial x}\right)\right]\left(\frac{\partial}{\partial \xi}\right)$$

$$= \left(\frac{\partial^2}{\partial \xi^2}\right)\left(\frac{\partial \xi}{\partial x}\right) + \left(\frac{\partial}{\partial \xi}\right)\left(\frac{\partial^2 \xi}{\partial x \partial \xi}\right) + \left(\frac{\partial^2}{\partial \eta \partial \xi}\right)\left(\frac{\partial \eta}{\partial x}\right) + \left(\frac{\partial}{\partial \eta}\right)\left(\frac{\partial^2 \eta}{\partial x \partial \xi}\right)$$

$$\left(\frac{\partial^2}{\partial x \partial \eta}\right) = \left(\frac{\partial}{\partial x}\right)\left(\frac{\partial}{\partial \eta}\right) = \left[\left(\frac{\partial}{\partial \xi}\right)\left(\frac{\partial \xi}{\partial x}\right) + \left(\frac{\partial}{\partial \eta}\right)\left(\frac{\partial \eta}{\partial x}\right)\right]\left(\frac{\partial}{\partial \eta}\right)$$

$$= \left(\frac{\partial^2}{\partial \xi \partial \eta}\right)\left(\frac{\partial \xi}{\partial x}\right) + \left(\frac{\partial}{\partial \xi}\right)\left(\frac{\partial^2 \xi}{\partial x \partial \eta}\right) + \left(\frac{\partial^2}{\partial \eta^2}\right)\left(\frac{\partial \eta}{\partial x}\right) + \left(\frac{\partial}{\partial \eta}\right)\left(\frac{\partial^2 \eta}{\partial x \partial \eta}\right)$$

$$\left(\frac{\partial^2}{\partial y \partial \xi}\right) = \left(\frac{\partial}{\partial y}\right)\left(\frac{\partial}{\partial \xi}\right) = \left[\left(\frac{\partial}{\partial \xi}\right)\left(\frac{\partial \xi}{\partial y}\right) + \left(\frac{\partial}{\partial \eta}\right)\left(\frac{\partial \eta}{\partial y}\right)\right]\left(\frac{\partial}{\partial \xi}\right)$$

$$= \left(\frac{\partial^2}{\partial \xi^2}\right)\left(\frac{\partial \xi}{\partial y}\right) + \left(\frac{\partial}{\partial \xi}\right)\left(\frac{\partial^2 \xi}{\partial y \partial \xi}\right) + \left(\frac{\partial^2}{\partial \eta \partial \xi}\right)\left(\frac{\partial \eta}{\partial y}\right) + \left(\frac{\partial}{\partial \eta}\right)\left(\frac{\partial^2 \eta}{\partial y \partial \xi}\right)$$

$$\left(\frac{\partial^2}{\partial y \partial \eta}\right) = \left(\frac{\partial}{\partial y}\right)\left(\frac{\partial}{\partial \eta}\right) = \left[\left(\frac{\partial}{\partial \xi}\right)\left(\frac{\partial \xi}{\partial y}\right) + \left(\frac{\partial}{\partial \eta}\right)\left(\frac{\partial \eta}{\partial y}\right)\right]\left(\frac{\partial}{\partial \eta}\right)$$

$$= \left(\frac{\partial^2}{\partial \xi \partial \eta}\right)\left(\frac{\partial \xi}{\partial y}\right) + \left(\frac{\partial}{\partial \xi}\right)\left(\frac{\partial^2 \xi}{\partial y \partial \eta}\right) + \left(\frac{\partial^2}{\partial \eta^2}\right)\left(\frac{\partial \eta}{\partial y}\right) + \left(\frac{\partial}{\partial \eta}\right)\left(\frac{\partial^2 \eta}{\partial y \partial \eta}\right)$$

Because of the following relations all terms in the gray boxes evaluate to zero:

$$\left(\frac{\partial^2 \xi}{\partial x \partial \xi}\right) = \left(\frac{\partial}{\partial x}\right)\left(\frac{\partial \xi}{\partial \xi}\right) = \left(\frac{\partial}{\partial x}\right)(1) = 0$$

$$\left(\frac{\partial^2 \eta}{\partial x \partial \xi}\right) = \left(\frac{\partial}{\partial x}\right)\left(\frac{\partial \eta}{\partial \xi}\right) = \left(\frac{\partial}{\partial x}\right)(0) = 0$$

$$\left(\frac{\partial^2 \xi}{\partial x \partial \eta}\right) = \left(\frac{\partial}{\partial x}\right)\left(\frac{\partial \xi}{\partial \eta}\right) = \left(\frac{\partial}{\partial x}\right)(0) = 0$$

$$\left(\frac{\partial^2 \eta}{\partial x \partial \eta}\right) = \left(\frac{\partial}{\partial x}\right)\left(\frac{\partial \eta}{\partial \eta}\right) = \left(\frac{\partial}{\partial x}\right)(1) = 0$$

$$\left(\frac{\partial^2 \xi}{\partial y \partial \xi}\right) = \left(\frac{\partial}{\partial y}\right)\left(\frac{\partial \xi}{\partial \xi}\right) = \left(\frac{\partial}{\partial y}\right)(1) = 0$$

$$\left(\frac{\partial^2 \eta}{\partial y \partial \xi}\right) = \left(\frac{\partial}{\partial y}\right)\left(\frac{\partial \eta}{\partial \xi}\right) = \left(\frac{\partial}{\partial y}\right)(0) = 0$$

$$\left(\frac{\partial^2 \xi}{\partial y \partial \eta}\right) = \left(\frac{\partial}{\partial y}\right)\left(\frac{\partial \xi}{\partial \eta}\right) = \left(\frac{\partial}{\partial y}\right)(0) = 0$$

$$\left(\frac{\partial^2 \eta}{\partial y \partial \eta}\right) = \left(\frac{\partial}{\partial y}\right)\left(\frac{\partial \eta}{\partial \eta}\right) = \left(\frac{\partial}{\partial y}\right)(1) = 0$$

Therefore, the mixed partial derivatives can be simplified to:

$$\left(\frac{\partial^2}{\partial x \partial \xi}\right) = \left(\frac{\partial^2}{\partial \xi^2}\right)\left(\frac{\partial \xi}{\partial x}\right) + \left(\frac{\partial^2}{\partial \eta \partial \xi}\right)\left(\frac{\partial \eta}{\partial x}\right)$$

$$\left(\frac{\partial^2}{\partial x \partial \eta}\right) = \left(\frac{\partial^2}{\partial \xi \partial \eta}\right)\left(\frac{\partial \xi}{\partial x}\right) + \left(\frac{\partial^2}{\partial \eta^2}\right)\left(\frac{\partial \eta}{\partial x}\right)$$

$$\left(\frac{\partial^2}{\partial y \partial \xi}\right) = \left(\frac{\partial^2}{\partial \xi^2}\right)\left(\frac{\partial \xi}{\partial y}\right) + \left(\frac{\partial^2}{\partial \eta \partial \xi}\right)\left(\frac{\partial \eta}{\partial y}\right)$$

$$\left(\frac{\partial^2}{\partial y \partial \eta}\right) = \left(\frac{\partial^2}{\partial \xi \partial \eta}\right)\left(\frac{\partial \xi}{\partial y}\right) + \left(\frac{\partial^2}{\partial \eta^2}\right)\left(\frac{\partial \eta}{\partial y}\right)$$

Inserting the expressions for the mixed partial derivatives the second order derivatives can be written as:

$$\left(\frac{\partial^2}{\partial x^2}\right) = \left[\left(\frac{\partial^2}{\partial \xi^2}\right)\left(\frac{\partial \xi}{\partial x}\right) + \left(\frac{\partial^2}{\partial \eta \partial \xi}\right)\left(\frac{\partial \eta}{\partial x}\right)\right]\left(\frac{\partial \xi}{\partial x}\right) + \left(\frac{\partial}{\partial \xi}\right)\left(\frac{\partial^2 \xi}{\partial x^2}\right)$$

$$+ \left[\left(\frac{\partial^2}{\partial \xi \partial \eta}\right)\left(\frac{\partial \xi}{\partial x}\right) + \left(\frac{\partial^2}{\partial \eta^2}\right)\left(\frac{\partial \eta}{\partial x}\right)\right]\left(\frac{\partial \eta}{\partial x}\right) + \left(\frac{\partial}{\partial \eta}\right)\left(\frac{\partial^2 \eta}{\partial x^2}\right)$$

$$= \left(\frac{\partial^2}{\partial \xi^2}\right)\left(\frac{\partial \xi}{\partial x}\right)^2 + \left(\frac{\partial^2}{\partial \eta^2}\right)\left(\frac{\partial \eta}{\partial x}\right)^2 + 2\left(\frac{\partial^2}{\partial \eta \partial \xi}\right)\left(\frac{\partial \xi}{\partial x}\right)\left(\frac{\partial \eta}{\partial x}\right)$$

$$+ \left(\frac{\partial}{\partial\xi}\right)\left(\frac{\partial^2\xi}{\partial x^2}\right) + \left(\frac{\partial}{\partial\eta}\right)\left(\frac{\partial^2\eta}{\partial x^2}\right)$$

$$\left(\frac{\partial^2}{\partial y^2}\right) = \left[\left(\frac{\partial^2}{\partial\xi^2}\right)\left(\frac{\partial\xi}{\partial y}\right) + \left(\frac{\partial^2}{\partial\eta\partial\xi}\right)\left(\frac{\partial\eta}{\partial y}\right)\right]\left(\frac{\partial\xi}{\partial y}\right) + \left(\frac{\partial}{\partial\xi}\right)\left(\frac{\partial^2\xi}{\partial y^2}\right)$$

$$+ \left[\left(\frac{\partial^2}{\partial\xi\partial\eta}\right)\left(\frac{\partial\xi}{\partial y}\right) + \left(\frac{\partial^2}{\partial\eta^2}\right)\left(\frac{\partial\eta}{\partial y}\right)\right]\left(\frac{\partial\eta}{\partial y}\right) + \left(\frac{\partial}{\partial\eta}\right)\left(\frac{\partial^2\eta}{\partial y^2}\right)$$

$$= \left(\frac{\partial^2}{\partial\xi^2}\right)\left(\frac{\partial\xi}{\partial y}\right)^2 + \left(\frac{\partial^2}{\partial\eta^2}\right)\left(\frac{\partial\eta}{\partial y}\right)^2 + 2\left(\frac{\partial^2}{\partial\eta\partial\xi}\right)\left(\frac{\partial\xi}{\partial y}\right)\left(\frac{\partial\eta}{\partial y}\right)$$

$$+ \left(\frac{\partial}{\partial\xi}\right)\left(\frac{\partial^2\xi}{\partial y^2}\right) + \left(\frac{\partial}{\partial\eta}\right)\left(\frac{\partial^2\eta}{\partial y^2}\right)$$

For the mixed partial derivative the following transformation can be obtained analogously:

$$\left(\frac{\partial^2}{\partial x\partial y}\right) = \left(\frac{\partial}{\partial x}\right)\left(\frac{\partial}{\partial y}\right) = \left(\frac{\partial}{\partial x}\right)\left[\left(\frac{\partial}{\partial\xi}\right)\left(\frac{\partial\xi}{\partial y}\right) + \left(\frac{\partial}{\partial\eta}\right)\left(\frac{\partial\eta}{\partial y}\right)\right]$$

$$= \boxed{\left(\frac{\partial^2}{\partial\xi\partial x}\right)}\left(\frac{\partial\xi}{\partial y}\right) + \left(\frac{\partial}{\partial\xi}\right)\left(\frac{\partial^2\xi}{\partial x\partial y}\right) + \boxed{\left(\frac{\partial^2}{\partial\eta\partial x}\right)}\left(\frac{\partial\eta}{\partial y}\right) + \left(\frac{\partial}{\partial\eta}\right)\left(\frac{\partial^2\eta}{\partial x\partial y}\right)$$

This equation can be further simplified by inserting the already derived expressions for the terms in the gray boxes:

$$\left(\frac{\partial^2}{\partial x\partial y}\right) = \left(\frac{\partial}{\partial\xi}\right)\left(\frac{\partial^2\xi}{\partial x\partial y}\right) + \left(\frac{\partial}{\partial\eta}\right)\left(\frac{\partial^2\eta}{\partial x\partial y}\right)$$

$$+ \left[\left(\frac{\partial^2}{\partial\xi^2}\right)\left(\frac{\partial\xi}{\partial x}\right) + \left(\frac{\partial^2}{\partial\eta\partial\xi}\right)\left(\frac{\partial\eta}{\partial x}\right)\right]\left(\frac{\partial\xi}{\partial y}\right)$$

$$+ \left[\left(\frac{\partial^2}{\partial\xi\partial\eta}\right)\left(\frac{\partial\xi}{\partial x}\right) + \left(\frac{\partial^2}{\partial\eta^2}\right)\left(\frac{\partial\eta}{\partial x}\right)\right]\left(\frac{\partial\eta}{\partial y}\right)$$

$$= \left(\frac{\partial}{\partial\xi}\right)\left(\frac{\partial^2\xi}{\partial x\partial y}\right) + \left(\frac{\partial}{\partial\eta}\right)\left(\frac{\partial^2\eta}{\partial x\partial y}\right)$$

$$+ \left(\frac{\partial^2}{\partial\xi^2}\right)\left(\frac{\partial\xi}{\partial x}\right)\left(\frac{\partial\xi}{\partial y}\right) + \left(\frac{\partial^2}{\partial\eta^2}\right)\left(\frac{\partial\eta}{\partial x}\right)\left(\frac{\partial\eta}{\partial y}\right)$$

$$+ \left(\frac{\partial^2}{\partial\eta\partial\xi}\right)\left[\left(\frac{\partial\eta}{\partial x}\right)\left(\frac{\partial\xi}{\partial y}\right) + \left(\frac{\partial\xi}{\partial x}\right)\left(\frac{\partial\eta}{\partial y}\right)\right]$$

A.2.2 Transformation Metrics

The relation between the partial derivatives in the physical and the computational coordinate system can be described by the metrics of the transformation. By writing the

total differentials for both coordinate systems the following relations are obtained:

$$d\xi = \left(\frac{\partial \xi}{\partial x}\right) dx + \left(\frac{\partial \xi}{\partial y}\right) dy$$

$$d\eta = \left(\frac{\partial \eta}{\partial x}\right) dx + \left(\frac{\partial \eta}{\partial y}\right) dy$$

$$dx = \left(\frac{\partial x}{\partial \xi}\right) d\xi + \left(\frac{\partial x}{\partial \eta}\right) d\eta$$

$$dy = \left(\frac{\partial y}{\partial \xi}\right) d\xi + \left(\frac{\partial y}{\partial \eta}\right) d\eta$$

The partial derivatives of the coordinates of the computational system with respect to the physical coordinates are called the direct metrics or just metrics, the partial derivatives of the physical coordinates with respect to the computational coordinates are called computational or inverse metrics [56]. Written in matrix notation the equations above read:

$$\begin{bmatrix} d\xi \\ d\eta \end{bmatrix} = \begin{bmatrix} \frac{\partial \xi}{\partial x} & \frac{\partial \xi}{\partial y} \\ \frac{\partial \eta}{\partial x} & \frac{\partial \eta}{\partial y} \end{bmatrix} \begin{bmatrix} dx \\ dy \end{bmatrix}$$

$$\begin{bmatrix} dx \\ dy \end{bmatrix} = \begin{bmatrix} \frac{\partial x}{\partial \xi} & \frac{\partial x}{\partial \eta} \\ \frac{\partial y}{\partial \xi} & \frac{\partial y}{\partial \eta} \end{bmatrix} \begin{bmatrix} d\xi \\ d\eta \end{bmatrix}$$

From this notation it gets clear that the the following relation exists between the partial derivatives:

$$\begin{bmatrix} \frac{\partial \xi}{\partial x} & \frac{\partial \xi}{\partial y} \\ \frac{\partial \eta}{\partial x} & \frac{\partial \eta}{\partial y} \end{bmatrix} = \begin{bmatrix} \frac{\partial x}{\partial \xi} & \frac{\partial x}{\partial \eta} \\ \frac{\partial y}{\partial \xi} & \frac{\partial y}{\partial \eta} \end{bmatrix}^{-1} = \boldsymbol{A}^{-1}$$

Realizing that the determinant of the Jacobian matrix, usually just called the Jacobian, is given by

$$J = \det \boldsymbol{J} = \det \begin{bmatrix} \frac{\partial x}{\partial \xi} & \frac{\partial y}{\partial \xi} \\ \frac{\partial x}{\partial \eta} & \frac{\partial y}{\partial \eta} \end{bmatrix} = \det \boldsymbol{J}^{T} = \det \boldsymbol{A} = \frac{\partial x}{\partial \xi}\frac{\partial y}{\partial \eta} - \frac{\partial x}{\partial \eta}\frac{\partial y}{\partial \xi}$$

the inversion of Matrix $\boldsymbol{A}$ can be performed as:

$$\boldsymbol{A}^{-1} = \frac{1}{J} \begin{bmatrix} \frac{\partial y}{\partial \eta} & -\frac{\partial x}{\partial \eta} \\ -\frac{\partial y}{\partial \xi} & \frac{\partial x}{\partial \xi} \end{bmatrix}$$

The relations between the direct and inverse metrics can therefore be stated as:

$$\frac{\partial \xi}{\partial x} = \frac{1}{J}\frac{\partial y}{\partial \eta} \tag{A.5a}$$

$$\frac{\partial \xi}{\partial y} = -\frac{1}{J}\frac{\partial x}{\partial \eta} \tag{A.5b}$$

$$\frac{\partial \eta}{\partial x} = -\frac{1}{J}\frac{\partial y}{\partial \xi} \tag{A.5c}$$

$$\frac{\partial \eta}{\partial y} = \frac{1}{J}\frac{\partial x}{\partial \xi} \tag{A.5d}$$

A.2.3 Inverse Laplace Equation

Delivering smooth and unique solutions, elliptic partial differential equations are often used to generate structured grids [29, 60, 67]. The relation between the computational and the physical coordinates in the two dimensional case under consideration is given by a system of two Laplace equations, which is the most simple case of an elliptical system:

$$0 = \nabla^2 \xi = \left(\frac{\partial^2 \xi}{\partial x^2}\right) + \left(\frac{\partial^2 \xi}{\partial y^2}\right) \tag{A.6}$$

$$0 = \nabla^2 \eta = \left(\frac{\partial^2 \eta}{\partial x^2}\right) + \left(\frac{\partial^2 \eta}{\partial y^2}\right) \tag{A.7}$$

Because ξ and η are the known coordinates of a prescribed rectilinear or Cartesian grid in the computational domain this system has to be inverted to obtain the coordinates x and y in the physical domain. By inserting the relations for the transformed second partial derivatives the Laplace operator can be written as:

$$\nabla^2 = \left(\frac{\partial^2}{\partial x^2}\right) + \left(\frac{\partial^2}{\partial y^2}\right) = \left(\frac{\partial^2}{\partial \xi^2}\right)\underbrace{\left[\left(\frac{\partial \xi}{\partial x}\right)^2 + \left(\frac{\partial \xi}{\partial y}\right)^2\right]}_{A}$$

$$+ 2\left(\frac{\partial^2}{\partial \xi \partial \eta}\right)\underbrace{\left[\left(\frac{\partial \xi}{\partial x}\right)\left(\frac{\partial \eta}{\partial x}\right) + \left(\frac{\partial \xi}{\partial y}\right)\left(\frac{\partial \eta}{\partial y}\right)\right]}_{B}$$

$$+ \left(\frac{\partial^2}{\partial \eta^2}\right)\underbrace{\left[\left(\frac{\partial \eta}{\partial x}\right)^2 + \left(\frac{\partial \eta}{\partial y}\right)^2\right]}_{C}$$

$$+ \left(\frac{\partial}{\partial \xi}\right) \underbrace{\left[\left(\frac{\partial^2 \xi}{\partial x^2}\right) + \left(\frac{\partial^2 \xi}{\partial y^2}\right)\right]}_{D} + \left(\frac{\partial}{\partial \eta}\right) \underbrace{\left[\left(\frac{\partial^2 \eta}{\partial x^2}\right) + \left(\frac{\partial^2 \eta}{\partial y^2}\right)\right]}_{E}$$

Using the formulas for the grid metrics (Equation A.5) the following expressions can be obtained for the terms indicated by A, B, C:

$$A = \frac{1}{J^2} \left[\left(\frac{\partial x}{\partial \eta}\right)^2 + \left(\frac{\partial y}{\partial \eta}\right)^2\right] = \frac{1}{J^2} \alpha$$

$$B = -\frac{1}{J^2} \left[\left(\frac{\partial x}{\partial \xi}\right)\left(\frac{\partial x}{\partial \eta}\right) + \left(\frac{\partial y}{\partial \xi}\right)\left(\frac{\partial y}{\partial \eta}\right)\right] = -\frac{1}{J^2} \beta$$

$$C = \frac{1}{J^2} \left[\left(\frac{\partial x}{\partial \xi}\right)^2 + \left(\frac{\partial y}{\partial \xi}\right)^2\right] = \frac{1}{J^2} \gamma$$

The terms D and E can be identified with Equations A.6 and A.7 so that these terms can be set $D = E = 0$. Finally, the inverse system of Laplace equations in terms of x and y reads:

$$0 = \alpha \left(\frac{\partial^2 x}{\partial \xi^2}\right) - 2\beta \left(\frac{\partial^2 x}{\partial \xi \partial \eta}\right) + \gamma \left(\frac{\partial^2 x}{\partial \eta^2}\right) \tag{A.8}$$

$$0 = \alpha \left(\frac{\partial^2 y}{\partial \xi^2}\right) - 2\beta \left(\frac{\partial^2 y}{\partial \xi \partial \eta}\right) + \gamma \left(\frac{\partial^2 y}{\partial \eta^2}\right) \tag{A.9}$$

The geometrical coefficients in the equations above are defined as:

$$\alpha = \left(\frac{\partial x}{\partial \eta}\right)^2 + \left(\frac{\partial y}{\partial \eta}\right)^2$$

$$\beta = \left(\frac{\partial x}{\partial \xi}\right)\left(\frac{\partial x}{\partial \eta}\right) + \left(\frac{\partial y}{\partial \xi}\right)\left(\frac{\partial y}{\partial \eta}\right)$$

$$\gamma = \left(\frac{\partial x}{\partial \xi}\right)^2 + \left(\frac{\partial y}{\partial \xi}\right)^2$$

A.2.4 Grid Generation Procedure

Central differences are used to discretize the partial derivatives occurring in Equations A.8 and A.9. The first and second order partial derivatives can be approximated by the following equations:

$$\left(\frac{\partial x}{\partial \xi}\right)_{i,j} = \frac{x_{i+1,j} - x_{i-1,j}}{2\Delta \xi}$$

$$\left(\frac{\partial x}{\partial \eta}\right)_{i,j} = \frac{x_{i,j+1} - x_{i,j-1}}{2\Delta\eta}$$

$$\left(\frac{\partial y}{\partial \xi}\right)_{i,j} = \frac{y_{i+1,j} - y_{i-1,j}}{2\Delta\xi}$$

$$\left(\frac{\partial y}{\partial \eta}\right)_{i,j} = \frac{y_{i,j+1} - y_{i,j-1}}{2\Delta\eta}$$

$$\left(\frac{\partial^2 x}{\partial \xi^2}\right)_{i,j} = \frac{x_{i+1,j} - 2x_{i,j} - x_{i-1,j}}{\Delta\xi^2}$$

$$\left(\frac{\partial^2 x}{\partial \eta^2}\right)_{i,j} = \frac{x_{i,j+1} - 2x_{i,j} - x_{i,j-1}}{\Delta\eta^2}$$

$$\left(\frac{\partial^2 y}{\partial \xi^2}\right)_{i,j} = \frac{y_{i+1,j} - 2y_{i,j} - y_{i-1,j}}{\Delta\xi^2}$$

$$\left(\frac{\partial^2 y}{\partial \eta^2}\right)_{i,j} = \frac{y_{i,j+1} - 2y_{i,j} - y_{i,j-1}}{\Delta\eta^2}$$

Similarly the mixed partial derivatives can be approximated by:

$$\left(\frac{\partial^2 x}{\partial \xi \partial \eta}\right)_{i,j} = \frac{x_{i+1,j+1} - x_{i+1,j-1} - x_{i-1,j+1} + x_{i-1,j-1}}{4\Delta\xi\Delta\eta}$$

$$\left(\frac{\partial^2 y}{\partial \xi \partial \eta}\right)_{i,j} = \frac{y_{i+1,j+1} - y_{i+1,j-1} - y_{i-1,j+1} + y_{i-1,j-1}}{4\Delta\xi\Delta\eta}$$

Substituting the partial derivatives with their finite difference representations, the discretized Laplace equations are obtained:

$$
\begin{aligned}
0 = {} & \alpha_{i,j} \frac{x_{i+1,j} - 2x_{i,j} + x_{i-1,j}}{\Delta\xi^2} \\
& - 2\beta_{i,j} \frac{x_{i+1,j+1} - x_{i+1,j-1} - x_{i-1,j+1} + x_{i-1,j-1}}{4\Delta\xi\Delta\eta} \\
& + \gamma_{i,j} \frac{x_{i,j+1} - 2x_{i,j} + x_{i,j-1}}{\Delta\eta^2}
\end{aligned}
\tag{A.13}
$$

$$
\begin{aligned}
0 = {} & \alpha_{i,j} \frac{y_{i+1,j} - 2y_{i,j} + y_{i-1,j}}{\Delta\xi^2} \\
& - 2\beta_{i,j} \frac{y_{i+1,j+1} - y_{i+1,j-1} - y_{i-1,j+1} + y_{i-1,j-1}}{4\Delta\xi\Delta\eta} \\
& + \gamma_{i,j} \frac{y_{i,j+1} - 2y_{i,j} + y_{i,j-1}}{\Delta\eta^2}
\end{aligned}
\tag{A.14}
$$

In these equations the geometrical coefficients α, β, γ are also approximated by finite differences:

$$\alpha_{i,j} = \left(\frac{x_{i,j+1} - x_{i,j-1}}{2\Delta\eta}\right)^2 + \left(\frac{y_{i,j+1} - y_{i,j-1}}{2\Delta\eta}\right)^2 \tag{A.15a}$$

$$\beta_{i,j} = \frac{x_{i+1,j} - x_{i-1,j}}{2\Delta\xi}\frac{x_{i,j+1} - x_{i,j-1}}{2\Delta\eta} + \frac{y_{i+1,j} - y_{i-1,j}}{2\Delta\xi}\frac{y_{i,j+1} - y_{i,j-1}}{2\Delta\eta} \tag{A.15b}$$

$$\gamma_{i,j} = \left(\frac{x_{i+1,j} - x_{i-1,j}}{2\Delta\xi}\right)^2 + \left(\frac{y_{i+1,j} - y_{i-1,j}}{2\Delta\xi}\right)^2 \tag{A.15c}$$

A.2.5 Solution of the Discretized Equations

Rearranging the discrete versions of the inverse Laplace equations leads to the following equations for the grid coordinates x and y:

$$
\begin{aligned}
x_{i,j} = & \left[2\left(\frac{\alpha_{i,j}}{\Delta\xi^2} + \frac{\gamma_{i,j}}{\Delta\eta^2}\right)\right]^{-1} \Bigg[\frac{\alpha_{i,j}}{\Delta\xi^2}\left(x_{i+1,j} + x_{i-1,j}\right) \\
& - \frac{\beta_{i,j}}{2\Delta\xi\Delta\eta}\left(x_{i+1,j+1} - x_{i+1,j-1} - x_{i-1,j+1} + x_{i-1,j-1}\right) \\
& + \frac{\gamma_{i,j}}{\Delta\eta^2}\left(x_{i,j+1} + x_{i,j-1}\right)\Bigg]
\end{aligned}
\tag{A.16}
$$

$$
\begin{aligned}
y_{i,j} = & \left[2\left(\frac{\alpha_{i,j}}{\Delta\xi^2} + \frac{\gamma_{i,j}}{\Delta\eta^2}\right)\right]^{-1} \Bigg[\frac{\alpha_{i,j}}{\Delta\xi^2}\left(y_{i+1,j} + y_{i-1,j}\right) \\
& - \frac{\beta_{i,j}}{2\Delta\xi\Delta\eta}\left(y_{i+1,j+1} - y_{i+1,j-1} - y_{i-1,j+1} + y_{i-1,j-1}\right) \\
& + \frac{\gamma_{i,j}}{\Delta\eta^2}\left(y_{i,j+1} + y_{i,j-1}\right)\Bigg]
\end{aligned}
\tag{A.17}
$$

The actual values of the coordinates in the computational (ξ, η) plane have no influence on the solution of the aforementioned equations [56]. Therefore, the grid spacing is usually chosen as:

$$\Delta\xi = \Delta\eta = 1 \tag{A.18}$$

In this case, Equations A.16 and A.17 can be further simplified:

$$
\begin{aligned}
x_{i,j} = \frac{1}{2\left(\alpha_{i,j} + \gamma_{i,j}\right)} \Big[& \alpha_{i,j}\left(x_{i+1,j} + x_{i-1,j}\right) \\
& -\frac{1}{2}\beta_{i,j}\left(x_{i+1,j+1} - x_{i+1,j-1} - x_{i-1,j+1} + x_{i-1,j-1}\right) \\
& + \gamma_{i,j}\left(x_{i,j+1} + x_{i,j-1}\right) \Big]
\end{aligned}
\tag{A.19}
$$

$$
\begin{aligned}
y_{i,j} = \frac{1}{2\left(\alpha_{i,j} + \gamma_{i,j}\right)} \Big[& \alpha_{i,j}\left(y_{i+1,j} + y_{i-1,j}\right) \\
& -\frac{1}{2}\beta_{i,j}\left(y_{i+1,j+1} - y_{i+1,j-1} - y_{i-1,j+1} + y_{i-1,j-1}\right) \\
& + \gamma_{i,j}\left(y_{i,j+1} + y_{i,j-1}\right) \Big]
\end{aligned}
\tag{A.20}
$$

Analogously, the following expressions are obtained for the coefficients α, β, γ:

$$
\alpha_{i,j} = \frac{1}{4}\Big[\left(x_{i,j+1} - x_{i,j-1}\right)^2 + \left(y_{i,j+1} - y_{i,j-1}\right)^2\Big]
\tag{A.21a}
$$

$$
\beta_{i,j} = \frac{1}{4}\Big[\left(x_{i+1,j} - x_{i-1,j}\right)\left(x_{i,j+1} - x_{i,j-1}\right) + \left(y_{i+1,j} - y_{i-1,j}\right)\left(y_{i,j+1} - y_{i,j-1}\right)\Big]
\tag{A.21b}
$$

$$
\gamma_{i,j} = \frac{1}{4}\Big[\left(x_{i+1,j} - x_{i-1,j}\right)^2 + \left(y_{i+1,j} - y_{i-1,j}\right)^2\Big]
\tag{A.21c}
$$

The coefficients α, β, γ depend non-linearly on the grid coordinates, which of course are not known a priori. Hence, the above equations represent a coupled system of non-linear equations. Although there exist direct methods for the solution of such systems, an iterative approach is used because of its simpler implementation and lower need of resources. Furthermore, it is not necessary to obtain an exact solution of the already discretized (and therefore approximate) equations.

A formulation of an iterative procedure is already given by Equations A.19 and A.20. If all terms on the right hand side are considered to originate from the previous iteration step, the Jacobi method (JA) is obtained (only the x equation is shown in what follows):

$$
\begin{aligned}
x_{i,j,\text{JA}}^{(n+1)} = \frac{1}{2\left(\alpha_{i,j}^{(n)} + \gamma_{i,j}^{(n)}\right)} \Big[& \alpha_{i,j}^{(n)}\left(x_{i+1,j}^{(n)} + x_{i-1,j}^{(n)}\right) \\
& -\frac{1}{2}\beta_{i,j}^{(n)}\left(x_{i+1,j+1}^{(n)} - x_{i+1,j-1}^{(n)} - x_{i-1,j+1}^{(n)} + x_{i-1,j-1}^{(n)}\right) \\
& + \gamma_{i,j}^{(n)}\left(x_{i,j+1}^{(n)} + x_{i,j-1}^{(n)}\right) \Big]
\end{aligned}
\tag{A.22}
$$

Although it is possible to compute the coefficients α, β, γ during the solution process like the coordinates themselves, this approach is not used because in this case no consistent set of the coefficients is present during the iteration step. Another possibility is to calculate the coefficients lagging one iteration step for the whole grid [56]. This approach is used in the current implementation. By convention the iteration procedure is performed in a nested loop, looping over the second index j first. Usage of all already computed values at the current iteration step leads to the Gauß-Seidel Method:

$$
\begin{aligned}
x_{i,j,\text{GS}}^{(n+1)} = \frac{1}{2\left(\alpha_{i,j}^{(n)} + \gamma_{i,j}^{(n)}\right)} &\left[\alpha_{i,j}^{(n)}\left(x_{i+1,j}^{(n)} + x_{i-1,j}^{(n+1)}\right)\right. \\
&- \frac{1}{2}\beta_{i,j}^{(n)}\left(x_{i+1,j+1}^{(n)} - x_{i+1,j-1}^{(n)} - x_{i-1,j+1}^{(n+1)} + x_{i-1,j-1}^{(n+1)}\right) \\
&\left.+ \gamma_{i,j}^{(n)}\left(x_{i,j+1}^{(n)} + x_{i,j-1}^{(n+1)}\right)\right]
\end{aligned}
\tag{A.23}
$$

The Gauß-Seidel method can be improved by the Successive Over-Relaxation or SOR algorithm, which accelerates convergence by a combination of the solutions of the previous iteration and the current iteration level of the Gauß-Seidel method:

$$
x_{i,j,\text{SOR}}^{(n+1)} = (\omega - 1)x_{i,j,\text{SOR}}^{(n)} + \omega x_{i,j,\text{GS}}^{(n+1)}
\tag{A.24}
$$

It can be shown that the relaxation parameter ω has to lie in the range of $0 < \omega < 2$. Usually ω is chosen in the range of $1 < \omega < 2$ to obtain overrelaxation and therefore faster convergence. For $\omega = 1$ the SOR method is identical to the Gauß-Seidel method. The iteration procedure is stopped if a convergence criterion is satisfied or the maximum number of iterations is reached. In the current implementation convergence is judged based on the relative error of the solution variable x. The iteration process is stopped if the maximum relative error falls below a specified tolerance ϵ:

$$
\max\left(\frac{|x_{i,j}^{(n+1)} - x_{i,j}^{(n)}|}{\max|x|}\right) < \epsilon
\tag{A.25}
$$

A.3 Solution Method

To finally solve the governing equation of simplified meridional flow (Equation 2.68) the partial derivatives have to be transformed as was shown in Section A.2. After

introducing the appropriate terms, the transformed equation can be written as

$$\alpha\left(\frac{\partial^2\Psi}{\partial\xi^2}\right) - 2\beta\left(\frac{\partial^2\Psi}{\partial\xi\partial\eta}\right) + \gamma\left(\frac{\partial^2\Psi}{\partial\eta^2}\right) - \frac{\delta}{r}\left(\left(\frac{\partial\Psi}{\partial\eta}\right)\left(\frac{\partial z}{\partial\xi}\right) - \left(\frac{\partial\Psi}{\partial\xi}\right)\left(\frac{\partial z}{\partial\eta}\right)\right),$$

where δ is equal to the Jacobian J:

$$\delta = \frac{\partial z}{\partial\xi}\frac{\partial r}{\partial\eta} - \frac{\partial z}{\partial\eta}\frac{\partial r}{\partial\xi} = J$$

Substituting the partial derivatives with their central difference approximations and rearranging the whole equation yields:

$$\begin{aligned}
\Psi_{i,j} = \frac{1}{2\left(\alpha_{i,j}+\gamma_{i,j}\right)}&\left[\alpha_{i,j}\left(\Psi_{i+1,j}+\Psi_{i-1,j}\right) + \gamma_{i,j}\left(\Psi_{i,j+1}+\Psi_{i,j-1}\right)\right.\\
&- \frac{1}{2}\beta_{i,j}\left(\Psi_{i+1,j+1}-\Psi_{i+1,j-1}-\Psi_{i-1,j+1}+\Psi_{i-1,j-1}\right)\\
&\left.- \frac{1}{4}\frac{\delta_{i,j}}{r_{i,j}}\left((\Psi_{i,j+1}-\Psi_{i,j-1})(z_{i+1,j}-z_{i-1,j}) - (\Psi_{i+1,j}-\Psi_{i-1,j})(z_{i,j+1}-z_{i,j-1})\right)\right]
\end{aligned}$$

(A.26)

The value of the Jacobian δ at the grid location i,j is analogously discretized by:

$$\delta_{i,j} = \frac{1}{4}\left[\left(z_{i+1,j}-z_{i-1,j}\right)\left(r_{i,j+1}-r_{i,j-1}\right) - \left(z_{i,j+1}-z_{i,j-1}\right)\left(r_{i+1,j}-r_{i-1,j}\right)\right]$$

Equation A.26 is solved by the SOR method as described in Section 2.4.2 for the grid coordinates. Thus, the iteration step is defined as:

$$\Psi_{i,j,\text{SOR}}^{(n+1)} = (\omega - 1)\Psi_{i,j,\text{SOR}}^{(n)} + \omega\Psi_{i,j,\text{GS}}^{(n+1)}$$

(A.27)

Assuming again that the procedure loops over index j first, the Gauß-Seidel step can be written as:

$$\begin{aligned}
\Psi_{i,j,\text{GS}}^{(n+1)} = \frac{1}{2\left(\alpha_{i,j}+\gamma_{i,j}\right)}&\left[\alpha_{i,j}\left(\Psi_{i+1,j}^{(n)}+\Psi_{i-1,j}^{(n+1)}\right) + \gamma_{i,j}\left(\Psi_{i,j+1}^{(n)}+\Psi_{i,j-1}^{(n+1)}\right)\right.\\
&- \frac{1}{2}\beta_{i,j}\left(\Psi_{i+1,j+1}^{(n)}-\Psi_{i+1,j-1}^{(n)}-\Psi_{i-1,j+1}^{(n+1)}+\Psi_{i-1,j-1}^{(n+1)}\right)\\
&\left.- \frac{1}{4}\frac{\delta_{i,j}}{r_{i,j}}\left((\Psi_{i,j+1}^{(n)}-\Psi_{i,j-1}^{(n+1)})(z_{i+1,j}-z_{i-1,j}) - (\Psi_{i+1,j}^{(n)}-\Psi_{i-1,j}^{(n+1)})(z_{i,j+1}-z_{i,j-1})\right)\right]
\end{aligned}$$

(A.28)

Analogously to grid generation, convergence is judged based on the maximum relative error in the solution variable Ψ:

$$(\Delta\Psi)^*_{\max} = \max\left(\frac{|\Psi^{(n+1)}_{i,j} - \Psi^{(n)}_{i,j}|}{\max|\Psi|}\right) < \epsilon \qquad \text{(A.29)}$$

Once the stream function is computed on all the interior grid nodes the flow velocity can be calculated. Stokes' stream function Ψ is connected to the meridional flow velocities by the following equations:

$$c_z = \frac{1}{r}\frac{\partial\Psi}{\partial r} \qquad \text{(A.30a)}$$

$$c_r = -\frac{1}{r}\frac{\partial\Psi}{\partial z} \qquad \text{(A.30b)}$$

Inversion of above equations with the transformation rules for the partial derivatives leads to the following equations for the velocity components:

$$c_z = \frac{1}{r}\frac{\partial\Psi}{\partial r} = \frac{1}{r\delta}\left(\left(\frac{\partial\Psi}{\partial\eta}\right)\left(\frac{\partial z}{\partial\xi}\right) - \left(\frac{\partial\Psi}{\partial\xi}\right)\left(\frac{\partial z}{\partial\eta}\right)\right) \qquad \text{(A.31a)}$$

$$c_r = -\frac{1}{r}\frac{\partial\Psi}{\partial z} = \frac{1}{r\delta}\left(\left(\frac{\partial\Psi}{\partial\eta}\right)\left(\frac{\partial r}{\partial\xi}\right) - \left(\frac{\partial\Psi}{\partial\xi}\right)\left(\frac{\partial r}{\partial\eta}\right)\right) \qquad \text{(A.31b)}$$

These equations can be discretized and applied on the computational grid straightforwardly. The velocity components on the grid nodes (with uniform spacing $\Delta\xi = \Delta\eta = 1$) are computed by central difference approximations:

$$c_{z,i,j} = \frac{1}{4r_{i,j}\delta_{i,j}}\left[(\Psi_{i,j+1} - \Psi_{i,j-1})(z_{i+1,j} - z_{i-1,j}) - (\Psi_{i+1,j} - \Psi_{i-1,j})(z_{i,j+1} - z_{i,j-1})\right]$$
$$\text{(A.32a)}$$

$$c_{r,i,j} = \frac{1}{4r_{i,j}\delta_{i,j}}\left[(\Psi_{i,j+1} - \Psi_{i,j-1})(r_{i+1,j} - r_{i-1,j}) - (\Psi_{i+1,j} - \Psi_{i-1,j})(r_{i,j+1} - r_{i,j-1})\right]$$
$$\text{(A.32b)}$$

B Brumfield Criterion

The Brumfield Criterion as documented by Stripling and Acosta [66] is only applicable to swirl-free inlet conditions (or flow without pre-whirl). Thus, to extend this design criterion to inlet flow with swirl (or pre-whirl) Equation 3.6 has to be modified. Considering the general velocity triangle given in Figure 2.7a the absolute velocity at the inducer inlet can be expressed as:

$$c_1^2 = c_{m1}^2 + c_{\theta1}^2 = c_{m1}^2 + (1 - \delta_r)u_1^2 \tag{B.1}$$

Analogously to the steps explained in Section 3.4.1, the NPSH (Equation 3.6) is modified as follows:

$$H_s = \text{NPSH} = \frac{1}{2g}\left[(1 + \sigma_b)c_{m1}^2 + u_{1s}^2\left(\sigma_b\delta_r^2 + (1 - \delta_r)^2\right)\right] \tag{B.2}$$

Consequently, suction specific (Equation 3.9) has to be transformed to:

$$\Omega_{ss} = \frac{(\pi k \varphi)^{1/2}}{\left(\frac{1}{2}\left[(1 + \sigma_b)\varphi^2 + \sigma_b\delta_r^2 + (1 - \delta_r)^2\right]\right)^{3/4}} \tag{B.3}$$

The optimum flow coefficient is found by differentiation with respect to flow coefficient φ and setting $(\mathrm{d}\Omega_{ss}/\mathrm{d}\varphi) = 0$. This leads to the following formula for the optimum flow coefficient:

$$\varphi = \left(\frac{\sigma_b\delta_r^2 + (1 - \delta_r)^2}{2(1 + \sigma_b)}\right)^{1/2} \tag{B.4}$$

With this the blade cavitation number can be expressed as:

$$\sigma_b = \frac{2\varphi^2 - (1 - \delta_r)^2}{\delta_r^2 - 2\varphi^2} \tag{B.5}$$

It can be verified easily that for swirl-free inlet condition ($\delta_r = 1$) the original relations given in Equation 3.10 and 3.11 are restored. Inserting Equation B.5 into Equation B.3 Brumfield's criterion for inflow with swirl is obtained by:

$$\Omega_{ss}^* = \frac{\Omega_{ss}}{k^{1/2}} = \left(\frac{\pi\left(2\delta_r - \frac{1}{2}\right)^{3/2}\left(\delta_r^2 - 2\varphi^2\right)^{3/2}}{\varphi^2}\right)^{1/2} \tag{B.6}$$

C Conversion Factors for Suction Specific Speed

To convert the suction specific speed to or from its different but commonly used definitions the following relations can be used:

$$n_{ss} \to N_{ss}: \qquad N_{ss} = \left\{ \frac{\left(1.59 \times 10^4 \, \mathrm{gpm}/(\frac{\mathrm{m}^3}{\mathrm{s}})\right)^{1/2}}{(3.28\mathrm{ft}/\mathrm{m})^{3/4}} \right\} \cdot n_{ss} = 51.65 \cdot n_{ss}$$

$$\Omega_{ss} \to n_{ss}: \qquad n_{ss} = \left\{ \frac{60}{2\pi} g^{3/4} \right\} \mathrm{min}^{-1} \cdot \Omega_{ss} = 52.93 \, \mathrm{min}^{-1} \cdot \Omega_{ss}$$

$$\Omega_{ss} \to N_{ss}: \qquad N_{ss} = \left\{ \frac{60}{2\pi} \frac{\left(1.59 \times 10^4 \, \mathrm{gpm}/(\frac{\mathrm{m}^3}{\mathrm{s}})\right)^{1/2}}{(3.28 \, \mathrm{ft}/\mathrm{m})^{3/4}} g^{3/4} \right\} \mathrm{min}^{-1} \cdot \Omega_{ss}$$

$$= 2733.72 \, \mathrm{min}^{-1} \cdot \Omega_{ss}.$$

With the curly braces { } it is indicated, that only the numerical value of the enclosed expression is to be used for the conversion. The conversion factors are obtained by setting $g = 9.81 \, \mathrm{m/s}^2$.

D Impeller Design

The experimental investigations presented in this thesis are carried out with a modified version of the experimental pump developed by Knapp [43]. For this purpose a new impeller is produced, which on the one hand is modified to accommodate the inducer on the same shaft and on the other hand is able to handle the swirl that is generated by the upstream inducer. The meridional section of this impeller is displayed in Figure D.1a. Note that the hub and shroud curve in this plot are extended for the design purpose. An average absolute flow angle of $\alpha = 55°$ is assumed resulting in a swirl number distribution as depicted in Figure D.1b. The swirl number amounts approximately to $\delta_h = 0.66$ at the hub and $\delta_s = 0.80$ at the shroud section. As already indicated in Figure D.1a five blade sections are used for the impeller blade design. The Blade angle distribution is designed in ANSYS BladeGen [4] using Bézier-splines with four control points on each blade section. Figures D.2a and D.2b show the blade angle and blade wrap distributions designed for the impeller. At the leading edge the blade angle is varied from 40.6° at the hub to 22.5° at the shroud. A constant blade angle of 30° is set at the trailing edge. The blade thickness is kept constant at 3 mm and an elliptical rounding is performed at the leading edge. The final mechanical design of the impeller was done using the

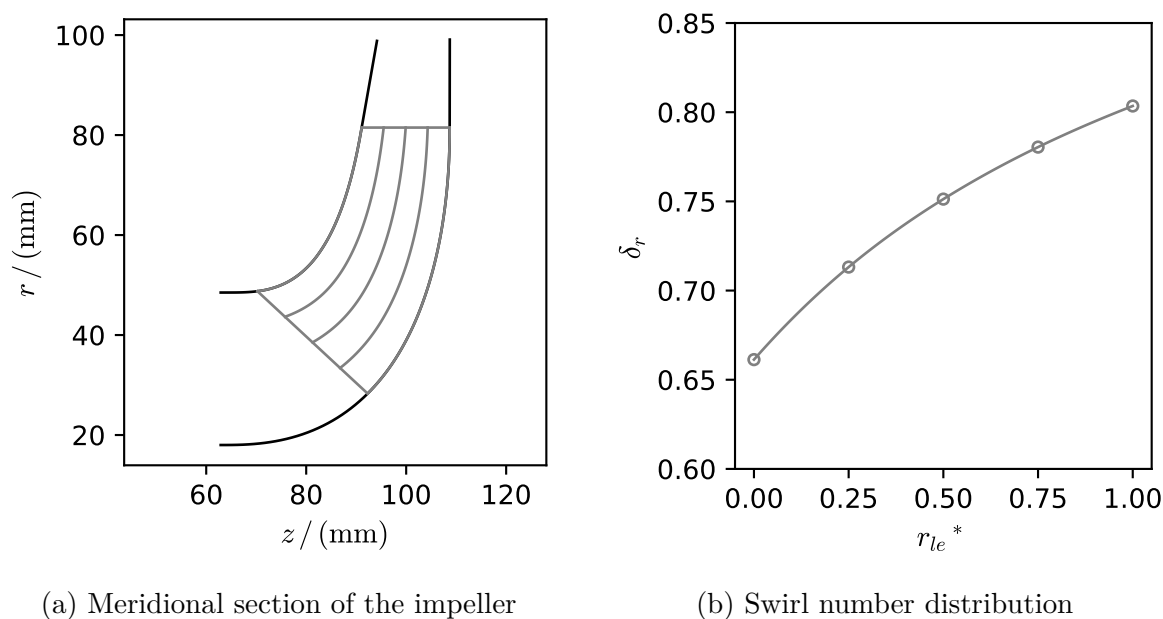(a) Meridional section of the impeller   (b) Swirl number distribution

Figure D.1: Impeller design - meridional section and swirl number

SIEMENS NX CAD system. Considering the requirements of CNC manufacturing the impeller hub and shroud are designed separately. Three countersunk-head bolts are used to fix the shroud to the blades. A threadlocker is used to secure and seal the threads.
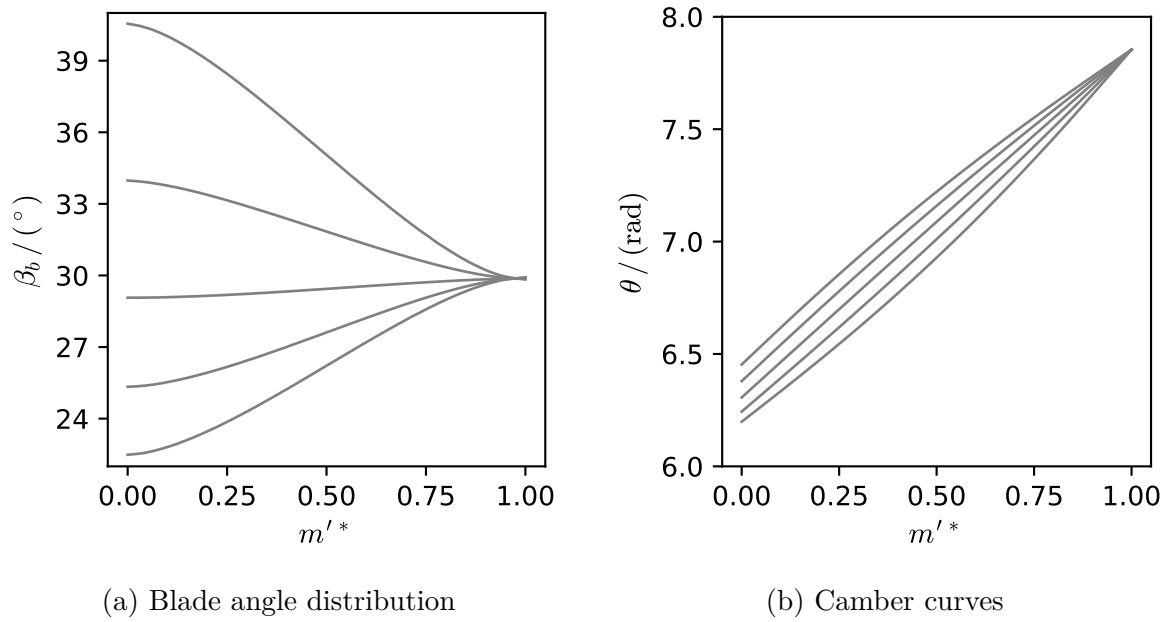
(a) Blade angle distribution

(b) Camber curves

Figure D.2: Impeller design - blade and wrap angle distributions

Because of the high accuracy of the university workshop's equipment nearly perfect fit of the blade tips and the inner shroud contour is obtained such that leakage flows can be assumed to be minimal. As a consequence of this split impeller design there is no fillet between the blade tip and the shroud surface. The fillet between the blade root and the hub is designed with a radius of $2\,\text{mm}$.

E Uncertainty Analysis

Experimental uncertainty analysis is performed based on the guidelines and remarks in DIN EN ISO 9906:2012 [26] and IEC 60193 [34]. The total uncertainty of a measured quantity x is composed of random and systematic uncertainty as follows:

$$u_x = \sqrt{u_{x,r}^2 + u_{x,s}{}^2} \tag{E.1}$$

The process of estimating the uncertainty of the measured data as given above is not uncontroversial. According to the *Guide to the expression of uncertainty in measurement (GUM)* [40] the procedure of separately considering and combining random and systematic uncertainties is equivalent to adding some safety margin to the uncertainty evaluation. In the *GUM* on the other hand no such assumption is made. It either considers random uncertainties, which are based on multiple measurements (Type A evaluation of uncertainty), or uncertainties that do not rely on multiple measurements and make use of other available data like manufacturer's specifications (Type B evaluation of uncertainty). Nevertheless, the method given by standard DIN EN ISO 9906:2012 [26] is applied in this thesis, since it is the currently available standard for pump acceptance tests. However, the law of propagation of uncertainty according to the GUM is used as will be shown below.

In case of repeated measurements as required by standard DIN EN ISO 9906:2012 [26] the random uncertainty can be estimated statistically from the measured data. If n repeated measurements of the quantity x are performed, the arithmetic mean $\overline{x}$ and the standard deviation s are given by:

$$\overline{x} = \frac{1}{n} \sum_{i=1}^{n} x_i \tag{E.2}$$

$$s = \sqrt{\frac{1}{n-1} \sum_{i=1}^{n} (x_i - \overline{x})^2} \tag{E.3}$$

According to standard DIN EN ISO 9906:2012 [26] the random uncertainty of the measured quantity is computed by application of the following formula:

$$u_{x,r} = \frac{t\,s}{\sqrt{n}} \tag{E.4}$$

The value of Student's t depends on the number of measurements n and the level of confidence chosen. Usually a 95 % level of confidence is applied, such that $t = 2.26$ in case of 10 repeated measurements. Values of t for different numbers of repeated measurements

are tabulated in DIN EN ISO 9906:2012 [26]. Since the characteristic values of head, efficiency, power and NPSH are not measured directly, the total uncertainty is composed of the uncertainty of the measured quantities used in their calculation. According to the law of propagation of uncertainty as given in the GUM [40] and with the formulas already provided in Section 4.5.4 the corresponding combined uncertainties can be estimated as follows:

$$u_{H,r/s} = \sqrt{\left(\frac{\partial H}{\partial(\Delta p)}\right)^2 u_{\Delta p,r/s}^2 + \left(\frac{\partial H}{\partial Q}\right)^2 u_{Q,r/s}^2} \tag{E.5a}$$

$$u_{P,r/s} = \sqrt{\left(\frac{\partial P}{\partial M}\right)^2 u_{M,r/s}^2 + \left(\frac{\partial P}{\partial n}\right)^2 u_{n,r/s}^2} \tag{E.5b}$$

$$u_{\eta,r/s} = \sqrt{\left(\frac{\partial \eta}{\partial(\Delta p)}\right)^2 u_{\Delta p,r/s}^2 + \left(\frac{\partial \eta}{\partial Q}\right)^2 u_{Q,r/s}^2 + \left(\frac{\partial \eta}{\partial M}\right)^2 u_{M,r/s}^2 + \left(\frac{\partial \eta}{\partial n}\right)^2 u_{n,r/s}^2} \tag{E.5c}$$

$$u_{\text{NPSH},r/s} = \sqrt{\left(\frac{\partial(NPSH)}{\partial p}\right)^2 u_{p,r/s}^2 + \left(\frac{\partial(NPSH)}{\partial Q}\right)^2 u_{Q,r/s}^2} \tag{E.5d}$$

Because above equations are applicable to the random uncertainty as well as to the systematic uncertainty either index r or s is valid, which is indicated by writing the index as r/s. The partial derivatives occurring in Equation E.5 are obtained from the formulas used for the computation of the characteristic values as given in Equations 2.25, 2.36, 2.37 and 2.38:

$$\left(\frac{\partial H}{\partial(\Delta p)}\right) = \frac{1}{\rho g}$$

$$\left(\frac{\partial H}{\partial Q}\right) = \frac{Q}{g}\left[\frac{1}{A_2^2} - \frac{1}{A_1^2}\right]$$

$$\left(\frac{\partial P}{\partial M}\right) = 2\pi n$$

$$\left(\frac{\partial P}{\partial n}\right) = 2\pi M$$

$$\left(\frac{\partial \eta}{\partial Q}\right) = \frac{\Delta p}{2\pi M n} + \frac{3\rho Q^2}{4\pi M n}\left[\frac{1}{A_2^2} - \frac{1}{A_1^2}\right]$$

$$\left(\frac{\partial \eta}{\partial(\Delta p)}\right) = \frac{Q}{2\pi M n}$$

$$\left(\frac{\partial \eta}{\partial M}\right) = -\frac{\Delta p Q}{2\pi M^2 n} - \frac{\rho Q^3}{4\pi M^2 n}\left[\frac{1}{A_2^2} - \frac{1}{A_1^2}\right]$$

$$\left(\frac{\partial \eta}{\partial n}\right) = -\frac{\Delta p Q}{2\pi M n^2} + \frac{\rho Q^3}{4\pi M n^2}\left[\frac{1}{A_2^2} - \frac{1}{A_1^2}\right]$$

$$\left(\frac{\partial \text{NPSH}}{\partial p}\right) = \frac{1}{\rho g}$$

$$\left(\frac{\partial \text{NPSH}}{\partial Q}\right) = \frac{Q}{g A_1^2}$$

Introducing these expressions into Equations E.5 the following formulas can be used to evaluate the combined uncertainties (either random or systematic) for head, power, efficiency and NPSH:

$$u_{H,r/s} = \sqrt{\left(\frac{1}{\rho g}\right)^2 u_{\Delta p,r/s}^2 + \left(\frac{Q}{g}\left[\frac{1}{A_2^2} - \frac{1}{A_1^2}\right]\right)^2 u_{Q,r/s}^2} \tag{E.7a}$$

$$u_{P,r/s} = 2\pi\sqrt{(n)^2 u_{M,r/s}^2 + (M)^2 u_{n,r/s}^2} \tag{E.7b}$$

$$u_{\eta,r/s} = \frac{1}{2\pi}\left\{\left(\frac{Q}{Mn}\right)^2 u_{\Delta p,r/s}^2 + \left(\frac{\Delta p}{Mn} + \frac{3\rho Q^2}{2Mn}\left[\frac{1}{A_2^2} - \frac{1}{A_1^2}\right]\right)^2 u_{Q,r/s}^2 \right.$$

$$+ \left(\frac{\Delta p Q}{M^2 n} + \frac{\rho Q^3}{2M^2 n}\left[\frac{1}{A_2^2} - \frac{1}{A_1^2}\right]\right)^2 u_{M,r/s}^2$$

$$\left. + \left(\frac{\Delta p Q}{2\pi M n^2} + \frac{\rho Q^3}{4\pi M n^2}\left[\frac{1}{A_2^2} - \frac{1}{A_1^2}\right]\right)^2 u_{n,r/s}^2\right\}^{1/2} \tag{E.7c}$$

$$u_{\text{NPSH},r/s} = \sqrt{\left(\frac{1}{\rho g}\right)^2 u_{p,r/s}^2 + \left(\frac{Q}{g A_1^2}\right)^2 u_{Q,r/s}^2} \tag{E.7d}$$

Note that these equation are derived under the assumption that gravitational acceleration g, vapor pressure p_v and the mean value of density ρ are free of uncertainties during measurements (see IEC 60193 [34]). To calculate the actual values of uncertainty of a quantity the mean values of the measured values are inserted in the above equations.

The systematic uncertainty is estimated based on the accuracy specifications provided by the sensor manufacturers. Typically the uncertainty $u_{x,s}^*$ relative to the full range $(\Delta x)_{\text{max}}$ of the sensor is specified by the manufacturer. Thus, the uncertainty can be calculated by:

$$u_{x,s} = u_{x,s}^* \cdot (\Delta x)_{\text{max}} \tag{E.8}$$

The relative (total) uncertainty, which is used to judge the class of acceptance test accuracy, is consequently obtained by calculating:

$$u_x^* = \frac{\sqrt{u_{x,r}^2 + u_{x,s}^2}}{\overline{x}} \tag{E.9}$$

Table 4.11 includes the estimated systematic uncertainties of the sensors employed in the measurements performed during the work on this thesis. Even though the uncertainty of efficiency measurement could be estimated with the help of the formulas presented in this section, standard DIN EN ISO 9906:2012 [26] provides the following, substantially simpler formula:

$$u_\eta^* = \sqrt{u_Q^* + u_H^* + u_M^* + u_n^*} \tag{E.10}$$

To keep the analysis consistent, this formula is not used in this thesis. Nevertheless, it was checked that similar values of uncertainty result from both formulas. Once the uncertainty is estimated, the real value of x can be assumed to lie in the range $\overline{x} \pm u_x$ with a certain level of confidence.

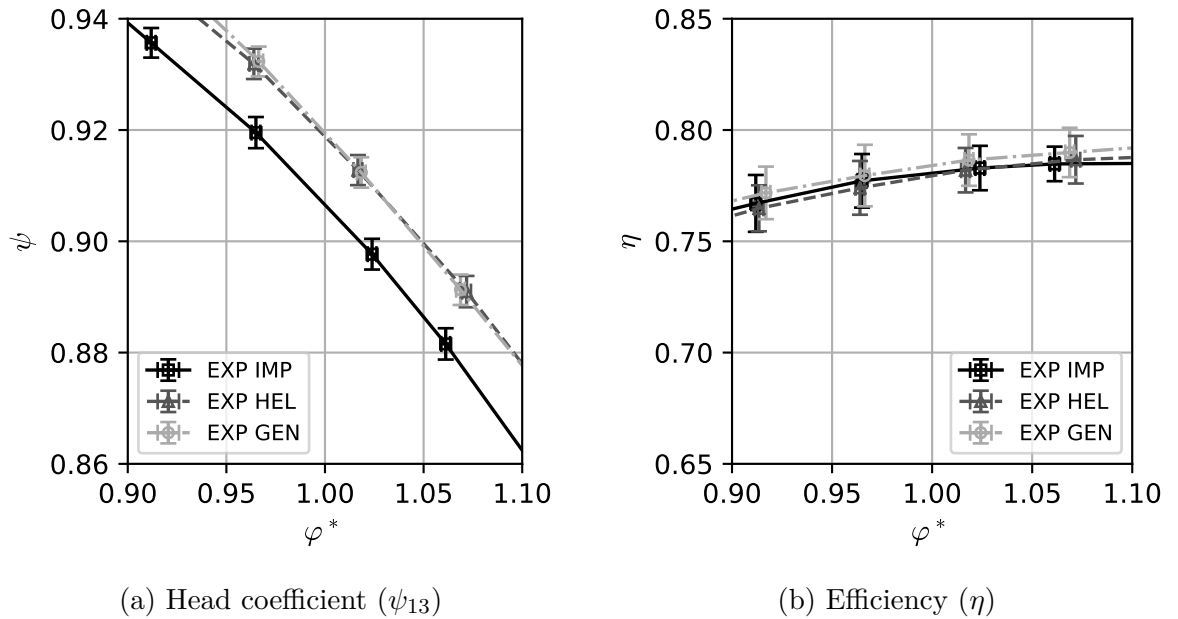(a) Head coefficient (ψ_{13})   (b) Efficiency (η)

Figure E.1: Uncertainty intervals of head measurement for all pump configurations

Uncertainty of the actual measurements performed in the course of this thesis is evaluated with help of the relations discussed above. In the detail view of the full head characteristic shown in Figure E.1a the confidence interval of each measured mean value is illustrated in form of error bars for flow and head coefficient. Obviously, the relative

uncertainty intervals are small for the flow coefficient as well as for the head coefficient and would be barely visible in the full plot of the head characteristic.

The same is true for the other quantities of interest and for NPSH test runs as well. Figure E.1b exemplarily shows the the uncertainty intervals for efficiency during the head measurements. Although the confidence intervals appear larger than the ones previously shown for head coefficient, the relative uncertainty for almost all operating conditions lies below the levels required by standard DIN EN ISO 9906:2012 [26].   This is illustrated

(a) Flow rate (Q)

(b) Head (H)
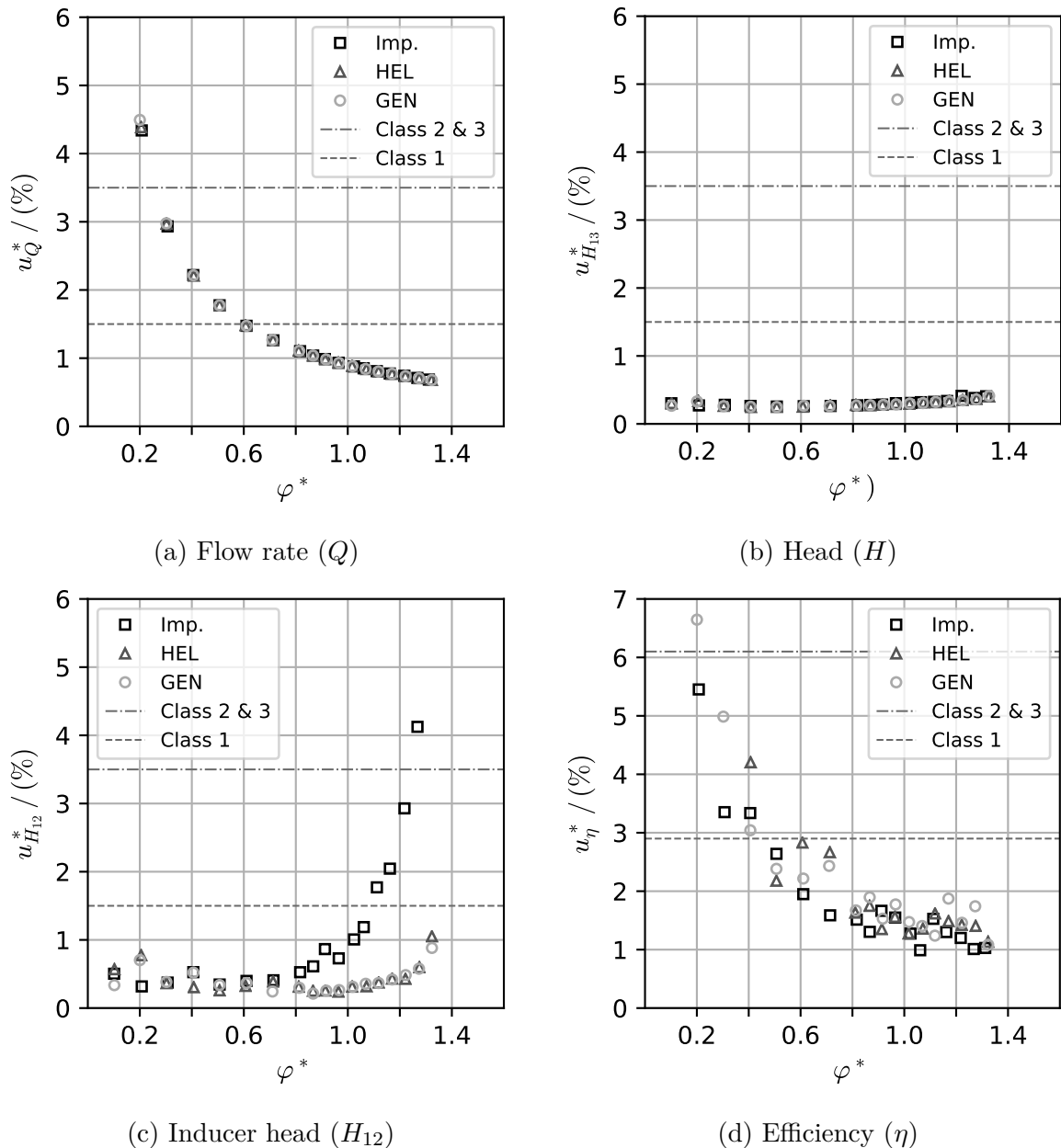
(c) Inducer head (H_{12})

(d) Efficiency (η)

Figure E.2: Relative uncertainties for head characteristic measurements

in Figures E.2 for the quantities obtained from a non-cavitating head characteristic

(a) Head (H_{13})

(b) Inducer head (H_{12})

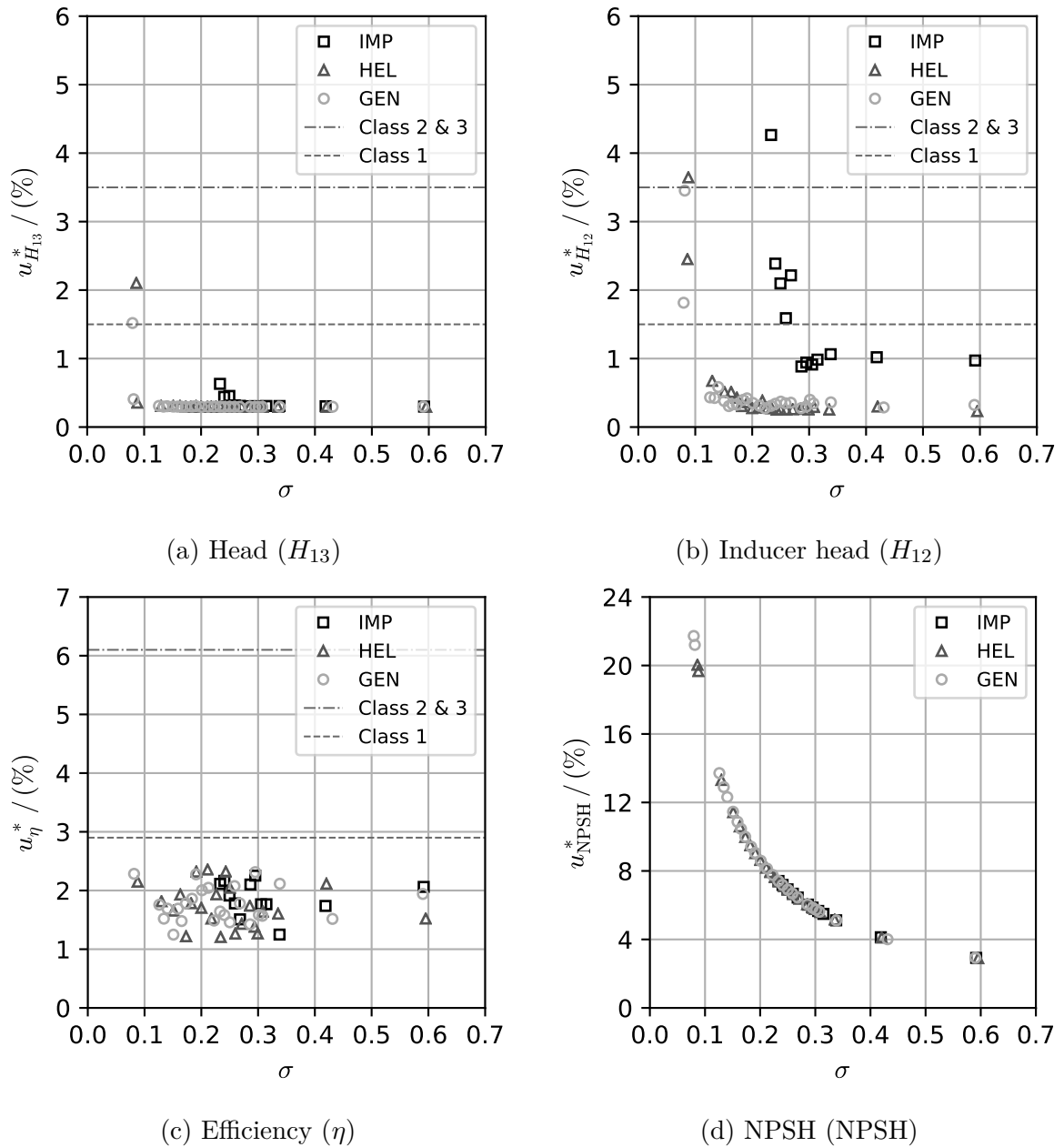(c) Efficiency (η)

(d) NPSH (NPSH)

Figure E.3: Relative uncertainties for NPSH characteristic measurements ($\varphi^* = 1$)

measurement and in Figure E.3 for the head drop (NPSH) measurements at design flow rate ($\varphi* = 1$). Besides the relative uncertainty of the measurements, the uncertainty levels according to standard DIN EN ISO 9906:2012 [26], if available, are included in the figure. Most of the operating points have been acquired with an uncertainty lower than the requirements of class 1. However, as soon as the signals approach the lower measuring range limit as is the case for flow rate (Figure E.2a) and NPSH (Figure E.3d) at the operating points at low values of flow and cavitation coefficient, respectively. In case of the head characteristic this also causes an increased uncertainty of efficiency

(Figure E.2d). The same effect is observed for the measurements of inducer head (H_{12}) as depicted in Figure E.2c for pump IMP where no inducer is installed. In this case the pressure differences approach zero at overload and thus the relative uncertainty rises. At the same time the pump head (H_{13}) remains basically unaffected (Figure E.2b). Induced by the identical mechanism the uncertainty rises for the head measurement when the differential pressure drops due to cavitation (see Figures E.3a and E.3b) during NPSH measurements. Nevertheless, relative uncertainties of pump head and efficiency (Figures E.3a and E.3c) remain acceptable. The effects discussed above are natural behavior and in general cannot be avoided without switching to different sensors during measurement or limiting the measurement range of the whole test bench. In case of the NPSH measurement, which depends mainly on the range and accuracy of the inlet absolute pressure sensor, a different sensor could be applied to reduce uncertainty at low inlet pressures. Measurement range of this sensor could at least be halved without limiting the operating range of the test bench. Another effect that might influence accuracy of NPSH measurements in the present test bench configuration is that at low cavitation coefficients vapor bubbles are recirculating upstream of the inducer and could possibly cause faulty suction pressure measurements.

Lebenslauf

Name: Matthias Mohr

Ausbildung

10/2007 - 04/2014   TU Kaiserslautern
Studium Maschinenbau und Verfahrenstechnik
Schwerpunktfach: Energietechnik
Abschluss: Diplom-Ingenieur Maschinenbau

02/2012 - 07/2012   Universidad del País Vasco, Spanien
Auslandssemester, Fachrichtung Ingeniería mecánica

10/2006 - 09/2007   Fachhochschule Trier, Standort Umwelt-Campus Birkenfeld
Studium im Studiengang Physikingenieurwesen

08/1997 - 06/2006   Gymnasium am Rotenbühl, Saarbrücken
Abschluss mit allgemeiner Hochschulreife

Beruflicher Werdegang

04/2020 - heute   Entwicklungsingenieur, KSB SE & Co. KGaA

05/2014 - 03/2020   Wissenschaftlicher Mitarbeiter
Technische Universität Kaiserslautern
Lehrstuhl für Strömungsmechanik und Strömungsmaschinen

03/2013 - 08/2013   Fachpraktikum
Voith Hydro Holding GmbH & Co. KG, Heidenheim

05/2011 - 04/2014   Wissenschaftliche Hilfskraft
Technische Universität Kaiserslautern
Lehrstuhl für Strömungsmechanik und Strömungsmaschinen

10/2010 - 01/2012   Wissenschaftliche Hilfskraft
Technische Universität Kaiserslautern
Lehrstuhl für Technische Mechanik

04/2009 - 12/2009   Werksstudent
Stetzer Ingenieurbüro für Umwelttechnik
und Analytik GmbH, St. Wendel